Single-molecule FRET studies in live bacteria

Anne Plochowietz

A thesis submitted in partial fulfilment of the requirements for the degree of

Doctor of Philosophy at the University of Oxford

Balliol College

University of Oxford

Trinity Term 2015

“Laß die Moleküle rasen,

was sie auch zusammenknobeln!

Laß das Tüfteln, laß das Hobeln,

heilig halte die Ekstasen!”

— Christian Morgenstern

Galgenlieder, 1905

Disclaimer

I hereby declare that the work in this thesis is that of the candidate alone, except where indicated at the end of each chapter, and as described below.

- The microscope setups were designed and built by Dr. Ludovic Le Reste (Appendix A.1), Dr. Geraint Evans, and Dr. Johannes Hohlbein (Appendix A.2).
- Single-molecule fluorescence burst analysis software was developed by Dr. Johannes Hohlbein.
- Hidden Markov Modelling analysis scripts were implemented by Dr. Kristofer Gryte.
- Initial localisation, tracking, and cell-normalisation software was developed by Dr. Seamus Holden, Dr. Stephan Uphoff, and Mathew Stracy, respectively.

Anne Plochowietz
December, 2015

SINGLE-MOLECULE FRET STUDIES IN LIVE BACTERIA

Anne Plochowietz, Balliol College
(Biological Physics Research Group, Department of Physics)

Thesis submitted for the degree of *Doctor of Philosophy* at the University of Oxford,
Trinity Term 2015.

ABSTRACT

Single-molecule fluorescence and single-molecule Förster resonance energy transfer (FRET) have proven enormously successful in understanding molecular and cellular processes over the last two decades. However, *in vivo* single-molecule FRET studies are still very difficult, mainly because they require site-specifically labelled biomolecules with photostable organic dyes.

In this work, I established single-molecule FRET studies in live bacteria and applied the developed method to study mechanisms of gene expression and gene regulation. To begin with, I optimised a recently developed internalisation method based on electroporation for the efficient loading of bacterial cells with organic dye-labelled nucleic acids and proteins while maintaining cell viability.

Next, I evaluated organic dyes for their performance in live-cell FRET studies and characterised *in vivo* single-molecule FRET efficiencies using DNA FRET standards. Combining the single-molecule FRET capability with single-particle tracking, I traced protected DNA FRET standards, probed the internalisation of doubly-labelled protein complexes, and studied protein conformational states, and the bending of a gapped DNA substrate in live *E. coli*.

Following these studies, I internalised labelled tRNA molecules, measured their diffusion coefficient, and showed that most tRNA molecules diffuse freely in live bacteria. I also showed that bound tRNA molecules are predominantly at the cell periphery and compete with the endogenous tRNA pool during translation using antibiotic controls and simulations.

Finally, I studied transcription initiation *in vivo* by internalising promoter DNAs with different FRET labelling schemes reporting on individual steps in transcription initiation. Thus, I observed single-molecule FRET signatures attributed to open complex formation, DNA scrunching during initial transcription, and promoter escape, which were not present in null-promoter DNA and antibiotic controls.

By carefully designing single-molecule FRET assays, I imagine single-molecule FRET studies to become a major tool in understanding protein dynamics, and elucidating mechanistic details of gene regulation processes in living cells.

Acknowledgements

I am very grateful to all the people who helped me during my DPhil studies – I would like to thank Prof. Achillefs Kapanidis for his constant support of my work and approving the PhD-motto “work hard and play ~~hard~~football”.

I very much enjoyed working in the Kapanidis group and I would like to thank all members of the group – old and new, downstairs and upstairs. Many thanks for advice and fruitful discussions go to Dr. David Bauer, Dr. Timothy Craggs, Dr. Stephan Uphoff, and Dr. Pawel Zawadzki. I would like to thank Dr. Louise Aigrain, Dr. Robert Crawford, and Marko Sustarsic for their help on the electroporation project, Federico Garca de Leon, and Mathew Stracy for comments on the tRNA project, and Dr. David Bauer, Dr. David Dulin, Dr. Anssi Malinen, Dr. Nicole Robb, and Dr. Alexandra Tomescu for their advice and suggestions on the *in vivo* transcription initiation project.

Special thanks and hugs go to Alexandra, David, FedeNouk, Marko, and Ronja for their friendship and getting me away from the lab and football every so often, and to Kat Coyte for getting us into football and other fun. I will also keep fond memories of the sportive night owls Bastiaan Leerkotte, and Athan Reines – many thanks for chats during night shifts and runs around Uni Parks, or the Pacific coast.

For comments on thesis chapters and editorial assistance I would like to thank Dr. David Bauer, Dr. Timothy Craggs, Dr. David Dulin, Felix Geyer, Dr. Anssi Malinen and Dr. Alexandra Tomescu.

I am grateful to my collaborators Dr. Afaf El-Sagheer and Prof. Tom Brown for the synthesis of protected DNA FRET standards, and my collaborators on the tRNA project: Dr. Ian Farrell, Dr. Zeev Smilansky, and Prof. Barry Cooperman.

This work would not have been possible without the financial support of the German National Academic Foundation (Studienstiftung), and the DTA studentship of the Engineering and Physical Sciences Research Council (EPSRC). Additionally, I am grateful to Balliol College, Oxford, for awarding me with the Phizackerley Senior scholarship in Medical Sciences and for the financial support of my conference travels. I am very thankful to Dr. Richard Berry, Prof. Jörg Enderlein, Prof. Achillefs Kapanidis, and Prof. Markus Sauer for their support of my applications for these fellowships.

Der größte Dank gilt jedoch meiner Mutter und meinem Vater für deren Liebe, Rückhalt und andauernde Unterstützung meiner Vorhaben und universitären Ausbildung. Ein wichtiger Rückzugspunkt und Kraftquelle für mich ist mein langjähriger Freund Felix Geyer – dafür vielen Dank! Weiterhin danke ich meiner Familie und Freunden, die noch kein einzelnes Molekül gesehen haben, für deren Fürsorge und Interesse an meiner Arbeit.

Anne Plochowietz, Oxford, August, 2015

Published work arising from the DPhil studies

TD Craggs*, M Sustarsic*, **A Plochowietz**, M Mosayebi, H Kaju, A Cuthbert, J Hohlbein, P Biggin, J Doye, and AN Kapanidis. “Structure and mechanism of DNA polymerase I revealed by in vitro, in vivo, and in silico single-molecule studies”, in preparation. *equal contribution.

A Afanzar, D Di Paolo, R Nevo, Y Ran, M Eisenstein, **A Plochowietz**, AN Kapanidis, RM Berry, and M Eisenbach. “Hidden dynamics of CheY at the switch of the bacterial flagellar motor”, in preparation.

A Plochowietz, AH El-Sagheer, T Brown, AN Kapanidis. Protected DNA FRET Standards for *In Vivo* Single-Molecule FRET Studies. *Angewandte Chemie Int Ed*, under review.

A Plochowietz, I Farrell, Z Smilansky, BS Cooperman, and AN Kapanidis. Single-molecule tracking of tRNA shows that most tRNA diffuses freely in live bacteria. *Nucleic Acid Res*, in revision.

A Plochowietz and AN Kapanidis. Single in the (Cell) City: a protein-folding story. *Nat Methods*, 12(8), 2015.

TJ Nott, E Petsalaki, P Farber, D Jervis, E Fussner, **A Plochowietz**, TD Craggs, DP Bazett-Jones, T Pawson, JD Forman-Kay, and AJ Baldwin. Phase Transition of a Disordered Nuage Protein Generates Environmentally Responsive Membraneless Organelles. *Mol Cell*, 57, 936-947, 2015.

L Aigrain, M Sustarsic, R Crawford, **A Plochowietz**, AN Kapanidis. Internalization and Observation of Fluorescent Biomolecules in Living Microorganisms via Electroporation. *JoVE*, 96, e52208, 2015.

A Plochowietz, R Crawford, AN Kapanidis. Characterization of organic fluorophores for *in vivo* FRET studies. *Phys Chem Chem Phys*, 16:12688-12694, 2014.

M Sustarsic, **A Plochowietz**, L Aigrain, Y Yuzenkova, N Zenkin, AN Kapanidis. Optimized delivery of fluorescently labeled proteins in live bacteria using electroporation. *Histochem Cell Biol*, 142(1), 2014.

R Crawford*, JP Torella*, L Aigrain*, **A Plochowietz***, K Gryte, S Uphoff, AN Kapanidis. Long-lived, ultrasensitive intracellular fluorescence using electroporated biomolecules. *Biophys J*, 105(11), 2013. *equal contribution.

Conference Presentations

21st Single Molecule Workshop
PicoQuant, Berlin, Germany September, 2015
Best student talk award: “Mobility and spatial distribution of transfer RNA (tRNA) in live bacteria using single-molecule tracking.”

11th Nucleic Acid Forum
Royal Chemical Society, London, UK July, 2015
Poster presentation: “Real-time transcription initiation by *E. coli* RNA polymerase *in vitro* and *in vivo*.”

59th Biophysical Society Meeting
Baltimore, USA February, 2015
Invited talk: “Real-time transcription initiation by *E. coli* RNA polymerase *in vitro* and *in vivo*.”

8th Biennial Single Molecule Biophysics Meeting
Aspen, USA January, 2015
Delivered talk: “Real-time transcription initiation by *E. coli* RNA polymerase *in vitro* and *in vivo*.”

Seminar “Fluorescence – Dye Synthesis and Application”
Hanse-Wissenschaftskolleg, Delmenhorst, Germany November, 2014
Invited talk: “FRET – Studying conformational changes *in vitro* and *in vivo*.”

Biennial British Biophysical Society Meeting
Warwick, UK July, 2014
Poster prize: “Characterization of single-molecule FRET in living bacteria using protected DNA FRET standards.”

10th Nucleic Acid Forum
Royal Chemical Society, London, UK July, 2014
Poster prize: “Characterization of single-molecule FRET in living bacteria using protected DNA FRET standards.”

58th Biophysical Society Meeting
San Francisco, USA February, 2014
Delivered talk: “Combining accurate FRET and tracking of single protein and DNA molecules in live bacteria.”

3rd Single-molecule localization microscopy symposium
Frankfurt, Germany August, 2013
Delivered talk: “Single-molecule fluorescence and FRET in live bacteria using electroporated biomolecules.”

9th Nucleic Acid Forum
Royal Chemical Society, London, UK July, 2013
Delivered talk: “Single-molecule FRET in live bacteria using electroporated molecules.”

Biological Physics Seminar
Oxford, UK November, 2012
Delivered talk: “Long-lived ultrasensitive fluorescence in living bacteria using electroporated biomolecules.”

Contents

Chapter 1

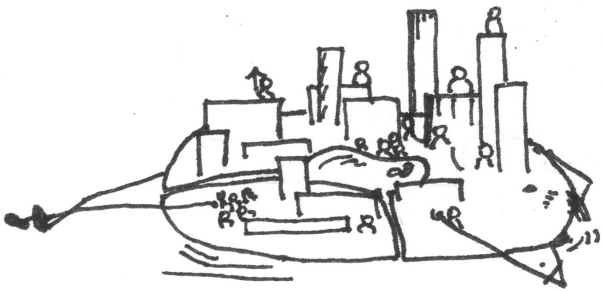

Introduction

Single-molecule fluorescence (1, 2) and super-resolution microscopy (3, 4) are non-invasive imaging tools that have revolutionised life science research within the last 10 years, allowing us to observe fundamental biological processes occurring at cell membranes (5, 6), in infectious and cancerous cells (7), as well as to understand the activity of important enzymes involved in gene expression and regulation (8, 9) with unforeseen high precision.

Single-molecule fluorescence studies report on states of individual biomolecules giving direct access to molecular heterogeneities, complex reaction trajectories, and conformational dynamics that are inaccessible to ensemble measurements (10). Imagine, for instance, a biomolecule that can exist in two states (green and red), and that can reversibly switch between these two states (Fig. 1.1). From ensemble measurements neither the individual state (static heterogeneity), nor the interconversion between the two states (dynamic heterogeneity) can be elucidated.

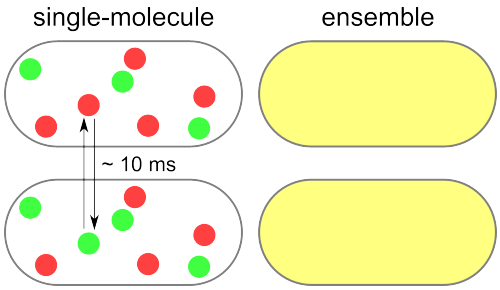

Figure 1.1: Single-molecule detection versus ensemble averaging.

Over the last two decades, single-molecule fluorescence microscopy has proven tremendously successful in understanding molecular and cellular processes. Pioneering work by the Keller group (11), the Moerner lab (12), and others boosted single-molecule detection capability from direct detection of single molecules in solution and crystals in the early 1990s (13, 14, 15) to the first single-molecule fluorescence detection in live cells about ten years later (16, 17, 8).

However, this would not have been possible without the development of novel fluorescent probes for live-cell imaging utilising exogenous fluorescent proteins like the green fluorescent protein (GFP) and aequorin (18). From the first expression of GFP in *Escherichia coli* and *Caenorhabditis elegans* in 1994 (19), GFP and its variants have been introduced and expressed as protein markers in many model organisms (20). Not surprisingly in 2008, the Nobel Prize in Chemistry was awarded to Martin Chalfie, Osamy Shimomura, and Roger Tsien "for the discovery and development of the green fluorescent protein (GFP)".

Further understanding and engineering of the properties of fluorescent proteins and organic fluorophores has helped to manipulate on/off-states of these fluorophores to obtain a low density of emitting fluorophores to support single-molecule detection (21, 22, 23). By utilising the stochastic cycling between on/off-states of fluorophores and the sequential localisation of fluorophores (24), imaging with a high spatial resolution beyond Abbé's diffraction limit[1] became possible as was first demonstrated by Eric Betzig and the Zhuang lab in 2006 (26, 27). These types of single-molecule localisation microscopy imaging were further developed, giving rise to PALM (28, 29), FPALM (30), STORM (31, 32), dSTORM (33), and PAINT (34) imaging techniques, which are now commonly used within the scientific community. In addition, the fluorescence emission can be manipulated by employing a doughnut-shaped laser beam

[1] In 1873, Ernst Abbé derived the diffraction-limited lateral resolution of a conventional light microscope: $\Delta x = \frac{\lambda}{2\mathrm{NA}}$, in which λ is the wavelength of light, and NA is the numerical aperture of microscope objective (25).

to selectively deactivate fluorophores and allow sub-diffraction limited imaging (35). Such termed stimulated emission depletion (STED) microscopy was first experimentally demonstrated by Hell and coworkers in 1999 (36). Last year, Eric Betzig, Stefan W Hell, and William E Moerner were awarded the Nobel Prize in Chemistry "for the development of super-resolved fluorescence microscopy".

Undoubtedly, the latest developments in single-molecule fluorescence imaging have strengthened the position of light microscopy as the most widely used technique in life sciences today.

Within the field of single-molecule fluorescence, researchers very quickly became aware of the importance of studying the structure of single proteins and their functioning under physiological conditions, inside the cellular environment (37). While *in vitro* experiments allow a better control over experimental variables, molecular crowding within the viscous cellular cytosol, compartmentalisation, macromolecular interactions, and cellular feedback systems drastically affect protein binding rates and conformational changes, and cannot be mimicked *in vitro* (38).

In vivo single-molecule fluorescence studies utilising fluorescent proteins (FP) were first performed in *Caulobacter crescentus* cells in 2004 (17) and in *E. coli* cells in 2006 (8). In these studies, FP fusions were used (i) to localise and track individual proteins and monitor changes in copy numbers (5, 39), (ii) to study gene expression and regulation at the single-molecule level (8, 40), and even proteome-wide (41), and (iii) to show how single molecule binding events are capable of altering cellular phenotypes (42), and mediate cellular stress responses (43).

But FP-based single-molecule fluorescence studies are limited by the 6-fold lower brightness and 100-fold lower photostability of fluorescent proteins compared to their organic dye counterparts (44, 45). First, the higher photon budget and slower photobleaching rates make organic fluorophores better suited for single-molecule localisation and single-particle tracking studies than FPs. Second, organic fluorophores

offer more freedom for site-specific protein labelling, and even intra-molecular labelling, since organic dyes are about 100-fold smaller compared to FPs and so are less likely to interfere with protein structure and function.

Intra-molecular labelling strategies are of great importance when performing single-molecule Förster resonance energy transfer (FRET) studies, another important single-molecule fluorescence technique. FRET serves as a molecular ruler in the 2-10 nm range offering down to 0.5 nm spatial resolution and hence, is ideally suited to studying protein structure and conformational changes (46). Compared to other structural methods, such as X-ray crystallography and cryo-electron microscopy, which mainly report on structural snapshots, FRET can directly capture protein dynamics, *in vitro* and *in vivo*. Förster resonance energy transfer describes the non-radiative energy transfer between a donor-dye and an acceptor-dye in close proximity, and is strongly dependent on the dye's spectral overlap, distance and orientation (47, 48). Mechanistic details of nucleic acid and protein folding (49, 50, 51) as well as different conformational states of DNA Polymerase I (52, 53, 54) were observed using single-molecule FRET *in vitro*. These observations helped to validate the fidelity of the replication machinery.

However, *in vivo* single-molecule FRET studies are limited by requirements on the FRET dye-pair fluorophores, *in vivo* labelling strategies, and imaging techniques offering high temporal and spatial resolution inside a living cell. To illustrate the challenge: Visualising conformational changes of ~ 10 ms for an individual protein molecule during one cell cycle is akin to observing a single person's movement amidst the hectic environment of a big city like London (Fig. 1.2). Streets, cars, and busses are crowded with millions of other people in the 10^9-times larger 'cell-like' city and the observation of, for instance, a specific person taking a seat becomes very challenging.

As a result, only a few live-cell FRET studies were reported so far. While studies using

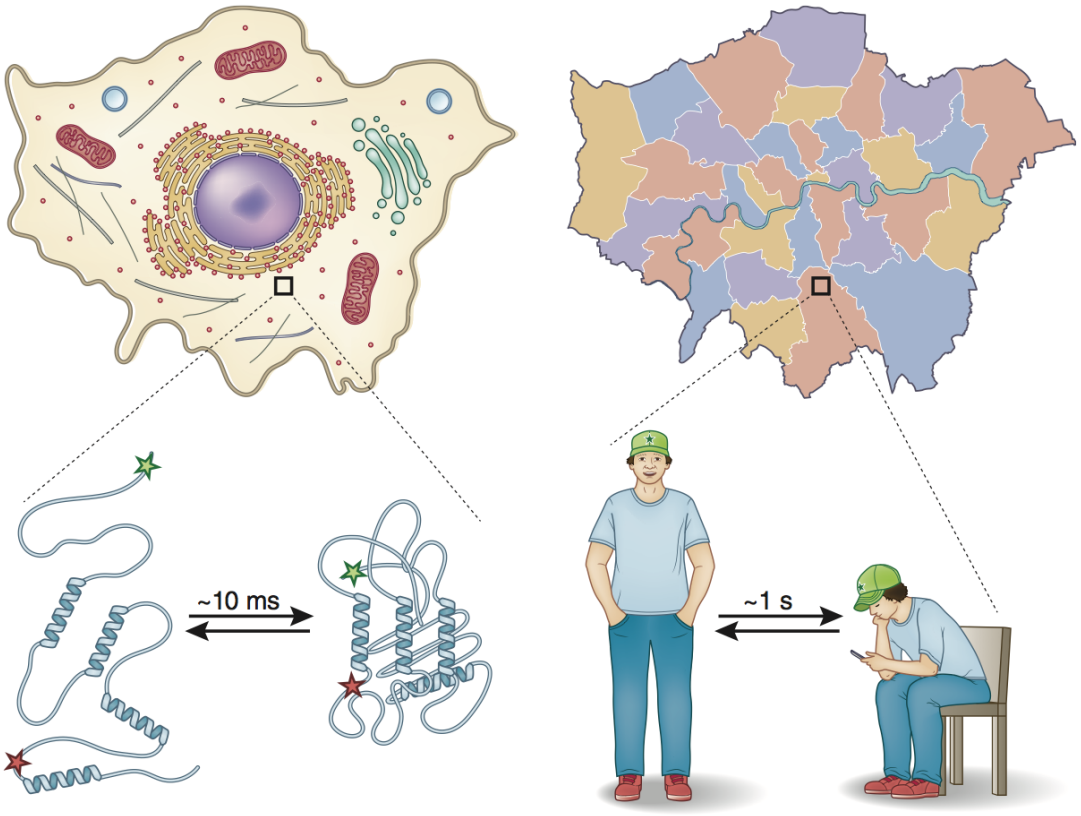

Figure 1.2: *In vivo* single-molecule FRET studies. Monitoring conformational changes of individual molecules (protein folding) in living cells using single-molecule FRET is as challenging as observing a single person's actions (taking a seat) among millions within a big city as viewed from a satellite. Taken from (55), artistic design by Debbie Maizels, Nature Publishing Group.

fluorescent proteins lack single-molecule sensitivity (56, 57, 58), more photostable organic fluorophores cannot be genetically encoded and, hence, need to be either introduced *in vivo* by internalising dyes for specific protein labelling via large polypeptide tags or unnatural amino acids, or through internalisation of organic dye-labelled proteins into living cells (59). The majority of single-molecule FRET studies in living cells apply the latter strategy, *in vitro* labelling followed by internalisation of the protein of interest. In an early study by Sakon and Weninger in 2010, a membrane-fusion protein was microinjected into mammalian cells and its binding to the cell membrane and complex formation was monitored (60). In this study, microinjection was first used to introduce doubly-labelled proteins into live mammalian cells. This year, König *et al.*

probed protein conformational dynamics with nanosecond to millisecond temporal resolution in live mammalian cells by performing single-molecule FRET spectroscopy studies on a temperature-controlled microscope optimised for microinjection and cell cultivation (61, 55). We recently presented a versatile and high-throughput method to internalise doubly-labelled DNA fragments and DNA binding proteins into live bacteria using electroporation (62). To successfully employ single-molecule FRET studies *in vivo*, the three major challenges must be overcome: (i) live-cell imaging, (ii) *in vivo* labelling, and (iii) FRET-dye pair selection (59).

Outline of thesis

In this work, I established single-molecule FRET capability *in vivo*, characterised single-molecule fluorescence and FRET signals, and employed single-molecule FRET assays to study processes related to gene expression and regulation in live bacteria. In chapter 2, I introduce the principles of single-molecule fluorescence and FRET detection and explain the imaging techniques used within this work. Next, I focus on the *in vivo* labelling aspect by optimising the electroporation protocol for the internalisation of organic dye-labelled nucleic acids and proteins into live bacteria in chapter 3; especially studying the balance of cellular uptake and cell viability. In chapter 4, I systematically evaluate organic fluorophores for their use in *in vivo* single-molecule FRET studies, and characterise FRET at the single-cell and single-molecule level using DNA FRET standards. Combining single-molecule FRET measurements with single-particle tracking *in vivo*, I present three initial single-molecule FRET studies reporting on: (i) the observation of a protein complex, (ii) conformational states and dynamics of a DNA binding protein, and (iii) bending of a gapped DNA fragment in live bacteria.

Single-molecule fluorescence and FRET *in vivo* can be also applied to the study of tRNAs (chapter 5), and multi-step, complex biological processes, such as initiation

of transcription in live bacteria (chapter 6). In chapter 5, I internalise organic dye-labelled transfer RNA (tRNA), and study their mobility and spatial organisation in live *E. coli*. I observe a non-uniform distribution of tRNA molecules, which is dependent of translation and supports nucleoid segregation studies. In chapter 6, I study *in vivo* transcription initiation by internalising doubly-labelled promoter DNA into live bacteria. Using a single-molecule FRET assay, I am able to observe individual steps in initial transcription, such as open complex formation, transcription bubble dynamics, and transcription initiation, on the single-molecule level, in live bacteria.
Finally, I briefly summarise my results, comment on the challenges of single-molecule FRET studies in live cells, and pose potential future developments.

The materials and methods as well as additional supporting figures for each result chapter (chapter 3-6) are moved to the end of the respective chapter as 'Supplementary Information' and are referred to in the main chapter as 'SI ♯' and 'SI Fig. ♯'. By placing the emphasis on the results in each chapter, I hope to offer a coherent reading of the entire thesis.

Chapter 2

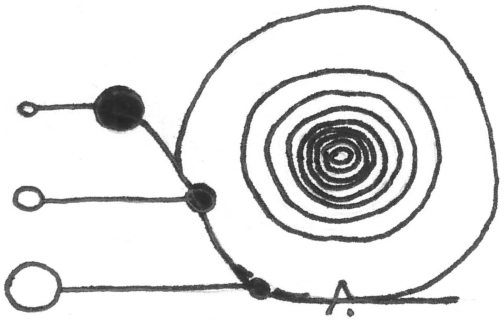

Single-molecule fluorescence

Single-molecule fluorescence is an important non-invasive tool in biological research to localise, count and trace biomolecules as well as to measure molecular distances. Individual fluorophores were first detected in aqueous solution by the Keller group in 1990 (11) and with our understanding of the photophysical properties of fluorophores and improvements in the sensitivity of optical imaging techniques, single-molecule fluorescence studies have even become possible in living cells (63).

In this chapter, I present the key principles of single-molecule fluorescence microscopy: (i) the important photophysical properties of fluorophores, (ii) Förster resonance energy transfer (FRET) and corrections for accurate molecular distance measurements, and (iii) the optical imaging techniques such as confocal and widefield microscopy that I used in this work to study single molecules.

2.1 Fluorescence

Single-molecule fluorescence studies rely on the information provided by the fluorophore attached to the biomolecule (e.g. detection, position, motion, or structural changes in case of single-molecule FRET measurements). Hence, determining the

photophysical properties of the fluorophores used during the experiments is of great interest for interpreting single-molecule fluorescence observations.

2.1.1 Absorption, emission, and Stokes shift

Fluorescence is the photon emission of a fluorophore that occurs upon the de-excitation of an electron in the first excited singlet state to the ground state. Thereby, the fluorophore's emission spectrum is spectrally red-shifted to the fluorophore's absorption spectrum due to radiationless deactivation processes in the excited state such as vibrational relaxation via interaction with other solvent molecules (64). The so-called Stokes shift is highlighted in the absorption and emission spectra of the organic dyes Cy3B and Atto647N (Fig. 2.1). Given the spectral difference between the excitation source and the fluorophore emitted photons, an optical filter (e.g. dichroic mirror) is used to separate the excitation source and the emitted photons. The detection is achieved using a semiconductor device (e.g. photodiode, camera) by converting the emitted photons into electrical current.

2.1.2 Jablonski diagram

An excited fluorophore can relax to the ground state in several ways, one of which is fluorescence emission. The Jablonski diagram illustrates the quantum states of the fluorophore molecule and the possible transitions between these states (Fig. 2.2). There are two types of quantum states; singlet states (paired electron spins) and triplet states (one set of unpaired electron spins). All quantum states are superimposed with vibrational and rotational states. The latter can be neglected at room temperature, since the energy of the rotational quantum state of $\sim 0.001\,\text{eV}$ is far below the thermal energy of $\sim 0.038\,\text{eV}$ at $20\,^{\circ}\text{C}$ (64).

The absorption of a photon by the fluorophore in the ground state S_0 can excite the

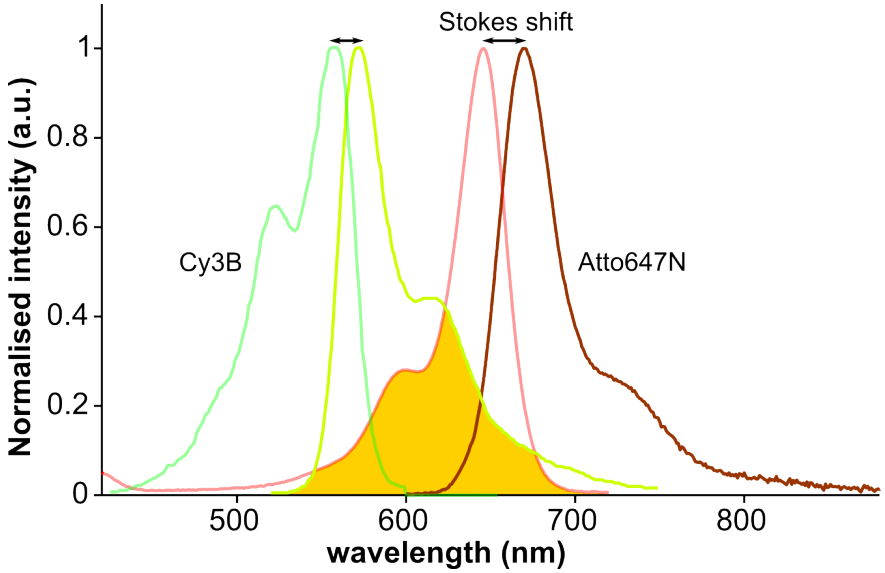

Figure 2.1: Absorption and emission spectra of fluorophore Cy3B (green) and Atto647N (red). The fluorophores' emission spectra are red-shifted relative to the fluorophores' absorption spectra; Stokes shift for Cy3B: 11 nm (65), and for Atto647N: 25 nm (66). Notably, the emission spectrum of Cy3B and the absorption spectrum of Atto647N overlap (orange), making the two organic dyes an ideal FRET-pair.

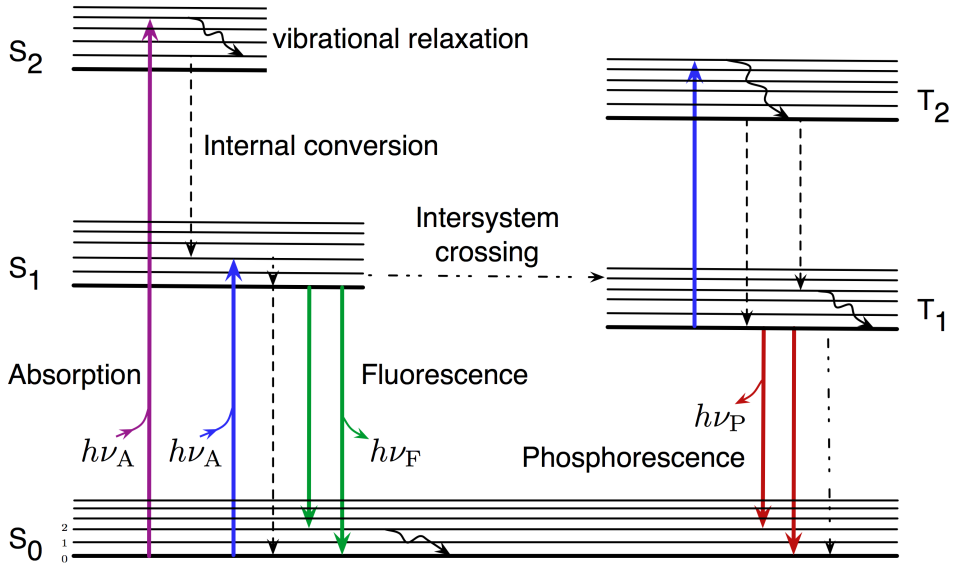

Figure 2.2: Jablonski diagram depicting ground and first two excited singlet states S_0, S_1 and S_2 and two triplet states T_1 and T_2 with first 5 vibrational states each. The state transitions are labelled and depicted with different arrows.

fluorophore either to the first excited state S_1, which can be considered instantaneous (< 1 fs), or in higher vibrational states of the singlet state, which relax to the

lowest vibrational state with about $k_{\text{vib}} \sim 10^{10}$-$10^{12}\,\text{s}^{-1}$ via thermal collision with molecules (67).

In the first excited singlet state S_1, the fluorophore can display the following phenomena: (i) radiative depopulation to S_0 by spontaneous emission of a photon (i.e. fluorescence), (ii) spin reversion by intersystem crossing into the first excited triplet state (spin forbidden but the probability increases with sufficient spectral overlap of higher vibrational levels of the triplet state with lower vibrational levels of the singlet state), (iii) radiationless internal conversion followed by vibrational relaxation to S_0, (iv) singlet-singlet absorption and subsequent ionisation of the fluorophore ($S_1 \rightarrow S_n$; one possible photobleaching pathway), and (v) a combination of (iv) and (iii).

While excited singlet state lifetimes are in the order of a few nanoseconds, triplet states exhibit very long lifetimes of up to 100 s. Triplet states can only relax to the ground state by vibrational collisions, intersystem crossing, or phosphorescence, in which phosphorescence emission rates are very slow and only occurs in highly viscous medium or at low temperatures due to many competing de-excitation pathways (64). The various depopulation pathways of excited fluorophore states are depicted in the Jablonski diagram (Fig. 2.2) and their kinetic rates are listed in Table 2.1.

Internal conversion	$S_n \rightarrow S_1, T_n \rightarrow T_1$	k_{ic}	$10^{10} - 10^{14}\ \text{s}^{-1}$
Internal conversion	$S_1 \rightarrow S_0$	k_{ic}	$10^{6} - 10^{7}\ \text{s}^{-1}$
Vibrational relaxation	$S_{1,\nu=n} \rightarrow S_{1,\nu=0}$	k_{vib}	$10^{10} - 10^{12}\ \text{s}^{-1}$
Singlet-singlet absorption	$S_1 \rightarrow S_n$	k_{exc}	$10^{15}\ \text{s}^{-1}$
Triplet-triplet absorption	$T_1 \rightarrow T_n$	k_{exc}	$10^{15}\ \text{s}^{-1}$
Intersystem crossing	$S_1 \rightarrow T_1, S_n \rightarrow T_n, T_n \rightarrow S_n$	k_{isc}	$10^{5} - 10^{8}\ \text{s}^{-1}$
Fluorescence	$S_1 \rightarrow S_0$	k_{f}	$10^{7} - 10^{9}\ \text{s}^{-1}$
Phosphorescence	$T_1 \rightarrow S_0$	k_{p}	$10^{-2} - 10^{-3}\ \text{s}^{-1}$

Table 2.1: List of depopulation pathways of excited fluorophores and their transition rates (67).

A fluorophore for long-lasting single-molecule fluorescence observation ideally only exhibits $S_0 \rightarrow S_1$ (with k_{exc}), and $S_1 \rightarrow S_0$ (with k_{f}) transitions, which results in

a quantum yield of 100%: $\varphi_\mathrm{f} = \frac{k_\mathrm{f}}{k_\mathrm{f}+k_\mathrm{nf}} = 1$, with a non-fluorescent transitions rate of $k_\mathrm{nf} = 0$. However, as described above, non-fluorescent competing depopulation pathways of S_1 occur, of which intersystem crossing into long-lived triplet states is the most prominent, and reduce the fluorescent quantum yield. Fluorophores for single-molecule fluorescence studies are often chosen for their high quantum yield and photostability (64).

2.1.3 Fluorophores

Fluorescent labels for single-molecule FRET studies, especially for labelling biomolecules *in vivo*, require certain photophysical properties (67):

(i) high quantum yield ($\varphi_\mathrm{f} > 0.1$), and

(ii) high extinction coefficient ($\epsilon > 10^5\,\mathrm{cm}^{-1}\mathrm{M}^{-1}$) to enable single-molecule fluorescence detection

(iii) short fluorescence lifetime ($\tau_\mathrm{f} < 5$ ns) to reduce the probability of non-fluorescence transitions

(iv) large Stokes shift (15-30 nm) to enable separation of fluorescence emission from excitation light

(v) high photostability to allow long-term observation

(vi) low phototoxicity to retain biological function

Many commercially available organic dyes, which were used in this work, fulfill these requirements, and can be structurally categorised in (i) cyanine dyes: Cy3, Cy3B, Cy5, Alexa647, and Cy5.5; (ii) rhodamine dyes: Rhodamine 6G, Atto532; (iii) carbopyronine dyes: Atto647, Atto647N; and (iv) oxazine dyes: Atto655 (45). These organic dyes are widely used in sensitive single-molecule fluorescence studies (68). Recent developments showed a strong enhancement of the fluorophore's photostability by conjugating the fluorophore to a triplet state quencher such as Trolox (69). Important properties such as the dye's fluorescence lifetime, extinction coefficient

and quantum yield are listed in Table 2.2, including the fluorescent proteins GFP, and mCherry for comparison.

Fluorophore	λ_{exc} (nm)	λ_{fl} (nm)	τ_{fl} (ns)	ϵ (10^5 cm^{-1}M^{-1})	φ_f
GFP (70)	475	504	$\sim$3.0	0.1	0.79
Rhodamine 6G (67)	526	556	3.8	1.16	0.95
mCherry (71)	587	607	1.46	0.72	0.22
Atto532 †	532	553	3.8	1.15	0.9
Cy3 ‡	548	562	$<$0.3	1.5	$>$0.15
Cy3B (72)	558	572	2.8	1.3	0.67
Atto647 †	645	669	2.4	1.2	0.2
Atto647N †	644	669	3.5	1.5	0.65
Cy5 ‡	647	664	1.0	2.5	$>$0.28
Alexa647 ♮	650	668	1.0	2.7	0.33
Atto655 †	663	684	1.8	1.25	0.30
Cy5.5 ‡	673	692	1.0	2.5	$>$0.28
Cy7 ♯	750	773	n.a.	2.0	$>$0.2

Table 2.2: List of fluorophores and their photophysical properties used in this work. Spectroscopic characteristics λ_{exc} – absorption maximum, λ_{fl} – emission maximum, τ_{fl} – fluorescence lifetime, ϵ – molar extinction coefficient (measured in ethanol), and φ_f – quantum yield were obtained directly from the commercial supplier †: ATTO-TEC GmbH (73), ‡: GE Healthcare (74), ♮: Invitrogen (75), ♯: Lumiprobe (76), or from literature as indicated.

To label biomolecules such as DNAs and proteins, the dye must carry a functional group allowing covalently binding to free amino or thiol groups. Amino modifications in DNA are commonly labelled with NHS (N-HydroxySuccinimide) ester conjugated dyes, whereas thiol groups in proteins, such as surface-exposed cysteine residues or residues introduced via cysteine mutagenesis, are commonly labelled with maleimide conjugated dyes *in vitro*.

One very elegant way of *in vivo* labelling commonly applied to proteins is to use genetically encoded fluorescent protein fusions. The DNA sequence of genetically encoded fluorescent proteins (FPs), such as the green fluorescent protein (GFP), is placed next to the sequence coding for the protein of interest and both proteins are

fused together during protein synthesis (20). Figure 2.3 shows the structure of the two organic fluorophores Cy3B and Atto647N, which were used in this study, and GFP, which consists of 238 amino acids forming a β-barrel cylindrical structure protecting the fluorophore in the middle. But fluorescent proteins are about ten times less photostable and bright compared to organic dyes and exhibit complicated photophysics (blinking behaviour, etc.) (21, 77). Furthermore, FPs are about 100-fold larger in volume (Fig. 2.3), which might influence the function of the labelled protein of interest, and FPs are mainly introduced at the protein termini, which hinders site-specific labelling of the protein of interest.

Other *in vivo* labelling strategies are discussed in chapter 3 (sec. 3.1), and the choice of fluorophores for *in vivo* single-molecule FRET studies is further discussed in chapter 4 (sec. 4.1).

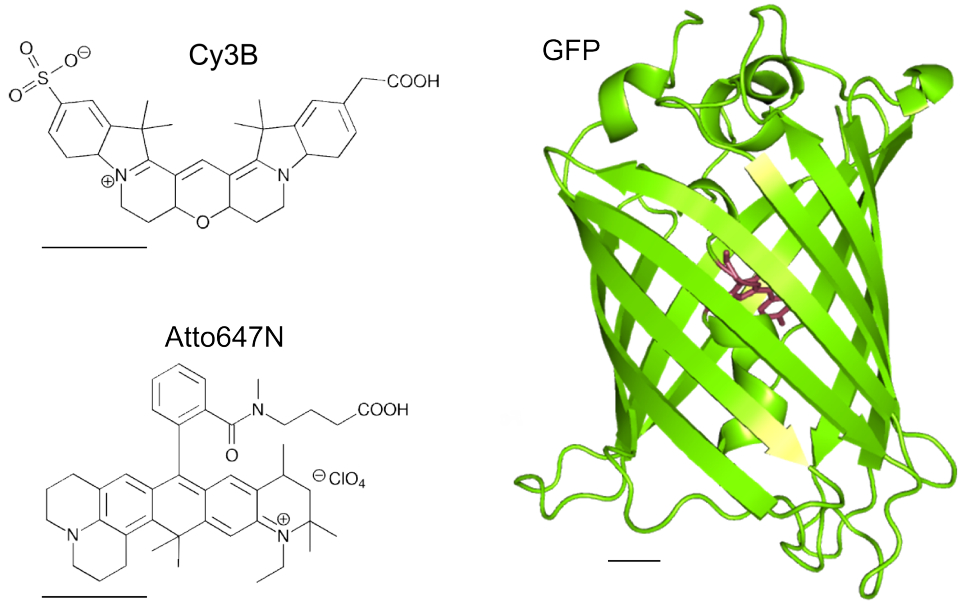

Figure 2.3: Schematic of the structure of organic dyes Cy3B and Atto647N (78), and the green fluorescent protein (GFP, pdb-file: 1GFL (79)). Scale bar: 0.5 nm

2.1.4 Photophysics of fluorophores

There are two main caveats that usually hinder long-term single fluorophore detection: (i) irreversible loss of fluorescence signal via photobleaching and (ii) fluctuating fluorescence signal due to blinking.

Photobleaching is the loss of the dye's ability to emit fluorescence due to an irreversible reaction changing the dye's absorption and emission properties. The pathways of photobleaching are complex, fluorophore-dependent, and vary with experimental settings (buffer systems, excitation settings) (80, 81). In general, fluorophore photobleaching is considered to occur via reactions with molecular oxygen, or oxygen radical ions upon excitation of the fluorophore to higher excited states in solution (82, 67). Photobleaching can be reduced by introducing enzymatic oxygen scavenging systems such as glucose oxidase/catalase systems (83, 84, 85).

However, the removal of oxygen results in an increase in triplet state lifetime, since the triplet state is usually quenched by molecular oxygen (68). The triplet state can last up to several milliseconds (86, 23, 87), which is very advantageous for any type of photoswitching localisation microscopy but such triplet state blinking is undesired for long-lasting single-molecule observations. There, alternative triplet state quencher such as reducing compounds, e.g. β-mercaptoethanol (BME), and β-mercaptoethylamine (MEA), or quencher of reduced or oxidised dark states populated from the triplet state, such as reducing-oxidizing system (ROXS, e.g. Trolox-Trolox quinone), were introduced (82, 88, 89). In addition, pulsed excitation with $>$1 µs interpulse time distance was employed to allow the relaxation of the triplet state (T-Rex or D-Rex) and increase the total fluorescence budget of the fluorophore (90). *In vitro* the buffer system can be actively controlled and ROXS can be added. However, these chemical reagents are toxic for cells, preventing their use for *in vivo* studies. In this work, I used photostable fluorophores such as Cy3B, and Atto647N, and relied on the aid of the overall reducing cellular environment (91).

2.2 Förster resonance energy transfer (FRET)

A very interesting photophysical process occurs if two fluorophores with sufficient spectral overlap of emission spectrum and absorption spectrum are in close proximity: FRET. Förster (or fluorescence) resonance energy transfer describes the non-radiative energy transfer from an excited "donor" molecule to an "acceptor" molecule via a dipole-dipole interaction (92, 47). The efficiency of the non-radiative energy transfer depends on the distance between the two fluorophores and their respective orientations (eq. 2.1). Using FRET, distances between 2 and 10 nm can be measured with a spatial resolution down to 0.5 nm (93), making FRET an ideal 'spectroscopic ruler' for measuring structural changes of single molecules far beyond the diffraction limit (Fig. 2.4a).

2.2.1 FRET efficiency

The distance dependence of the rate of energy transfer from the donor to the acceptor fluorophore (k_{FRET}) is given by

$$k_{\mathsf{FRET}}(r) = k_{\mathsf{D}} \left(\frac{R_0}{r} \right)^6 \tag{2.1}$$

where k_{D} is the donor relaxation rate (fluorescence decay or non-radiative relaxation) of the excited donor and R_0 is the Förster radius, a property of the FRET-dye pair and experimental conditions. The energy transfer efficiency (E) is defined as the ratio of energy transfer rate and total relaxation rate

$$E(r) = \frac{k_{\mathsf{FRET}}(r)}{k_{\mathsf{D}} + k_{\mathsf{FRET}}(r)} = \frac{1}{1 + \left(\frac{r}{R_0}\right)^6} \quad . \tag{2.2}$$

The r^6 dependence of the FRET efficiency (Fig. 2.4b) was verified by Stryer and Haugland in 1967 by measuring FRET between donor and acceptor dyes separated

by poly-L-proline oligomer spacers (48), and in 1993 by Clegg and coworkers using double stranded DNA as spacers (94).

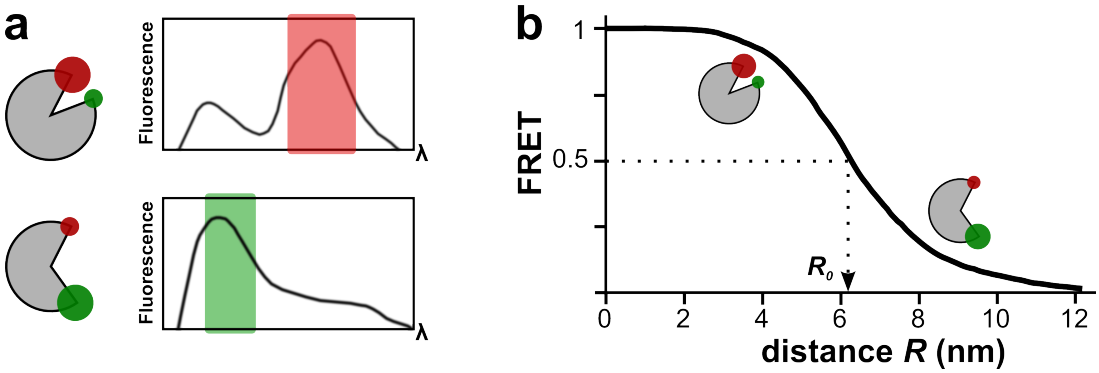

Figure 2.4: Schematic of fluorescence signature of FRET dye-pair and distance dependence of FRET efficiency. **a.** Schematic of relation of molecule structure to FRET fluorescence signal between donor fluorophore (green) and acceptor fluorophore (red); closed conformation (high acceptor signal upon donor excitation), open conformation (high donor signal upon donor excitation). **b.** FRET efficiency over dye-pair distance for Cy3B/Atto647N FRET dye-pair with R_0=6.2 nm (95).

The Förster radius R_0 is defined as $E(r = R_0) = 0.5$, and characterises the length scale over which FRET occurs. The Förster radius is given by

$$R_0{}^6 = \frac{9000 \ \ln 10 \ \varphi_\mathrm{D} \ \kappa^2 \ J}{128 \ \pi^5 \ n^4 \ N_\mathrm{A}} \tag{2.3}$$

where φ_D is the donor quantum yield, κ describes the relative orientation of donor and acceptor fluorophores, J is the spectral overlap integral between donor and acceptor fluorophore, n is the refractive index of the medium, and N_A is Avogadro's number. Experimentally obtained FRET values of popular organic fluorophore FRET-dye pairs range from Cy3/Cy5[1]: 3.6 nm, Alexa488/Alexa546: 5.5 nm, Atto495/Atto590: 5.6 nm (67), and Cy3B/Atto647N: 6.2 nm (95), whereas R_0-values for popular fluorescent protein FRET-pairs range from ECFP/EYFP: 4.9 nm to EGFP/EYFP: 5.6 nm (96).

The FRET efficiency E can be obtained by measuring the fluorescence lifetime of the donor dye with ($\tau_{\mathrm{D,\,FRET}}$) and without ($\tau_{\mathrm{D,\,0}}$) the acceptor dye present ($E = 1 - \frac{\tau_{\mathrm{D,\,FRET}}}{\tau_{\mathrm{D,\,0}}}$). The fluorescence lifetime (τ_fl) describes a characteristic time of a fluorophore

[1] FRET dye-pair notation: donor fluorophore/acceptor fluorophore.

spends in the excited state and the number of excited fluorophores is proportional to the fluorescence intensity, $I(t) = I_0 \exp(-\frac{t}{\tau_{\text{fl}}})$. Thus, the FRET efficiency can also be measured by the quenching of the donor fluorescence ($E = 1 - \frac{I_{\text{D, FRET}}}{I_{\text{D, 0}}}$), or by measuring the enhanced acceptor fluorescence ($I_{\text{A, FRET}}$) in presence of the donor dye (67):

$$E = \frac{I_{\text{A, FRET}}}{I_{\text{D, FRET}} + \gamma\, I_{\text{A, FRET}}} \tag{2.4}$$

where the γ factor, $\gamma = \frac{\nu_{\text{A}}\ \varphi_{\text{A}}}{\nu_{\text{D}}\ \varphi_{\text{D}}}$ corrects for different detector sensitivity for donor and acceptor fluorescence, in which ν_i are the detector efficiencies for both channels and φ_i are the fluorescence quantum yields of donor and acceptor dye (97). The γ-factor compensates for different detector sensitivities to the donor and acceptor fluorescence and has to be obtained for each optical setup and FRET dye pair.

However, in cases where absolute distance measurements are not required, and FRET changes can be monitored, we can assume $\gamma = 1$ and calculate 'uncorrected' FRET values E* (the so-called 'proximity ratio'), which is already corrected for background fluorescence. In confocal single-molecule FRET studies, fluorescence burst time-traces are filtered for background fluorescence levels by applying a threshold (median + 3-times the standard deviation of fluorescence intensity time-traces) to the burst time-traces in each fluorescence channel, whereas in widefield imaging single-molecule FRET studies, the 2D-Gaussian fitting of the diffraction-limited image of the fluorophore (PSF) accounts for background levels in the respective fluorescence channel.

$$E^* = \frac{I_{\text{DA}}}{I_{\text{DD}} + I_{\text{DA}}} \tag{2.5}$$

In this work, I mainly measured the proximity ratio, if not stated otherwise, and labelled the measured intensities I_{XexYem}, which corresponds to Y emission channel

under X excitation, and the calculated proximity ratio: E^*, 'FRET efficiency', 'FRET value', or 'Transfer efficiency'.

2.2.2 Accurate distance measurements

To obtain accurate molecular distances using single-molecule FRET studies, accurate FRET efficiencies, and the Förster radius of the used FRET-dye pair have to be measured.

Accurate FRET measurements

To obtain accurate FRET efficiencies, the proximity ratio (eq. 2.5) has to be corrected for cross-talk between donor and acceptor fluorescence channel and different detection efficiencies of donor and acceptor fluorescence (γ-correction). Specifically the acceptor intensity has to be corrected for other contributions than FRET: donor leakage into the acceptor channel, which is proportional to the donor intensity ($Lk = l \cdot I_{\text{D-only, FRET}}$), and direct excitation of the acceptor fluorophore at the donor excitation wavelength ($Dir = d \cdot I_{\text{A-only, dir}}$). The cross-talk corrected and γ factor corrected FRET efficiency is given by

$$\begin{aligned} F_{\text{FRET}} &= I_{\text{DA}} - l\ I_{\text{D-only, FRET}} - d\ I_{\text{A-only, dir}} \\ E_{\text{corr}} &= \frac{F_{\text{FRET}}}{I_{\text{DD}} + \gamma F_{\text{FRET}}} \end{aligned} \tag{2.6}$$

The last step for accurate FRET measurements, the γ-correction for different detection efficiencies of the respective FRET-dyes has to be performed for each optical setup individually. A detailed discussion of FRET corrections for accurate single-molecule FRET measurements *in vitro* using confocal microscopy is given in (98, 99).

Förster radius

To relate accurate FRET measurements to accurate molecular distance measurements, the Förster radius R_0 has to be measured for the respective FRET-dye pair (eq. 2.3).

First, the spectral overlap integral J of donor and acceptor dye has to be measured

$$J = \int f_{\mathsf{D}}(\lambda)\ \epsilon_{\mathsf{A}}(\lambda)\ \lambda^4\ d\lambda \tag{2.7}$$

where $f_{\mathsf{D}}(\lambda)$ is the normalised donor emission ($\int_0^\infty f_{\mathsf{D}}(\lambda)\ d\lambda = 1$), and the acceptor absorption spectrum is expressed via the extinction coefficient ϵ_{A}.

Second, κ^2, a measure of the relative orientation of the donor and acceptor dipoles, has to be obtained. The κ^2 value ranges from 0 (perpendicular dipoles) to 4 (parallel dipoles) and in cases of free rotating dyes, and averaging over all possible orientations, yields $\kappa^2 = 2/3$ (100), which is often a popular assumption in the field but has to be validated. The high rotational freedom of organic dyes attached to DNA FRET standards was measured by Holden *et al.* (95) and $\kappa^2 = 2/3$ was assumed throughout this work.

The correction of measured FRET efficiencies, and the experimental determination of R_0 allow the measurement of accurate distances between acceptor and donor fluorophore. It is noteworthy that for measuring molecular distances, the average position of donor and acceptor dyes attached to the biomolecule have to be also considered to relate dye positions to actual molecular distances and distance changes. Therefore, software was developed by the Michaelis lab (101), and the Seidel lab (102). The software packages consider the dimensions of the planar organic dye, the dye linker length and the attachment point of the dye linker to the molecule of interest (e.g. DNA or protein PDB-file) and then evaluate the accessible volume of the dye and the average dye position relative to the molecule of interest.

2.2.3 Alternating laser excitation (ALEX) scheme

A powerful tool for molecular sorting is alternating laser excitation (ALEX), which was initially developed to extend and aid single-molecule FRET measurements using confocal microscopy (103). Using an ALEX scheme molecules can be categorised dependent on the number and types of fluorophores present. In single-molecule FRET studies, molecules can be sorted into Donor-only (cyan, I), Acceptor-only (cyan, V), and doubly-labelled FRET molecules (magenta, II-IV) as depicted in Fig. 2.5 using the direct excitation of the donor fluorophore alternated with the direct excitation of the acceptor fluorophore. The presence of the acceptor fluorophore can be verified by relating the total fluorescence after donor excitation to the total fluorescence after donor and acceptor excitation, which is defined as the uncorrected stoichiometry ratio S^*.

$$S^* = \frac{I_{\mathrm{DD}} + I_{\mathrm{DA}}}{I_{\mathrm{DD}} + I_{\mathrm{DA}} + I_{\mathrm{AA}}} \tag{2.8}$$

The measured intensities I_{XexYem} correspond to intensities measured in the Y emission channel under X excitation. Gaining direct information of the presence of the acceptor fluorophore helps for instance to distinguish Donor-only molecules from low-FRET molecules, which exhibit similar FRET efficiencies (I and III, Fig. 2.5b). For Donor-only molecules $S^* \sim 1$ holds, whereas for Acceptor-only molecules $S^* \sim 0$ holds. Excitation intensities have to be tuned accordingly, such that doubly-labelled species exhibit stoichiometry values that are clearly distinguishable from donor-only and acceptor-only species.

Employing the ALEX-scheme, information of the donor-only and acceptor-only species can be used to obtain the leakage of donor fluorescence into the acceptor FRET signal ($Lk = l \cdot I_{\text{D-only, FRET}}$) and direct excitation of the acceptor fluorophores by donor

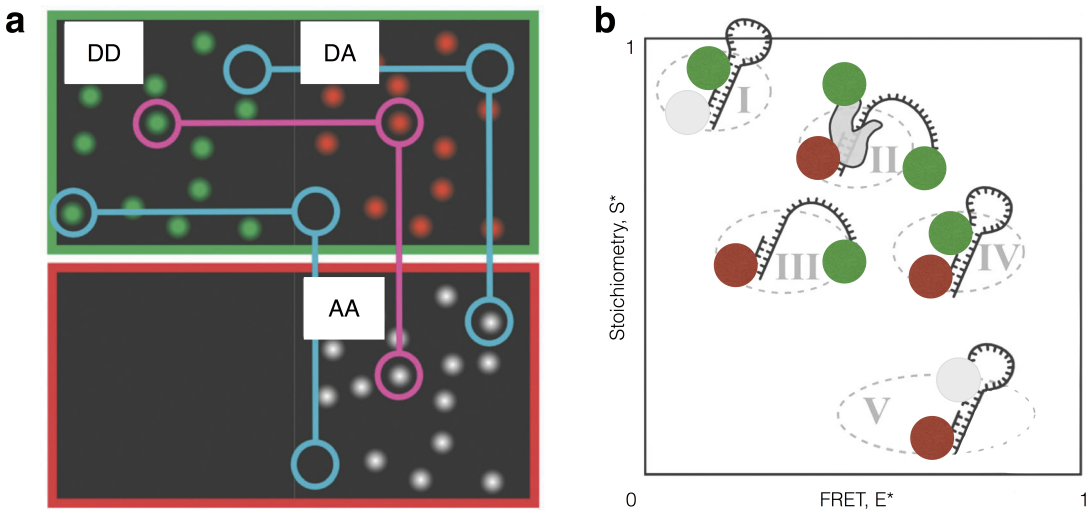

Figure 2.5: Schematic of single-molecule FRET studies using an alternating laser excitation scheme. **a.** Detection of single molecules in donor fluorescence and acceptor fluorescence channel upon donor excitation (DD and DA, respectively) and in acceptor fluorescence channel upon acceptor excitation (AA). Molecule exhibiting single-molecule FRET signature is highlighted in magenta and donor-only, and acceptor-only molecules are highlighted in cyan. **b.** Stoichiometry-FRET histogram showing different molecular species; donor-only molecules (I), acceptor-only molecules (V), and different doubly-labelled FRET molecules (II-IV). The schematics were adapted from (99).

excitation ($Dir = d \cdot I_{\text{A-only, dir}}$) for accurate FRET corrections (eq. 2.6) (99).

$$l = \frac{E^*_{\text{D-only}}}{1 - E^*_{\text{D-only}}} \tag{2.9}$$

$$d = \frac{S^*_{\text{A-only}}}{1 - S^*_{\text{A-only}}} \tag{2.10}$$

2.3 Single-molecule detection

Two basic microscopy techniques are employed for single-molecule fluorescence and single-molecule FRET detection; confocal microscopy and widefield microscopy. Confocal microscopy is a point-detection method, in which the photons emitted within a diffraction limited area ($<1\,\mu m^2$) are collected onto a single avalanche photodiode, whereas, in widefield microscopy a large field of view ($>100\,\mu m^2$) is imaged on a sensitive camera chip.

2.3.1 Confocal microscopy

In confocal microscopy the excitation laser beam is collimated in the objective back focal plane and hence focused in the specimen (buffer solution, adherent cells, cell membranes, etc.) (11). Fluorescently labelled molecules present in the solution give rise to a photon burst when they cross the confocal volume ($\sim$1 fL). The detection of fluorescence bursts within the confocal volume is not uniform and out of focus light, especially in axial direction, can be rejected by using a small pinhole in the emission path (Fig. 2.6). All excitation, emission, and collection properties can be described by the 'molecule detection function' (MDF), which for a Gaussian laser profile becomes (67)

$$\mathrm{MDF}(r,z) = I_0 \exp\left(-2\Big(\frac{r}{w_0}\Big)^2\right) \exp\left(-2\Big(\frac{z}{z_0}\Big)^2\right) \tag{2.11}$$

where r is the radial distance from the origin of the focal spot in $x-y$, and z is the axial distance along the optical axis, w_0 and z_0 are the radial and axial radii at which the laser intensity drops by $1/e^2$.

Confocal microscopy can achieve nanosecond- to millisecond temporal resolution but it is limited to a concentration of hundreds of pico-molar of the labelled biomolecule of interest to allow single-molecule detection in the confocal volume. Additionally, confocal measurements only capture molecular snapshots and do not give access to the dynamic of the molecule.

Early single-molecule FRET studies were performed on confocal setups (97, 104) elucidating protein folding kinetics (49, 50), and structural changes of DNA Polymerase I (53), and promoter DNA during transcription initiation (105).

In this work, confocal single-molecule FRET measurements employing the ALEX scheme were performed *in vitro* to compare *in vivo* single-molecule FRET measurements to *in vitro* FRET efficiencies. The confocal microscope used is described in

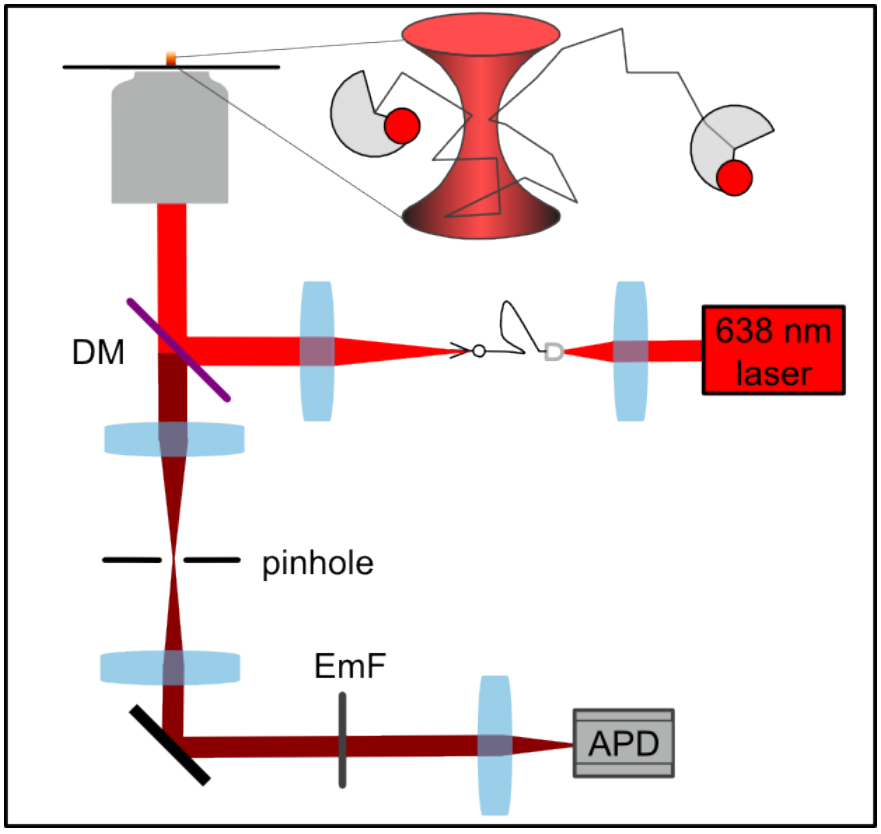

Figure 2.6: Schematic of an inverted single-molecule fluorescence confocal microscope. Fluorescence bursts from labelled biomolecules diffusing through the confocal volume are filtered from excitation light via a dichroic mirror (DM), separated from out of focus fluorescence via a small pinhole ∼100 µm and emission filter (EmF), and collected on a single photon avalanche diode (APD).

Appendix A.2 in more detail.

Fluorescence correlation spectroscopy (FCS)

Fluorescence correlation spectroscopy is another confocal microscopy technique that was employed for control measurements in this work. Briefly, the fluorescence burst signal is autocorrelated providing information of the self-similarity of the signal and showing characteristic time constants of the underlying processes. The autocorrela-

tion function $G(\tau)$ is given by (106)

$$G(\tau) = \frac{\langle \delta I(t) \cdot I(t+\tau) \rangle}{\langle I(t) \rangle^2} \tag{2.12}$$

$$= A_0 + \frac{1}{V_{\text{eff}}\, c} \frac{1}{1+\tau/\tau_D} \frac{1}{\sqrt{1+\tau/(E^2\tau_D)}} \Big(1 + \frac{T e^{-\tau/\tau_T}}{1-T}\Big) \quad \text{with} \tag{2.13}$$

A_0 : offset

V_{eff} : effective confocal volume

τ_D : characteristic diffusion time through confocal volume

E : elongation factor of confocal volume

T : fraction of molecules in non-fluorescent triplet state

τ_T : characteristic residence time in triplet state.

The effective volume in case of a Gaussian shaped laser beam $V_{\text{eff}} = \pi^{3/2} w_0^2 z_0$, axial radii w_0 and z_0 as for the MDF curve (eq. 2.11), and the concentration of the fluorescent molecules $c = \frac{1}{V_{\text{eff}}\, G(0)}$. The diffusion time ($\tau_{\text{D}}$), which describes the average time a molecule stays in the confocal volume, is anti-proportional to the diffusion coefficient $\tau_{\text{D}} = \frac{w_0^2}{4\, D} \propto \frac{1}{D}$. For absolute diffusion coefficient or concentration measurements, the dimensions of the confocal volume need to be calibrated. Usually the characteristic diffusion time of a well-characterised fluorophore with high quantum yield, such as Rhodamine 6G (R6G, φ_{f}=0.95), is measured. The autocorrelation function for Rhodamine 6G (Fig. 2.7) exhibits a characteristic diffusion time of $\tau_{\text{D}} = 0.33$ ms with D(R6G)$\sim$300 µm^2/s at room temperature (107).

2.3.2 Widefield microscopy techniques

An alternative to confocal microscopy is widefield imaging in which a larger area containing up to hundreds of molecules is imaged on a sensitive camera, usually an electron multiplying charge coupled device (EMCCD) or active pixel sensors such

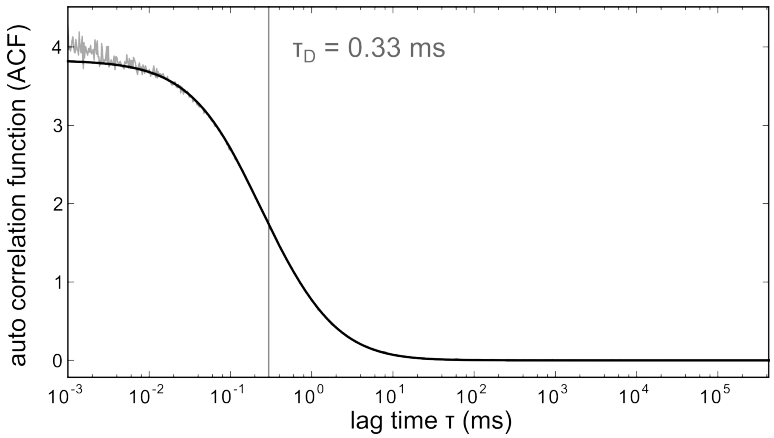

Figure 2.7: Autocorrelation function of fluorescence burst signal of Rhodamine 6G fluorophore in aqueous buffer showing a characteristic diffusion time of 0.33 ms through the confocal volume.

as complementary metal-oxide-semiconductor (CMOS) cameras. While hundreds of molecules can be imaged in parallel, the time-resolution is limited to several milliseconds. There are three popular widefield illumination techniques, which can be differentiated by the position of the focused excitation light relative to the optical axis at the back focal plane of the microscope objective (Fig. 2.8a). For all three types, the emitted fluorescence is separated from the excitation light by a dichroic mirror and directed onto the camera chip (Fig. 2.8b). In this work, I used an EMCCD camera technology and an inverted microscope setup shown in Appendix A.1 for more details.

Epi-fluorescence In epi-fluorescence mode, the laser light is focused into the back focal plane of the objective, which results in a wider illuminated area than the focus in the object plane (108). The fluorescence light is then collected and separated from the backscattered excitation light using a dichroic mirror. For FRET measurements, this dichroic mirror is a multi-bandpass mirror that allows both donor and acceptor emitted photons to be transmitted towards the imaging channel where they are separated by another dichroic mirror and directed onto separate halves of the camera chip.

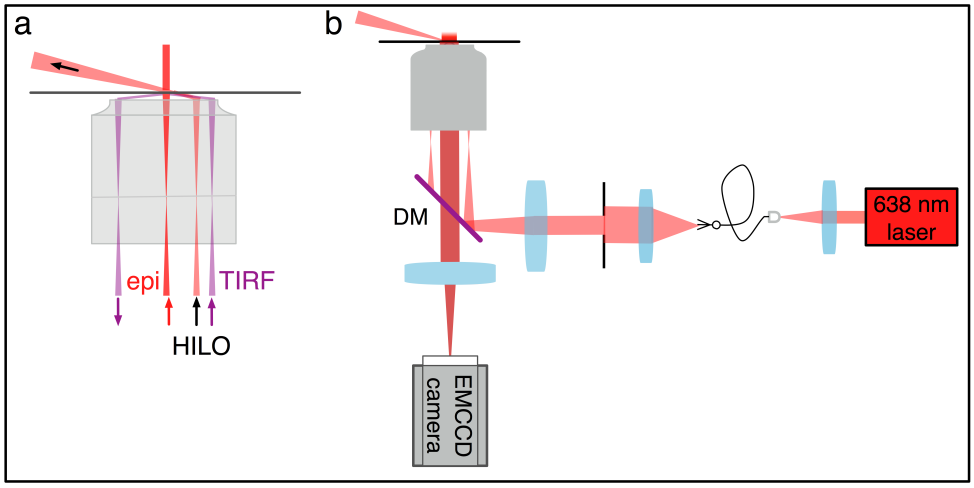

Figure 2.8: Widefield microscopy imaging scheme. **a.** Different widefield illumination types; epi-fluorescence (red arrow), highly inclined and laminated optical sheet illumination (HILO, black arrow), and total internal reflection fluorescence illumination (TIRF, purple arrow). **b.** Inverted objective widefield microscope. Laser light from the excitation module is coupled into an optical fibre and focused in the back focal plane of the objective. Fluorescence light is collected through the same objective, separated by a dichroic mirror (DM) from the excitation light, and directed onto the chip of an electron multiplying charge coupled device (EMCCD) camera.

TIRF illumination In total internal reflection fluorescence (TIRF) mode (109, 110), the properties of the evanescent field of a total internal reflected wave on a thin surface (microscope coverslip) is used to reduce the excitation volume and increase the signal to noise ratio. The evanescent wave is generated upon the total reflection of light on the surface from higher to lower optical density (glass to oil or water), and the evanescent wave decays exponentially into the medium, $I(d) = I_0 \exp(-z/d)$, with optical axis z, and d $\sim$100 nm the characteristic depth of the TIRF illumination. It is noteworthy, that there are two types of TIRF microscopes, objective-type TIRF (as shown in Fig. 2.8) and prism-type TIRF, in which the evanescent wave is generated at the surface of a quartz slide and a prism being placed on top of the objective.

HILO illumination Highly inclined and laminated optical sheet (HILO) illumination is mainly used in live-cell imaging, since it enables larger penetration depth than TIRF illumination by minimising scattered out of focus light (111). HILO illumination

is essentially epi-fluorescence imaging using a highly inclined excitation laser beam (Fig. 2.8a). The high inclination results in a smaller illuminated volume directly above the objective, which can also be translated along the optical axis into the specimen.

Data analysis

The main advantage of widefield microscopy is the high-throughput data acquisition, given the observation of multiple molecules at once, and the possibility of real-time observation and synchronisation of biological processes. These new possibilities come with more complex data analysis routines than point-based methods.

Recorded fluorescence movies were analysed frame-by-frame. In each frame the position and photon count of the single molecules was acquired by fitting the point spread function (PSF)[2] to a 2D Gaussian function (112, 95) (Fig. 2.9a) or by calculating the centre of mass (30). Both localisation precision and accuracy are dependent on the image of the emitter image determined by the microscope setup and fluorophore properties. In a recent review different localisation algorithms were summarised and categorised regarding the experimental properties (113).

Next, the centroids of the single molecules were linked in consecutive frames to obtain single-molecule trajectories and observe individual molecules in real-time (114, 43, 115) (Fig. 2.9b). Again, many different tracking algorithm depending on experimental needs were reported and recently an open competition was initiated to test the tracking algorithms on different commonly defined data sets (116).

Additionally, in single-molecule FRET studies, molecules in donor and acceptor emission channel have to be colocalised to obtain their FRET signatures over time. From single-molecule trajectories, the mobility of the molecule can be obtained by calculating the mean squared displacement (MSD) and relating the MSD values to an apparent diffusion coefficient (Fig. 2.9c-d).

[2]The point spread function is the intensity distribution of a single molecule, point source, in the image plane of the microscope setup.

In chapter 4, I present the developed analysis routines, such as channel mapping, localisation and tracking of single FRET molecules in live cells in more detail. The apparent diffusion coefficient analysis is presented in chapter 5. There, I also performed Brownian motion simulations in a confined cell-shaped environment to relate the measured apparent diffusion coefficient to an accurate diffusion coefficient.

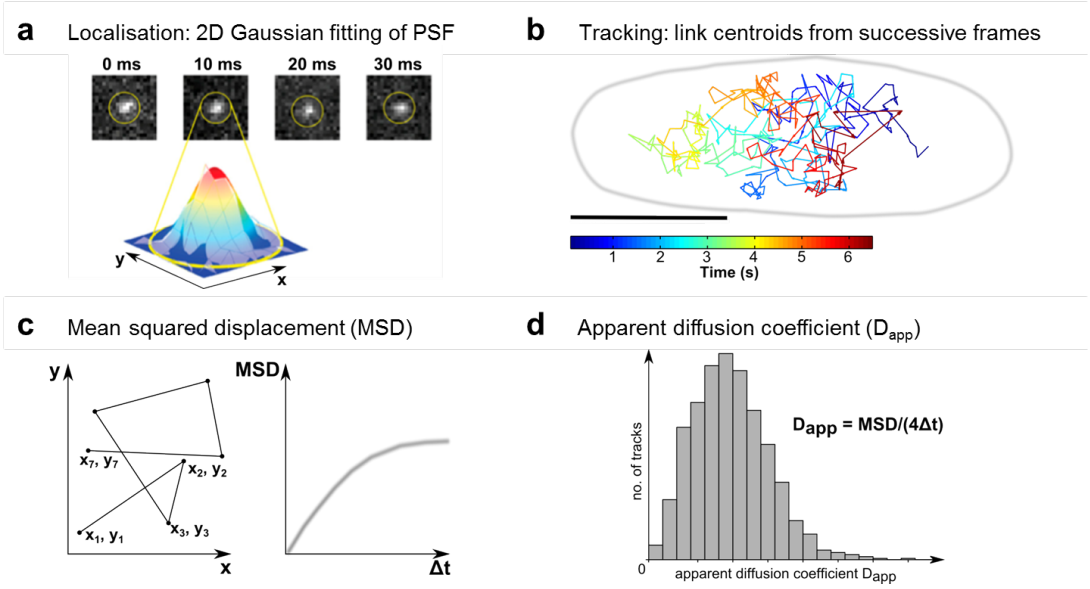

Figure 2.9: Schematic showing individual steps in the analysis of single-molecule fluorescence data from live-cell imaging movies. **a.** Localisation of individual molecules in each movie frame (0-30 ms). The diffraction-limited single-molecule images are fitted with a 2D-Gaussian distribution and the molecule position is given as the centroid from the fitted intensity profile. Adapted from (43). **b.** Single-particle tracking analysis. Linking centroids from consecutive movie frames to molecule trajectory. **c.** Calculating the mean-squared displacement (MSD) for each single-molecule trajectory. The MSD plateaus due to cellular confinement, and localisation inaccuracy (117). **d.** Diffusion coefficient analysis. Calculation of an apparent diffusion coefficient from the mean squared displacements, $D_{app}=MSD_{4\ steps}/(4\Delta t)$.

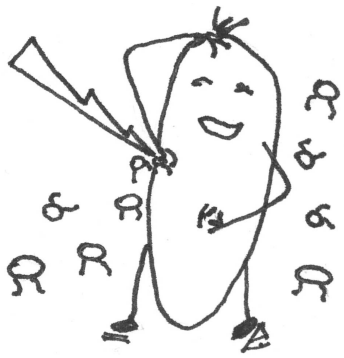

Chapter 3

Internalisation of biomolecules into live bacteria

The work presented in this chapter has been partly published in

- R Crawford*, JP Torella*, L Aigrain*, A Plochowietz*, K Gryte, S Uphoff, AN Kapanidis. Long-lived, ultrasensitive intracellular fluorescence using electroporated biomolecules. *Biophys J*, 105:2439-2450, 2013. *equal contribution.
- M Sustarsic, A Plochowietz, L Aigrain, Y Yuzenkova, N Zenkin, AN Kapanidis. Optimized delivery of fluorescently labeled proteins in live bacteria using electroporation. *Histochem Cell Biol*, 142:113-124, 2014.
- A Plochowietz, R Crawford, AN Kapanidis. Characterization of organic fluorophores for *in vivo* FRET studies. *Phys Chem Chem Phys*, 16:12688-12694, 2014.
- A Plochowietz, AH El-Sagheer, T Brown, AN Kapanidis. Protected DNA FRET Standards for *In Vivo* Single-Molecule FRET Studies. *Angewandte Chemie Int Ed*, under review.

3.1 Introduction

While fluorescent proteins (FPs) are commonly used in *in vivo* studies, organic dyes are much better suited. As I have discussed in chapter 2, sec. 2.1.3, organic dyes are brighter, much more photostable, and can be employed for intra-molecular labelling.

However, since organic dyes cannot be genetically encoded, they must be introduced into the live cell either (i) for *in vivo* labelling by internalising dyes for specific protein labelling via large polypeptide tags (SNAP, HALO, or TMP tags (32, 118, 33)), FPs (Nanobodies (119)), or unnatural amino acids (120) or (ii) through internalisation of *in vitro* organic-dye labelled proteins. Labelling strategies using polypeptide tags and FPs are limited to end-labelling (121) and thus unsuitable for FRET-pair labelling. *In vitro* labelling strategies, on the other hand, allow for more specificity control steps and are better suited for site-specific doubly-labelling of molecules for single-molecule FRET studies (122, 123, 124, 125). We therefore decided to pursue this latter approach and hence explored different internalisation methods of *in vitro*-labelled biomolecules into live cells.

Internalisation methods, such as endocytosis, detergent-mediated internalisation (126, 127), and sonication (128) are based on cell membrane permeabilisation. Microinjection (129) and syringe loading (130) offer more control of the amount of molecules added to the cellular environment and can target different cell compartments. Despite needing to load one cell at the time, microinjection became the method of choice for single-molecule fluorescence studies (131, 132, 133), and single-molecule FRET reports (60, 61) in live cells. However, these methods are mainly applied to large mammalian cells (size on the order of tens of micrometer) and are not suitable for bacterial cells (1-3 µm in size), as the microinjection needle has a diameter of about 0.5-5 µm. Furthermore, these techniques can often only penetrate through single membranes of eukaryotic cells and are often not harsh enough to penetrate through cell wall and membrane of prokaryotic cells. For bacteria, electroporation (134) and heat-shock (135) are commonly used internalisation methods. In this work, electroporation is used to introduce organic dye-labelled biomolecules into bacterial cells.

Electroporation was developed in the 1980s to transform or transfect prokaryotic and eukaryotic cells with plasmids or short DNA fragments (136, 137). During electro-

poration, the cell wall and membrane is permeabilised by exposing the low ionic cell suspension to the discharge of a high voltage electric field. The cell membrane gets rearranged by the high voltage electric field, forming transient pores through which biomolecules can enter the cell. Due to the movement of charged molecules within the cell suspension, the conductance of the cell suspension increases, leading to the exponential decay of the electric field (138).

In this chapter, I introduce electroporation as an efficient internalisation method for a large variety of labelled biomolecules into live bacteria (62), and I optimised the electroporation protocol for the internalisation of nucleic acids and proteins. Specifically, aggregation issues of double-stranded DNA upon electroporation were overcome (139) and the removal of free dye and non-internalised fluorescence for protein samples were studied (140). Lastly, I studied the balance between cell viability and cell loading and determined the optimal electroporation voltage (140, 141).

3.2 Internalisation of different biomolecules into *E. coli* using electroporation

In a proof-of-principle study, I examined the internalisation of a large variety of different organic dye-labelled biomolecules into *E. coli* cells using electroporation.

Successful internalisation of biomolecules via electroporation is strongly dependent on the electrocompetency of the bacterial cells. In general, cells are made electrocompetent by washing them several times with ice-cold water, which increases cell wall and membrane permeability and lowers the ionic strength of the cell suspension, to avoid arcing in the electroporation cuvette (142). To ensure less variations between cell batches and thus better reproducibility of experiments, we purchased electrocompetent *E. coli* DH5α from a commercial supplier (SI 3.6.3).

In line with the established protocol (62), prior to electroporation, electrocompetent

cells are incubated with labelled biomolecules. After electroporation, it is important to immediately recover the cells in a rich medium for up to 30 min to maintain cell viability. Next, a washing step follows, where the cells are spun down four times in phosphate buffer to remove non-internalised biomolecules (SI 3.6.4). Finally, cells are resuspended in a small volume of phosphate buffer and deposited on agar-coated cover slides, allowing for imaging on a fluorescence microscope (Fig. 3.1). Immobilisation on agarose pads is a simple and efficient way of imaging cells on cover slides without harming cells' integrity (62, 141), SI 3.6.5.

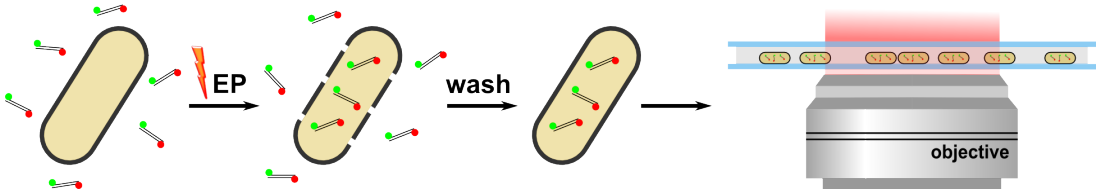

Figure 3.1: Schematic of electroporation method. Fluorescently labelled biomolecules are incubated with electrocompetent cells before electroporation. Cells are recovered, washed and placed on agarose pads for live-cell imaging. Adapted from (62).

Following sample preparation, cell imaging can be performed in epi-fluorescence mode, using total internal reflection fluorescence (TIRF, (109)) or by employing highly inclined and laminated optical sheet illumination (HILO, (111)), see sec. 2.3.2 for more details. I performed all measurements in HILO mode or epi-fluorescence mode on an inverted custom-built fluorescence microscope (Appendix A.1).

I used HILO mode for single-molecule tracking studies, since the laser beam penetrates deeper into the specimen than in TIRF mode, yet it does not illuminate the entire sample as in epi-fluorescence mode, and so increases the signal to noise ratio. As an alternative, I employed epi-fluorescence illumination for initial cell loading studies to evenly illuminate the entire cell and characterise organic dyes and FRET-dye pairs *in vivo*.

Typical initial internalisation experiments are shown in Fig. 3.2. I displayed the results as overlay images of the inverted brightfield images and false-coloured fluorescence

images. A successful internalisation study shows negligible fluorescence of the negative controls (Fig. 3.2, top) and significant cellular fluorescence of the electroporated cells (Fig. 3.2, mid-bottom). A closer examination of the cell images shows a wide distribution of cellular intensities. Assuming a correlation between cellular brightness and amount of internalised biomolecules, I often observed heavily loaded and also very few loaded cells. The main reasons for such heterogeneity and day-to-day variations could be the electrocompetent state of the *E. coli* cells ('weakness' of cell membranes before electroporation), which varies with and within cell batches, and day-to-day variations during sample preparation. For example, in Fig. 3.2, dsDNA-Cy3B appeared to be more efficiently internalised than RNA polymerase subunit ω-Cy3B, but in both samples some cells were not loaded at all.

During the course of this research, we internalised a large variety of different biomolecules: I internalised nucleic acids ranging from short single-stranded and double-stranded DNA fragments (62, 141), short single-stranded RNA fragments and transfer RNA (143), to long DNAs of 1 kbp; we acquired a large library of data from multiple protein internalisation studies, including proteins smaller than 20 kDa such as the ω subunit of RNA polymerase (140), the DNAse domain of the colicin protein E9 and its immunity protein Im9[1], chemotaxis protein CheY[2], and proteins up to 100 kDa including proteins important for gene regulation (Catabolite activator protein, CAP, and T7 RNA polymerase) and the Klenow fragment of DNA Polymerase I (62). A detailed list of successfully internalised biomolecules, fluorescent labels, molecular sizes, and an evaluation of the loading efficiency is presented in Table 3.1.

[1] collaboration with Colin Kleanthous' group, Biochemistry, Oxford.
[2] collaboration with Richard Berry's group, Physics, Oxford.

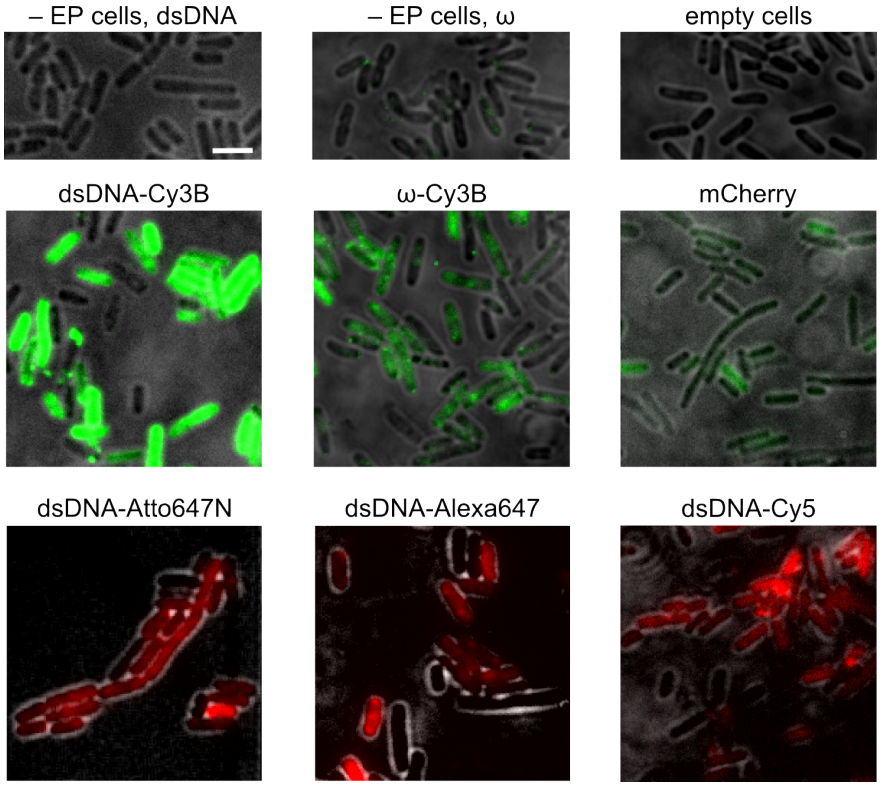

Figure 3.2: Example fields-of-view (FOV) showing cell images of typical electroporation experiments. Overlay of inverted brightfield image and fluorescence images of negative controls and cells loaded with 0.5 µM dsDNA, and 2.5 µM protein, ω subunit of RNA polymerase labelled with Cy3B and fluorescent protein, mCherry. Top: Non-electroporated or '– EP' cells (cells incubated with labelled biomolecules, recovered and washed, but not electroporated) and 'empty cells' (cells electroporated, recovered, and washed, but no fluorescent biomolecules were added) show autofluorescence in green fluorescence channel. Middle: dsDNA-Cy3B, ω-Cy3B, and mCherry are efficiently internalised. Bottom: dsDNA labelled with different red fluorophores (Atto647N, Alexa647, and Cy5) exhibit a wide distribution in brightness. Scale bar: 3 µm.

3.3 Internalisation of nucleic acids

To characterise the internalisation of nucleic acids into live bacteria, I used singly-labelled and doubly-labelled 45 bp dsDNA fragments (SI 3.6.1). First, I examined the impact of electroporation on dsDNA using a single-molecule FRET assay *in vitro*. Specifically, I electroporated two dsDNA fragments *in vitro*, an intermediate FRET DNA standard (dyes spaced between 18 bp, expected FRET value: E*=0.45$\pm$0.08), and a high FRET DNA standard (distance between dyes: 8 bp, expected FRET value: E*=0.87$\pm$0.05) and then probed their FRET signatures before and after electropora-

Biomolecule	Fluorescent label	Molecular size / Weight	Performance
ssRNA	Cy5	25 nt	+
ssDNA	various*	45 nt	+
dsDNA	various*	45-82 bp	++
bulk *E. coli* tRNA	Cy3, Cy5, Cy5.5	76-90 nt	++
dsDNA	Cy3B, Atto647N	1000 bp	++
RNA polymerase ω subunit (140)	Cy3B	10 kDa	++
immunity protein Im9[1]	Cy3B	10 kDa	++
colicin E9 DNAse domain[1]	Atto647N	15 kDa	+
chemotaxis protein CheY[2]	Cy3B, Cy5	14 kDa	++
flagellar motor switch protein FliM[2]	Atto647	38 kDa	+
fluorescent protein mCherry (141)	autofluorescent	29 kDa	++
catabolite activator protein (CAP, (144))	Atto647N	45 kDa	+
DNA Polymerase I Klenow fragment (145)	Cy3B, Atto647N	66 kDa	-
T7 RNA polymerase (62)	EmGFP	98 kDa	-

Table 3.1: List of internalised biomolecules into live *E. coli*. The evaluation of the internalisation performance is based on high loading efficiency of the electroporated sample and low cellular fluorescence of the negative controls (SI 3.6.9); '++': very good, '+': good, '-': poor. We note that larger proteins get internalised less efficiently, but this has to be evaluated for each protein sample independently, see sec. 3.4. *various dyes: Cy3, Cy3B, Atto532, Alexa647, Cy5, Atto647N, Atto647, Atto655.

tion. Second, I introduced 'protected' dsDNA fragments with chemically linked DNA-ends that are not targeted by DNA degradation mechanisms *in vivo*, by which gapped and nicked DNA intermediates are cleaved by endonucleases and recombinases in DNA repair pathways (146). These protected DNA standards have the same FRET-pair labelling scheme as previous DNA standards for single-molecule FRET studies, and offer long-lasting FRET signatures *in vivo*. Finally, I probed the internalisation efficiency of dsDNA-Cy3B for six different electroporation voltages and optimised cellular uptake while maintaining cell viability.

3.3.1 Electroporation of nucleic acids

DNA aggregation upon electroporation

I investigated the impact of electroporation on nucleic acids by checking molecule integrity using dsDNA FRET standards and measured FRET efficiencies before ('– EP') and after ('+ EP') electroporation. In this chapter, I always performed *in vitro* single-molecule FRET measurements on a confocal microscope in aqueous solution. Initially, I electroporated 1 nM of intermediate and high FRET DNA standards in ddH_2O at 1.4 kV and probed their FRET signature *in vitro*. To my surprise, I could not reproduce the expected FRET efficiencies with electroporated samples (Fig. 3.3). Therefore, I ran the electroporated dsDNA samples on a native polyacrylamide gel and visualised them on a gel scanner (SI 3.6.6). I observed a smeary band for the electroporated intermediate FRET DNA standard and electroporated high FRET DNA probes stuck in the well, which indicated a heterogenous sample and aggregation of the sample upon electroporation (Fig. 3.3i).

Next, I employed confocal single-molecule FRET measurements (sec. 2.3.1, and SI 3.6.7) to further probe this observation. Again, I could not differentiate distinct intermediate (yellow) and high (red) FRET populations in the single-molecule FRET histograms from single-molecule detections within the confocal volume, after electroporation (Fig. 3.3ii). Looking at the individual FRET photon burst time traces (gray), I observed very long dwell times (> 1 ms) and about 100-times higher photon burst counts for the electroporated samples (highlighted in blue). Moreover, I had to increase the concentration of electroporated sample to 1 nM to obtain signal of the electroporated sample within the confocal volume, whereas I was able to work at 20 pM for the non-electroporated sample, which suggested larger aggregates that depleted within the electroporated DNA sample.

To further confirm the aggregation hypothesis, I examined the autocorrelation func-

tion of FRET photon bursts (sec. 2.3.1, and SI 3.6.8). The decay of the autocorrelation curve is a measure of the diffusion time of labelled molecules through the confocal volume ($\tau_D \propto \frac{1}{D} \propto R$, D: diffusion coefficient, R: Stokes radius (147)). The decay half-life (τ_D) of non-electroporated FRET DNA standards is highlighted with a vertical black line and the electroporated samples show a 10 to 30-fold increase in τ_D (Fig. 3.3iii). Thus, more than 10-times larger aggregates diffused through the confocal volume after electroporation.

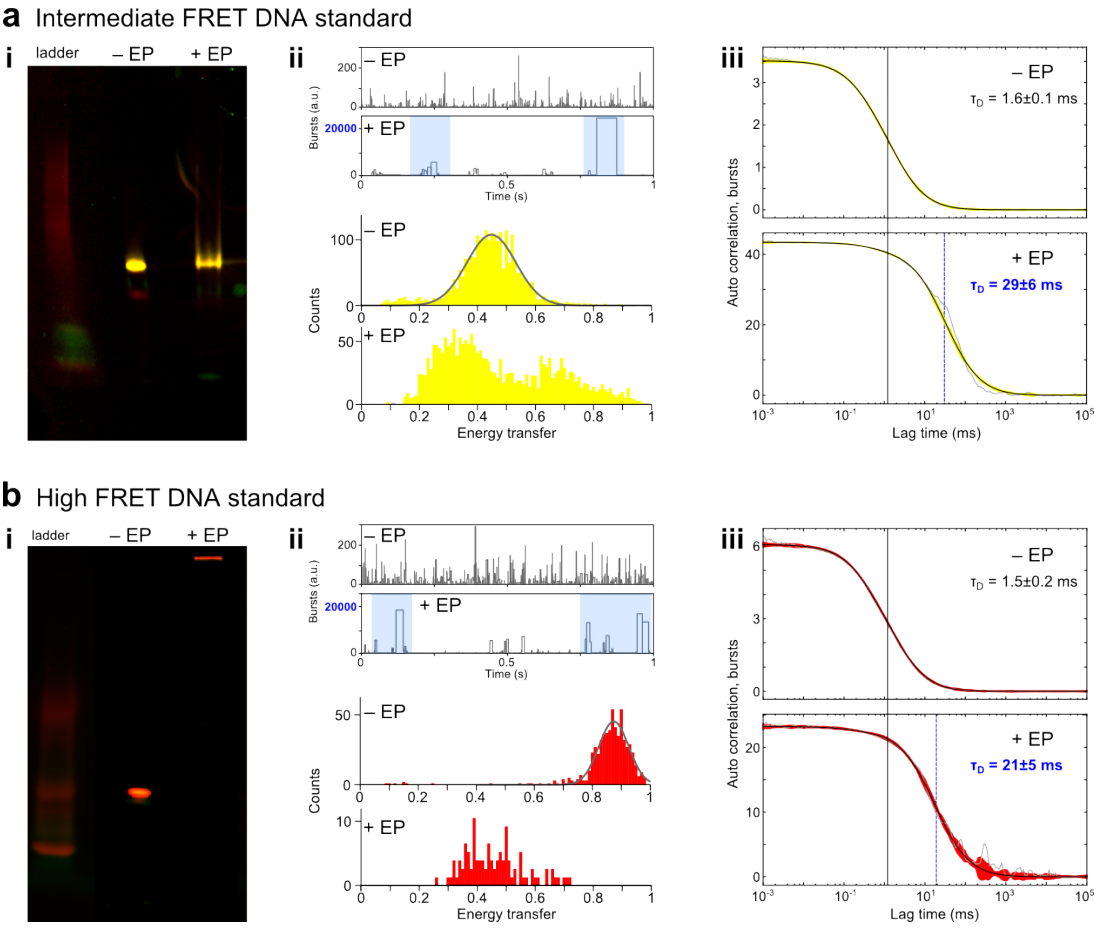

Figure 3.3: Aggregation of dsDNA standards after electroporation. **a.** Intermediate FRET DNA standard and **b.** high FRET DNA standard, non-electroporated (– EP) and electroporated (+ EP, 1.4 kV), were analysed using biochemical and single-molecule fluorescence assays. i. Coloured native gels of + EP samples show smeary band or dsDNA stuck in the well in comparison to – EP sample. ii. Burst time traces (gray) from single-molecule FRET confocal data show long dwell times for +EP sample and intermediate and high FRET histograms (highlighted in blue), which were not present in the – EP sample. iii. Autocorrelation analysis of FRET bursts show more than 10-fold larger molecule complexes crossing the confocal volume.

In addition to the previous experiments, I tested the impact of electroporation voltage on dsDNA aggregation and again could not reproduce distinct FRET populations for intermediate and high FRET DNA standards for all six electroporation voltages, most likely due to aggregation (SI Fig. 3.12). Furthermore, I excluded the impact of the fluorescent label by changing the acceptor dye from Atto647N to the less hydrophobic variant Atto647 for the high FRET DNA standard (66). Still, I could not reproduce the high FRET species (SI Fig. 3.13a). I also tried to stabilise dsDNA by increasing salt to a maximum concentration of 3 mM NaCl in the electroporation buffer (140), which did not decrease the aggregation effect (SI Fig. 3.13b).

Addition of EDTA

To overcome DNA aggregation, I referred to a study by Kooijmans *et al.* (148), which reports on aggregation of small interfering RNA (labelled and unlabelled) upon electroporation in presence and absence of extracellular vesicles. They successfully reduced aggregation by adding 1 mM ethylendiaminetetraacetic acid (EDTA), or an acid citrate to the electroporation buffer. Kooijmans and coworkers hypothesised that during the electroporation process, positively charged Al^{3+}-ions are released from the electroporation cuvette electrodes (made of aluminium), which then interfere with the negatively charged nucleic acid backbone (148). EDTA, on the other hand, chelates the Al^{3+}-ions preventing them from interacting with nucleic acid and thus reduces aggregation. Kooijmans *et al.* also used novel conductive polymer electrodes that do not consist of aluminium for electroporation to eliminate aggregation.

Intrigued by their results, I tested these novel conductive polymer electrodes (nucleocuvettes, Lonza) using the 4D Nucleofector (Lonza). Unfortunately, while no DNA aggregation was observed upon electroporation, neither was the successful internalisation of dsDNA standards into live *E. coli* using the conductive polymer electrodes, since the Lonza nucleofector did not allow to access and edit electroporation settings

such as number of pulses, strength, and duration. The Nucleofector settings were optimised for the electroporation of human cell lines, which have proven to be too weak for bacteria internalisation.

Next, I decided to try the addition of EDTA to the DNA sample before electroporation. Since the dsDNA annealing and storage buffer already contains 1 mM EDTA, addition of EDTA to the electroporation buffer was expected to have little to adverse effect. Also, electroporated cells are immediately diluted after electroporation into the recovery medium leading to a final EDTA concentration of less than 10 µM, which did not affect cell recovery. In light of this, I added EDTA to a final concentration of 1 mM to our dsDNA standards prior to electroporation. Again, I analysed intermediate and high FRET DNA standards before and after electroporation (Fig. 3.4). From the fluorescent native gels (Fig. 3.4i) no difference was observed between – EP and + EP sample. The FRET histograms showed very similar distributions before and after electroporation and burst time traces of – EP and + EP sample appeared very similar in burst length and amplitude (Fig. 3.4ii). These results showed that my DNA FRET standards were intact and that electroporation in presence of 1 mM EDTA had no effect on the measured FRET efficiencies. Furthermore, fluorescence correlation spectroscopy (FCS) data showed similar decay half-times and similar particle sizes (Fig. 3.4iii).

To summarise: addition of EDTA to the electroporation buffer circumvents dsDNA aggregation during the electroporation process and DNA FRET standards show similar FRET efficiency distributions with and without electroporation. In further internalisation experiments of nucleic acids into live bacteria, 1 mM EDTA was always added prior to electroporation, if not stated otherwise.

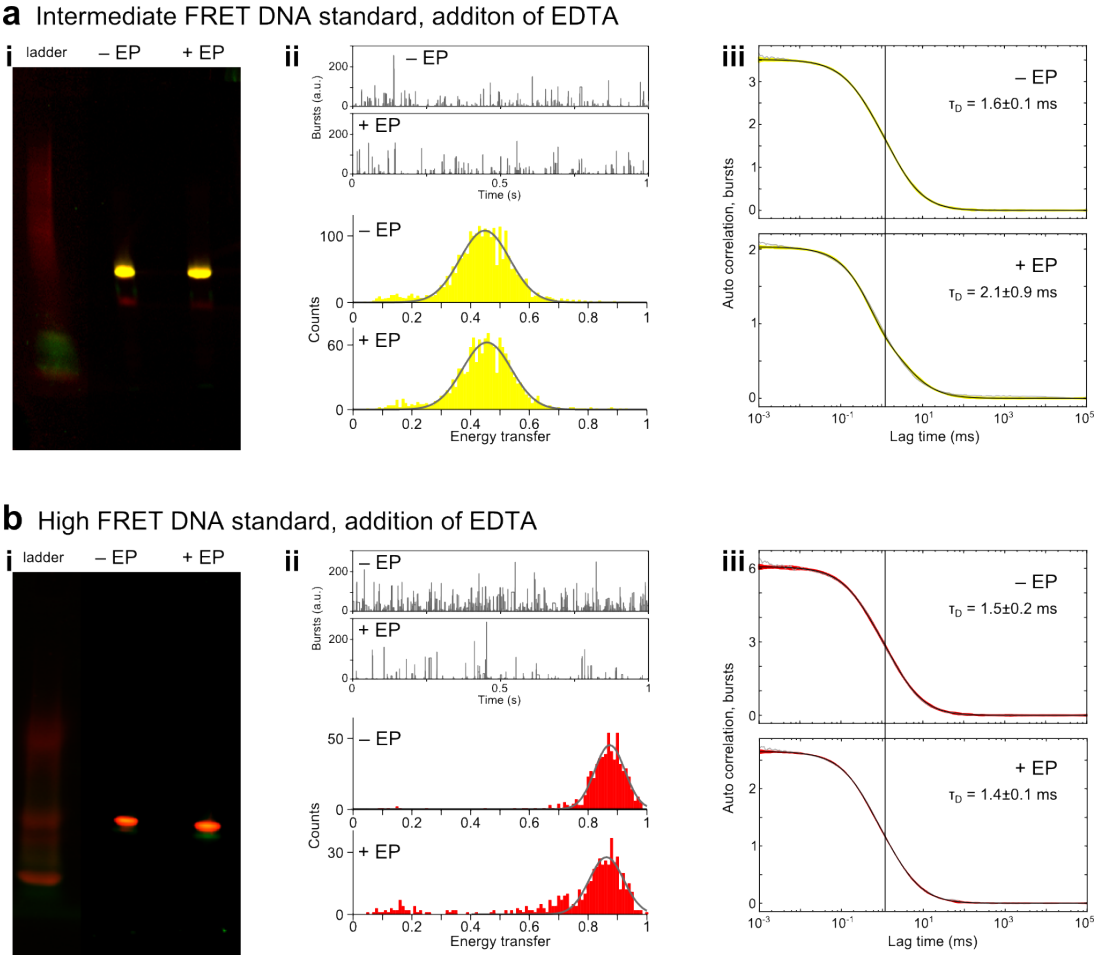

Figure 3.4: Addition of EDTA prior to electroporation circumvents aggregation of dsDNA. Electroporation of dsDNA standards in presence of 1 mM EDTA at 1.4 kV. **a.** Intermediate FRET DNA standard and **b.** high FRET DNA standard, non-electroporated (– EP) and electroporated (+ EP), were analysed using biochemical and single-molecule fluorescence assays. i. Coloured native gels of – EP and + EP sample show no difference. ii. Burst time traces (gray) from single-molecule FRET confocal data and intermediate and high FRET distributions appear very similar after electroporation and were fitted with a single Gaussian centered at 0.45±0.08 (– EP), and 0.46±0.08 (+ EP) for the intermediate FRET standard, and at 0.87±0.05 (– EP), and 0.86±0.06 (+ EP) for the high FRET standard. iii. Autocorrelation analysis of FRET bursts show very similar decay half-time and thus rule out aggregation.

Protected DNA standards

The loss of FRET after electroporation of dsDNA FRET standards without addition of EDTA led me to hypothesise that the hydrogen bonds between the two DNA strands in the helix break upon electroporation and electrostatic interaction of negatively charged single-stranded DNA backbone with Al^{3+}-ions cause aggregation. Furthermore, blunt DNA ends are also recognised by endonucleases and recombinases in

DNA repair pathways in living cells, avoiding the accumulation of toxic gapped and nicked DNA intermediates (146). In previous studies (62), we already observed a shift in the distribution of FRET values obtained for intermediate and high FRET DNA standards towards lower FRET values at the single-cell and single-molecule level *in vivo*, which we attributed to acceptor photobleaching and DNA degradation. Thus, blunt-ended DNA FRET standards are not ideally suited for *in vivo* FRET studies.

Therefore, we designed 'protected DNA standards' in which both DNA ends are chemically linked using azide-alkyne click chemistry (149) and connected by a short 8-carbon-linker. Our collaborators[3] synthesised intermediate and high FRET protected DNA standards using the same dye labelling scheme and Cy3B-Atto647N FRET dye pair (SI 3.6.1). First, I checked the FRET distributions using *in vitro* confocal single-molecule FRET microscopy and obtained very similar FRET-Stoichiometry (ES)- histograms for the protected DNA FRET standards as for the previously studied unprotected (blunt-ended) DNA FRET standards (Fig. 3.5); showing that the DNA-ends modifications did not change the fluorescence properties.

Interestingly, electroporated protected DNA standards reproducibly showed the same FRET distribution as non-electroporated protected DNA standards without the addition of EDTA for all six probed electroporation voltages (SI Fig. 3.14). From the fluorescent native gels (Fig. 3.6i) no difference was observed between – EP and + EP sample. The FRET histograms were reproducible and burst time traces of – EP and + EP sample appeared very similar in burst length and amplitude (Fig. 3.6ii). Fluorescence correlation spectroscopy analysis showed very similar decay half-time (Fig. 3.6iii) and no aggregation was observed upon electroporation. This work shows that linking both DNA-ends prevents aggregation and therefore makes protected DNA FRET standards ideally suited for single-molecule FRET measurements in live bacteria.

[3] collaboration with Afaf El-Sagheer from Tom Brown's group, Chemistry, Oxford.

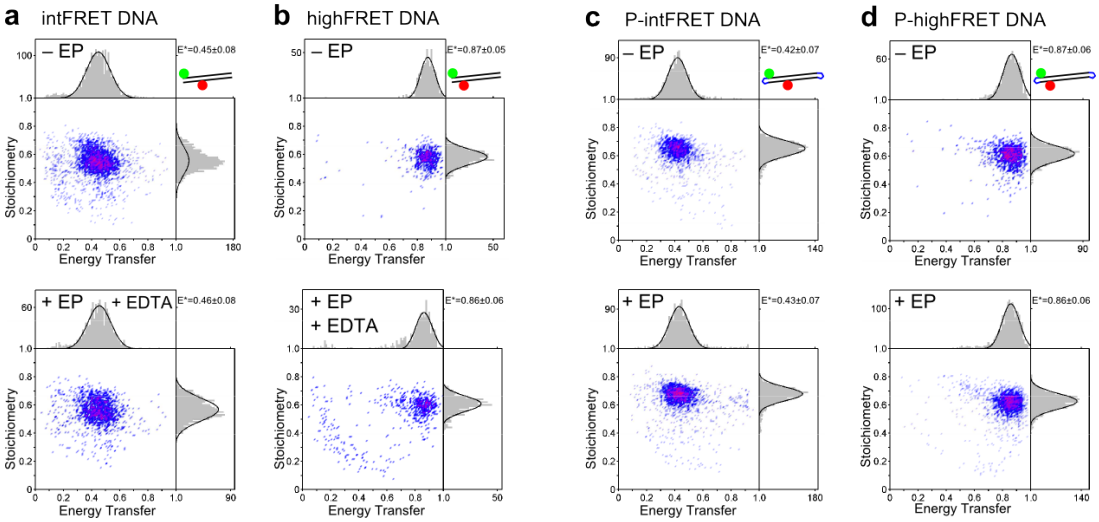

Figure 3.5: FRET-Stoichiometry (ES)-histograms of blunt-ended and protected (P) DNA FRET standards. **a.-d.** ES-histograms of non-electroporated '– EP' and electroporated '+ EP' samples are in very good agreement for all different intermediate and high FRET DNA standard; electroporation was performed at 1.4 kV. No significant difference between ES-histograms of **a.** unprotected and **c.** protected intermediate FRET DNA standard as well as **b.** unprotected and **d.** protected high FRET DNA standard was observed. FRET distributions were fitted with a single Gaussian and fitting results are shown in the top right corner of the respective ES-histogram (mean $\pm$ standard deviation).

3.3.2 Cell viability and cell loading

Following the characterisation of the effect of electroporation on dsDNA, I performed cell imaging studies to evaluate the impact of electroporation on cell viability and explore the cellular uptake of such DNA standards into live bacteria dependent on the applied electroporation voltage (SI 3.6.9). The aim of these experiments was to identify an electroporation voltage, which yields high cellular loading while maintaining cell viability.

Cell viability

First, I electroporated 2 µM of singly-labelled dsDNA-Cy3B into *E. coli* and checked the dependence of cell viability on the applied electroporation voltage. For measuring cell viability, I followed the growth and division of a single cell in time-lapse brightfield images on the microscope over the course of up to 1.5 h. I observed three different

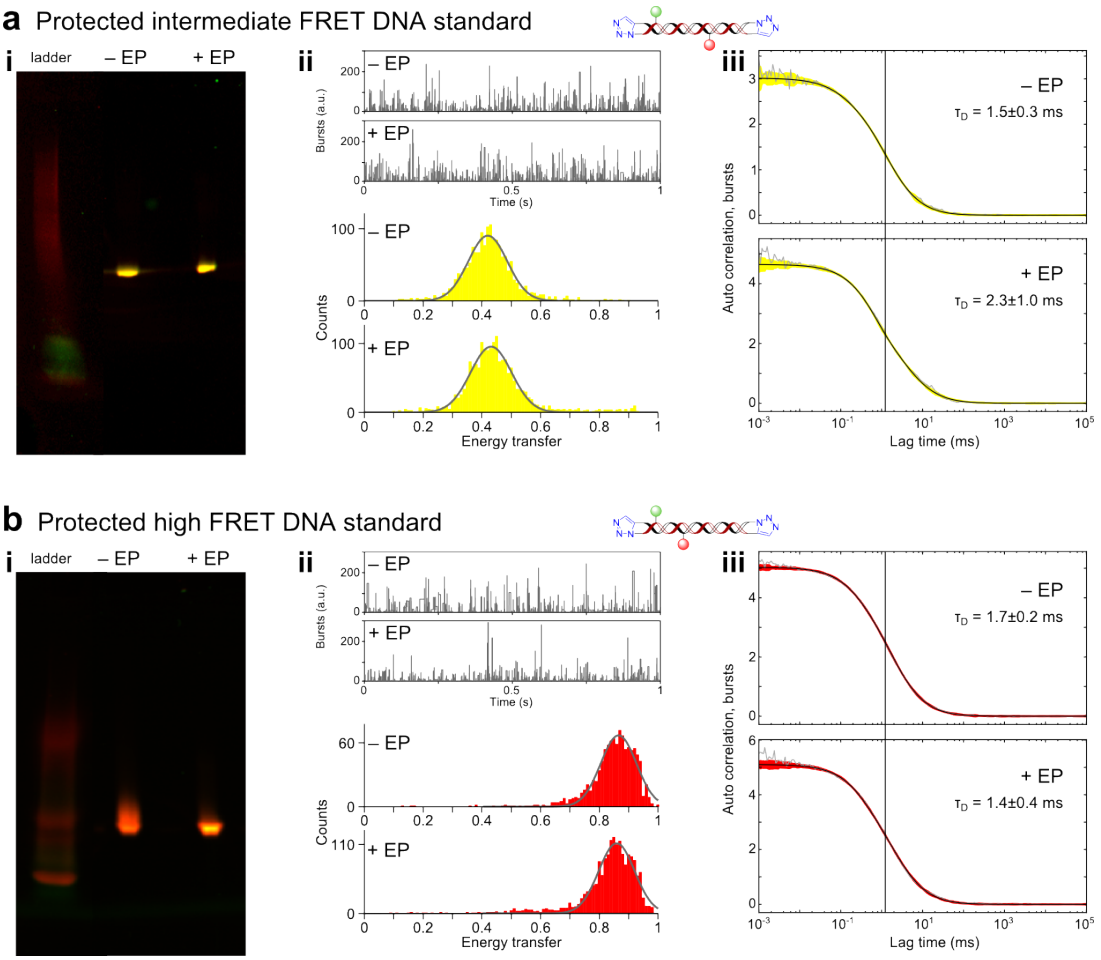

Figure 3.6: Electroporation has no impact on molecule integrity of protected dsDNA standards. **a.** Protected intermediate FRET DNA standards and **b.** protected high FRET DNA standards, non-electroporated (– EP) and electroporated (+ EP, 1.4 kV), are analysed using biochemical and single-molecule fluorescence assays. i. Color-coded native gels of – EP and + EP sample show no difference. ii. Burst time traces (gray) from single-molecule FRET confocal data and intermediate and high FRET distributions appeared very similar and were fitted with a single Gaussian centered at 0.42±0.07 (– EP), and 0.43±0.07 (+ EP) for the intermediate FRET standard, and at 0.87±0.06 (– EP), and 0.86±0.06 (+ EP) for the high FRET standard. iii. Autocorrelation analysis of FRET bursts show very similar decay half-time and thus rule out aggregation.

classes of cells: (i) 'growing and dividing' cells, which grew in length or divided into daughter cells during the course of imaging (Fig. 3.7a, green); (ii) 'not growing' cells, which neither divided nor grew during the observation time (Fig. 3.7a, purple); and (iii) 'damaged' cells, with visibly compromised cell membranes (Fig. 3.7a, black).

When cells were imaged in rich medium agarose pads heated to 37 °C (SI 3.6.5), I observed 81±7 % of 'growing and dividing' cells in my non-electroporated sample

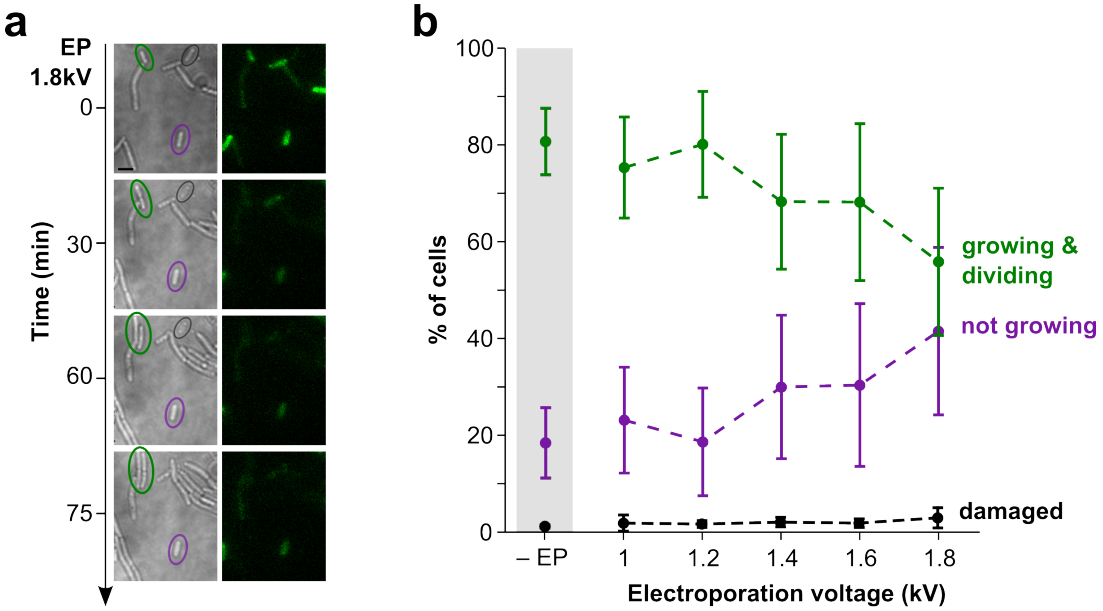

Figure 3.7: Characterisation of cell viability dependent on the applied electroporation voltage. **a.** Brightfield and fluorescence images of electroporated cells at 1.8 kV taken over the course of 75 min at 37 °C. Growth and division of cells is monitored as a measure of viability. **b.** The percentage of cells showing growth and division, retaining their shape (not growing) and showing compromised membranes (damaged) is measured at 6 different voltages (–EP, 1 to 1.8 kV). The percentage of growing and dividing cells drops from 81±7 % without electroporation under these imaging conditions down to 56±15 % under the harshest conditions of 1.8 kV, but the percentage of damaged cells stays below 3 %. Viability curves show mean and standard deviation of 3 data sets (1 data set: 500-800 cells per electroporation voltage). Scale bar: 3 µm.

(Fig. 3.7b, gray bar). With increasing electroporation voltage, I observed a decrease in percentage of 'growing and dividing' cells and an increase in percentage of 'not growing' cells (Fig. 3.7b); less than 3 % of 'damaged' cells were observed under all electroporation voltages. When electroporation was performed at 1.4 kV and 1.6 kV, a similar percentage of cells were found to be 'growing and dividing' (70 %), while at 1.8 kV, the harshest electroporation conditions used in this study, viability decreased only marginally to 56%. Notably, the 3 data sets for each electroporation voltage were taken on three different days and the large error bars of up to 15 % indicate a large sample-to-sample variation. Furthermore, the time window of observation after cell recovery is important, since cells might show different lag-time after electroporation where cells will not divide and consequently would be classified as 'not growing'

using this viability assay. To summarise: I maintained more than 50 % of cell viability throughout all six electroporation voltages.

Cell loading

Next, I studied cell loading by internalising singly-labelled dsDNA-Cy3B (2 µM in electroporation buffer) at these six different electroporation voltages. Already, I saw a clear increase in the number of loaded cells with increasing electroporation voltage in the green fluorescence channel (Fig. 3.8, inset images). Under these imaging conditions, 14.8$\pm$1.5 % of cells were loaded at 1.0 kV and about 30 % of the cells were loaded at 1.4 kV and 1.6 kV (Fig. 3.8). I could increase loading up to 60 % at 1.8 kV. Here, I was using a conservative loading threshold where cells were classified as loaded when the overall cell intensity normalised by cell area was larger than the mean plus three times the standard deviation of non-electroporated cells. Using this loading threshold, only 0.6$\pm$0.4 % of non-electroporated cells were classified as loaded, despite the higher autofluorescence of the cells in the green fluorescence channel (Fig. 3.8, gray bar). At this loading threshold, only cells with few internalised biomolecules (N$>$5) are classified as loaded and cells with only very few loaded molecules would be classified as non-loaded. It is worth noting that in a previous study (62), we achieved more than 90 % loading at 1.8 kV under the same conservative threshold, but using the red fluorescent dye Atto647N instead of Cy3B. The discrepancy between these two results can be explained due to the significantly smaller cellular autofluorescence in the red fluorescence channel.

For further studies, I used an electroporation voltage of 1.4 kV, which offers a good compromise between sufficient cellular loading and high cell viability.

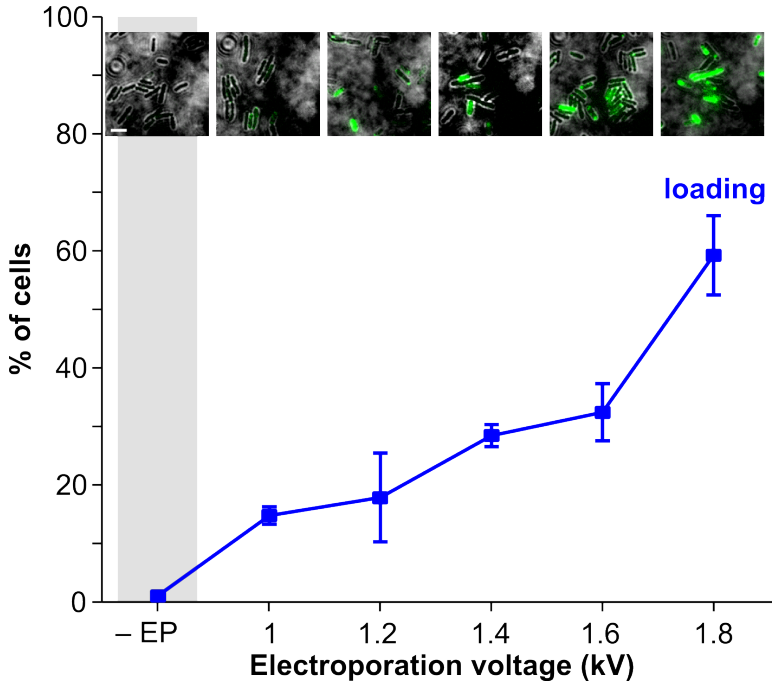

Figure 3.8: Characterisation of cell loading dependent on the applied electroporation voltage. Inset images: overlay of the inverted brightfield and fluorescence images of example FOVs of cells electroporated at 0 to 1.8 kV (left to right). Loaded cells appeared brighter at higher voltages, which is in good agreement with a previous study of cellular uptake at 1.8 kV and 0.9 kV (150). A clear increase in loading from 15±2 % at 1 kV to 60±7 % at 1.8 kV was observed; cells were considered as loaded when initial cell intensities normalised by cell area were larger than the mean plus three times the standard deviation of non-electroporated cells. Loading curve shows mean and standard deviation of 3 data sets (1 data set: 300-500 cells per electroporation voltage). Scale bar: 3 µm.

3.4 Internalisation of proteins

While internalisation of nucleic acids is straightforward (62, 141, 143), precautions need to be taken when internalising labelled proteins using electroporation. This is mostly due to the fact that electroporation might affect protein structure and function. Thus, when this method is used for internalising proteins, their function has to be checked for each sample. For this purpose, we developed a protocol that can be followed when internalising any small and medium-sized fluorescently-labelled protein into bacteria (140, 142).

3.4.1 Electroporation of proteins

First, the impact of the electroporation method on the protein integrity should be tested. Again, we used an intra-molecular FRET assay to show that electroporation does not change the expected FRET signal for the protein of interest and tested protein specific function before and after electroporation to validate protein integrity. Here, we electroporated doubly-labelled Klenow fragment (KF), a subunit of *E. coli* DNA Polymerase I, and measured the FRET signature before and after electroporation using confocal single-molecule FRET microscopy (Fig. 3.9, (62)). Klenow fragment protein (L744C-Cy3B, K550C-Atto647N) was previously characterised *in vitro* using single-molecule FRET and it was shown that the labels did not affect protein structure and function (53). In the *in vitro* study KF displayed millisecond-timescale dynamics between two structural states, an open conformation ($E^*_{open}\sim0.48$) and a closed conformation ($E^*_{closed}\sim0.66$), Fig. 3.9a. Upon addition of template DNA (dideoxy-terminated to prevent extension of the 3' terminus) a shift towards the open conformation could be observed (Fig. 3.9b) both in the electroporated and non-electroporated sample. Further addition of complementary nucleotide (A-dTTP) resulted in a pronounced increase in the population of the closed conformation, again for both samples. These results were in excellent agreement with previous studies (53, 54) and showed that electroporation does not affect the structure and function of the Klenow fragment.

Second, most proteins have a preference for specific storage buffer conditions, which ensure protein stability and function over time. Nonetheless, electroporation has to be carried out under low salt conditions to ensure high internalisation efficiency and avoid shorting (arcing) during the electroporation pulse. In a study by Sustarsic *et al.* (140), a working buffer of 50 mM Tris (pH 7.4) and up to 50 mM NaCl (or equivalent) was successfully tested for electroporation using up to 1.8 kV. Additionally, a minor, but significant positive effect was observed by adding glycerol to the protein storage

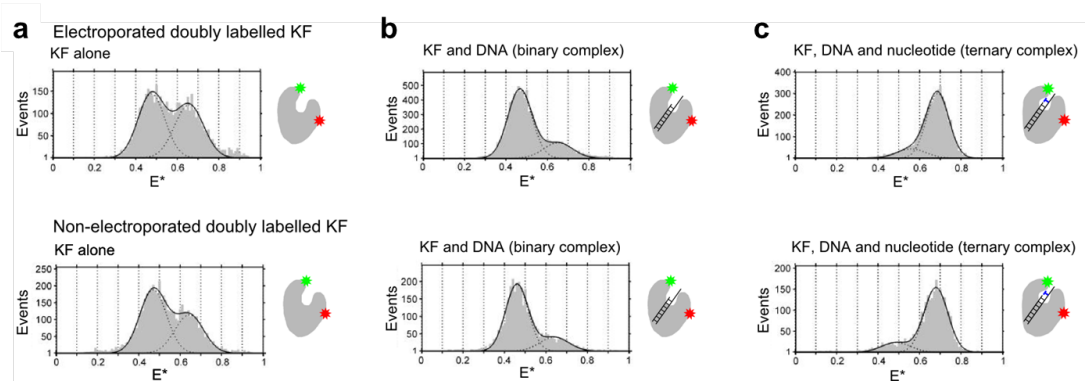

Figure 3.9: *In vitro* measurements of doubly-labelled Klenow fragment (KF, subunit of DNA Polymerase I) electroporated (top) and non-electroporated (bottom). **a.** KF alone before and after electroporation exhibited two main FRET distributions corresponding to open conformation ($E^*_{open} \sim 0.48$), and closed conformation ($E^*_{closed} \sim 0.66$). **b.** Presence of template DNA (dideoxy terminated) led to a shift towards the open conformation whereas **c.** further addition of complementary nucleotide (A-dTTP) led to a more pronounced population of the closed conformation; again no significant difference between electroporated and non-electroporated sample was observed. Adapted from (62). Experiments were performed by Dr. Louise Aigrain.

buffer.

Third, protein samples might still contain a small percentage of free dye, which was not successfully removed in protein purification steps after labelling. These free dye molecules are more than 100 times smaller than protein molecules and are consequently preferentially internalised. To ensure significant uptake of fluorescently labelled proteins instead of free dye, the labelled protein stock must contain less than 2 % of free dye (140).

Finally, non-internalised labelled proteins could also stick to the bacterial cell wall after electroporation. This phenomenon was protein dependent and therefore must be determined for each protein separately. Non-internalised proteins could be removed by further washing steps after cell recovery. Washing buffers containing fairly high concentration of salt (to disrupt non-specific electrostatic interactions), and detergent (to disrupt non-specific hydrophobic interactions) could be tested (SI 3.6.4). For aggregation-prone proteins, an additional cell-filtration step using a 0.22 µm filter can be added after recovery to remove non-internalised protein aggregates, however,

this step usually diminishes cell viability (sec. 3.4.2).

3.4.2 Cell viability and cell loading

Employing the established guidelines by Sustarsic *et al.* (140), we carried out quantitative investigation of the internalisation of the 10 kDa ω subunit of bacterial RNA polymerase, labelled with Cy3B, while also studying cell viability. As shown earlier in this chapter (Fig. 3.2), the protein, ω-Cy3B, was efficiently internalised, while both negative controls (non-electroporated and empty cells) show no significant fluorescence background. Additionally, the ω-Cy3B sample contained about 1 % of free dye and hence is ideally suited to characterise cellular uptake and cell viability upon electroporation (140).

Cell loading

First, we explored the dependence of internalisation efficiency of 2.5 µM ω-Cy3B on the applied electroporation voltage. Again, we tried a set of six different electroporation voltages and I analysed the cellular uptake and loading efficiency (SI 3.6.9). As expected, the increase in electroporation voltage led to an increase in the percentage of loaded cells (Fig. 3.10a), however, there was significant day-to-day variation in loading efficiency (3 independent repeats). Particularly, non-electroporated cells occasionally exhibited very high inner-cell fluorescence, most often corresponding to cells already exhibiting compromised cell membranes, which would be classified as 'damaged cells' according to our previous viability classification. This phenomenon increased the effective fluorescence background, especially for the non-electroporated cell control, which had to be taken into account when interpreting loading efficiencies. While absolute loading efficiencies varied from 40 % to 70 % (Fig. 3.10a), loading efficiencies normalised by the background fluorescence of non-electroporated cells (25 %, Fig. 3.10a, gray bar) ranged from 15 % to 45 %.

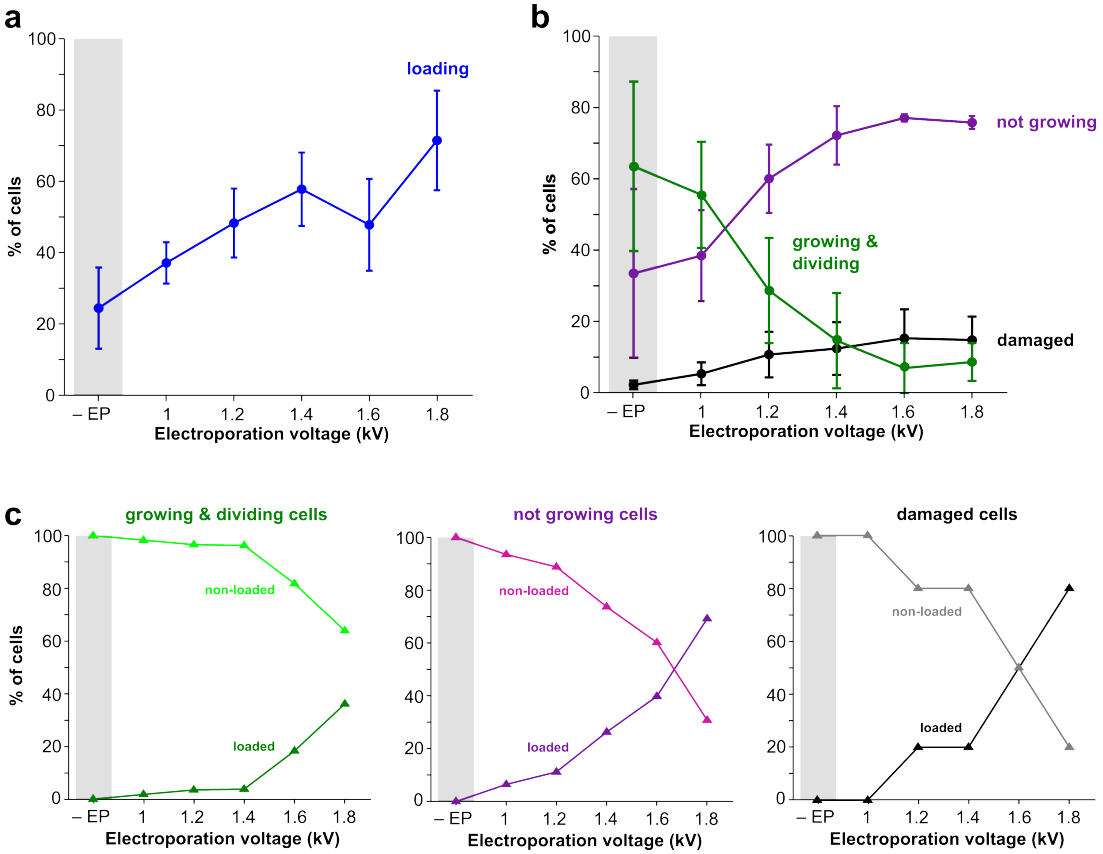

Figure 3.10: Characterisation of **a.** internalisation efficiency and **b.** cell viability for protein internalisation dependent on electroporation voltage. Cells were electroporated with 2.5 µM RNA polymerase ω-Cy3B at 1 to 1.8 kV, filtered, washed, and recovered for 1.5 h in rich medium. **a.** The internalisation efficiency is plotted relative to empty cells and non-electroporated cells are shown as a reference (gray bar). **b.** Cells were imaged in bright field mode and again classified as 'growing and dividing', 'not growing', and 'damaged'. **c.** Correlation between cell loading and cell viability. Loading and viability were measured simultaneously and the effect of voltage on the proportion of loaded and non-loaded cells is shown for each class of cells separately: growing and dividing, not growing, and damaged cells. Three independent data sets of $>$ 300 cells per electroporation voltage were analysed for each experiment, and mean $\pm$ standard deviation is plotted.

Cell viability

The previously discussed protocol for protein internalisation includes a cell filtration step (0.22 µm filter, SI 3.6.4) after cell recovery, to wash off non-internalised protein. In order to determine the compromising effect of filtration on cell viability, I studied cell viability for all electroporation voltages using the same experimental conditions as for nucleic acid loading experiments, but with the addition of a filtration step. I examined cells in brightfield mode over the course of 2 h following electroporation, recovery,

and cell filtration step, and again classified cells into: (i) 'growing and dividing' cells, (ii) 'not growing' cells, and (iii) 'damaged' cells. Quantifying the percentage of cells in each category, I observed a decrease in the number of 'growing and dividing' cells with electroporation voltage, while the number of 'not growing' and 'damaged' cells increased (Fig. 3.10b). To rule out concerns that only damaged cells get loaded with ω-Cy3B, we determined the correlation between cell viability and cell loading by performing both studies simultaneously. As expected, I observed an effect of applied voltage across all viability categories (Fig. 3.10c). I found the effect of voltage on loading was stronger for 'damaged' cells than for 'not growing', and 'growing and dividing' cells. Since only a small percentage of cells was classified as 'damaged' ($<15\,\%$ at $1.4\,$kV), however, I reasoned that the majority of loaded cells corresponded to both 'not growing', and 'growing and dividing' cells under any applied electroporation voltage.

In contrast to nucleic acid internalisation, we employed an electroporation voltage of $1.2\,$kV for initial protein internalisation experiments, since the lower electroporation voltage offers higher cell viability with significant cellular uptake for ω-Cy3B sample. Notably, sample preparation steps and internalisation efficiency have to be tested and optimised for each new protein sample individually.

3.5 Conclusion

We developed a facile and efficient internalisation method of organic-dye labelled biomolecules into live bacteria using electroporation. First, I described a general electroporation experiment and showed qualitative representation of the experimental results. The many studies of successful internalisation of organic dye-labelled biomolecules into live *E. coli*, ranging from short RNA and DNA fragments to proteins up to $100\,$kDa, showed the broad applicability of the electroporation method and should

give way to many interesting *in vivo* single-molecule fluorescence studies.

Second, I optimised the electroporation method for internalisation of nucleic acids, especially avoiding the aggregation of nucleic acids upon electroporation, which had been observed using 45 bp intermediate and high FRET DNA standards and characterised using *in vitro* biochemical and single-molecule fluorescence assays. In this experiments, the addition of EDTA has proved ideal to prevent aggregation and was hypothesised to chelate Al^{3+}-ions being released from electroporation electrodes during electroporation pulses and thus preventing their interference with the negatively charged DNA backbone (148). I suspect that membrane pores, formed through electroporation, also act as a filter for the more than 10-fold larger DNA aggregates, since I did not observe aggregates (multiple fluorophore labels per molecule) in previous *in vivo* single-molecule photobleaching studies using our dsDNA standards (62). However, the impact of electroporation on molecule integrity should be tested for each new nucleic acid incorporation: the electroporation with EDTA of short ssRNA fragments and *E. coli* bulk transfer RNA for instance did not affect molecule integrity, which is shown in chapter 5.

In addition, I introduced protected DNA FRET standards (chemically linked DNA ends) as ideal standards for single-molecule FRET measurements in live bacteria. Single-molecule FRET distributions were reproducible *in vitro* for all electroporation conditions and no aggregation was observed, even without EDTA present. This result also makes me believe that dehybridisation of short double-stranded DNA fragments might occur for blunt-ended DNA standards, enhancing aggregation. Protected DNA FRET standards are particularly suited for *in vivo* studies since they do not present a target for DNA repair or degradation machineries unlike the blunt-ended dsDNA standards and thus, should be great markers to report on single-molecule FRET levels *in vivo* (chapter 4).

In order to optimise electroporation conditions, I studied dsDNA-Cy3B uptake and

cell growth and division for six different electroporation voltages, based on this, I proposed 1.4 kV as an optimal electroporation voltage for nucleic acid incorporation (70 % viability, 30 % loading).

Third, we characterised the electroporation method for internalisation of organic dye-labelled proteins into live bacteria (140). We defined optimal buffer conditions compatible with efficient loading of cells with the labelled protein of interest and proposed washing buffers (higher salt, non-ionic detergent) to remove non-internalised proteins. These washing buffers have to be adapted for each protein sample individually taking protein properties (e.g. surface charge, protein stability) into account. Next, we showed that it is necessary to have less than 2 % of free dye in the protein sample in order to avoid preferential uptake of dye molecules over labelled proteins. In addition, cell filtration has proven beneficial to remove non-internalised labelled proteins and protein aggregates. However, cells exposed to cell filtration displayed lower viability than cells washed with buffer (sec. 3.3.2 versus sec. 3.4.2). Nevertheless, less than 15 % of cells were visibly damaged, showing that most of the loaded cells were suitable for live-cell single-molecule imaging. If absolute viability is required, imaged cells can be examined for their viability by following their division or by employing other cell-viability indicators, such as metabolic activity indicator, nucleic acids (nucleoid) staining, or membrane staining assays (151, 152).

In this study, the internalisation of organic dye-labelled nucleic acids and proteins was successfully optimised. Using the developed protocol, single-cell and single-molecule FRET studies in live cells now become possible. Next, the characterisation of organic fluorophores as FRET-dye pairs, single-cell FRET, and single-molecule FRET measurements in live bacteria will be presented in chapter 4.

Contributions

I performed all experiments and data analysis of nucleic acids internalisation studies, which are presented in two published reports (62, 141). Protected DNA FRET standards were synthesised by Dr. Afaf El-Sagheer.

Protein internalisation studies were performed by Marko Sustarsic and Dr. Louise Aigrain, and I wrote analysis software in MATLAB (MathWorks) and analysed data. For the characterisation of protein internalisation and cell viability (sec. 3.4.2), Marko Sustarsic performed sample preparations, and I performed cell viability and loading measurements and analysed the data.

3.6 Supplementary information

3.6.1 Preparation of labelled DNA standards

Oligonucleotides were purchased from IBA GmbH. The sequences used are shown below; the highlighted **T** base was labelled either with Cy3B (STD45T) or Atto647N, Alexa647, or Cy5 (STD45B series).

DNA sequences 5' to 3'

STD45T (unlabelled): TAA ATC TAA AGT AAC ATA AGG TAA CAT AAC GTA AGC TCA TTC GCG

STD45T: **T**AA ATC TAA AGT AAC ATA AGG TAA CAT AAC GTA AGC TCA TTC GCG

STD45B (unlabelled): CGC GAA TGA GCT TAC GTT ATG TTA CCT TAT GTT ACT TTA GAT TTA

STD45B – dT28: CGC GAA TGA GCT TAC GTT ATG TTA CCT **T**AT GTT ACT TTA GAT TTA

STD45B – dT38: CGC GAA TGA GCT TAC GTT ATG TTA CCT TAT GTT ACT T**T**A GAT TTA

DNA labelling Briefly, 5 nmol of ssDNA (50 µL out of 100 µM stock) was ethanol precipitated and then dissolved in 100 µL sodium borate ($NaBO_3$, 0.1 M, pH 9.0). Labelling at the 5'-end of oligonucleotides (STD45T) was performed using a 5'-amino-C6-modifying group with a 10-fold excess of N-hydroxy-succinimidyl ester of Cy3B (GE Healthcare); 50 nmol of dye dissolved in 5 µL dimethyl sulfide (DMSO) was added to the DNA; wrapped in foil and placed on a shaker for 5 h or overnight. Internal labelling (STD45B series) was performed by incubating ten-fold excess of dye, Atto647N (ATTO-TEC GmbH), Cy5 (GE Healthcare), or Alexa647 (Invitrogen) at 50 °C for 2 h or longer. Then another ten-fold excess of dye was added and incubated again as before (150, 153).

DNA purification The 45-bp ssDNA fragments were purified using denaturing polyacrylamide gel electrophoresis (PAGE). An acrylamide concentration of 20 % (29:1) was used and the gel was run at 550 V for 6 h in TBE buffer. The main labelled DNA

fraction was cut out, crushed and eluted in ddH_2O overnight. The gel fragments were removed by centrifugation and filtering with a 0.45 µm pore size spin column. The DNA filtrate was de-salted on a P6 column (BioRad) into ddH_2O and evaporated in speedvac. The pellet was dissolved in 10-20 µL ddH_2O, and the concentration of labelled DNA was measured on UV-Vis Spectrophotometer NanoDrop1000 (Thermo Scientific).

DNA annealing Singly-labelled double-stranded DNA, intermediate and high FRET dsDNA standards were prepared by annealing unlabeled or labelled STD45T (top strand) to either STD45B unlabelled, STD45B-dT28 or -dT38 (bottom strands), respectively. Oligonucleotides were annealed in a low-salt annealing buffer (20 mM Tris-HCl (pH 8.0), 10-100 mM NaCl, 1 mM EDTA) by heating to 94 °C and subsequent cooling to 4 °C over 45 min in steps of 10 °C. DNAs were stored in 1-5 µM stocks at -20 °C.

3.6.2 Preparation of proteins

ω-RNA polymerase C-terminal His_6-tagged ω [Cys68] was expressed using pET expression system and purified by Ni^{2+}-affinity chromatography in denaturing conditions as described and characterised in (140). Labelled proteins were stored at -20 °C in 50 mM Tris-HCl, pH 7.5, 1 mM DTT, and 40 % glycerol.

Klenow fragment DNA Polymerase I Klenow fragment (KF) was prepared as described in (53). Labelled proteins were stored at -20 °C in 50 mM Tris-HCl, pH 7.5, 1 mM DTT, and 40 % glycerol. The extent of labelling, calculated from the UV-Vis spectrum, was 70 %.

3.6.3 Electrocompetent cells

ElectroMAX DH5α-E Competent Cells (Invitrogen), a commercially available electrocompetent *E. coli* cell line was used for electroporation. The cells were diluted 1:1 with ddH_2O and stored at $-80\,^{\circ}$C. For each electroporation experiment 20 µL of electrocompetent cells were used.

3.6.4 Electroporation protocol

Up to 5 µL of labelled dsDNA standards stored in low-salt annealing buffer, 1-10 µM stock concentration, were added to 20 µL of electrocompetent cells to a final concentration of 0.5 to 5 µM. The cell suspension and organic fluorophore labelled biomolecules were added into a pre-chilled electroporation cuvette (1 mm gap, Bio-Rad). The cell suspension was then exposed to the discharge of a high voltage electric field. For all experiments carried out in this thesis, the initially applied electroporation voltages ranged from 1.0 to 1.8 kV and the electric field decayed with a time constant of 3 to 6 ms ensuring efficient internalisation (MicroPulser, Bio-Rad). The cells were rapidly recovered in 500 µL of rich medium (super optimal broth with catabolite repression, SOC) for about 20 min shaking at 37 °C. Then, the cells were washed 4 times with phosphate buffered saline (PBS) by pelleting the cells by centrifugation at 3300 g for 1 min at 4 °C, followed by resuspension. Finally, the cells were resuspended in 80-150 µL PBS and stored on ice.

For protein internalisation, cells were recovered by incubation with 500 µL of SOC for only 3 min at 37 °C. After recovery, cells were pelleted for 1 min at 3300 g and 4 °C, and washed with phosphate buffered saline (PBS) solution containing 100 mM NaCl and 0.005 % Triton X100. Washing was repeated 2 more times with the same buffer, and 3 more times with PBS only. For cell filtration, cells were transferred to an Ultrafree-MC centrifugal filter tube (0.22 µm pore diameter, GE Healthcare) after the

first wash and spun 3x for 3 min at 800 g and 4 °C.

3.6.5 Agarose pad preparation

The 1% agarose-M9 pads were prepared by adding 500 µL of heated agarose-M9-salt medium on a cover slide and let cool. The cells were vortexed briefly to limit any potential of cell clustering. About 5-10 µL of the cell suspension were spread on the agarose pad. Finally, a burned cover slide was placed on top of the agarose pad which was turned towards the immersion oil objective for imaging.

For long-term observation of cells for several hours (viability and loading experiments) 1 % agarose pads were prepared with M9 salts and EZ rich defined medium (Teknova). Furthermore, a channel system was cut out off the pad (Fig. 3.11) and the agarose was kept wet by adding about 100 µL EZ rich defined medium into the channel system every 1 h.

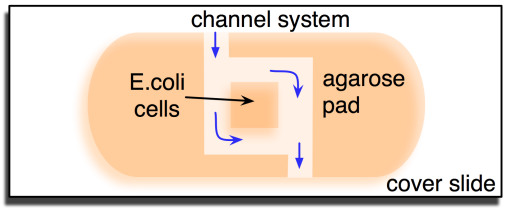

Figure 3.11: Schematic of channel system in agarose pad for buffer supply for long-term observation. Adapted from (150).

3.6.6 Native PAGE

Electroporated and non-electroporated sample were characterised using Native PAGE (non-denaturing gel electrophoresis) and sample homogeneity was qualitatively evaluated. About 10 µL of each sample was run on Native-PAGE gel (Mini-PROTEAN

TGX Precast Gels, Bio-Rad) in Tris-Glycine buffer at 130 V for 1 h. In-gel fluorescence was imaged (PharosFX Plus Molecular Imager, Bio-Rad), and overlay images of green and red fluorescence images were generated in Fiji open-source image-processing software.

3.6.7 Single-molecule FRET confocal microscopy

In vitro single-molecule FRET microscopy using an ALEX scheme was performed on a custom-built confocal setup as sketched in Appendix A.2; 120 µW green and 30 µW red laser power were used; measured before laser beam enters the objective. 20 µL of DNA FRET standards diluted in ddH_2O to 10-50 pM final concentration were added onto a burned cover slide and the laser beam was focused about 20 µm into solution. Two 10 min data sets were acquired for each sample. The single-molecule fluorescence bursts from *in vitro* single-molecule FRET confocal microscopy were analysed in MATLAB as described in (154). Information on photon arrival times, excitation cycle, and detection channel, enables the calculation of fluorescence bursts (donor or acceptor) arising due to molecules traversing the confocal spot under either donor or acceptor excitation. FRET efficiency (E^*, uncorrected), and relative probe stoichiometry (S^*) were calculated as follows:

$$E^* = \frac{F_{\text{Dex}}^{\text{Aem}}}{F_{\text{Dex}}^{\text{Aem}} + F_{\text{Dex}}^{\text{Dem}}} \qquad (3.1)$$
$$S^* = \frac{F_{\text{Dex}}^{\text{Aem}} + F_{\text{Dex}}^{\text{Dem}}}{F_{\text{Dex}}^{\text{Aem}} + F_{\text{Dex}}^{\text{Dem}} + F_{\text{Aex}}^{\text{Aem}}},$$

where $F_{\text{Xex}}^{\text{Yem}}$ represents the fluorescence of a burst arising in the Y emission channel under X excitation.

3.6.8 Fluorescence correlation spectroscopy

Fluorescence correlation spectroscopy (FCS) measurements were performed on a custom-built confocal microscope as sketched in Appendix A.2. 20 µL of DNA FRET standards diluted in ddH_2O to 1-5 nM final concentration were added onto a burned cover slide and the laser beam was focused about 20 µm into solution; two 5 min data sets were acquired for each sample at 120 µW green continuous wave and separated into green and red fluorescence channel for detection. Calibration measurements were carried out using Rhodamine 6G using the same settings (data shown in sec. 2.3.1). The correlation was calculated using a computer-implemented correlator (Flex 02-01D, Correlator.com, USA). Data was analysed using PyCorrFit, an open-source software package by Paul Müller (Schwille lab, (155)).The data was fitted using the implemented Levenberg-Marquardt algorithm to the autocorrelation function (156).

$$G(\tau) = A_0 + \frac{1}{N}\frac{1}{1+\tau/\tau_D}\frac{1}{\sqrt{1+\tau/(E^2\tau_D)}}\left(1+\frac{Te^{-\tau/\tau_T}}{1-T}\right) \quad \text{with}$$

A_0 : offset

N : effective number of molecules in confocal volume

τ_D : characteristic diffusion time through confocal volume

E : elongation factor of confocal volume

T : fraction of molecules in non-fluorescent triplet state

τ_T : characteristic residence time in triplet state,

describing three dimensional diffusion of a single species (labelled biomolecule) through the confocal volume (assuming ideal Gaussian laser beam profile) and including one triplet state of the fluorophore.

3.6.9 Live-cell imaging

Live-cell imaging experiments were performed on a custom-built inverted widefield microscope as laid out in Appendix A.1. Internalisation and cell viability experiments were performed at 50 ms using low laser powers ranging from 300 µW (red channel) to 600 µW (green channel). Internalisation images were obtained in Fiji by overlaying brightfield image (inverted) and fluorescence images (averaged over 10 frames, false coloured). Cells were segmented using the programme 'Schnitzcells' (Elowitz lab, (157)), which was adapted for brightfield cell images (150), and cell intensities were quantified and normalised by cell area using custom-written MATLAB scripts. Intensities were corrected for mean intensity of empty cells to account for cellular autofluorescence; cells were classified as loaded if the calculated intensity was larger than the mean intensity of empty cells plus three times the standard deviation of empty cells. The loading efficiency is the percentage of classified loaded cells from the entire pool of segmented cells. Samples were categorised according to their loading performance as 'very good' ($>$60 % loading), 'good' ($>$30 % loading), and 'poor' ($>$10 % loading), see tab. 3.1. Viability was analysed by manually comparing brightfield images of cells taken every 20-40 min, and classifying cells as 'growing and dividing', 'not growing' or 'damaged' (140, 141). For comparative analysis of loading and viability, the microscope stage was set to image an area of the pad first in the fluorescence mode for loading, and then in the brightfield mode for viability analysis using Micromanager open-source microscopy software.

3.7 Supplementary figures

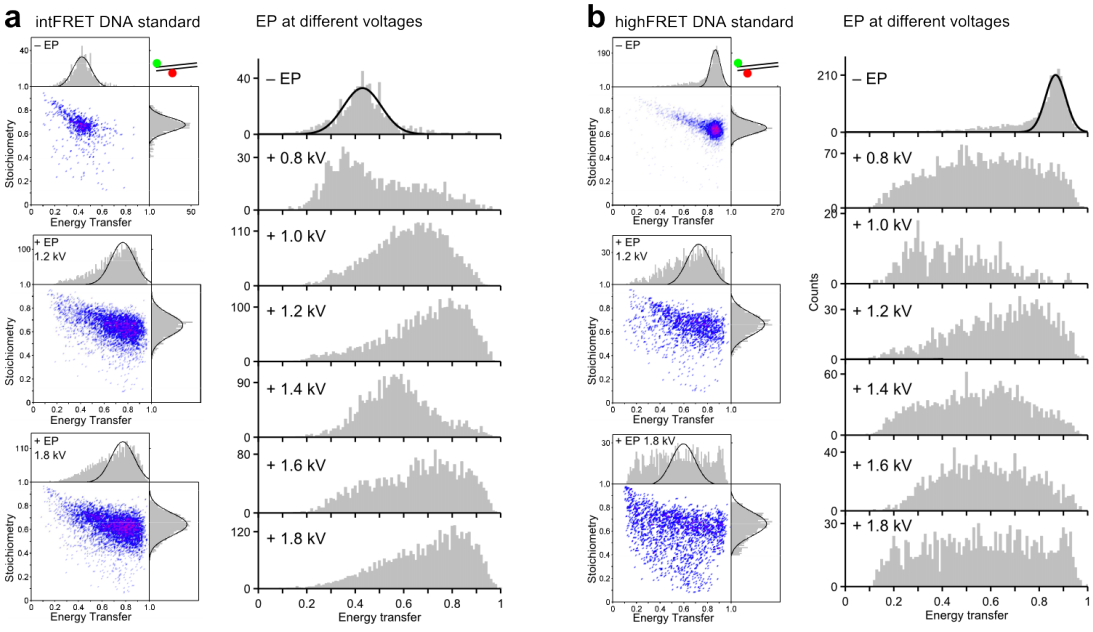

Figure 3.12: Aggregation of dsDNA standards after electroporation at six different electroporation voltages. **a.** Intermediate FRET DNA standard and **b.** high FRET DNA standards, non-electroporated (– EP) and electroporated (+ EP), are analysed using single-molecule confocal microscopy. Intermediate and high FRET histograms of – EP sample could not be reproduced and example FRET-stoichiometry histograms for 1.2 kV and 1.8 kV show wide spread of FRET efficiencies.

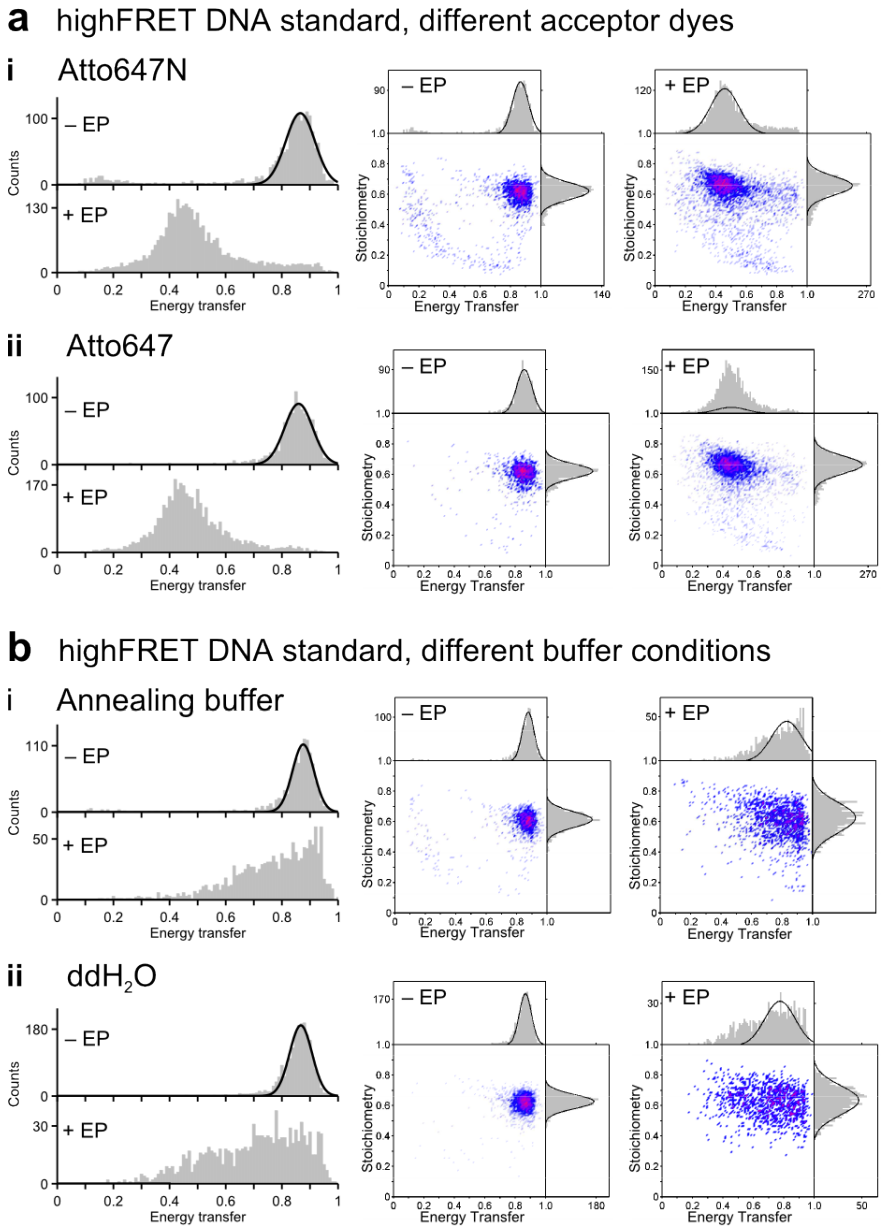

Figure 3.13: Aggregation of dsDNA standards after electroporation at 1.4 kV. **a.** Electroporation of high FRET DNA standards with Atto647N and Atto647 acceptor dyes. **b.** Electroporation of high FRET DNA standard in low-salt annealing buffer (3 mM NaCl) and ddH_2O. Single-molecule FRET confocal data of – EP sample was again not reproducible upon electroporation.

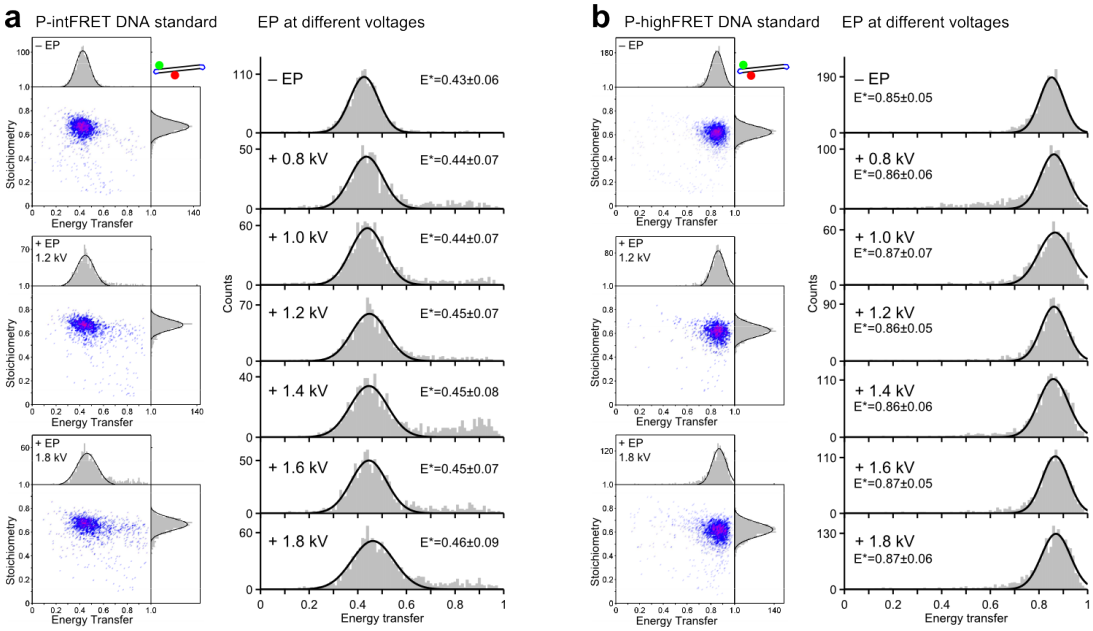

Figure 3.14: Protected DNA FRET standards withstand electroporation. FRET histograms for **a.** intermediate and **b.** high FRET protected DNA standards (P-intFRET and P-highFRET DNA standards) do not show a significant change between – EP sample and + EP sample. Example ES-histograms for '– EP', 1.2 kV and 1.8 kV sample show no significant difference.

Chapter 4

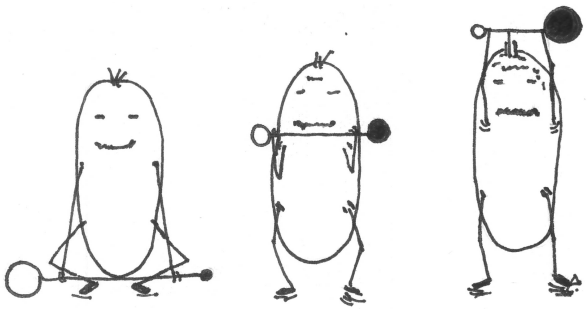

In vivo single-molecule FRET characterisation and applications

The work presented in this chapter has been partly published in

- R Crawford*, JP Torella*, L Aigrain*, A Plochowietz*, K Gryte, S Uphoff, AN Kapanidis. Long-lived, ultrasensitive intracellular fluorescence using electroporated biomolecules. *Biophys J*, 105:2439-2450, 2013. *equal contribution.
- A Plochowietz, R Crawford, AN Kapanidis. Characterization of organic fluorophores for *in vivo* FRET studies. *Phys Chem Chem Phys*, 16:12688-12694, 2014.
- A Plochowietz, AH El-Sagheer, T Brown, AN Kapanidis. Protected DNA FRET Standards for *In Vivo* Single-Molecule FRET Studies. *Angewandte Chemie Int Ed*, under review.
- TD Craggs*, M Sustarsic*, A Plochowietz, M Mosayebi, H Kaju, A Cuthbert, J Hohlbein, P Biggin, J Doye, AN Kapanidis. Structure and mechanism of DNA polymerase I revealed by *in vitro*, *in vivo*, and *in silico* single-molecule studies. in preparation. *equal contribution.

4.1 Introduction

Single-molecule FRET is well suited for studying protein structure and dynamics *in vitro* and in the natural environment of the living cell. As previously described in

chapter 2 (sec. 2.2), FRET relies on a non-radiative energy transfer between a donor and an acceptor fluorophore in close proximity (2-10 nm) with sufficient spectral overlap. A typical application of *in vitro* single-molecule FRET studies is to measure conformational changes of a biomolecule labelled with a donor and acceptor fluorophore pair. These experiments have helped to understand the function of complex proteins, such as DNA Polymerase I and RNA Polymerase (105, 158, 52, 53, 54), and showed how function relates to protein structure. Additionally, nucleic acids and protein folding have been studied using *in vitro* single-molecule FRET methods (50, 159, 51).

Since the FRET signal is highly dependent on the fluorophore properties, the performance of FRET-dye pairs has to be evaluated and optimised. A study by di Fiori and Meller showed that high FRET signals of donor and acceptor fluorophores, which were less than 8 bp on dsDNA apart, were obstructed due to fluorophore collisions (160). For *in vitro* studies, the FRET-dye pair Cy3/Cy5 is a popular choice in many studies (68, 103, 161). While Cy3 and Cy5 show strong environment dependent fluorescence, such as protein induced fluorescence enhancement (162, 163, 164), Cy5 also exhibits thiol-dependent photochemistry (87, 23), which is beneficial for super-resolution imaging studies, but both effects are unwanted for robust and long-lasting single-molecule FRET measurements. Hence, FRET-dye pair fluorophores have to be carefully chosen dependent on the application. For measuring protein conformational changes and protein-substrate interactions, Alexa488/Alexa594 (49, 165, 166) and the very bright FRET-dye pair Cy3B/Atto647N (167, 53, 168) are frequently used.

Despite the common use of single-molecule FRET *in vitro*, *in vivo* single-molecule FRET studies are still very challenging, mainly due to the difficulty of site-specific FRET dye-pair labelling of biomolecules in live cells, see chapter 3 (sec. 3.1). Until now, the most employed *in vivo* FRET dye-pair is the fluorescent protein pair CFP/YFP (68). But the blinking behavior of CFP and YFP (21), the very poor pho-

tostability of CFP, and the very high cellular autofluorescence in the blue excitation channel make single-molecule FRET measurements very challenging (169). Moreover, the size of the FPs (see chapter 2, Fig. 2.3) might interfere with the structure and function of the protein of interest and often only an on/off FRET signal can be studied. In single-cell FRET studies, the fluorescent protein FRET-pair CyPet/YPet was used to study protein-binding dynamics in living cells (170). Using fluorescence lifetime imaging approaches, the fluorescent protein pair GFP/mCherry was employed to measure temperature-dependent protein folding in live mammalian cells (57, 58). Nevertheless, such FP-based FRET studies lack single-molecule sensitivity due to the limited photon budget of fluorescent proteins.

A handful of *in vivo* single-molecule FRET reports have been published using organic fluorophores, *in vitro* labelling, and internalisation techniques. In initial proof of principle studies, Fessl and coworkers internalised DNA constructs labelled with Atto680/Atto740 into live *E. coli* cells using heat shock and measured in-cell time-resolved FRET signatures using TIRF microscopy (135).

The first study of single-molecule FRET in mammalian cells was performed by Sakon and Weninger in 2010, in which they introduced a membrane-fusion protein SNAP-25 labelled with Cy3/Cy5, or Alexa555/Alexa647 into human kidney cells (60). Again, using TIRF microscopy they observed high FRET signals upon protein binding to the SNARE complex at the cell membrane. They also demonstrated single-particle tracking for SNAP-25 labelled with Cy3/Cy5, but only for membrane-tethered SNARE proteins and not in the cellular cytosol. The Cy3/Cy5 single-molecule FRET time-traces lasted for about 1 s.

Very recently, König *et al.* studied protein conformational dynamics employing confocal single-molecule FRET measurements in live HeLa cells (61). Using a temperature-controlled microscope stage optimised for microinjection and cell cultivation, König and coworkers monitored temperature-dependent conformations of a marginally stable

protein labelled with Atto532/Atto647N and observed both cold and heat denaturation in live cells. Using confocal single-molecule FRET microscopy, they showed that an intrinsically disordered protein (Atto532/Biotium CF680R) remains unstructured, exhibiting intra-molecular fluctuations at $\sim$ 60 ns, and monitored the folding kinetics of a small protein (Atto532/Abberior Star 635); showing that interconversion between folded and unfolded states occurs on a $\sim$ 10 ms time-scale (55).

Until now, a thorough characterisation of single-molecule FRET signals and evaluation of FRET-dye pairs has been missing in live cells. Also, the combination of single-molecule FRET measurements and single-particle tracking in living cells (Fig. 4.1), which should give insight to molecular conformational changes and link them with the molecule's mobility and spatial organisation inside the cell, has yet to be demonstrated.

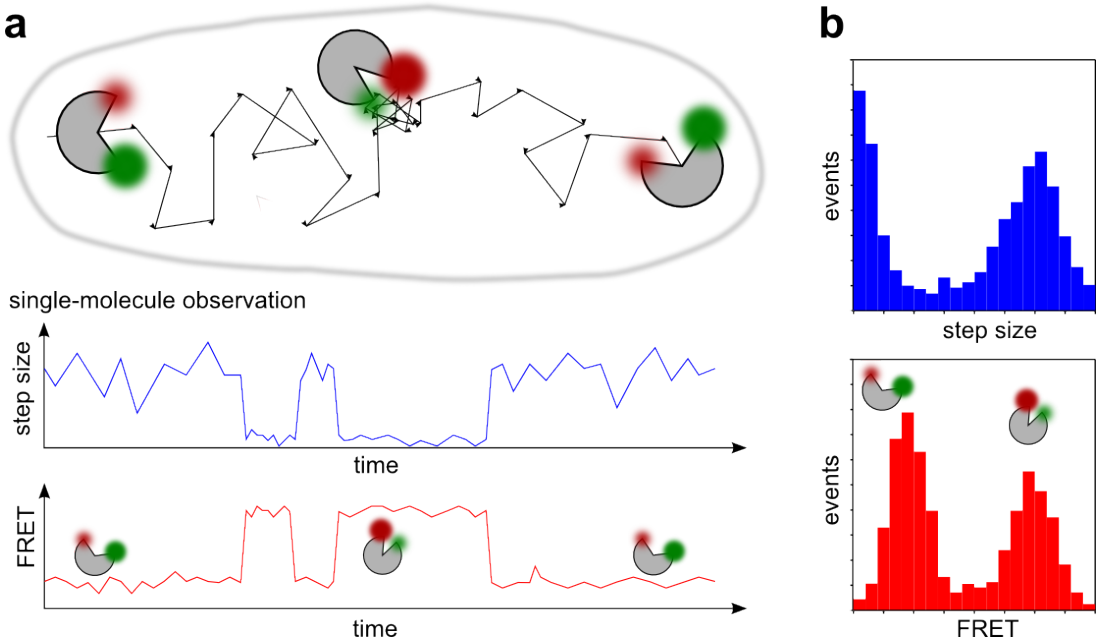

Figure 4.1: Combination of single-molecule FRET studies and single-particle tracking in live cells is a powerful tool as it monitors conformational states of proteins (between open and closed conformation) and links them to the mobility of the molecule (fast diffusion, e.g. searching for target sites, or slow diffusion, e.g. bound to DNA substrate). Such measurements will help to elucidate protein binding kinetics, and conformational dynamics, as well as link protein structure to protein function *in vivo*.

In this chapter, I established *in vivo* single-molecule FRET capability using DNA

FRET standards in live bacteria. First, I characterised the photostability and brightness of 7 organic dyes (3 donor dyes, and 4 acceptor dyes) and evaluated FRET-dye pairs for their performance in single-cell and single-molecule FRET studies. Second, I used low, intermediate, and high FRET DNA standards to characterise single-molecule FRET signatures *in vivo*; specifically, I showed that *in vivo* single-molecule FRET distributions of protected DNA FRET standards were in very good agreement with *in vitro* measurements. Finally, I applied the single-molecule FRET capability and studied three biological systems in live bacteria: (i) probing the internalisation and FRET distribution of a doubly-labelled protein complex, (ii) observing conformational states of a doubly-labelled DNA binding protein, and (iii) showing the bending of a gapped DNA substrate *in vivo*.

4.2 Characterisation of organic fluorophores

To successfully employ single-molecule FRET studies *in vivo*, fluorophore properties have to be quantified to allow robust and long-lasting FRET measurements. A large set of organic fluorophores was already characterised *in vitro* (45, 68), and some of these organic fluorophores were characterised *in vivo* (171, 172). These classifications are mainly for the use of fluorophores in super-resolution imaging (173, 174, 45) and not for continuous imaging of single-molecule FRET signatures for long observation times. For such an application, organic fluorophores with a high photon budget (photostable and bright) are desired.

The photostability of a fluorophore dictates the time frame in which the single fluorophore can be tracked within consecutive movie frames before the fluorophore bleaches. The fluorophore's brightness is a measure for the photon budget of the fluorophore per unit time and is theoretically estimated as the product of the molar extinction coefficient and quantum yield of the fluorophore (in $(\mathrm{M\ cm})^{-1}$, Ref (64)). A high fluoro-

phore brightness is important to localise a single fluorophore with high precision[1].

4.2.1 Single-cell photobleaching studies

To evaluate the photostability and brightness of seven different organic fluorophores *in vivo*, I established single-cell photobleaching studies of internalised singly-labelled dsDNA into *E. coli* cells, where I photobleached entire fields-of-view in epi-fluorescence mode. Next, I implemented computer-assisted cell segmentation routines and analysed the decay of the total cellular fluorescence normalised by cell area over time (SI 4.7.5). The half-time of the fluorescence decay serves as a measure for the fluorophore photostability (in s). Figure 4.2a shows an example fluorescence photobleaching time-trace of more than 100 singly-labelled dsDNA molecules per cell (highlighted in gray), in which even after 3 min a fluorescence signal could still be observed. The time-trace can be used to measure the fluorescence decay half-time. To find the fluorophore brightness, I electroporated singly-labelled dsDNA molecules at 50-100 times lower concentration and analysed the cellular fluorescence decay (Fig. 4.2b). The single-cell fluorescence time-traces decrease in distinct steps that correspond to bleaching events of single fluorophores; the step height of each bleaching event is used as a measure of the fluorophore brightness *in vivo* (unitary intensity, in u.a., or ph/s).

It is noteworthy that the laser power and exposure time were fixed for all measurements (SI 4.7.5). This choice was made since the dyes' photostability and brightness are strongly dependent on the excitation intensity (176, 177).

4.2.2 Photostability of organic fluorophores

The photostability of organic dyes Cy3B, Cy3, Atto532, Atto647, Atto647N, Alexa647, and Cy5 were evaluated *in vivo*. To do this, I electroporated cells with 1 µM of singly-

[1] The lateral localisation precision scales with $1/\sqrt{N}$, N: number of photons per frame (175).

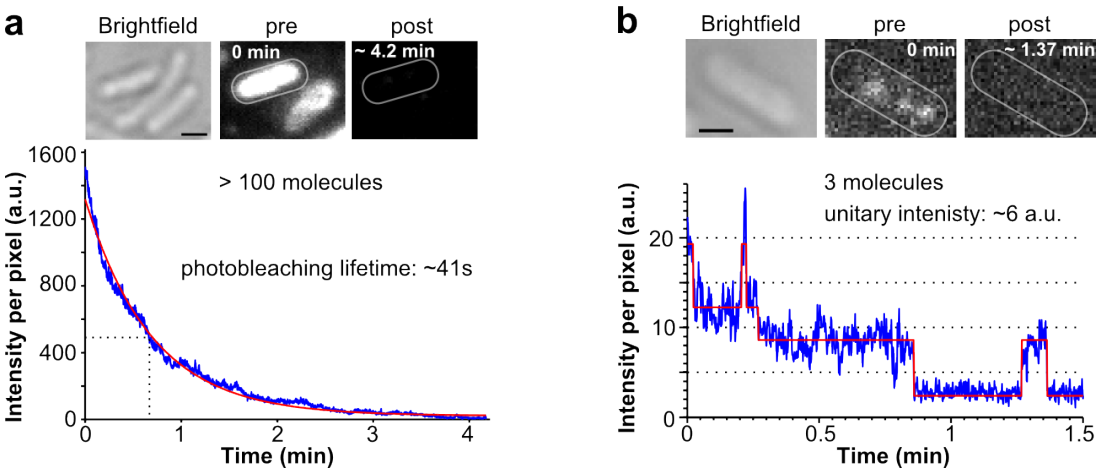

Figure 4.2: Single-cell photobleaching studies to evaluate photostability and brightness of organic dyes (here: dsDNA-Atto647) *in vivo*. **a.** Measuring the fluorescence decay of heavily loaded cells ($>$ 100 molecules/cell) with singly-labelled dsDNA standards. The photobleaching time-traces (blue) were fitted with a single-exponential (red) to obtain the photobleaching lifetime as a measure of dye photostability. **b.** Measuring the fluorescence decay of less loaded cells (1-6 molecules) with singly-labelled DNA standards. The photobleaching time-traces (blue), showing single step photobleaching events, were analysed using Hidden Markov Modelling (HMM, SI 4.7.5, red time-traces) to obtain step height distributions as a measure of dye brightness. Scale bar: 1 µm.

labelled dsDNA (SI 4.7.1), and carried out single-cell photobleaching studies as described above (141). For simplicity, I show the photostability analysis for two example organic fluorophores, namely Cy3B (green fluorescence channel) and Atto647 (red fluorescence channel), in Fig. 4.3. A similar analysis for Cy3, Atto532 (green fluorescence channel) and Cy5, Alexa647, Atto647N (red fluorescence channel) can be found in the supplement (SI Fig. 4.19).

For each organic fluorophore, I analysed about 300-500 cells and obtained 200-400 photobleaching time-traces (SI 4.7.5), since I only included cells into the analysis that were classified as loaded[2]. Next, I fitted the raw single-cell photobleaching time-traces (Fig. 4.3, gray time-traces) with a single-exponential (Fig. 4.3, red curves), since the photobleaching lifetime of the agarose pad and the background fluorescence was more than an order of magnitude smaller ($\sim$ 1 s in green fluorescence channel, and $\sim$ 0.5 s in red fluorescence channel, SI Fig. 4.19), and therefore neg-

[2]The loading threshold is defined in chapter 3 as mean + 3 standard deviation of empty (not treated) cells.

ligible. The photobleaching life-time distributions for Cy3B and Atto647 are shown as insets in Fig. 4.3. I obtained mean photobleaching lifetimes of 20±9 s (median: 17 s) for Cy3B, and 46±13 s (median: 44 s) for Atto647; Atto647N has the highest photobleaching lifetime of 92±37 s (median: 86 s, SI Fig. 4.19).

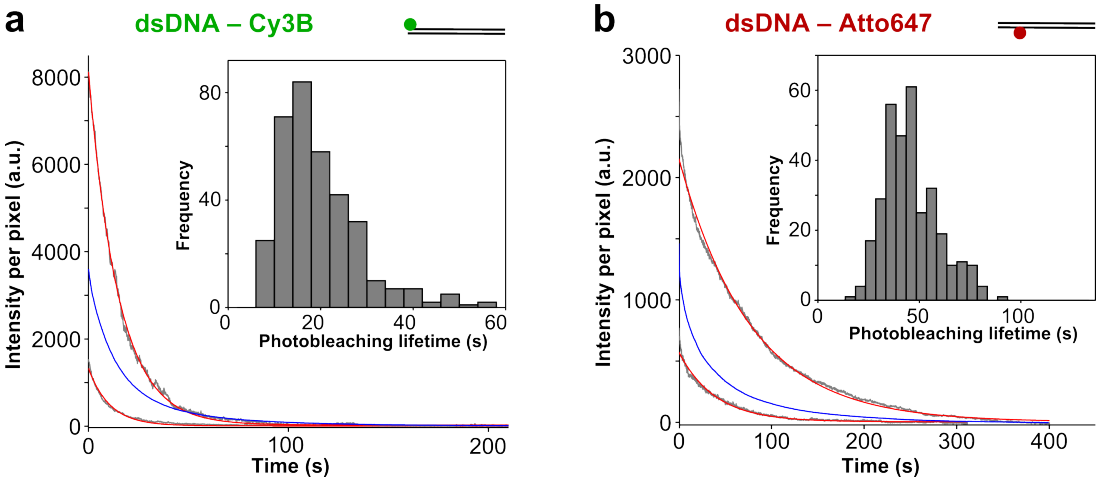

Figure 4.3: Photostability study of organic fluorophores *in vivo*. **a.** Single-cell photobleaching study of internalised dsDNA-Cy3B into live *E. coli* as a measure for photostability. Main: Two example single-cell photobleaching time-traces (gray), single-exponential fit of time-traces (red) and average single-cell photobleaching time-trace (blue). Inset: Histogram of photobleaching lifetime obtained by single-exponential fit of single-cell photobleaching time-traces. **b.** Single-cell photobleaching lifetime measurement of dsDNA-Atto647 as described in a. Acceptor fluorophore Atto647 showed a photobleaching lifetime of (46±13 s; 44 s), whereas donor fluorophore Cy3B showed a photobleaching lifetime of (20±9 s; 17 s); (values: mean ± standard deviation; median). Each data set consisted of 300-500 cells.

I also electroporated the fluorescent protein mCherry into live *E. coli* and obtained a photobleaching lifetime of 18±5 s (median: 17 s), showing that the photostability of organic fluorophores and fluorescent proteins in the green fluorescence channel were very similar under these illumination conditions (SI Fig. 4.19). This result also ensured that the electroporated FP was structurally still intact after electroporation.

4.2.3 Brightness of organic fluorophores

Here, I used the characteristic single photobleaching steps in fluorescence decay time-traces of sparsely loaded cells as a measure of fluorophore brightness *in vivo* (141).

To obtain sparsely loaded cells, I electroporated *E. coli* with 10-30 nM singly-labelled dsDNA-Cy3B and dsDNA-Atto647 to be able to observe only a few DNA molecules per cell; the results for other organic dyes are shown in SI Fig. 4.20. Only cells loaded with less than six fluorescent molecules were used for further analysis.

I fitted the steps in the photobleaching time-traces by Hidden Markov Modeling (HMM) as described in SI 4.7.5 (Fig. 4.4, blue time-traces: raw data, red curves: HMM fit). Afterwards, I examined the photobleaching step height (unitary intensity) distribution generated from more than 100 single-step photobleaching time-traces and fitted the histogram to a single Gaussian (Fig. 4.4, right). I obtained a brightness value[3] of about 3400$\pm$1500 ph/s for Cy3B and 3900$\pm$1700 ph/s for Atto647.

In certain cases, especially for less photostable dyes (Alexa647, Cy5), I noticed that the HMM analysis missed single photobleaching steps due to the insufficient data support for certain fluorescence levels, through which double-steps were picked instead. Thus, I presented the unitary intensity histograms fitted to a single and double Gaussian in the supplement (SI Fig. 4.20) to accommodate for double-steps in the analysis.

The brightness of mCherry could not be obtained at these illumination conditions, since at such low copy numbers, the single-cell photobleaching time-traces were too noisy and no single-step bleaching events were picked up by the HMM algorithm. For dsDNA-Cy3, I still detected single photobleaching steps using HMM analysis and obtained a brightness value of about 2800 ph/s (SI Fig. 4.20). Hence, I concluded that the brightness of mCherry is lower than 2800 ph/s under the same illumination conditions.

The fluorophore performance after photostability and brightness analysis are listed in Table 4.1 and the organic fluorophores were evaluated for their use in *in vivo* single-molecule fluorescence and FRET studies. As previously discussed, very photostable

[3]The brightness value was obtained by multiplying the unitary intensity (in a.u.) by 190 ph/s per arbitrary unit, which was previously measured for this microscope setup (150).

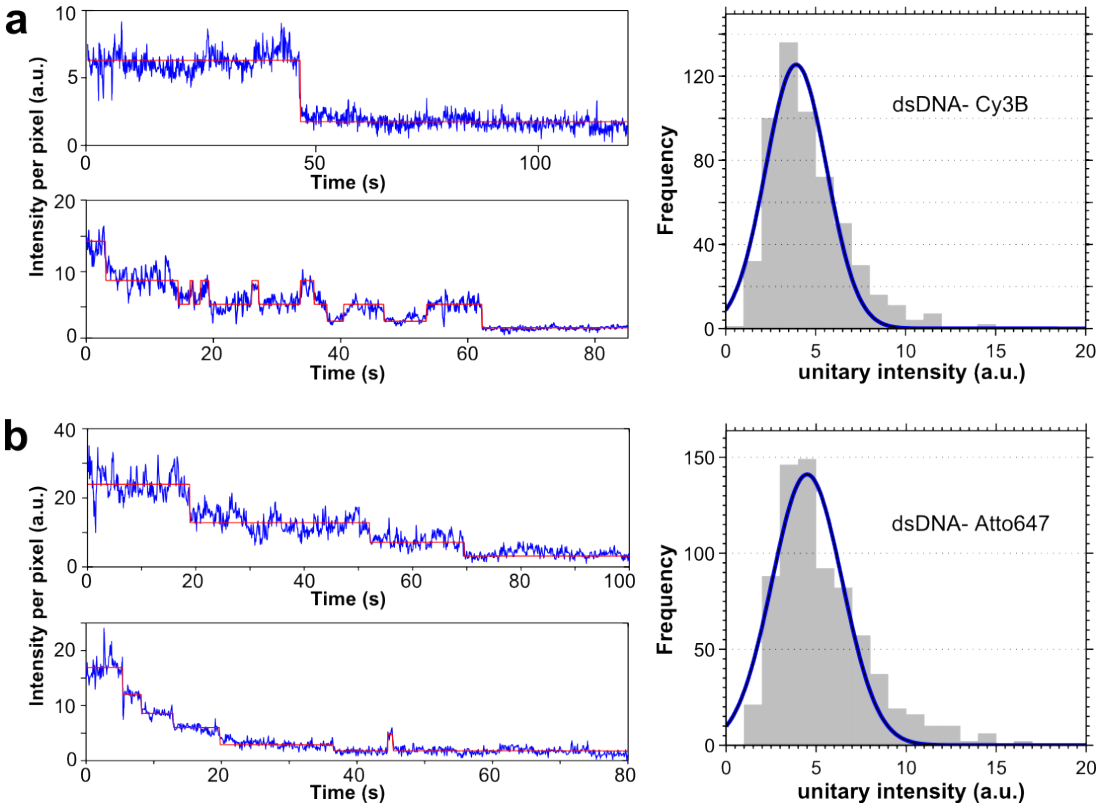

Figure 4.4: Brightness study of organic fluorophores *in vivo*. **a.** Internalisation of dsDNA-Cy3B and single-cell photobleaching step height analysis. Left: Example of single-cell photobleaching time-traces (blue: raw data, red: HMM fit). Right: Histogram of single step height intensities from fitted steps ($>$ 100 cells). Single-Gaussian fit (blue) was centered at 3.9$\pm$1.7 a.u., corresponding to a unitary intensity of 3400$\pm$1500 ph/s. **b.** Internalisation of dsDNA-Atto647 and similar single-cell photobleaching step height analysis. Here, the single-Gaussian fit (blue) was centered at 4.5$\pm$2.0 a.u., corresponding to a unitary intensity of 3900$\pm$1700 ph/s.

and bright organic dyes aid towards long-term single-molecule FRET observations to study single-molecule conformational changes from sub-second timescale up to several seconds.

Evaluating the dye performance using these criterias (SI 4.7.5), I selected Cy3B as the best performing donor dye (Table 4.1), since it is more photostable than Atto532 and it does not exhibit any protein induced fluorescence enhancement (PIFE) effects compared to Cy3 (162, 163, 164), which would make the interpretation of FRET efficiencies *in vivo* challenging. For acceptor dyes, I put Cy5 (highest photon counts), Atto647, and Atto647N (highest photostability) forward for further evaluation as FRET

	photostability	brightness	
organic dye	photobleaching lifetime (s)	unitary intensity (ph/s)	performance
green channel			
Cy3B	20±9	3400±1500	++
Cy3	18±7	2800±1100	+
Atto532	14±8	3600±1400	+
red channel			
Atto647N	92±37	3500±1300	++, sticky*
Atto647	46±13	3400±1100	++
Alexa647	6±4	3500±1200	–
Cy5	10±5	4500±1500	+

Table 4.1: Comparison of organic fluorophore photostability and brightness of 3 donor (green channel) and 4 acceptor (red channel) fluorophores. The evaluation of the fluorophore performance for *in vivo* single-molecule fluorescence and single-particle tracking studies is based on both, high photostability and high brightness (SI 4.7.5); '++': very good, '+': good, '–': poor. *Atto647N is hydrophobic (low polarity) and, thus, tends to bind ('stick') to cell membranes and should not be used for accurate diffusion coefficient measurements.

acceptor dyes.

In the next section, I studied the performance of the three proposed FRET dye-pairs (Cy3B/Cy5, Atto647, Atto647N) on the single-cell level in live bacteria.

4.3 Characterisation of single-cell FRET studies

Using single-cell FRET measurements, it is possible to quickly characterise different FRET states or induced FRET changes on the overall cell level. Furthermore, the evaluation of FRET on the cell-level is much easier than working at the single-molecule level, and it should allow high-throughput screening over many cells. Here, I used single-cell FRET studies to evaluate acceptor fluorophores for their performance in FRET measurements and to differentiate main FRET species in live bacteria (141).

4.3.1 ALEX scheme

I used an alternating laser excitation (ALEX) scheme to characterise FRET at the single-cell level (103, 99). As already introduced in chapter 2 (sec. 2.2.3), the ALEX scheme is based on the direct excitation of the donor fluorophore (DD: donor emission upon donor excitation, and DA/FRET: acceptor emission upon donor excitation) that is alternated with the direct excitation of the acceptor fluorophore (AD: donor emission upon acceptor excitation, and AA: acceptor emission upon acceptor excitation). Consequently, ALEX-measurements give direct access of the stoichiometry of donor-only, acceptor-only and FRET populations within the sample, which means that such measurements are ideally suited for initial single-cell FRET characterisation.

After the internalisation of blunt-ended high FRET DNA standards (Fig. 4.5), I observed heavily loaded cells under green excitation (DD and DA-channel) and high fluorescence signal upon acceptor excitation, mainly in the AA-channel. The fluorescence overlay image of the DD- and the DA-channel reports on the FRET signals and it shows cells exhibiting a high FRET signal (red) and cells showing no FRET signal (green, donor-only signal). Overall, single-cell FRET studies using blunt-ended DNA FRET standards always showed a high amount of donor-only molecules, which implies a shift of FRET distributions towards smaller FRET values.

4.3.2 FRET-dye pairs for single-cell FRET studies

In this section, I evaluated the performance of the three favourable acceptor dyes (Cy5, Atto647, Atto647N) in *in vivo* FRET studies. I electroporated three different high FRET DNA standards labelled with the FRET-dye pairs Cy3B/Cy5, Cy3B/Atto647, and Cy3B/Atto647N into live *E. coli* cells. From *in vitro* confocal single-molecule FRET measurements (sec. 3.6.7), I expected FRET values ranging in the order of

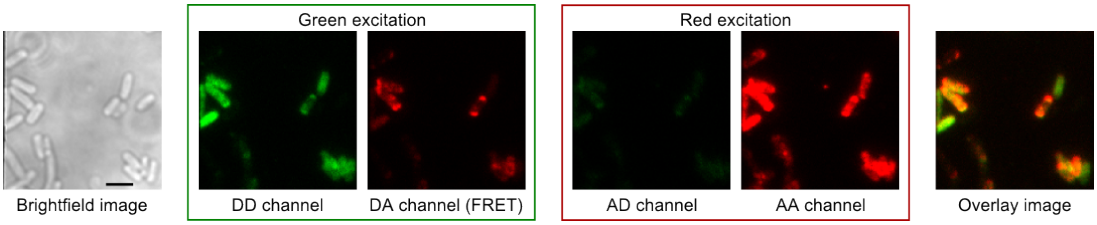

Figure 4.5: *In vivo* single-cell FRET studies of high FRET DNA standards using an alternating laser excitation (ALEX) scheme. Example images (raw data, false-coloured) illustrate switching of green and red excitation and acquisition of fluorescence data during one ALEX-cycle. Left: brightfield image of cells. Green box: donor (D) and acceptor (A) emission channel upon donor excitation; DD and DA/FRET channel, respectively. Red box: donor and acceptor emission channel upon acceptor excitation; AD and AA channel, respectively. Right: Overlay image of DD channel (green) and DA channel (red) encoding FRET signature in false-colour code: green-yellow-red visualising low, intermediate, and high FRET signals. Scale bar: 3 µm.

E^*=0.86±0.05, E^*=0.87±0.04, and E^*=0.88±0.04 (SI Fig. 4.21c-e) for the three FRET-dye pairs, respectively.

Following live-cell imaging (SI 4.7.4), I manually analysed cells showing high signals in the DA/FRET channel and thus potentially high single-cell FRET values (Fig. 4.6). The manual segmentation resulted in fewer statistics, but I was able to retrieve high FRET populations at the single-cell level for Cy3B/Atto647 and Cy3B/Atto647N DNA FRET standards (Fig. 4.6). A low-FRET distribution corresponding to donor fluorescence leaking into the FRET channel (donor-only signal) was observed for Cy3B/Cy5 mainly due to fast acceptor photobleaching, and potentially due to Cy5 photoswitching (23).

The observed fast photobleaching of Cy5 compared to Atto647 and Atto647N was in good agreement with previously obtained photostability studies of acceptor fluorophores (Table 4.1). The photobleaching of Cy5 is about 5-fold to 10-fold faster than that of Atto647 and Atto647N, respectively. Nevertheless, I obtained benchmarks for *in vivo* single-cell FRET studies using Cy3B/Atto647 and Cy3B/Atto647N as FRET dye-pairs. Additionally, I decided to use Cy3B/Atto647N as my preferred FRET dye-pair for further single-cell and single-molecule FRET studies, due to the exceptionally high photostability of Atto647N, which had already proven helpful for single-cell FRET

studies.

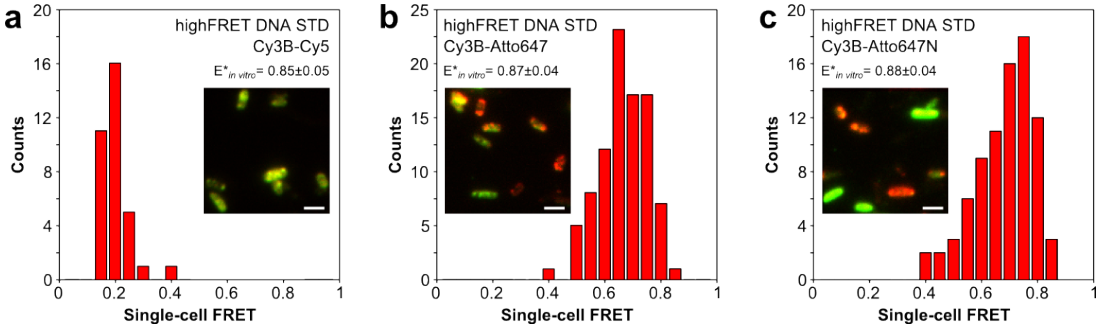

Figure 4.6: *In vivo* single-cell FRET studies of three different FRET-dye pairs. Manual single-cell FRET analysis of high FRET DNA standards labelled with Cy3B/Cy5, Cy3B/Atto647 and Cy3B/Atto647N (left to right). Insets: Overlay images of example FOVs showing heterogeneity within single-cell FRET signals. Main: Histograms of single-cell FRET values obtained by manual cell selection of cells showing high DA signals and locally corrected for autofluorescence (SI 4.7.7). Scale bar: 3 µm.

4.3.3 DNA FRET standards for single-cell FRET studies

Intrigued by the single-cell FRET results from sec. 4.3.2, I was interested whether I would be able to distinguish different FRET species on the single-cell level. To do this, I used low, intermediate, and high FRET blunt-ended DNA standards labelled with Cy3B/Atto647N (SI 4.7.1). Initial single-molecule FRET characterisations *in vitro* showed FRET distributions centered at E^*=0.17±0.04, E^*=0.42±0.07, and E^*=0.88±0.04 for low, intermediate and high FRET standards, respectively (SI Fig. 4.21a-c).

Next, I electroporated *E. coli* cells with 1 µM of dsDNA FRET standards and used automated cell segmentation and FRET analysis routines to obtain single-cell FRET distributions for each DNA FRET standard (SI 4.7.7). Examining the *in vivo* single-cell FRET distributions (Fig. 4.7), I noticed that the low-FRET distribution was shifted to higher FRET values, whereas the high-FRET distribution was shifted to lower FRET values. I attributed this difference to the employed FRET corrections for cellular autofluorescence of non-treated cells used for the entire *in vivo* single-cell fluorescence

data set in the automated analysis (SI 4.7.7), which did not take into account potentially different cell background values. Especially, the single-cell FRET distribution of the high FRET DNA sample appeared very wide, which could be due to the faster acceptor photobleaching of the high FRET standards, or to DNA degradation. I was able to observe sub-cellular high FRET regions, but they merged with a donor-only signal on the overall single-cell level which resulted in intermediate single-cell FRET values of around 0.4. Being unable to detect sub-cellular high FRET species, also illustrates the advantages of single-molecule fluorescence measurements over these ensemble averaging studies on the cell-level.

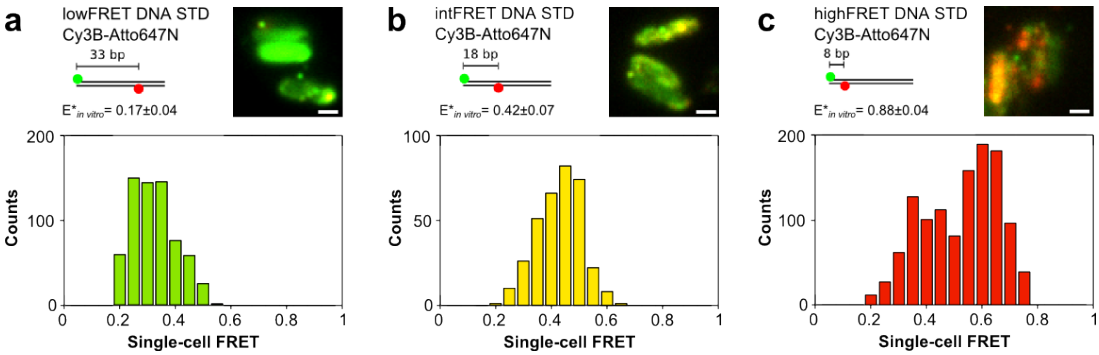

Figure 4.7: Characterisation of single-cell FRET levels *in vivo* using low, intermediate and high FRET blunt-ended DNA standards (left to right). Top: Overlay images of three example FOVs and *in vitro* FRET values. Bottom: Histograms of single-cell FRET values obtained by automated cell segmentation and corrected for overall autofluorescence of non-treated cells (SI 4.7.7). Scale bars: 1 µm.

Despite the presence of the donor-only signal, I could still differentiate the single-cell FRET distributions from low, intermediate and high FRET blunt-ended DNA standards *in vivo*. This quick single-cell FRET assay provides an attractive way for studying FRET states and induced intramolecular FRET changes. The FRET assay could also help to differentiate between bound and unbound molecule species, and to study protein complex formation on the cellular basis over hundreds of living cells at a time.

4.4 Characterisation of single-molecule FRET studies

After I successfully managed to differentiate low, intermediate and high FRET species at the single-cell level, I was interested in performing FRET studies at the single-molecule level. First, I characterised *in vivo* single-molecule FRET populations using blunt-ended and protected DNA FRET standards and compared these results with *in vitro* single-molecule FRET populations, which were discussed in chapter 3 (sec. 3.3.1). Working at low copy numbers of doubly-labelled DNA standards, single-molecule fluorescence localisation became possible in each fluorescence channel; elucidating single-molecule FRET distributions in live bacterial cells. Second, I combined single-molecule FRET measurements with single-particle tracking analysis (SI 4.7.8) and observed FRET trajectories of single DNA molecules for more than 10 s.

4.4.1 Blunt-ended DNA FRET standards

In light of the previous single-cell FRET studies, I next performed FRET measurements at the single-molecule level with 20 ms temporal resolution under green continuous illumination. For sample preparation, I electroporated 20-50 nM of DNA FRET standards into live *E. coli* cells, which resulted in cellular uptake of only a few molecules per cell (N:$\sim$1-6).

In the localisation analysis, which is described in more detail in SI 4.7.8, I only included molecules which had total photon counts (DD+DA channel counts) larger than 400 ph/frame. After, I localised molecules in the DA channel, and then I force-fitted the fluorescent signal in the DD channel, which was mapped onto the DA channel. Into the further analysis, I only included molecules with photon counts that were at least 40 ph/frame above the autofluorescence in the donor channel. To ensure an accurate Gaussian fitting of the diffraction-limited images of the single molecules (PSFs) in the respective channels, I filtered for the shape of the fitted 2D Gaussian

and only included molecules with full widths at half maximum ranging from 50-400 nm. While the 2D Gaussian fitting of the PSF already accounted for different cellular autofluorescence levels in the respective fluorescence channels, adjacent biomolecules, especially in the green fluorescent channel, led to the majority of discarded fits when filtering for PSF-shape.

In vivo single-molecule FRET histograms for low, intermediate, and high blunt-ended DNA FRET standards (Fig. 4.8) were centered at E^*=0.22$\pm$0.08, E^*=0.39$\pm$0.14, and E^*=0.85$\pm$0.11, respectively. The *in vivo* results were in good agreement with *in vitro* FRET values, which ranged from E^*=0.17$\pm$0.04, E^*=0.42$\pm$0.07, and E^*=0.88$\pm$0.04, for the low, intermediate, and high FRET standard, respectively.

The increased standard deviation (width of fitted Gaussian distribution) showed that *in vivo* single-molecule FRET signals were noisier than *in vitro* signals, which I mainly attributed to the effect of molecular motion, cellular autofluorescence, and adjacent biomolecules on *in vivo* FRET measurements. While *in vivo* single-molecule FRET distributions (Fig. 4.8) showed less heterogeneity in FRET efficiencies than single-cell FRET distributions (Fig. 4.7), especially the *in vivo* intermediate, and high FRET species were shifted towards smaller FRET values, which could be attributed to acceptor photobleaching and DNA degradation (141). Nevertheless, the single-molecule FRET analysis showed much clearer main FRET distributions than the single-cell FRET measurements, since donor-only populations could be excluded from the analysis compared to averaging over fluorescence intensities on the cell-level.

4.4.2 Protected DNA FRET standards

An idea which was already mentioned for *in vitro* studies in chapter 3, sec. 3.3.1, was to use 'protected' DNA FRET standards to preserve FRET signatures *in vivo*, since the chemically linked DNA-ends do not provide a target for the bacterial DNA

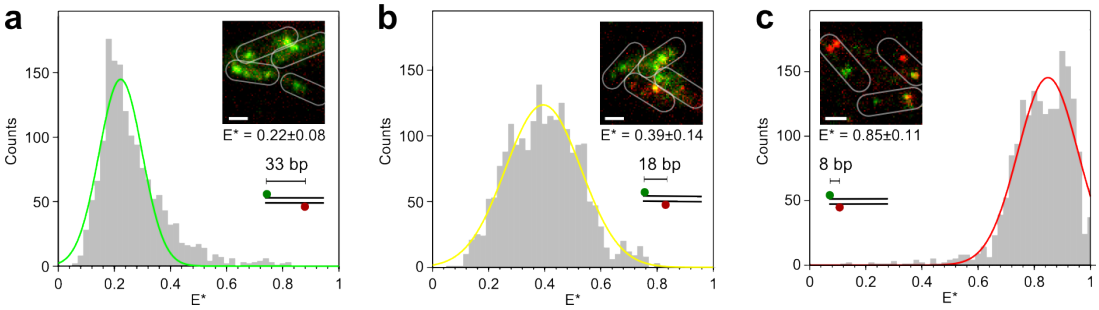

Figure 4.8: *In vivo* single-molecule FRET studies using blunt-ended DNA FRET standards. **a.** Low, **b.** intermediate and **c.** high FRET DNA standards show distinct FRET distributions that were fitted with a single Gaussian. Insets: Overlay images of example FOVs. Scalebar: 1 µm.

degradation machinery anymore. Therefore, I electroporated protected DNA FRET standards into live *E. coli* cells. The protected DNA standards have previously already proven to withstand electroporation even without EDTA present compared to their blunt-ended counterparts (sec. 3.3.1).

Interestingly, the FRET efficiencies obtained *in vivo* (Fig. 4.9) were in excellent agreement with *in vitro* FRET values (chapter 3, Fig. 3.5): the intermediate FRET species was centered at E^*=0.42±0.12 (*in vitro*: E^*=0.42±0.07), and the high FRET species was centered at E^*=0.84±0.06 (*in vitro*: E^*=0.87±0.06). Especially the high FRET protected DNA distribution was narrower than the blunt-ended DNA distribution, and only a very small amount of autofluorescence signal or acceptor photobleaching events was potentially picked up for the protected DNA FRET standards.

To be able to filter *in vivo* FRET distributions for acceptor photobleaching events in donor-only, and acceptor-only species, I performed single-molecule FRET measurements using the ALEX scheme (sec. 4.3.1) with a frame time of 20 ms. As for *in vitro* single-molecule FRET experiments (Fig. 3.5), I was able to obtain FRET-stoichiometry histograms for the protected intermediate and high FRET DNA standard *in vivo* (Fig. 4.10, red colour-code).

I performed the same localisation analysis routine, and now also included information from the AA-channel. There, I only included bright enough molecules; in theory

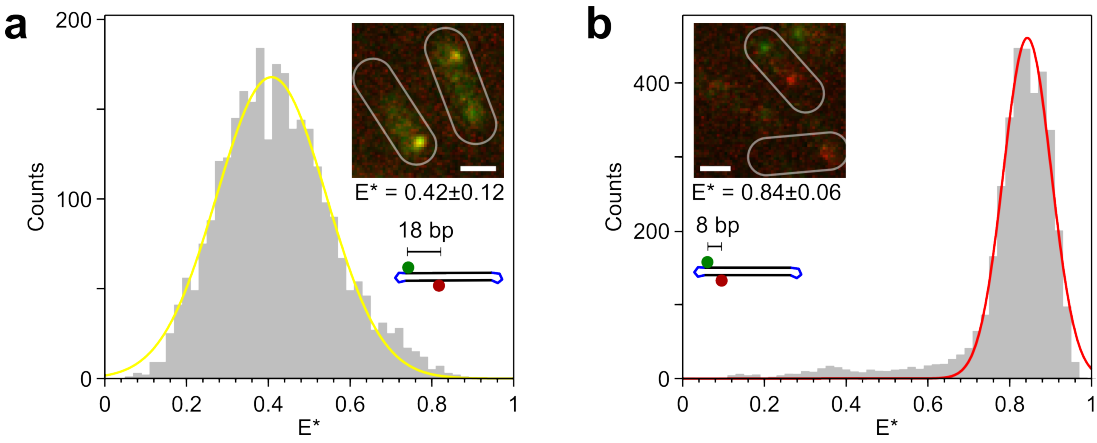

Figure 4.9: *In vivo* single-molecule FRET studies using protected DNA FRET standards. Intermediate and high FRET distributions showed distinct FRET species (fitted with single Gaussians) that were in excellent agreement with *in vitro* FRET values. Insets: Overlay images of example FOVs. Scale bar: 1 µm.

the (DD+DA)-threshold of 400 ph/frame could be used, but I found that filtering for the width of the 2D Gaussian and for a photon count larger than 130 ph/frame was sufficient to filter for molecules in the AA-channel (SI 4.7.8). Notably, the filtering in the AA-channel resulted in the exclusion of donor-only molecules, whereas the filtering in the DD-channel was mainly to differentiate donor-signal from internalised organic fluorophores above the higher intrinsic autofluorescence in the green channel (SI Fig. 4.22).

The FRET-Stoichiometry distributions were fitted with single Gaussians, which were centered at E^*=0.42±0.12/ S^*=0.63±0.12, and E^*=0.85±0.06/ S^*=0.57±0.11 for the protected intermediate and high FRET standard, respectively (Fig. 4.10).

Another interesting aspect is the molecule's history during the measurement. I traced individual FRET molecules throughout the cell while monitoring their FRET signature simultaneously. Therefore, I performed single-molecule fluorescence imaging at 20 ms in green continuous wave-mode to allow a higher temporal resolution compared to imaging using the ALEX scheme and combined the single-molecule FRET localisation analysis with single-particle tracking. I localised molecules as described above and linked these localisations to a trajectory if the PSFs appeared in con-

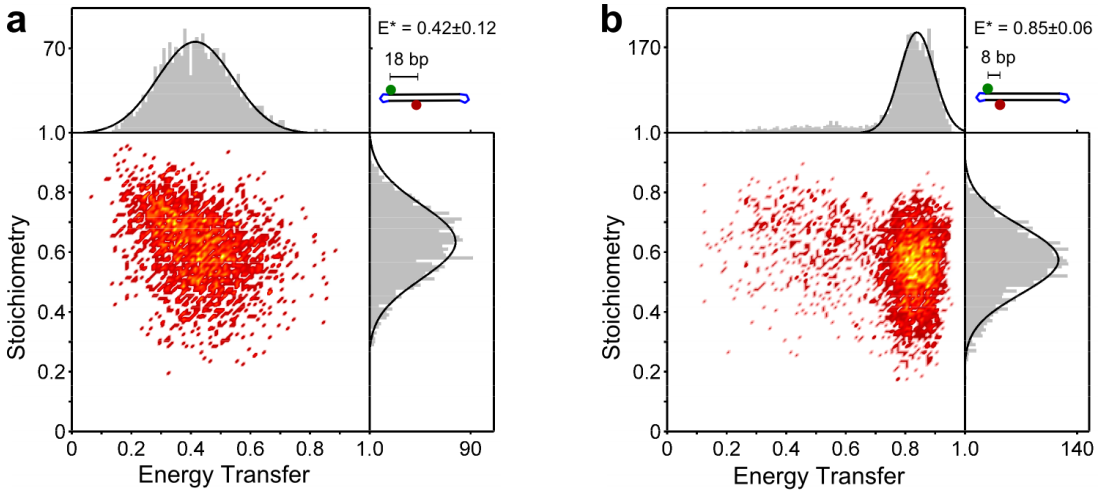

Figure 4.10: *In vivo* single-molecule FRET-Stoichiometry histograms for **a.** intermediate, and **b.** high FRET protected DNA standards. Single-molecule data was filtered for a total fluorophore intensity of $>$400 ph/frame, $>$40 ph/frame in the DD-, and $>$130 ph/frame in the AA-channel. FRET distributions were centered at E^*=0.42$\pm$0.12, and E^*=0.85$\pm$0.06 with stoichiometry distributions centered at S^*=0.63$\pm$0.12, and S^*=0.57$\pm$0.11 for intermediate and high FRET standards, respectively.

secutive frames within a window of 7 pixels ($\sim$0.69 µm). This window size ensured that 98 % of the steps were correctly linked for an apparent diffusion coefficient of 1.0 µm^2/s and 20 ms exposure time (117, 115). To account for transient disappearance of the PSF within a trajectory due to blinking or missed localisation, I used a memory parameter of 1 frame; see SI 4.7.8 for more details.

I tracked individual FRET molecules for more than 10 s and obtained long-lasting FRET signatures *in vivo*. Some example time-traces for the protected intermediate and high FRET DNA standard are shown in Fig. 4.11. These single-molecule FRET time-traces showed anti-correlated DD and DA-signal, which is a clear indication of single-molecule FRET events in which, for instance, in time-trace Fig. 4.11a, the bleaching of the acceptor fluorophore (lost DA-signal), leads to an increase in the donor fluorescence signal.

The single-molecule FRET time-traces showed different levels of noise due to molecular motion and especially nearby molecules. The single-molecule FRET time-trace in Fig. 4.11d shows the challenge of force-fitting low fluorescence signals in the

donor channel of high FRET molecules in presence of nearby donor-only molecules, which contribute to the high intensity peaks in the donor fluorescence intensity time-trace and result in a drop in the single-molecule FRET time-trace.

Since I tracked the single molecules in the less autofluorescent DA-channel, in which only FRET molecules appeared, molecules showing a high FRET signal could be traced better than intermediate FRET molecules. Notably, for other projects, I was struggling to obtain single-molecule FRET time-traces for expected FRET efficiencies below 0.15 due to the very weak FRET signal.

To summarise: I was able to differentiate three different FRET DNA standards *in vivo* and compared the *in vivo* FRET signature with expected *in vitro* FRET values. Protected DNA FRET standards have proven beneficial for *in vivo* single-molecule FRET measurements and I obtained FRET-Stoichiometry histograms using the ALEX scheme. The *in vitro* and *in vivo* experimentally-obtained single-molecule FRET efficiencies (Table 4.2) agreed remarkably well, keeping in mind that I was using two different microscope setups, wide-field and confocal illumination techniques, and studied signals in the cellular environments and aquaeous buffer conditions. This result indicates that the cross-talk contributions to the FRET signal might be similar on both setups and that the cellular environment does not drastically affect the fluorophore properties.

In the conclusion section of this chapter (sec. 4.6), I commented on the necessary steps to obtain accurate FRET efficiencies and measure actual molecular distances *in vivo*. But for now, and in most cases the study of relative distance changes is sufficient, I applied the developed *in vivo* single-molecule FRET assay to three biological systems.

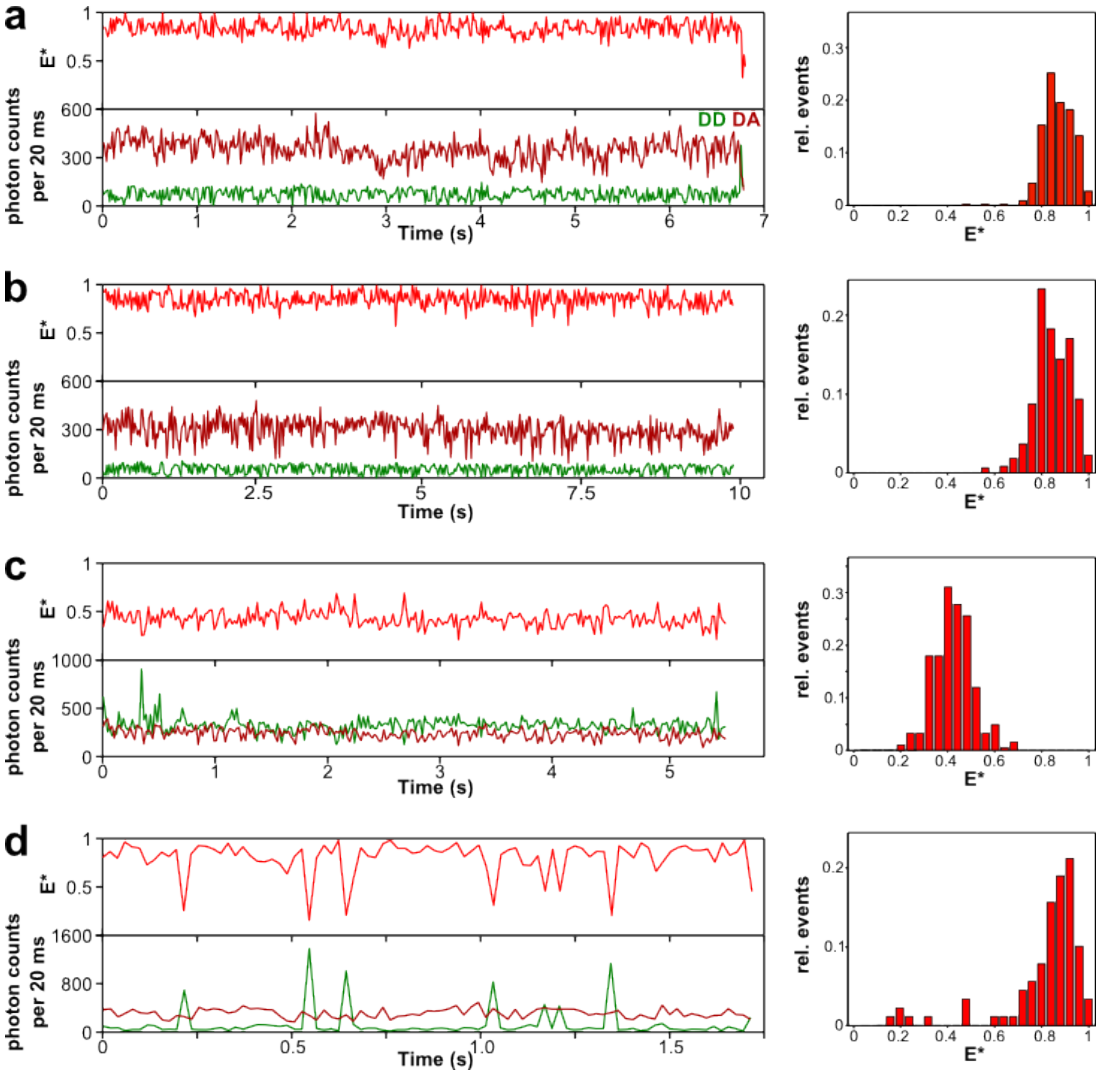

Figure 4.11: *In vivo* single-molecule FRET time-traces (left) and single-molecule FRET histograms (right) obtained under green continuous illumination. **a.** High FRET single-molecule time-trace showing acceptor photobleaching event and increase in donor signal, and **b.** high FRET time-trace lasting about 10 s. **c.** Intermediate FRET single-molecule time-trace. **d.** High FRET single-molecule time-trace showing the influence of nearby donor-only molecules in donor channel and their impact on donor intensity time-trace (peaks) and single-molecule FRET time-trace (drops).

4.5 First applications of the *in vivo* single-molecule FRET tool box

In this section, I tested my newly established single-molecule FRET capability combined with single-particle tracking analysis on three interesting biological systems. First, we observed the *in vivo* single-molecule FRET signature of the colicin E9-

DNA standard	Blunt-ended DNA FRET standards		Protected DNA FRET standards	
	in vitro	*in vivo*	*in vitro*	*in vivo*
low FRET	0.17±0.04	0.22±0.08	—	—
intermediate FRET	0.42±0.07	0.39±0.14	0.42±0.07	0.42±0.12
high FRET	0.88±0.04	0.85±0.11	0.87±0.06	0.85±0.06

Table 4.2: Comparison of *in vitro* and *in vivo* single-molecule FRET efficiencies of blunt-ended and protected DNA FRET standards. *In vitro* and *in vivo* FRET efficiencies were in very good agreement, and protected DNA FRET standards showed smaller error estimates. Values: center of fitted Gaussian ± standard deviation.

Im9 protein complex, a model system for protein-protein interaction. Second, we visualised conformational states and dynamics of the Klenow fragment of DNA Polymerase I *in vivo*, and finally, we studied the bend states of gapped DNA fragments in live bacteria, always comparing the results with *in vitro* FRET measurements.

4.5.1 Observation of colicin E9-Im9 complex *in vivo*

Brief introduction

Colicins are natural toxins that are used by bacteria to kill their competitors. More than 20 different colicins have been identified sharing a basic modular design and mode of entry into the host cell (178). Interestingly, colicins possess very cytotoxic activity and only one molecule is sufficient to kill the host cell (179). Colicins cytotoxicity is mediated by the nuclease activity (179) and the molecule's entry into the host cells lies on many specific molecular interactions (Tol system or TonB system), raising hope for the evaluation of these molecules as probiotics in antibiotic drug development (180). To avoid self-destruction, colicin producing bacteria have a system to inactivate nuclease activity of the colicin, a highly specific immunity protein, which is synthesised simultaneously to the respective colicin.

Results

Here, we studied the E9 DNAse domain of the colicin E9 (requiring the TolB system for cell entry) and its immunity protein Im9[4]. The E9-Im9 complex shows very high affinity, $K_d \sim 10^{-16}$ M (181, 182). The aim of this project was to study the interactions of the E9-Im9 complex *in vivo* and to measure binding kinetics. To monitor the intermolecular interactions of the E9 and Im9 proteins, and their binding affinity, we used a single-molecule FRET assay in live cells. The E9 protein was labelled with Alexa647 (S3C or D40C) and the Im9 protein was labelled with Cy3B (S81C), Fig. 4.12a, SI 4.7.2. As a first characterisation step, we were interested in the efficient internalisation of the E9-Im9 protein complex into live bacteria.

Following the established protocol for protein internalisation (sec. 3.4), we first checked the integrity of the E9-Im9 complex upon electroporation using an *in vitro* single-molecule FRET assay (Fig. 4.12a). We could not observe a significant difference in shape and peak position between the FRET distributions of the non-electroporated (E^*=0.8$\pm$0.1), and electroporated sample (E^*=0.77$\pm$0.1) for the E9(S3C)-Im9 complex and the E9(D40C)-Im9 complex (SI Fig. 4.23). Thus, we reasoned that electroporation was not affecting the molecular structure and binding affinity of the E9 DNAse domain with the immunity protein Im9.

Fortunately, the E9-Im9 complex could be successfully internalised (inset in Fig. 4.12b), and cells were washed with phosphate buffered saline (PBS) with 0.005% Triton X100, and 100mM NaCl to remove non-internalised protein complexes. No additional cell filtration step was needed. Next, we performed single-molecule FRET studies of electroporated and non-electroporated cells as previously described (sec. 4.4.1 and SI 4.7.8). While observing very few FRET molecules in the non-electroporated sample, we observed a main single-molecule FRET population in the electroporated sample, which was centered at E^*=0.76$\pm$0.12. This result was in excellent agree-

[4] collaboration with Colin Kleanthous' group, Biochemistry, Oxford.

ment with *in vitro* single-molecule FRET studies and as expected from modelling the average position of the FRET dye-pair with respect to the crystal structure of the E9-Im9 complex (Fig. 4.12a).

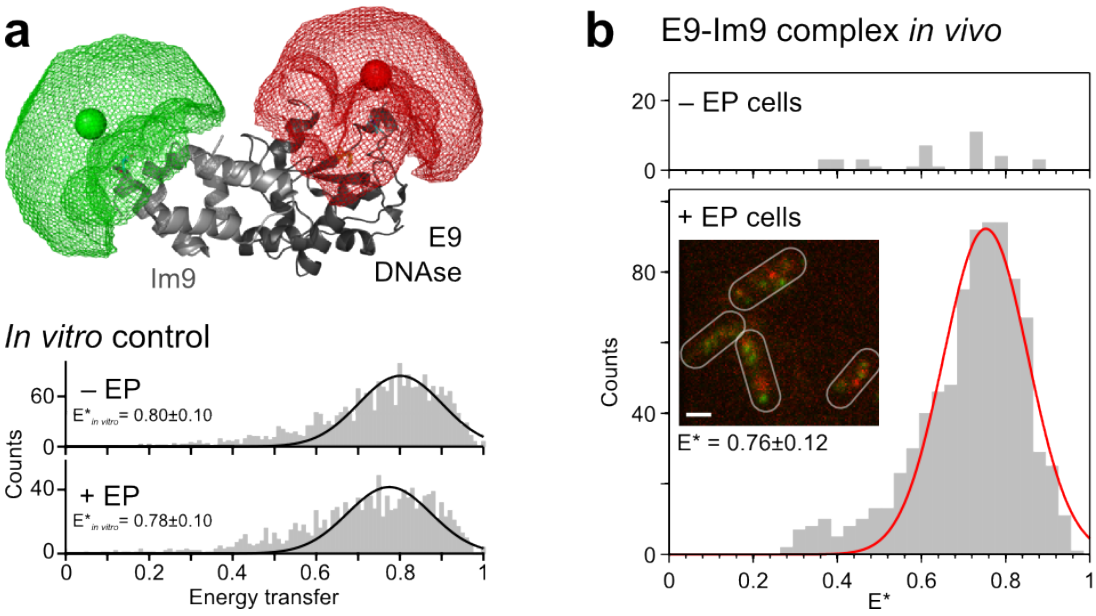

Figure 4.12: Single-molecule FRET studies of E9-Im9 complex *in vitro* and *in vivo*. **a.** Top: Labelling scheme of E9(S3C)-Im9 complex with Alexa647, and Cy3B, respectively, resulting in an expected FRET value of E$\sim$0.75. The labelling schematic was generated by Dr. Louise Aigrain using software by the Seidel lab (102) and E9-Im9 crystal structure; pdb-file: 1EMV (183). Bottom: *In vitro* characterisation of single-molecule FRET efficiencies of E9-Im9 complex before and after electroporation. FRET distributions were centered at E*=0.8$\pm$0.10 ('– EP') and E*=0.77$\pm$0.10 ('+ EP'). **b.** Single-molecule FRET study of E9(S3C)-Im9 in live *E. coli*. Top: Very few molecules were localised in the negative control ('– EP' cells), and bottom: FRET distribution of localised molecules (N=829, $>$200 cells) in electroporated cells was centered at E*=0.76$\pm$0.12, which was in excellent agreement with the expected FRET value from crystal structures, and *in vitro* controls. Inset: Overlay images of example FOV. The data was acquired by Andrei Lei under my supervision. Scale bar: 1 µm.

To summarise: We were able to internalise a doubly-labelled protein complex into live bacteria and observed a main single-molecule FRET distribution *in vivo*, which was in excellent agreement with *in vitro* controls and expected values from the crystal structure.

Discussion

The direct observation of protein complex formation and binding kinetics *in vivo* remains still challenging. Until now, only a single report by Phillip *et al.* (170) measured binding kinetics of bacterial proteins in live eukaryotic cells by utilising microinjection. For studying complex formation of the E9 DNAse domain and its immunity protein Im9 *in vivo*, or for studying binding kinetics of the protein complex to endogenous DNA, further obstacles have to be overcome: First, about 10% of free dye (SI 4.7.2) have still to be removed from the protein samples by further purification steps, such as HPLC or Ni-NTA column. While the high level of internalised free dye into live bacteria did not give rise to fluorescence signal in the FRET channel, it complicated linking of FRET-DD localisations, and hence the evaluation of FRET efficiencies. Second, for long-lasting FRET observation, as it is needed for studying complex formation and binding kinetics, the acceptor fluorophore, Alexa647, should be substituted to a more photostable dye, such as Atto647 or Atto647N (141). Nevertheless, the successful internalisation of the E9-Im9 complex and single-molecule FRET observation were a promising start and should enable the observation of complex formation in live bacteria using single-molecule FRET.

4.5.2 Conformational states of Klenow fragment *in vivo*

Brief introduction

The Klenow fragment (KF) consists of the polymerase and 3'-5' exonuclease domains of DNA Polymerase I and is involved in DNA synthesis during DNA repair and the replacement of RNA primers of Okazaki fragments with DNA (184). The structure and conformational changes of Klenow fragment have been intensively studied *in vitro* using confocal single-molecule FRET microscopy (53, 54, 168). In chapter 3 (sec. 3.4.1), the conformational dynamics of KF were already described; the flexibility

of the fingers subdomain of KF interconverts between two conformations: an open conformation ($E^* \sim 0.48$) when bound to DNA template, and a closed conformation ($E^* \sim 0.66$) while incorporating nucleotides (Fig. 3.9). Although Klenow fragment has been well characterised *in vitro*, we have little understanding of its conformational dynamics *in vivo*.

Results

We were interested in the conformational states of KF *in vivo*, and hence electroporated 250 nM of doubly-labelled Klenow fragment (L744C-Cy3B, K550C-Atto647N, inset in Fig. 4.13a) into live *E. coli* cells. Notably, the internalisation of KF is not straightforward and non-internalised proteins and protein aggregates have to be removed using cell filtration (140). Combining single-molecule FRET measurements and single-particle tracking, we were able to localise and trace single KF molecules inside *E. coli* cells. We obtained an overall FRET distribution, which fitted best to a single Gaussian distribution centered at $E^*=0.46 \pm 0.11$ (Fig. 4.13a). This result was in good agreement with *in vitro* values for the open conformation ($E^* \sim 0.48$) and with previously measured FRET values of immobilised KF molecules in live bacteria ($E^*=0.51 \pm 0.13$, Ref. (62)). We also obtained some KF molecules exhibiting high FRET states, but overall, we reasoned that KF is predominantly in an open conformation *in vivo*.

Next, I examined single-molecule trajectories of mobile KF molecules more closely, which should exhibit a slightly higher apparent diffusion coefficient than previously measured for full-length DNA Polymerase I of about $D_{app} \sim 1\,\mu m^2/s$ *in vivo* (115). Specifically, I was interested in the correlation of conformational states of KF and its mobility (apparent diffusion, D_{app}) inside the cell. Unfortunately, I only observed a few mobile KF trajectories lasting longer than 1 s. An example trajectory is presented in Fig. 4.13c, showing different diffusive states: slow diffusion and short fast-diffusive

states ($D_{app}\sim 1\,\mu m^2/s$, highlighted in blue). Intriguingly, the slow diffusive states tend to correlate with the high-FRET states, in which KF molecules could be bound to DNA damage sites and incorporate nucleotides, whereas the fast-diffusive species tend to coincide with intermediate FRET states, corresponding to KF open conformation (Fig. 4.13c). However, conformational changes of KF corresponding to single nucleotide incorporation events could not be observed using these experimental conditions, since DNA binding and nucleotide incorporation seems to occur on faster time-scales than the 20 ms frame-time of the *in vivo* experiment.

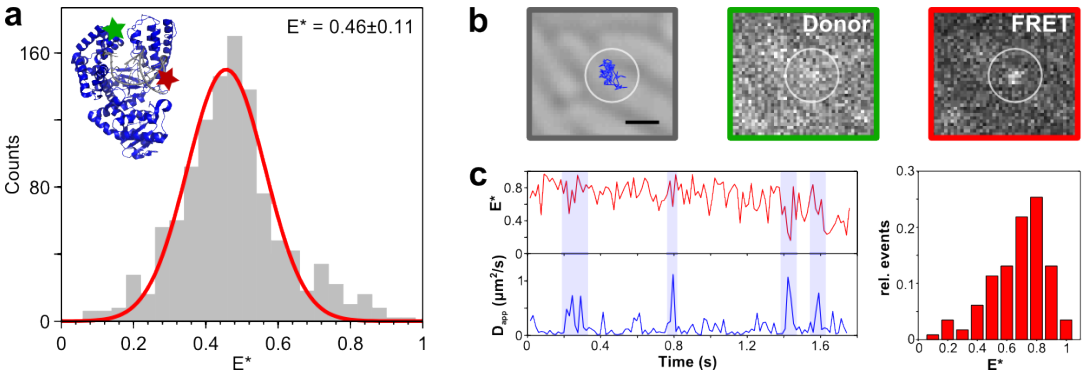

Figure 4.13: Single-molecule FRET measurements and single-particle tracking of electroporated doubly-labelled Klenow fragment (KF, domain of DNA Polymerase I). **a.** Single-molecule FRET distribution of KF (inset: KF labelling scheme with Cy3B, and Atto647N) showed a main peak centered at E^*=0.46±0.11. **b.** Example single-molecule FRET trajectory overlaid on cell brightfield image, and single-molecule fluorescence shown in donor fluorescence channel (green box), and FRET fluorescence channel (red box). **c.** Left: Single-molecule FRET time-trace of KF molecule and apparent diffusion coefficient, D_{app}=$MSD_{\Delta t}/(4\Delta t)$, with fast diffusive states ($D_{app} \sim 1\,\mu m^2/s$) highlighted in blue. Right: FRET histogram from respective single-molecule FRET time-trace, showing a main peak at about $E^* \sim 0.75$. The movie analysed in **b-c.** was provided by Dr. Louise Aigrain. Scale bar: 1 µm.

Discussion

We demonstrated the capability of single-molecule FRET measurements in combination with single-particle tracking to study the conformational states and protein dynamics of the doubly-labelled Klenow fragment in live bacteria. However, for a comprehensive interpretation of KF conformational changes, KF motion, and its binding kinetics to DNA *in vivo*, further studies and rigorous controls, such as induced DNA

damage, the analysis of non-DNA binding proteins, and others, have to be carried out. In addition, the electroporation method needs further improvement for the internalisation of KF; the protein size of 66 kDa and surface charge of the Klenow fragment might hinder its efficient internalisation. Non-internalised molecules and protein aggregates must be thoroughly removed (140) before studying KF conformational changes and motion *in vivo*, since non-internalised molecules stuck to the cell wall or inner cell membrane obstruct single-particle tracking analysis.

Once these obstacles have been overcome, single DNA repair events could be studied *in vivo*. Using the single-molecule FRET assay and diffusion analysis, DNA binding events could be visualised and the conformational states of KF molecules could be monitored at the same time. In previous work by Uphoff *et al.*, DNA Pol I was genetically tagged to PAmCherry, a photoactivatable fluorescent protein, and the change of mobility of DNA Pol I during DNA repair was monitored. However, the poor photostability of fluorescent proteins, and consequently short average observation time of $\sim$50 ms prevented the study of complete DNA repair event $>$1 s, and thus the use of organic dye-labelled DNA Polymerase I could be advantageous. For measuring the conformational changes of KF during single nucleotide incorporation events (on the order of a few milliseconds *in vitro*, Dr. Geraint Evans, unpublished data), measurements at higher temporal resolution would be needed. Frame-rates down to 5 ms are achievable using wide-field microscopy, but for the exploitation of faster protein dynamics on the sub-milliseconds to 10 ms time-scale confocal single-molecule FRET studies in combination with recurrence analysis methods (185, 61) would be the method of choice.

4.5.3 Gapped DNA bending *in vivo*

Introduction

In a study by Dr. Timothy Craggs, and Marko Sustarsic *et al.* (in preparation), the recognition and binding of the Klenow fragment, and the full-length DNA Polymerase I (sec. 4.5.2) of a gapped DNA substrate were examined *in vitro*. They used confocal single-molecule FRET microscopy, coarse-grained modelling of the gapped DNA substrate[5], and all-atom molecular dynamics simulations of the DNA substrate bound to KF[6] to study bending angles of the DNA substrate alone and protein-substrate recognition.

Using confocal single-molecule FRET microscopy *in vitro*, they studied the FRET efficiencies of doubly-labelled gapped DNA substrates and observed an increase in FRET upon addition of KF, which could be explained by the bending of the gapped DNA substrate by the polymerase. Next, they systematically examined 34 FRET-dye pair distances on DNA-DNA, and 39 distances on KF-DNA, and related single-molecule FRET efficiencies into accurate distance measurements. Later, they examined the best FRET-constrained model of KF bound to the gapped DNA substrate using rigid body docking, and bootstrapping their structures using a software developed by the Seidel

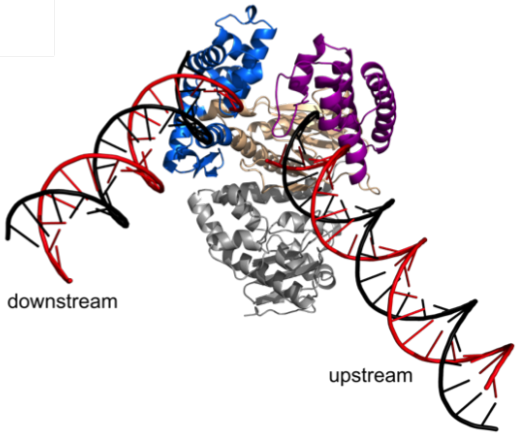

Figure 4.14: Bending of gapped DNA substrate bound to KF; 120°-angle between downstream and upstream DNA. Results from rigid body docking analysis: template DNA (red), non-template DNA (black), KF finger domain (blue), and thumb domain (purple); KF pdb-file: 1L3U (186). The figure was generate by Dr. Timothy Craggs using software presented in (102).

[5]OxDNA, collaboration with Majid Mosayebi, and Jonathan Doye, Physics, Oxford.
[6]Collaboration with Phil Biggin, Biochemistry, Oxford.

lab (102). The modelled upstream DNA was found in excellent agreement with the position of the DNA fragment present in a x-ray structure (186), and most strikingly, a significant kink between downstream and upstream DNA, showing a 120° bend angle from the straight duplex DNA structure, was observed (Fig. 4.14).

Next, we were interested in the *in vivo* evidence of the bending of the gapped DNA substrate.

Results

To test the *in vivo* relevance of the gapped DNA bend state, we internalised doubly-labelled gapped DNA substrates into live *E. coli* cells and investigated changes in their FRET efficiency upon binding of endogenous DNA Polymerase I (Fig. 4.15). A small number of gapped DNA molecules (1-5 molecules per cell) were electroporated into *E. coli* cells using the previous optimised electroporation protocol for nucleic acid internalisation (sec. 3.3). These molecules were then individually tracked and their FRET efficiency was monitored (SI 4.7.8).

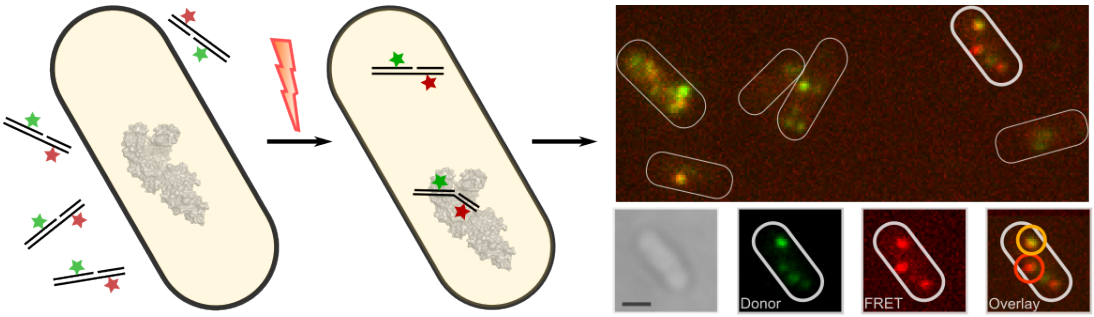

Figure 4.15: Schematic showing internalisation of doubly-labelled gapped DNA fragments into live *E. coli* cells using electroporation and single-molecule FRET measurements (left to right). Right: Overlay image of example FOV. Example cell (bottom) is shown in the brightfield image, the donor fluorescence channel, the FRET fluorescence channel, and the latter both combined in the overlay image. The overlay image is false-coloured such that intermediate FRET molecules appear orange and high FRET molecules appear red; two example molecules are highlighted accordingly. Scale bar: 1 µm.

Initially, we internalised the T(-12, Cy3B)T(+8, Atto647N) gapped DNA substrate (SI 4.7.1), as the *in vitro* experiments showed a large change in FRET upon poly-

merase binding (unbound: E=0.46, bound to KF: E=0.73, SI Fig. 4.24). Also in live cells, we observed a bimodal FRET distribution consistent with the existence of both bound (22±7%, E*=0.83±0.09) and unbound (E*=0.40±0.12) populations of the gapped DNA substrate (Fig. 4.16a). Conversely, a duplex DNA control only showed a single, intermediate FRET peak (E*=0.38±0.11, Fig. 4.16b, and *in vitro* data – SI Fig. 4.24c). These results were consistent with endogenous polymerase binding a bent conformation of the gapped DNA. Whilst this labelling scheme provided good discrimination between the FRET signals arising from DNA-only (unbound DNA) and bent DNA (bound to DNA Pol I), we could not resolve the smaller difference between two different bent states, which were present with increasing KF concentration in our *in vitro* single-molecule FRET controls (SI Fig. 4.24).

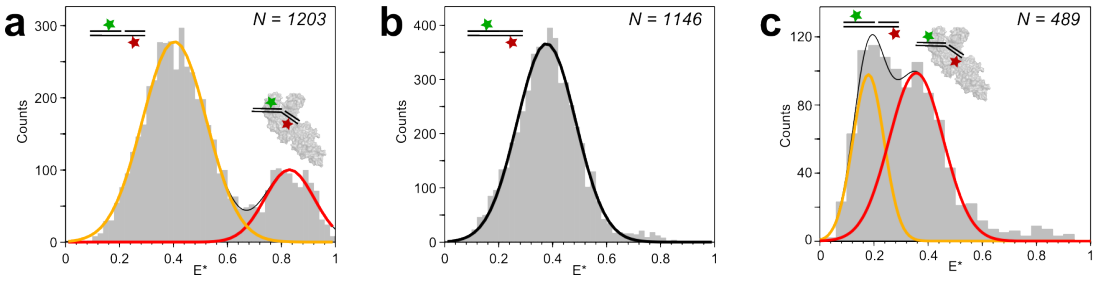

Figure 4.16: Gapped DNA bends in live bacteria. **a.** FRET histogram of gapped DNA (T-12:Cy3B,T+8: Atto647N) trajectories *in vivo*. Two major FRET species were observed; attributed to gapped DNA only (orange) and bent DNA (red). Free double-Gaussian fitting resulted in $E^*_{\text{gapped DNA}}$=0.40±0.12 (orange, *in vitro*: 0.47±0.10), and $E^*_{\text{bent DNA}}$=0.83±0.09 (red, *in vitro*: 0.75±0.10 and 0.92±0.05). **b.** Internalised duplex DNA control (B-11:Cy3B, T+8: Atto647N) resulted in a single FRET species, which was fitted to $E^*_{\text{duplex DNA}}$= 0.38±0.11 (black, *in vitro*: 0.46±0.10). DNA bending was observed *in vivo* with (22±7)% of gapped DNA in a bent conformation and showed very good agreement with *in vitro* FRET measurements (SI Fig. 4.24). **c.** *In vivo* FRET histogram of gapped DNA construct (T-18: Cy3B, T+15: Atto647N) showed two major FRET species, gapped DNA only (orange, E = 0.18±0.06) and bent DNA (red, E = 0.36±0.1); no second bent species at high-FRET was observed, consistent with *in vitro* DNA Pol I experiments (Dr. Tim Craggs, unpublished data). Values: center of Gaussian fit ± standard deviation.

To address this issue, we internalised the T(-18)T(+15) gapped DNA substrate, which exhibited a large difference in *in vitro* FRET values of unbent and bent DNA species upon KF titration to the gapped DNA substrate (bimodal distribution of bent DNA states: E = 0.44, and E = 0.83, DNA-only: E = 0.2; SI Fig 4.24). The resulting FRET

histogram from live cells lacked the significant high FRET peak, but did exhibit the low and intermediate FRET peaks, consistent with the presence of unbound DNA, and a single bent DNA species (Fig. 4.16c). This result suggests that the second high FRET bent state is not physiologically relevant *in vivo*. Interestingly, *in vitro* experiments on the full-length DNA Pol I (rather than the Klenow fragment) also showed a lack of the second high FRET bent state (Dr. Tim Craggs, unpublished data).

Discussion

We were able to observe DNA bending *in vivo* for two different gapped DNA labelling schemes and the measured *in vivo* single-molecule FRET efficiencies were in good agreement with the *in vitro* measurements. In additions, we showed that a second bent state, which was observed in KF titration experiments to the gapped DNA substrate *in vitro*, was not physiological relevant *in vivo*, and in fact did not exist for the full-length DNA Pol I *in vitro*, too. For both internalised gapped DNA constructs we observed a higher proportion of DNA-only FRET species (60-80%), than expected from our *in vitro* experiments, and assuming previous estimates of the cellular concentration of DNA Pol I of 400 nM (400 copies in live *E. coli* (115), assuming 1 fL cell volume). This may be due to competitive binding of the internalised DNA by other cellular proteins preventing DNA Pol I binding, partial degradation of the DNA, or fewer copies of 'free' DNA Pol I in live cells, i.e. not involved in other DNA replication and repair mechanisms.

Unfortunately, we were unable to produce a DNA Pol I knockout strain for further control experiments, since the cells were not viable and could not be cultured. However, the similarity between the *in vitro* and *in vivo* FRET behaviour observed for the unbound and bound species suggests that the DNA is bent to the same extent both *in vitro* and *in vivo*. It seemed unlikely that another protein would have generated the exact same FRET signature, and thus we concluded that the bent states, which we

observed *in vivo*, were due to the binding of the gapped substrates by endogenous polymerase.

4.6 Conclusion

In this chapter, I characterised organic-dyes for their use in live-cell FRET studies, characterised FRET at the single-cell level, and evaluated single-molecule FRET efficiencies using DNA FRET standards. Combining single-molecule FRET measurements and single-particle tracking, I was able to observe and trace single FRET molecules for more than 10 s in live bacterial cells. Finally, I applied the single-molecule FRET capability to three very interesting biological systems, in which I studied single-molecule FRET signatures of a protein complex, conformational changes of a DNA binding protein, and bending of a gapped DNA substrate *in vivo*.

First, I measured the photostability and brightness of 7 organic fluorophores using single-cell photobleaching studies, in which I rated Cy3B as best performing donor fluorophores and Cy5 (high brightness), Atto647, and Atto647N (both very photostable) as best performing acceptor fluorophores. It is noteworthy that Atto647N is hydrophobic and is known to stick to cell membranes (66), and thus should be used with care for accurate diffusion coefficient measurements *in vivo*. In this work, Atto647N, which is also known to exhibit different intensity levels (68) did not seem to effect FRET signatures at least at the resolution available in live cells. In addition, the presented single-cell photobleaching analysis can be used as a general method to screen for even more labels (organic fluorophores or fluorescent proteins) for their use in single-cell and single-molecule fluorescence studies in live cells.

Second, I examined the performance of three FRET-dye pairs using single-cell FRET studies *in vivo*; identifying Cy3B-Atto647N as the best performing FRET dye-pair. When characterising FRET signals using low, intermediate, and high FRET DNA

standards on the single-cell level, I faced two challenges: (i) fast acceptor photobleaching and (ii) DNA degradation, which both led to the decrease of single-cell FRET signals. Nevertheless, I was able to distinguish low, intermediate and high FRET states *in vivo*, establishing single-cell FRET studies as an easy-to-use and quick assay to study for instance induced intra-molecular changes, protein-protein interactions, and cell-to-cell variations.

Third, I studied FRET signals at the single-molecule level, again using DNA FRET standards labelled with Cy3B-Atto647N. Still, I observed very wide FRET distributions especially for the low- and high-FRET DNA standards, which I did not observe in *in vitro* experiments. I reasoned that the blunt-ended DNA FRET standards were not ideally suited for *in vivo* single-molecule FRET measurements, since the blunt DNA ends could be recognised by endonucleases as DNA breaks, and short dsDNA fragments might get degraded (146).

Hence, as introduced in chapter 3, I used protected DNA FRET standards with chemically linked ends as standards for further single-molecule FRET characterisation. Interestingly, I was able to obtain FRET distributions and FRET-Stoichiometry histograms *in vivo*, which were in very good agreement with *in vitro* single-molecule FRET measurements, and I was able to track single FRET molecules for more than 10 s. These results, as well as their tolerance to electroporation pulses (chapter 3, sec. 3.3.1), make protected DNAs ideal standards for single-molecule FRET characterisation measurements in living cells.

However, some shortcomings of the single-molecule tracking capability in tracing doubly-labelled protected DNA, and proteins *in vivo* need to be mentioned. Due to the wide distribution of internalised molecules (ranging from 0-10 molecules/cells, cell-to-cell variations, and also sample-to-sample variations), the single-particle tracking routine sometimes failed, since the cells were too crowded (5-10 molecules per cell) and ideally the molecule density should range around 1 mol/μm^2 (187). To control

the molecule density (i) cells could be pre-bleached before starting data acquisition and as performed in this study, (ii) automated cell segmentation and selection of cells that were loaded with only a few molecules could be performed, or (iii) single-particle tracking could be combined with photoactivated localisation microscopy, such as demonstrated in sptPALM (28), to control the number of activated molecules.

Next, the donor green-fluorescence channel shows still high autofluorescence and often bright (PSF-shaped) spots that were even present in non-electroporated cells and that I attributed to stress-responses of electrocompetent cells. These 'spots' were picked up by the localisation routine and impeded the linking of donor, and FRET signal. Thus, performing single-molecule FRET measurements with red-infrared FRET-dye pairs such as Cy5/Cy7 or Atto680/Atto740 (68, 135) would be advisable, since the red fluorescence channel shows far less cellular autofluorescence than the green fluorescent channel (SI Fig. 4.19). Nonetheless, the infrared dyes Cy7 and Atto740 need to be characterised first for their use in single-particle tracking studies.

In addition, adjacent biomolecules (especially in the Donor-channel) obstruct single-molecule FRET signatures of the molecule of interest, since the fitting routine relies on the assumption that only a single fluorophore (PSF) is present, and the tracking algorithm might connect trajectories incorrectly. To overcome this problem, the molecule's history (e.g. FRET state) could be implemented into the tracking algorithm, such that molecules are linked with a similar FRET state and switch only to a new FRET state, if the new state has enough data support. Meanwhile, other tracking algorithms could also be tested for their performance on single-molecule FRET data (188, 116).

Furthermore, single-molecule FRET trajectories might also be interrupted due to donor and acceptor fluorophore blinking. However, the impact of blinking on single-particle tracking can be partially influenced by the choice of fluorophores. Organic dyes such as Cy3B, and Atto647N, which were used in this work, were photostable

and showed very few blinking events, whereas other acceptor fluorophores such as Alexa647, Cy5, and Atto655, are prone to blinking. The fluorophores' blinking behaviour could also be used to our advantage by implementing photoswitching as described in (23, 27) and other studies to perform live-cell super-resolution imaging. In combination with single-molecule FRET and different FRET-dye pairs, switchable FRET could be employed to monitor several distances within the same molecule as first shown *in vitro* by Uphoff *et al.* (189).

It is worth mentioning that the *in vivo* single-molecule FRET values presented in this work are 'uncorrected' FRET values. This means, that these FRET efficiencies were not corrected for cross-talk and γ-corrections, as described in chapter 2, sec. 2.2.2, (98, 99). However, using the alternating laser excitation scheme FRET corrections can be implemented *in vivo* and accurate FRET values can be obtained. I briefly outline the necessary corrections and measurements needed: First, the already background corrected DA intensity values have to be corrected for cross-talk. The donor-leakage into the acceptor channel ($Lk = l \cdot I_{\text{D-only, FRET}}$) can be directly measured by internalising donor-only labelled DNAs and measuring their fluorescence contribution in the FRET channel, and the direct excitation of the acceptor fluorophore at the donor excitation wavelength ($Dir = d \cdot I_{\text{A-only, dir}}$) can be obtained by measuring the acceptor-only labelled DNAs under green continuous illumination. Both cross-talk properties l and d can be obtained from FRET-Stoichiometry histograms according to eq. 2.10 (chapter 2) and the cross-talk corrected FRET values (E_{corr}) can be calculated. Second, the γ-factor can be obtained from the slope of the plot of $1/S_i$ versus $E_{\text{corr, }i}$ for (i) FRET species (99), such as the protected intermediate and high FRET DNA standards. Finally, the FRET values can be corrected for the obtained γ-factor (eq. 2.6, chapter 2) giving accurate single-molecule FRET values *in vivo*.

For single-molecule FRET studies of doubly-labelled proteins *in vivo*, the main chal-

lenges remain: (i) the efficient internalisation of the protein of interest, which seems very protein dependent, (ii) the removal of non-internalised proteins and protein aggregates (as for the KF internalisation experiments), (iii) the removal of free dye after protein labelling (as for the E9-Im9 complex experiments). Whereas non-internalised protein molecules stuck to the cell wall make single-particle tracking challenging, the preferential internalisation of free dye obscures signals in donor channel and acceptor-only channel and makes linking of FRET molecules with the donor, and acceptor localisations error prone. Nevertheless, I was able to observe similar single-molecule FRET states *in vitro* and *in vivo* when studying doubly-labelled proteins and protein-DNA interactions. These results show that the conformational states of the biomolecules *in vivo* did not differ significantly from *in vitro* settings. However, I am expecting significant differences in kinetic rates of biochemical reactions *in vivo* compared to *in vitro* settings (molecular crowding, higher viscosity, higher local substrate concentrations *in vivo*, etc.) as presented in chapter 6 in the study of transcription initiation *in vivo*.

The internalisation of nucleic acids is straightforward and *in vivo* single-molecule FRET values were in excellent agreement with *in vitro* measurements. Protected DNA FRET standards have proven ideal standards for characterising *in vivo* single-molecule FRET efficiencies and the transformation to accurate FRET measurements was outlined and can be performed if absolute distance measurements are needed. In the next two chapters, comprehensive single-molecule fluorescence and single-molecule FRET studies follow, in which I studied the mobility and spatial distribution of tRNA molecules (chapter 5), and FRET changes of promoter DNA during transcription initiation (chapter 6) *in vivo*.

Contributions

I performed all experiments and data analysis for the characterisation of organic dyes, single-cell FRET, and single-molecule FRET in live bacteria, which are partially presented in published work (141, 139). I developed software for the analysis of single-cell photobleaching studies (SI 4.7.5), fluorescence channel mapping (SI 4.7.6), single-cell FRET studies (SI 4.7.7), and *in vivo* single-molecule FRET studies combined with single-particle tracking (SI 4.7.8).

The protected DNA FRET standards were synthesised by Dr. Afaf El-Sagheer.

Protein labelling of E9 DNAse domain and Im9 protein were performed by Andrea Lei and Renata Kaminska, and KF labelling was performed by Marko Sustarsic. All experiments on the E9-Im9 project were performed by Andrea Lei (Doctoral Training Center rotation student) under my supervision, and I analysed the data. The movie showing long-lasting KF single-molecule FRET signature was taken by Dr. Louise Aigrain and I performed single-molecule particle tracking and single-molecule FRET analysis. Marko Sustarsic and I performed experiments of gapped DNA *in vivo*, and I analysed the data, whereas Dr. Timothy Craggs performed and analysed all *in vitro* experiments for the gapped DNA substrates.

4.7 Supplementary information

4.7.1 DNA samples

DNA labelling, purification, and annealing was performed as described in chapter 3, sec. 3.6.1.

The sequences used are shown below; the highlighted **T** base was labelled either with STD45T: Cy3B, Cy3, Alexa532; STD45B dT38: Atto647N, Alexa647, Atto647, or Cy5; STD45B dT13, and STD45B dT28: Atto647N; gappedDNA (T-12,T+8): Cy3B/Atto647N; gappedDNA (T-18,T+15): Cy3B/Atto647N.

DNA sequences 5' to 3'

STD45T (unlabelled): TAA ATC TAA AGT AAC ATA AGG TAA CAT AAC GTA AGC TCA TTC GCG

STD45T: **T**AA ATC TAA AGT AAC ATA AGG TAA CAT AAC GTA AGC TCA TTC GCG

STD45B (unlabelled): CGC GAA TGA GCT TAC GTT ATG TTA CCT TAT GTT ACT TTA GAT TTA

STD45B – dT13: CGC GAA TGA GC**T** TAC GTT ATG TTA CCT TAT GTT ACT TTA GAT TTA

STD45B – dT28: CGC GAA TGA GCT TAC GTT ATG TTA CCT **T**AT GTT ACT TTA GAT TTA

STD45B – dT38: CGC GAA TGA GCT TAC GTT ATG TTA CCT TAT GTT ACT T**T**A GAT TTA

gapped DNA (T-12,T+8): CCT CAT TCT TCG TCC CAT **T**AC CAT ACA TCC TAG AGA G**T**A GAG CCT GCT TCG TGG

gapped DNA (T-18,T+15): CCT CAT TCT TCG **T**CC CAT TAC CAT ACA TCC TAG AGA GTA GAG CC**T** GCT TCG TGG

gapped DNA (bottom, unlabelled): GGA GTA AGA AGC AGG GTA ATG GTA TGT AGG G ATC TCT CAT CTC GGA CGA AGC ACC

4.7.2 Preparation of proteins

Klenow fragment As described in chapter 3, sec. 3.6.2.

E9-Im9 complex Protein expression, purification, labelling, and complex construction was performed in the Kleanthous group (Biochemistry, Oxford) by Andrea Lei and Renata Kaminska. The extent of free dye for the individual protein complex samples, calculated from in-gel fluorescence, was E9(D40C)-Im9: 18% Alexa647, 15% Cy3B, and E9(S3C)-Im9: 4% Alexa647, and 10% Cy3B.

4.7.3 Electroporation

As described in chapter 3, sec. 3.6.3, and sec. 3.6.4. Except that cells were always electroporated at 1.4 kV, which showed highest loading while maintaining cell viability (chapter 3, sec. 3.3.2).

4.7.4 Cell imaging

Single-cell and single-molecule fluorescence microscopy in live bacteria was performed on the setup described in appendix A.1.

Single-cell photobleaching measurements were obtained in epi-fluorescence mode at 100 ms temporal resolution and 600 µW-green and 300 µW-red excitation powers for donor and acceptor fluorophores, respectively. Single-cell FRET measurements were carried out using an alternating laser excitation scheme (103, 98). Typical exposure times and excitation powers were 50 ms, 1 mW-green and 0.5 mW-red. Single-molecule FRET measurements were performed under HILO illumination (111) using 2 mW green excitation power and 20 ms exposure time in green continuous wave-mode, and using 2 mW green excitation power, 1 mW red excitation power, and 20 ms exposure time in ALEX-mode.

4.7.5 Single-cell photobleaching analysis

Cells were segmented automatically by adapting the MATLAB (MathWorks) implementation of Schnitzcells (157) for brightfield cell images. The manually adjustable cell masks were used to extract in-cell fluorescence data by calculating the total fluorescence intensity per cell area within each cell mask for each movie frame. The cellular autofluorescence per cell area after photobleaching was subtracted from the photobleaching time-trace. Baseline-subtracted photobleaching time-traces of heavily loaded cells ($>$100 molecules/cell) were fitted with a single exponential to obtain the cell-based photobleaching lifetime as a measure of fluorophore photostability. Baseline-subtracted photobleaching time-traces of cells loaded with 1-5 molecules/cell, i.e. showing less than 6 quantised steps were fitted with a hidden Markov model (HMM) as described in (62, 141) to obtain the fluorophore brightness. Briefly, HMM is a stochastic model that maps measured values to unobserved (or hidden) states. Here, the time trajectories were modelled as a sequence of up to 10 hidden states (different cell intensity levels) and transitions between these states (photobleaching events). A custom-written MATLAB script was run recursively; keeping only the state values for the last photobleaching step and removing this data before the next iteration step. Each iteration allowed up to 10 hidden states to be fitted. Such an analysis routine took advantage of the exponential photobleaching kinetics: the last photobleaching step was likely to last significantly longer than previous steps, and thus fitting the last step was likely to have the greatest data support. For the step size estimate of the fitted steps, the absolute difference between consecutive intensity states was calculated taking fluorophore blinking into account. Only step sizes from about 70-100 cells per sample with photobleaching time-traces with less than 6 steps recovered by the HMM algorithm were plotted in the step height histograms. The step height histograms were fitted with a single one-dimensional-Gaussian (free fitting parameters: position1, width1, amplitude1) for donor fluorophores and two

Gaussians (free fitting parameters: position1, width1, amplitude1, amplitude2; position2 = 2·position1, width2 = $\sqrt{2}\cdot$ width1) for acceptor fluorophores. The single-molecule unitary intensity was given as the center of the Gaussian fitting the main peak.

4.7.6 Channel mapping

For mapping the donor, green fluorescence channel onto the FRET, red fluorescence channel, fluorescent beads images were acquired. The beads in two fluorescence channels were linked to each other and a spatial transformation matrix was obtained. Using the software TwoTone[7], the control points (beads positions in both channels) were chosen manually and a projective transformation matrix from the green onto the red channel was calculated using functions already implemented into MATLAB (*cp2tform.m*). With this transform type optical aberrations like distortions and tilts were taken into account. The major problem here was that the control points were selected manually, resulting in a linking-inaccuracy of about 1 pixel ($\sim$ 100 nm), SI Fig. 4.17a, which should be decreased below the localisation precision of about 40 nm to achieve high performance single-particle tracking in live cells.

Channel mapping was automated using MATLAB, such that the beads were fitted with a 2D elliptical Gaussian in both channels (centre of 2D elliptical Gaussian = control point). Then, control points in the red channel were linked with control points in the green channel using a nearest-neighbour algorithm (MATLAB, *knnsearch.m*). Three different transformation types were tested to map the control points in the green channel onto the corresponding control points in the red channel. The performance of the channel mapping was evaluated using two metric values (FRE and

[7] 'TwoTone' software was developed by Dr. Seamus Holden (95).

TRE) as established by Churchman *et al.* (190)

$$\text{FRE} = \Big(\frac{1}{N}\sum_{i=1}^{N}[\mathbf{x}_{i,1} - t(\mathbf{x}_{i,2})]^2\Big)^{1/2} \tag{4.1}$$

$$\text{TRE} = \Big(\frac{1}{N}\sum_{i=1}^{N}[\mathbf{x}_{i,1} - t_i(\mathbf{x}_{i,2})]^2\Big)^{1/2} \tag{4.2}$$

where '1' and '2' denote channel '1' (red emission) and channel '2' (green emission), respectively, $\mathbf{x}_{1/2}$ denotes the position vector of the control points (N) in channel '1/2', t denotes the transformation generated from all control points from channel '2' to '1', t_i denotes the transformation generated without including control point i. FRE is useful to check the performance of the transformation on the fitted control points (optimal scenario) whereas TRE describes the linking-inaccuracy of points not used for generating the transformation matrix (realistic scenario).

The performance of the automated channel mapping using the different transformation types (projective, piecewise linear and local weight mean) was tested on beads images where 130 control points were fitted and used for transformation (SI Fig. 4.17b). The piecewise linear transformation uses local linear mappings within triangles spanned by control points (hence, FRE $\sim$ 0) whereas the local weight mean uses local second-order mappings within polygons formed by 12 control points.

Mapping accuracy could be reduced down to $\sim$10 nm using the local weight mean transformation mode, which was far below the localisation accuracy of $\sim$40 nm for single-particle tracking experiments, and thus, automated channel mapping using local weight mean transformation-mode was used for all FRET analysis.

4.7.7 Single-cell FRET analysis

Single-cell FRET efficiencies were obtained by measuring the variation in acceptor emission intensity upon donor excitation on the cell-level. For low, intermediate and

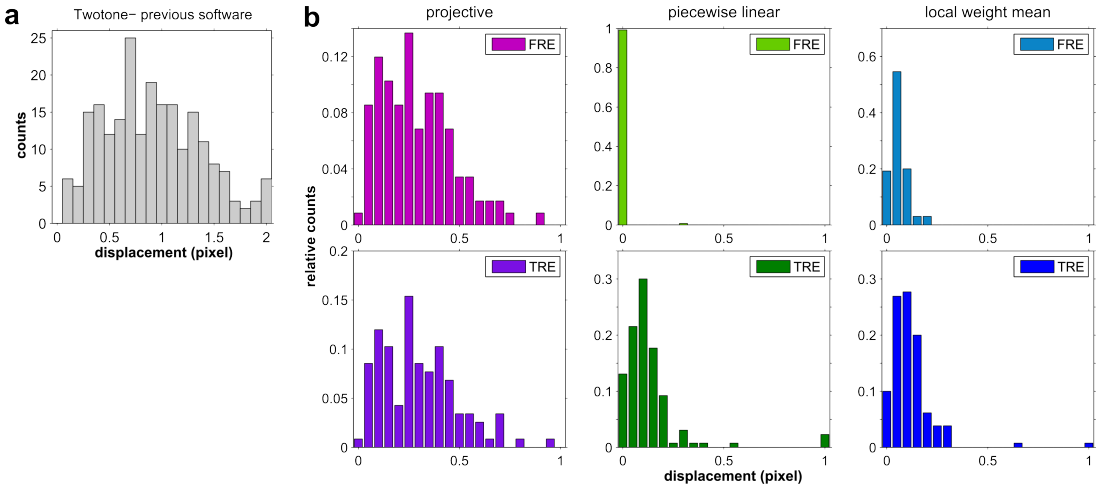

Figure 4.17: Performance test of different channel mapping methods on spatial accuracy. **a**. Channel mapping as used by our lab so far (Twotone, (95)). The manual selection of about ∼200 control points from 5 beads images results in linking-inaccuracy of ∼0.94 pixel/ ∼90 nm. **b**. Left to right: Automated channel mapping using projective, piecewise linear and local weight mean transformation algorithms evaluated using two different metric values FRE and TRE (top to bottom). Mapping inaccuracy could be decreased down to ∼0.30 pixel/ ∼29 nm (TRE, projective), ∼0.15 pixel/ ∼14 nm (TRE, piecewise linear) and ∼0.11 pixel/ ∼10.6 nm (local weight mean- preferred transformation type). The mapping accuracy of about 10 nm is sufficient for single-molecule FRET tracking, since the tracking accuracy is dominated by the localisation accuracy of ∼40 nm (experimental), ∼20 nm (theoretical, Thompson formula (175)).

high FRET dsDNA Cy3B/Atto647N cells were automatically segmented, whereas for high FRET dsDNA Cy3B/Cy5, Cy3B/Atto647, Cy3B/Atto647N cells were manually segmented using custom-written MATLAB scripts. Cells were segmented in the brightfield image corresponding to the red emission channel and the mask was transformed onto the green emission channel. The cell masks were used to extract in-cell fluorescence data in the red and green emission channel. The fluorescence intensity was corrected for autofluorescence background. In the case of automated cell segmentation the average pixel intensity from non-treated cells was subtracted as a background value for each emission channel. In case of manual segmentation, the background around the cells was locally obtained for each cell. Background subtracted fluorescence intensities were then used to calculate background corrected

single-cell FRET efficiencies as follows

$$E_{\text{cell}} = \frac{\mathrm{F}^{\mathrm{Aem}}_{\mathrm{Dex}} - \mathrm{AF}^{\mathrm{Aem}}_{\mathrm{Dex}}}{\mathrm{F}^{\mathrm{Aem}}_{\mathrm{Dex}} - \mathrm{AF}^{\mathrm{Aem}}_{\mathrm{Dex}} + \mathrm{F}^{\mathrm{Dem}}_{\mathrm{Dex}} - \mathrm{AF}^{\mathrm{Dem}}_{\mathrm{Dex}}} \tag{4.3}$$

where $\mathrm{F}^{\mathrm{Yem}}_{\mathrm{Xex}}$ and $\mathrm{AF}^{\mathrm{Yem}}_{\mathrm{Xex}}$ represent the fluorescence (F) and autofluorescence background signal (AF) in the Y emission channel under X excitation, respectively. Fluorescence overlay images were obtained by overlaying the DD-channel and DA-channel, false-coloured green and red, respectively. The DD-channel was transformed onto the DA-channel using channel mapping routine described above (SI 4.7.6). The autofluorescence signal was estimated as the mean fluorescence signal of about 500 'empty cells' (non-treated cells) in the respective emission channel, $\mathrm{AF}^{\mathrm{Dem}}_{\mathrm{Dex}}$, $\mathrm{AF}^{\mathrm{Aem}}_{\mathrm{Dex}}$, and $\mathrm{AF}^{\mathrm{Aem}}_{\mathrm{Aex}}$, acquired on the same day. The distribution of autofluorescence in the green and red emission channel within four different data sets for CW and ALEX-mode illumination is shown in Fig. 4.18.

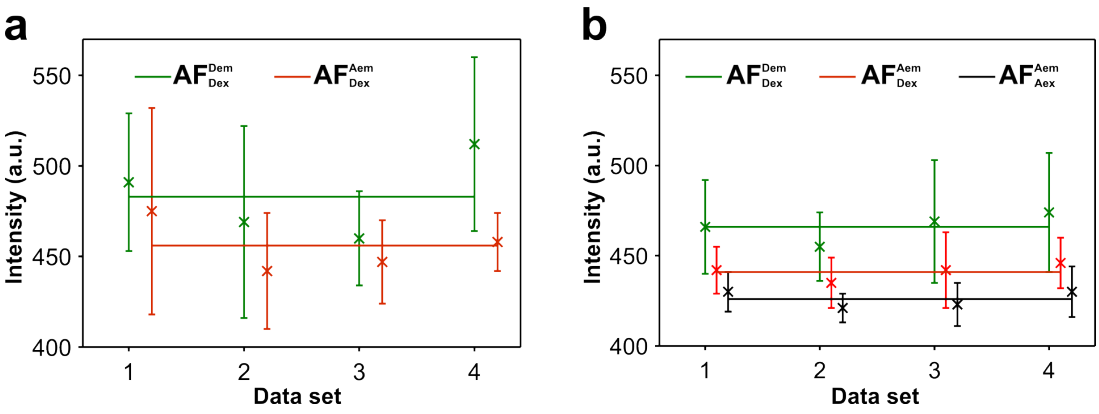

Figure 4.18: Variation of cellular autofluorescence within four different data sets. **a**. Autofluorescence of 'empty cells' (non-treated cells) in green continuous wave-mode in the green emission channel upon green excitation ($\mathrm{AF}^{\mathrm{Dem}}_{\mathrm{Dex}}$, green) and in red emission channel upon green excitation ($\mathrm{AF}^{\mathrm{Aem}}_{\mathrm{Dex}}$, red). **b**. Autofluorescence of 'empty cells' in ALEX-mode using same notation and introducing a new fluorescence signal, red emission upon red excitation ($\mathrm{AF}^{\mathrm{Aem}}_{\mathrm{Aex}}$, black). In general, the cellular fluorescence in ALEX-mode is smaller and less noisy than in green continuous wave-mode due to pre-exposure of the sample with laser light for about 10 frames and thus photobleaching of the cellular autofluorescence.

4.7.8 Single-molecule FRET analysis

Single-molecule fluorescence localisation Custom-written MATLAB software was used to analyse single-molecule FRET measurements in live bacteria as described in (115, 62). Briefly, PSFs in the DA/FRET channel in each movie frame were fitted by a 2D elliptical Gaussian (free fit parameters: x/y position, x/y width, elliptical rotation angle, amplitude, background) using initial position guesses from applying a fixed localisation-intensity threshold on the bandpass filtered fluorescence image (95). After I localised molecules in the DA/FRET channel, I force-fitted the fluorescent signal in the DD-channel, which was mapped onto the DA-channel using a transformation matrix (SI 4.7.6). Only molecules with higher photon counts than 400 ph/frame in the (DD+DA)-channel, and 40 ph/frame in the DD-channel (for green continuous wave-mode, gCW) and also higher photon counts than 130 ph/frame on the AA-channel (ALEX-mode) were considered for further analysis; frame time: 20 ms (gCW), and 20 ms (ALEX).

The FRET efficiencies were calculated as described below (eq. 4.4). For measurements using an ALEX scheme, PSFs were also fitted in the AA channel and the stoichiometry value was calculated (eq. 4.5). Single-molecule FRET and stoichiometry histograms were fitted with a 1D Gaussian using least squares fitting routine implemented in MATLAB (MathWorks).

Background corrected single-molecule FRET and stoichiometry values were calculated from photon counts (phC) of the single molecule (integral of fitted 2D elliptical Gaussians) in the respective emission channel, $\mathrm{phC}_{\mathrm{Dex}}^{\mathrm{Aem}}$ and $\mathrm{phC}_{\mathrm{Dex}}^{\mathrm{Dem}}$.

$$E^*_{\mathrm{mol}} = \frac{\mathrm{phC}_{\mathrm{Dex}}^{\mathrm{Aem}}}{\mathrm{phC}_{\mathrm{Dex}}^{\mathrm{Aem}} + \mathrm{phC}_{\mathrm{Dex}}^{\mathrm{Dem}}} \tag{4.4}$$

$$S^*_{\mathrm{mol}} = \frac{\mathrm{phC}_{\mathrm{Dex}}^{\mathrm{Aem}} + \mathrm{phC}_{\mathrm{Dex}}^{\mathrm{Dem}}}{\mathrm{phC}_{\mathrm{Dex}}^{\mathrm{Aem}} + \mathrm{phC}_{\mathrm{Dex}}^{\mathrm{Dem}} + \mathrm{phC}_{\mathrm{Aex}}^{\mathrm{Aem}}} \tag{4.5}$$

Single-particle tracking Single-particle tracking was performed in the red emission channel by adapting the MATLAB script based on a published algorithm (114). Localised PSFs in the FRET channel (gCW), and FRET and AA channel (ALEX) were linked to a track if they appeared in consecutive frames within a window of 7 pixels (0.69 µm). This window size ensures that 98 % of steps are correctly linked for an apparent diffusion coefficient of $1.0\,\mu m^2/s$ and 20 ms exposure time (117, 115). To account for PSF disappearance due to blinking or missed localisation, I used a memory parameter of 1 frame. To eliminate noise, only molecules appearing in 5 consecutive frames were included in the analysis.

4.8 Supplementary figures

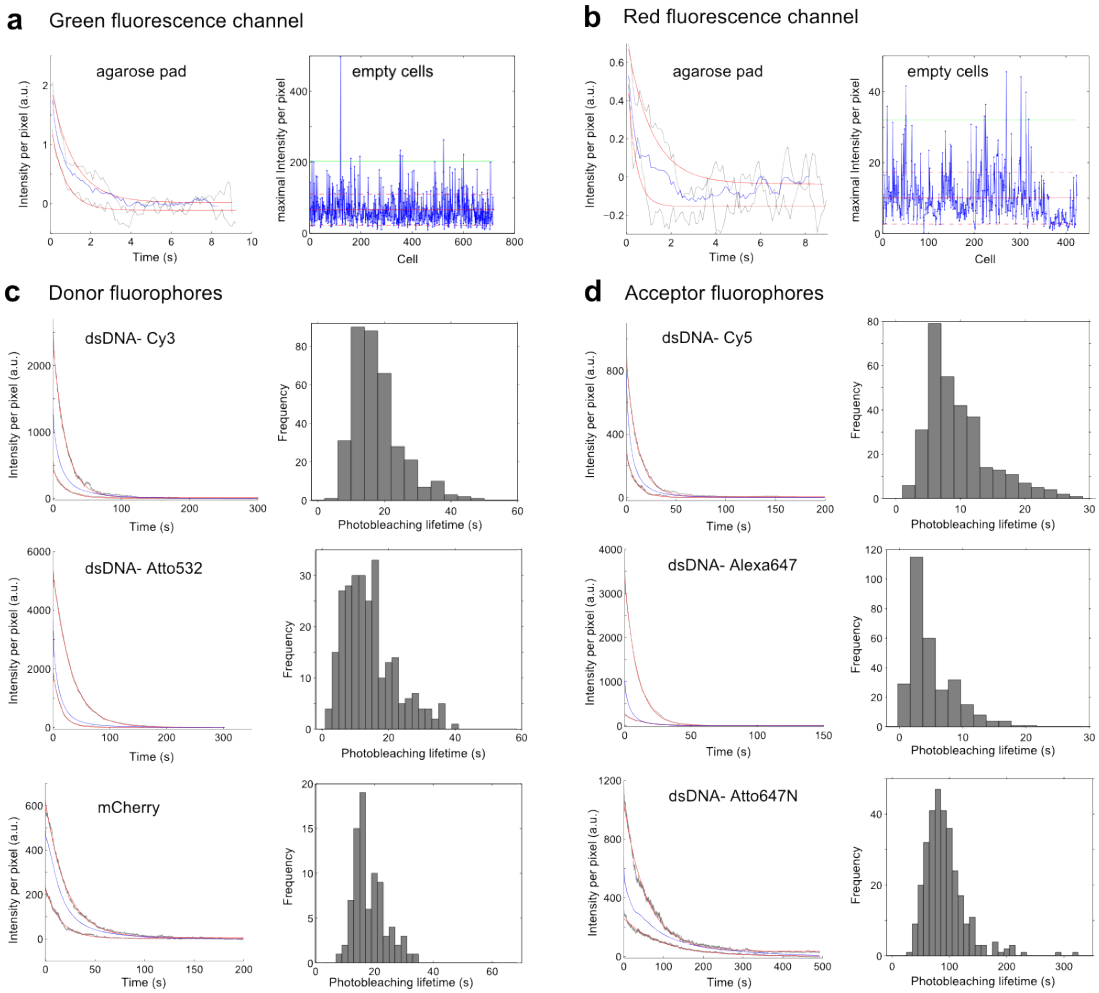

Figure 4.19: Cell-based photobleaching studies of organic fluorophores in green and red fluorescence channel. **a.** Autofluorescence signal in green fluorescence channel. Left: Autofluorescence decay of agarose pad only; two photobleaching time-traces (gray), single-exponential fits (red) and average photobleaching time-trace (blue). The photobleaching lifetime of the agarose pad is less than 1 s. Right: Maximal cell intensity normalised by cell area of non-treated cells ('empty cells') with loading threshold of mean plus 3 standard deviation of empty cells (green line); here about 1% of non-treated cells would be classified as loaded. **b.** Same analysis as in a. for agarose pad and empty cells in red fluorescence channel. The photobleaching lifetime of agarose pads is about 0.5 s, and less than 2% of empty cells would be classified as loaded. **c.** Cell-based photobleaching studies of dsDNA-Cy3 and dsDNA-Atto532, and mCherry, respectively. Left: Cell-based photobleaching time-traces (gray), single-exponential fits (red) and average photobleaching time-traces (blue). Right: Histogram of photobleaching lifetime obtained by single-exponential fit of cell-based photobleaching time-traces. Photobleaching lifetime of 18$\pm$7 s (median: 16 s), 14$\pm$8 s (median: 13 s), and 18$\pm$5 s (median: 17 s), were obtained for Cy3, Atto532, and mCherry respectively. Each data set consisted of 300-600 cells. **d.** Same analysis of cell-based photobleaching studies of dsDNA-Cy5, dsDNA-Alexa647, and dsDNA-Atto647N resulted in photobleaching lifetimes of 10$\pm$5 s (median: 8 s), 6$\pm$4 s (median: 5 s), and 92$\pm$37 s (median: 86 s), respectively. Each data set consisted of 250-450 cells.

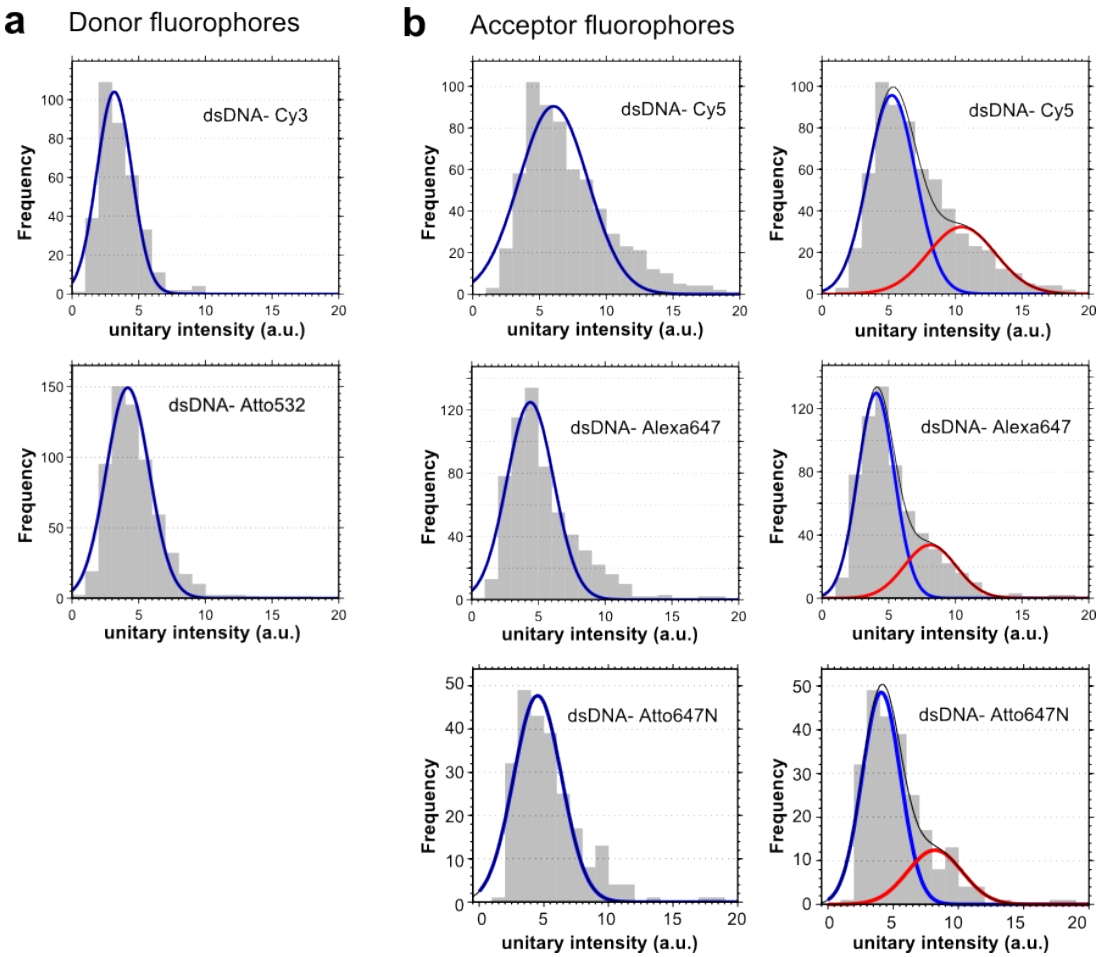

Figure 4.20: Characterisation of organic fluorophore brightness in green and red fluorescence channel. **a.** Top to bottom: Histograms of single photobleaching step heights obtained from single-cell photobleaching studies of dsDNA-Cy3 and dsDNA-Atto532, respectively. Single Gaussian fits are centered at a unitary single-molecule fluorescence intensity of 3.2$\pm$1.3 a.u. and 4.2$\pm$1.6 a.u. corresponding to 2800$\pm$1100 ph/s and 3600$\pm$1400 ph/s for dsDNA-Cy3 and dsDNA-Atto532, respectively. **b.** Top to bottom: Histograms of single photobleaching step heights obtained from single-cell photobleaching studies of dsDNA-Cy5, dsDNA-Alexa647, and dsDNA-Atto647N, respectively. Single Gaussian fits not always resemble step height distribution accurately. Double Gaussians are fitted to the step height distribution to include double-steps (quasi simultaneous photobleaching of two fluorophores) due to short photobleaching lifetime of acceptor fluorophores into analysis; Gaussians are centered at x_0 and $2\ x_0$ with x_0 the unitary single-molecule fluorescence intensity. The following unitary single-molecule fluorescence intensities were obtained from double Gaussian fitting. dsDNA-Cy5: 5.2$\pm$1.8 a.u., 4500$\pm$1500 ph/s. dsDNA-Alexa647: 4.1$\pm$1.4 a.u., 3500$\pm$1200 ph/s. dsDNA-Atto647N: 4.1$\pm$1.5 a.u., 3500$\pm$1300 ph/s.

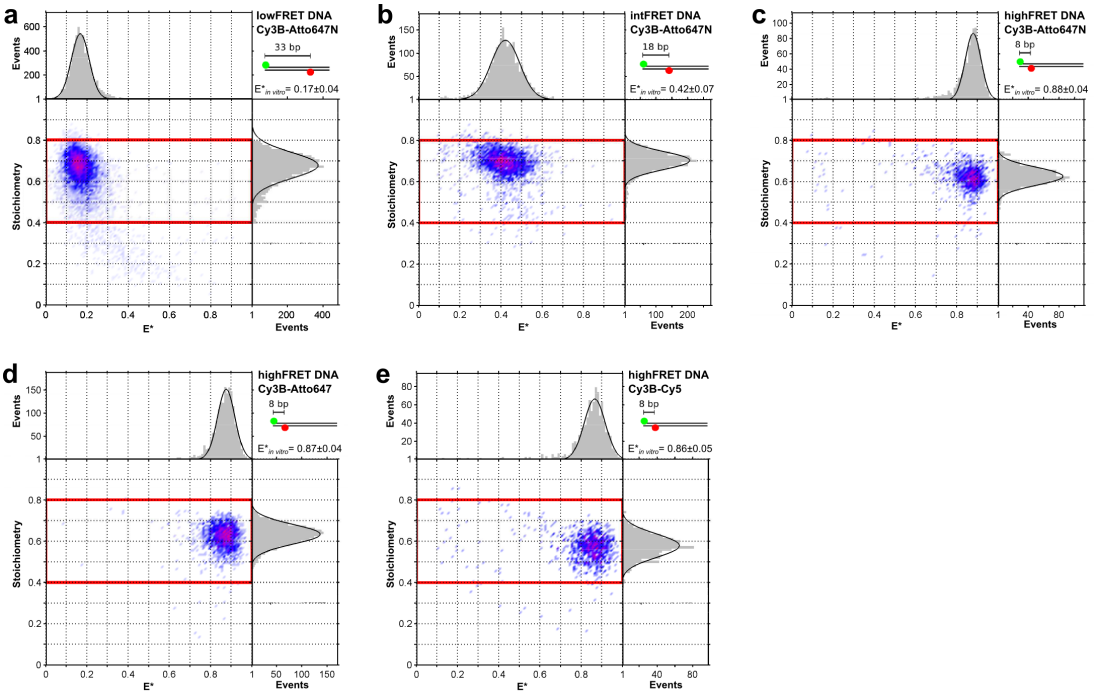

Figure 4.21: *In vitro* measurements of blunt-ended DNA FRET standards using single-molecule confocal microscopy and an alternating laser excitation scheme. **a-c.** Analysed low, intermediate and high FRET DNA standards Cy3B-Atto647N give uncorrected FRET efficiencies of 0.17±0.04, 0.42±0.07 and 0.88±0.04, respectively. **d-e.** Uncorrected FRET efficiencies of 0.87±0.04 and 0.85±0.05 were obtained for high FRET DNA standards labelled with Cy3B-Atto647 and Cy3B-Cy5, respectively.

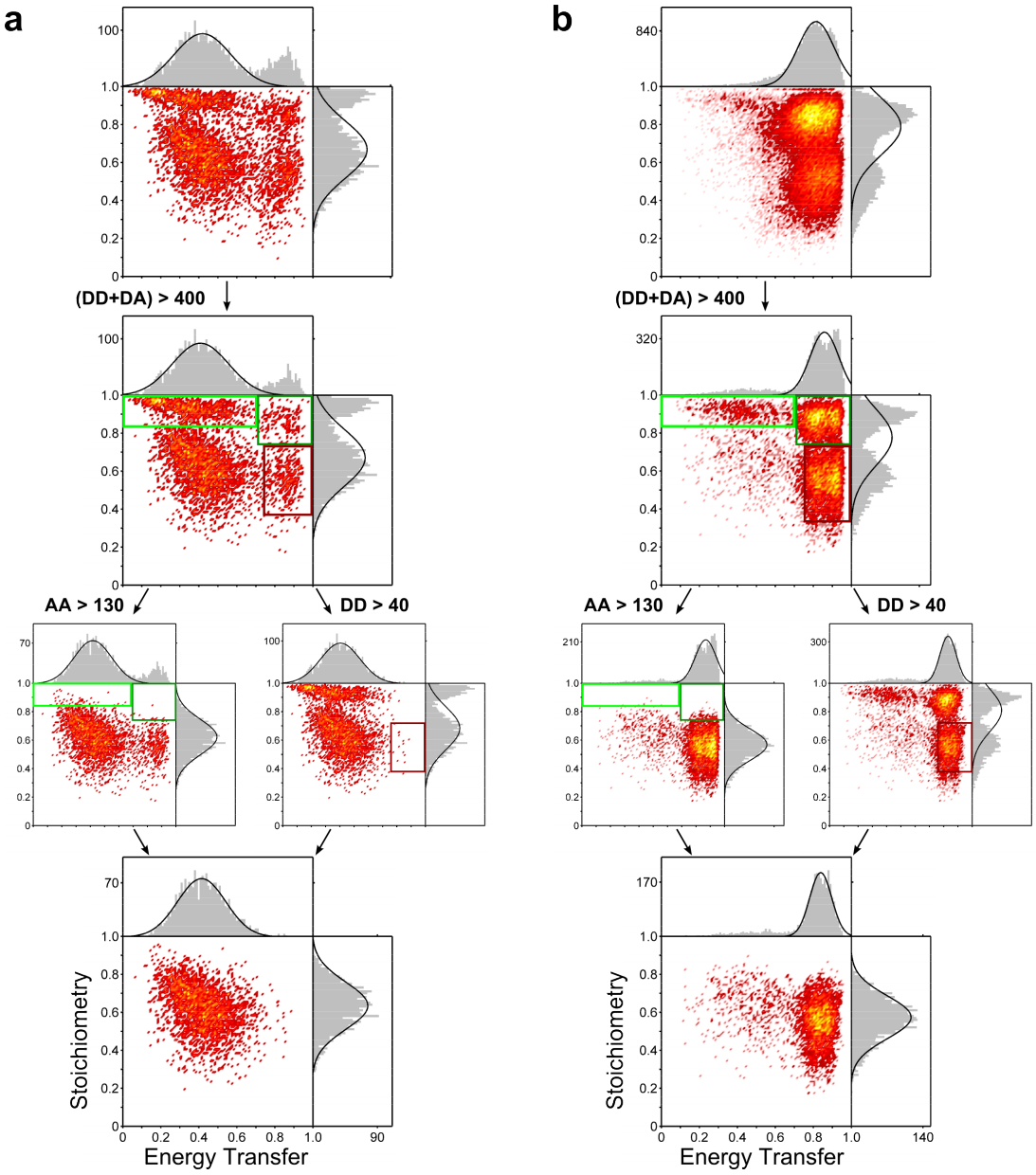

Figure 4.22: *In vivo* single-molecule FRET-Stoichiometry histograms for **a.** intermediate and **b.** high FRET protected DNA standards. Single-molecule data was filtered for a total fluorophore intensity of $>$400 ph/frame, $>$130 ph/frame in the AA-channel , and $>$40 ph/frame in the DD-channel, respectively. Frame-time: 20 ms.

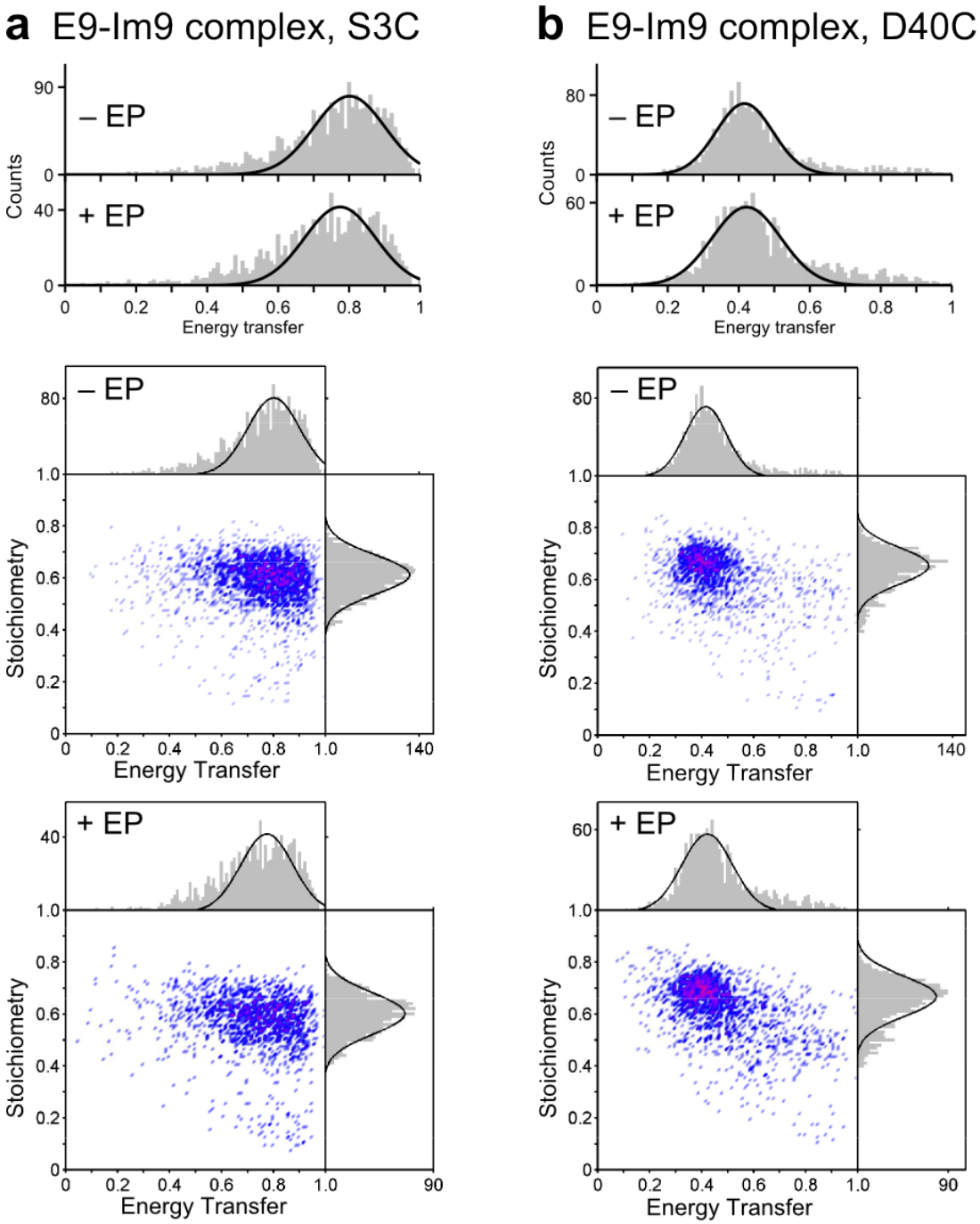

Figure 4.23: *In vitro* single-molecule FRET studies of E9-Im9 complex before and after electroporation. **a.** Complex E9(S3C-Alexa647)-Im9(S81C-Cy3B) showed single-molecule FRET distributions centered at E*=0.8±0.10 ('– EP') and E*=0.77±0.10 ('+ EP'). **b.** Complex E9(D40C-Alexa647)-Im9(S81C-Cy3B) showed single-molecule FRET distributions centered at E*=0.42±0.08 ('– EP'), and E*=0.42±0.10 ('+ EP'). Expected FRET values from crystal structures and dye cloud modelling (102) yield E*=0.75, S3C labelling scheme, and E*=0.45, D40C labelling scheme. No effects of electroporation on the FRET distributions were observed and the experimental *in vitro* FRET efficiencies were in very good agreement with expected FRET values.

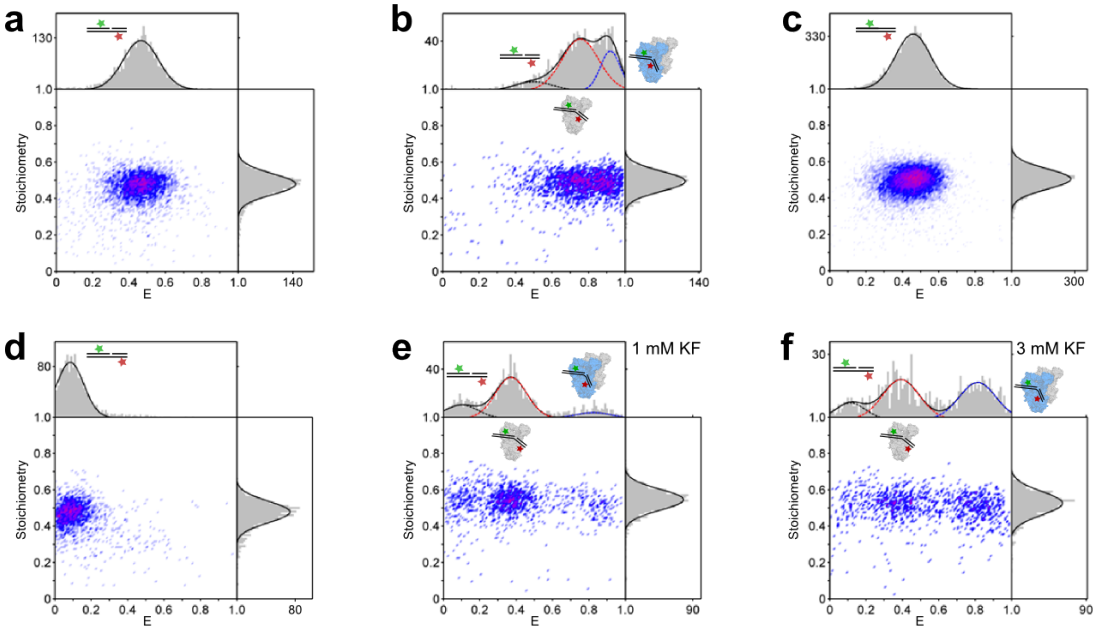

Figure 4.24: FRET histograms of *in vitro* controls for gapped DNA bending assay. **a.** Gapped DNA only, E=0.47±0.10. **b.** Gapped DNA in presence of 3 mM KF(DNA Pol I) showing three FRET species, $E_{\text{gapped DNA}}$=0.50±0.10, $E_{\text{bend DNA}}$=0.75±0.10, and $E_{\text{dimer formation}}$=0.92±0.05. **c.** Duplex DNA only, E=0.46±0.10. d-f. Dimer formation assay *in vitro*. **d.** *In vitro* control of gapped DNA only, $E_{\text{gapped DNA}}$=0.08±0.07. **e-f.** *In vitro* control of gapped DNA in presence of 1 mM and 3 mM KF(DNA Pol I) resulting in 3 FRET species, free three Gaussian fitting resulted in $E_{\text{gapped DNA}}$= 0.11±0.08, $E_{\text{bend DNA}}$=0.39±0.10, and $E_{\text{dimer formation}}$=0.81±0.10 in presence of 3 nM KF. *In vivo* and *in vitro* FRET values are in very good agreement for gapped DNA bending assay, showing DNA bending *in vivo*, however only less than 12% dimer formation was observed *in vivo*.

Chapter 5

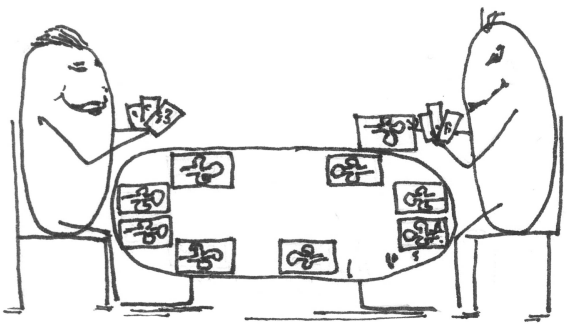

Mobility and spatial distribution of tRNA in live bacteria

The work presented in this chapter is prepared for publication in

- A Plochowietz, I Farrell, Z Smilansky, BS Cooperman, and AN Kapanidis. Single-molecule tracking of tRNA shows that most tRNA diffuses freely in live bacteria. *Nucleic Acid Res*, in revision.

5.1 Introduction

Studying the localisation of single RNA molecules in living cells is important for understanding the spatial organisation of gene expression (191). The non-uniform distribution of RNA molecules is an important mechanism to spatially control translation and efficiently alter local protein concentrations. Local enrichment of RNA molecules has been observed for different mRNAs in both eukaryotic cells (yeast, oocytes, neurons) (192, 193) and, unexpectedly, even in bacteria (194).

Most of these studies are performed at the cellular level, precluding observation of individual mRNA molecules and measurement of molecular heterogeneity. As I have presented in chapter 1, single-molecule fluorescence is an important tool to report

on such heterogeneous localisation patterns and is thus ideally suited for studying RNA distributions in living cells. Initial studies to visualise single mRNA molecules in cells employed fluorescence *in situ* hybridisation (FISH) in fixed cells (195). *In vivo* studies of mRNA dynamics became possible by tagging mRNA with fluorescent proteins (FP) fused to the bacteriophage MS2 coat protein and its variants (PP7 system) (196, 197), or to the human U1A protein (198), which directly bind to a specific RNA hairpin sequence. However, as mentioned in previous chapters 2-3, FPs are less bright and photostable than organic fluorophores (44, 45) and thus more than 24 copies of MS2 binding sites accommodating 48 GFPs were needed to localise single mRNA molecules (199), making it a very bulky label (200x5x3 nm) that might perturb mRNA interaction. Tracing the localisation of singly-labelled mRNA molecules in living cells has been demonstrated using organic fluorophores. These were either tagged to the coat protein via a polypeptide linker (SNAP tags (200, 201)), or directly bound to RNA aptamers (202, 203). Using aptamer RNA labelling, single mRNA molecules could be traced throughout mammalian cells (204).

Another RNA species important for translation is transfer RNA (tRNA), which is a short and stable RNA (74-93 nt in length) that act as the adapter molecules between the nucleotide sequence in a mRNA and the amino-acid sequence in a protein. The transfer RNAs exhibit a distinctive 'three-leafed clover' structure formed by three hairpin loops. One hairpin loop contains the anti-codon sequence (three-nucleotide sequence), which can decode the mRNA codon. On the other end of the tRNA, a specific amino acid is attached (each type of tRNA can only hold one type of amino acid) and thus, when the tRNA is binding to the mRNA codon at the ribosome, the appropriate amino acid is added to the growing polypeptide chain. Despite the obvious importance of tRNA in translation, its intracellular mobility and subcellular localisation remained unexplored until now. This could be due to the difficulty of endogenously labelling tRNA with common methods, since large RNA hairpin sequences, accom-

modating coat proteins or aptamers attached to tRNA molecules (74-93 nucleotides) might alter tRNA function in protein synthesis. However, tRNA molecules have been labelled *in vitro* by either derivatisation of the charged amino acid (205), or via covalent attachment of fluorophores to modified nucleosides with unique chemical reactivity (206, 207, 208, 209, 210, 211). The abundant dihydrouridine (DHU) position in the D-loop of tRNA was utilised to attach proflavine (212, 213, 214, 215) or, as used in this study, to introduce hydrazides for cyanine dye labelling (216). Thus, tRNA dynamics during elongation were studied *in vitro* using single-molecule fluorescence imaging (207, 217) and single-molecule Förster resonance energy transfer (FRET) on labelled tRNA and ribosomes (210, 218). Recently, single-molecule FRET and multi-color single-molecule fluorescence assays of labelled tRNA and labelled ribosomes were developed *in vitro* (201), elucidating translational dynamics in great mechanistic detail in real-time (219, 220).

In fixed cells, snapshots of pre-translocation and post-translocation sub-states of tRNA movement at the ribosome were revealed using electron cryomicroscopy (221). In addition, protein synthesis was visualised in fixed mammalian cells using organic-dye labelled tRNAs (Cy3, Cy5) exhibiting FRET signals when being bound at adjacent ribosomal sites (222, 223).

To date, there are no reports on single tRNA localisations and their interactions at the ribosomal complex during translation in live cells. However, the distribution of ribosomes have been studied using super-resolution imaging techniques (26, 4) in live bacteria showing the exclusion of ribosomes from the cell nucleoid (224). Further studies have shown that ribosomal subunits S30 and S50 can penetrate the entire cell and are not excluded from the nucleoid (225). A co-translational transcription mechanism was proposed upon the observation of the tight control of the elongation rate of transcription by translation (226), which was recently supported by clusters of dense transcription sites at the nucleoid periphery (227), very similar to ribosome

enrichment at the cell periphery (224, 228).

Thus, tRNA localisation, the spatial distribution of tRNA molecules in live bacteria, and the way tRNA localisation fits into the bigger picture of nucleoid segregation and co-translational transcription mechanism are of great interest. Until now, single-molecule fluorescence studies of organic-dye labelled tRNA in live bacteria were mainly limited due to the difficulty of internalising exogenously labelled tRNA molecules through the bacterial cell wall and membrane while maintaining cell viability.

In this chapter, I employed the previously established electroporation protocol (chapter 3) to internalise organic-dye labelled RNA into live *E. coli*, showing efficient loading of a 25-mer ssRNA-Cy5 and bulk *E. coli* tRNA labelled with Cy3, Cy5, or Cy5.5. Counting the number of molecules per cell, I was able to employ single-molecule fluorescence imaging and localised single tRNA molecules in live bacteria. Using single-particle tracking (28, 43, 115), I traced individual tRNA molecules in live cells. I observed two modes of diffusion: a fast diffusing species (assigned to free tRNA), and a slow diffusing species (assigned to bound tRNA at the ribosome), and I measured the diffusion coefficient of free tRNA in live *E. coli*. Transfer RNA molecules displayed a non-uniform distribution within bacterial cells, in which bound tRNA molecules localised predominantly at the cell periphery; very similar to the spatial distribution of ribosomes. Antibiotic treatments and controls showed that the uneven tRNA distribution was translation-dependent, supporting the idea of the exclusion of ribosomal complexes from the nucleoid and the co-translational transcription mechanism (226, 229).

5.2 Efficient internalisation of bulk *E. coli* tRNA

5.2.1 Proof-of-principle and cell loading

First, I investigated whether organic-dye labelled short RNA molecules could be internalised into live *E. coli* using electroporation, similar to previous studies showing efficient internalisation of 45-bp dsDNA fragments (chapter 3, sec. 3.3.2), small protein subunits (chapter 3, sec. 3.4.2), and proteins of up to 100 kDa (62). Bulk *E. coli* tRNA (hydrodynamic radius, R_h = 2.6 nm, SI 5.4.1) and short 25-mer ssRNA are both smaller than previously internalised 45-bp dsDNA molecules (62, 141). Additionally, I stabilised the negatively-charged RNA by adding 1 mM EDTA to the electroporation buffer, since this had been proven to stabilise and helped to internalise DNA into live bacteria (chapter 3, sec. 3.3.1). I initially selected the hydrazide dyes Cy3, Cy5, and Cy5.5 as fluorophore labels for tRNA single-molecule fluorescence studies, due to their availability from collaborators[1], and their high brightness, measured in chapter 4 (sec. 4.2), which is a prerequisite for single-molecule localisation above the cellular background. Then, I further evaluated their performance in single-particle tracking studies. Organic dye-labelled bulk *E. coli* tRNA molecules (Fig. 5.1a) and 25-mer ssRNA fragment were electroporated into electrocompetent *E. coli* DH5α cells (SI 5.7.2) and imaged under highly-inclined and laminated optical sheet (HILO) illumination (111) in the respective fluorescence channel (Fig. 5.1b).

I showed that bulk *E. coli* tRNA molecules labelled with Cy3, Cy5, and Cy5.5, and short ssRNA-Cy5 could be efficiently internalised into bacterial cells using electroporation (Fig. 5.1c). For all samples, electroporated cells showed higher intra-cellular fluorescence than non-electroporated cells (Fig. 5.1c, SI Fig. 5.13). The internalisation efficiency was calculated relative to the non-electroporated cell control where labelled RNAs were added, not electroporated, and washed and recovered like the

[1] collaboration with Ian Farrell, Barry Cooperman (Chemistry, UPenn), and Zeev Smilansky (Anima Inc.).

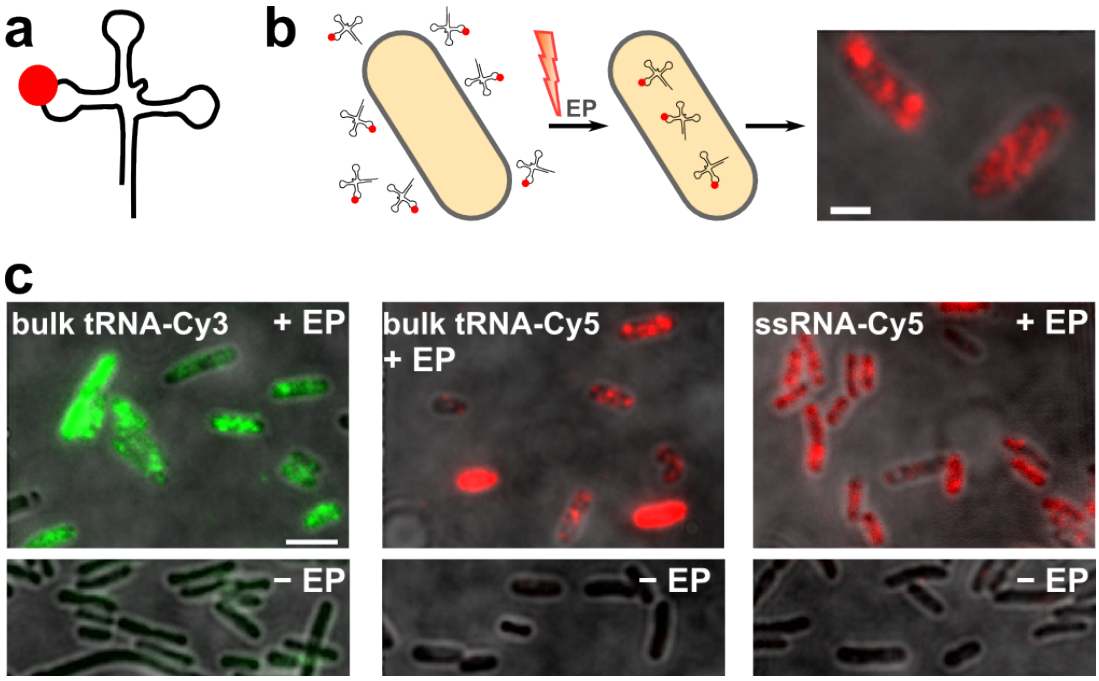

Figure 5.1: Internalisation of labelled tRNA molecules into live *E. coli*. **a.** Labelling schematic of example tRNA molecule. **b.** Schematic of the internalisation method using electroporation (EP). Labelled tRNA molecules were added to the cell suspension of electrocompetent cells and were exposed to the discharge of a high-voltage electric field. Cells were quickly recovered and non-internalised tRNA molecules were washed off. Cell imaging was carried out on an inverted microscope using HILO illumination (Appendix A.1). Scale bar: 1 µm **c.** Efficient loading of *E. coli* cells with tRNAs labelled with organic fluorophores of different spectral range. Cells showed high inner-cell fluorescence upon electroporation with 1 µM of tRNA-Cy3, -Cy5, and ssRNA-Cy5 (top row, left to right) and basal fluorescence of non-electroporated cells corresponding to cellular autofluorescence in the respective spectral channel (bottom row). More than 85% of cells were loaded when internalising tRNA-Cy3, tRNA-Cy5, and ssRNA-Cy5 (more than 500 cells per data set). Scale bar: 3 µm.

electroporated sample. More than 85% of cells showed significant uptake of tRNA-Cy3, tRNA-Cy5, and ssRNA-Cy5 (Fig. 5.1c, left to right), and $>$ 60% of cells were loaded with tRNA-Cy5.5 (SI Fig. 5.13).

5.2.2 Electroporation of tRNA and cell viability

I used the previously optimised electroporation conditions for nucleic acid internalisation (chapter 3, sec. 3.3), and showed that RNAs were not perturbed. Therefore, I ran the electroporated 25-mer ssRNA-Cy5 and tRNA-Cy5 samples on a native polyacrylamide gel and imaged them on a gel scanner. I observed very similar bands in shape

and intensity for the non-electroporated and electroporated samples and no sample aggregates were left in the wells (Fig. 5.2a). Thus, I reasoned that electroporation is not affecting the dye label and structure of ssRNA fragment and bulk *E. coli* tRNA. In addition, a reverse phase HPLC (Fig. 5.2b) was run by Anima Inc. showing similar retention time and peak shape for tRNA after labelling (black), tRNA purified after labelling but not electroporated (blue), and purified and electroporated tRNA (red), which was also a good indication that the tRNA molecules did not aggregate during electroporation.

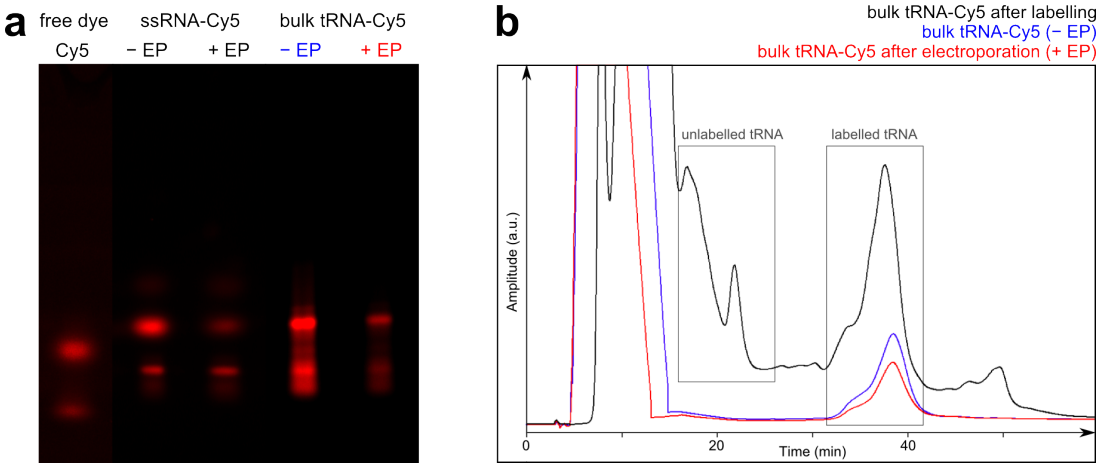

Figure 5.2: Single-stranded RNA, and tRNA show no structural changes after electroporation. **a.** Native PAGE of ssRNA-Cy5 and bulk *E. coli* tRNA-Cy5 show similar bands before and after electroporation; no ssRNA, and tRNA was aggregated in wells. **b.** Reverse phase HPLC of bulk tRNA-Cy5 after labelling (black), non-electroporated tRNA-Cy5 (blue), and electroporated tRNA-Cy5 (red) show similar retention time and peak shape. The reverse phase HPLC was performed by Dr. Ian Farrell.

Next, I studied the cell viability of cells electroporated with 1 µM of bulk *E. coli* tRNA-Cy5 similar to previous studies on the internalisation of dsDNA (chapter 3, sec. 3.3.2). Again, I monitored the growth and division of single cells in time-lapse brightfield images over the course of 2 h (Fig. 5.3). As in the previous study (141), I observed more than 60% of growing and dividing cells (15 out of 24 cells) and concluded that the internalised tRNA molecules did not affect cell viability.

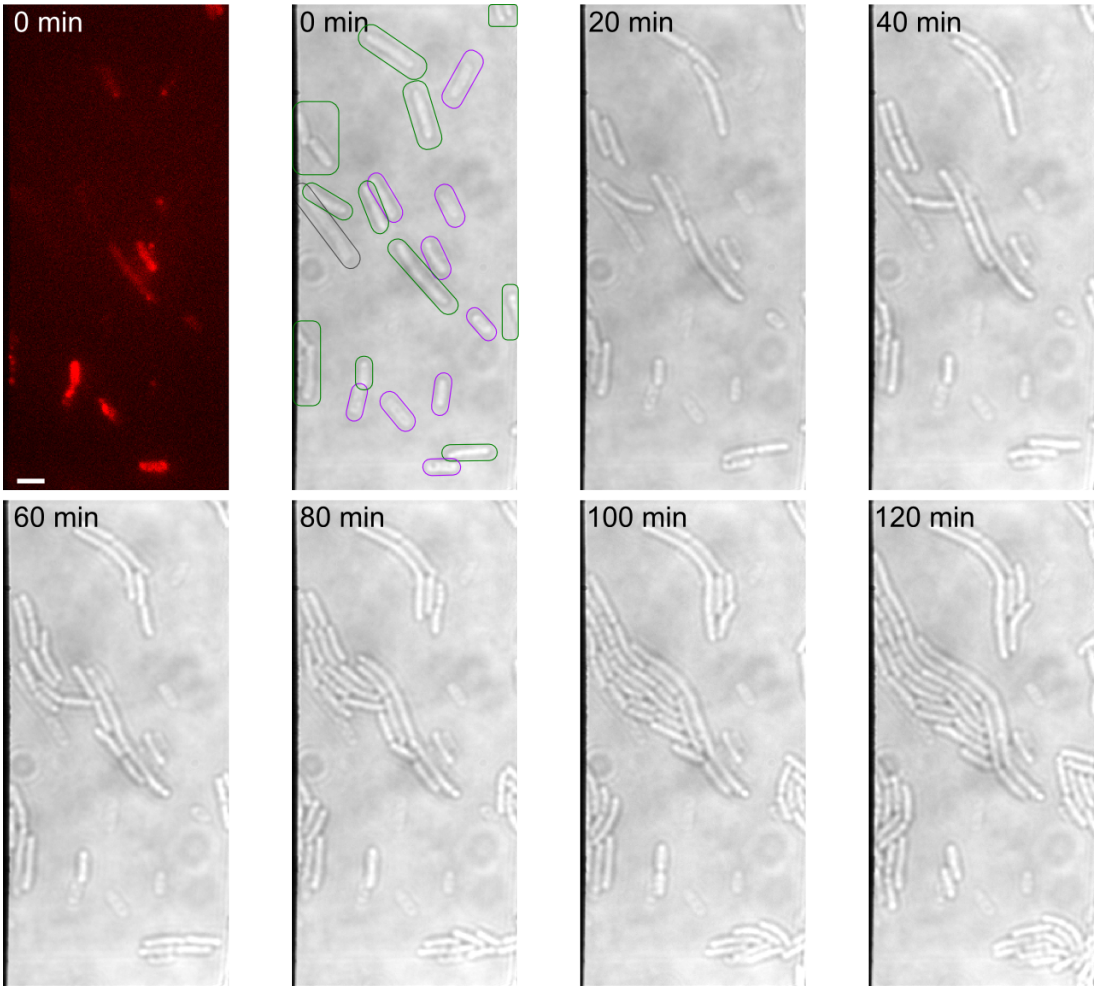

Figure 5.3: Cell viability assay. Cell growth and division was followed on agarose pads at 37 °C for 2 h. Cells were categorised as growing and dividing (green), not growing (purple), and damaged (black). I obtained more than 60% of growing and dividing cells when internalising tRNA molecules at 1 µM initial concentration using 1.4 kV initial electroporation voltage. This is in very good agreement with previous studies on the electroporation of 45 bp dsDNA fragments (chapter 3, sec. 3.3.2). Scale bar: 3 µm.

5.3 Counting the number of internalised tRNA molecules per cell

5.3.1 Counting single tRNA molecules

To perform single-molecule fluorescence studies *in vivo*, I characterised the amount of internalised tRNA molecules per *E. coli* cell. Specifically, I employed single-cell

photobleaching studies as introduced in chapter 4 (sec. 4.2.1) to count individual tRNA-Cy5 molecules per cell and controlled the number of tRNA molecules per cell down to the single-molecule level.

Again, I measured the photobleaching decay of the overall cellular fluorescence of individual cells and obtained single-cell photobleaching time-traces, Fig. 5.4. For example, one cell was loaded with a single Cy5-labelled tRNA molecule (red false-coloured single molecule signal, Fig. 5.4a), which photobleached at about 5 s and resulted in the loss of the fluorescence signal. The time-trace of fluorescence intensity over time showed distinct single-step drops of the overall cellular fluorescence, which could be attributed to the photobleaching of a single organic fluorophore (blue: single-cell intensity time-trace, Fig. 5.4a), and were used to relate the number of photobleaching steps to the number of internalised tRNA-Cy5 molecules per cell. The single-cell photobleaching time-traces were fitted using Hidden Markov Modelling (HMM, chapter 4, SI 4.7.5) to obtain the unitary intensity for each single-molecule photobleaching step (HMM fit in red, gray bar highlights unitary intensity, Fig. 5.4a). Single-cell photobleaching time-traces from tRNA-Cy5 experiments (50 nM tRNA-Cy5 in electroporation buffer) showed distinct step-like behaviour (N=160, Fig. 5.4b), and HMM analysis revealed the internalisation of 1-3 molecules/cell (Fig. 5.4b, SI Fig. 5.14a). The unitary intensity for tRNA-Cy5 was obtained to 8.7 ± 2.4 a.u. corresponding to Cy5 brightness of about 8000 ph/s (Fig. 5.4c; tRNA-Cy3, and tRNA-Cy5.5 in SI Fig. 5.14b-c) under these illumination conditions (SI 5.7.5).

5.3.2 Working at the single-molecule and single-cell level

I next used the measured unitary intensity for each fluorophore to relate the overall cellular fluorescence to the number of internalised labelled tRNA molecules per cell. To be able to localise single tRNA molecules within the cells, I examined different initial concentrations of labelled tRNA-Cy5 in the cell suspension before electropora-

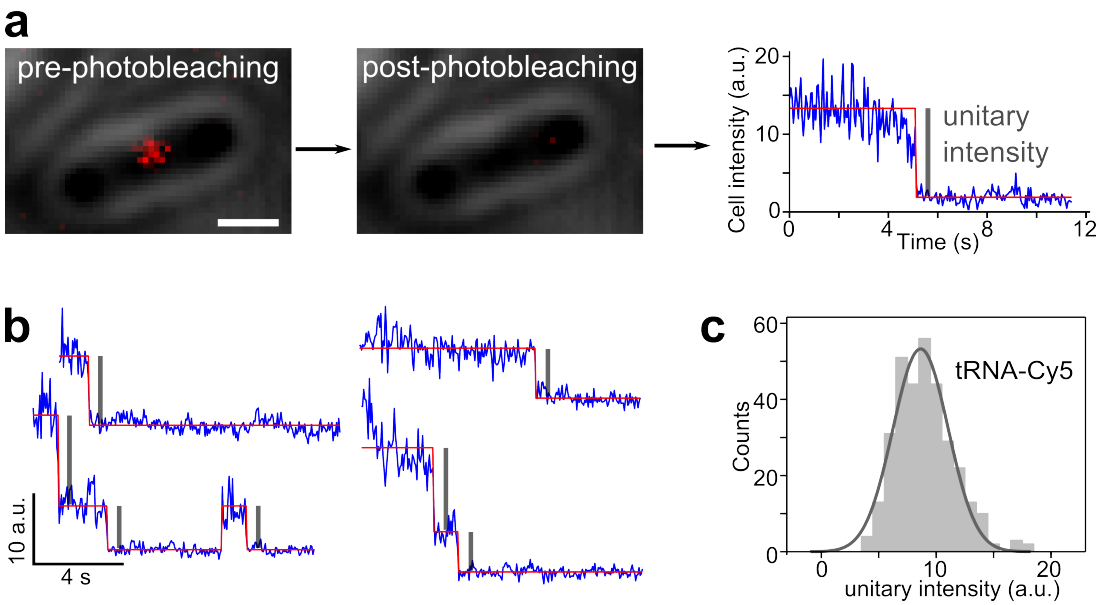

Figure 5.4: Counting the number of internalised tRNA molecules per cell. **a.** Single-cell photobleaching step analysis of tRNA-Cy5 in live bacteria. **b.** Photobleaching time-trace example (blue) and Hidden-Markov Model fit (red) of single photobleaching steps corresponding to the single-molecule unitary intensity (gray bars). **c.** Unitary intensity distribution of tRNA-Cy5 (160 photobleaching time-traces, 324 fitted single photobleaching steps = unitary intensity) and Gaussian fit centred at 8.7±2.4 a.u. corresponding to Cy5 brightness of 7500±2100 ph/s. Scale bar: 1 µm.

tion and counted the number of internalised tRNA molecules/cell. The internalisation histogram shows a wide distribution of internalised tRNA molecules/cell (Fig. 5.5). I observed two regimes: i. a single-molecule regime with 1-3 labelled molecules/cell (50-250 nM tRNA-Cy5: mean ∼1.5, median ∼1.0), and ii. a small ensemble regime with up to hundreds of molecules per cell (at 1 µM tRNA-Cy5: mean ∼140, median ∼100; SI Fig. 5.15 for tRNA-Cy3 and tRNA-Cy5.5).

Next, I used single-cell photobleaching studies of cells in the small ensemble regime (∼100 molecules/cell) and measured the decay of the fluorescence signal over time to obtain the photobleaching lifetime of the fluorescent dye *in vivo* under these illumination conditions. I obtained photobleaching lifetimes for the different fluorescent dyes of several seconds (SI Fig. 5.16, Cy5: 3.4±1.1 s, Cy3: 21.4±5.8 s, and Cy5.5: 4.6±1.5 s). The photobleaching lifetime defines the observation time of single tRNA molecules. In bacteria, tRNA molecules deliver 10-20 amino acids to the ribosome

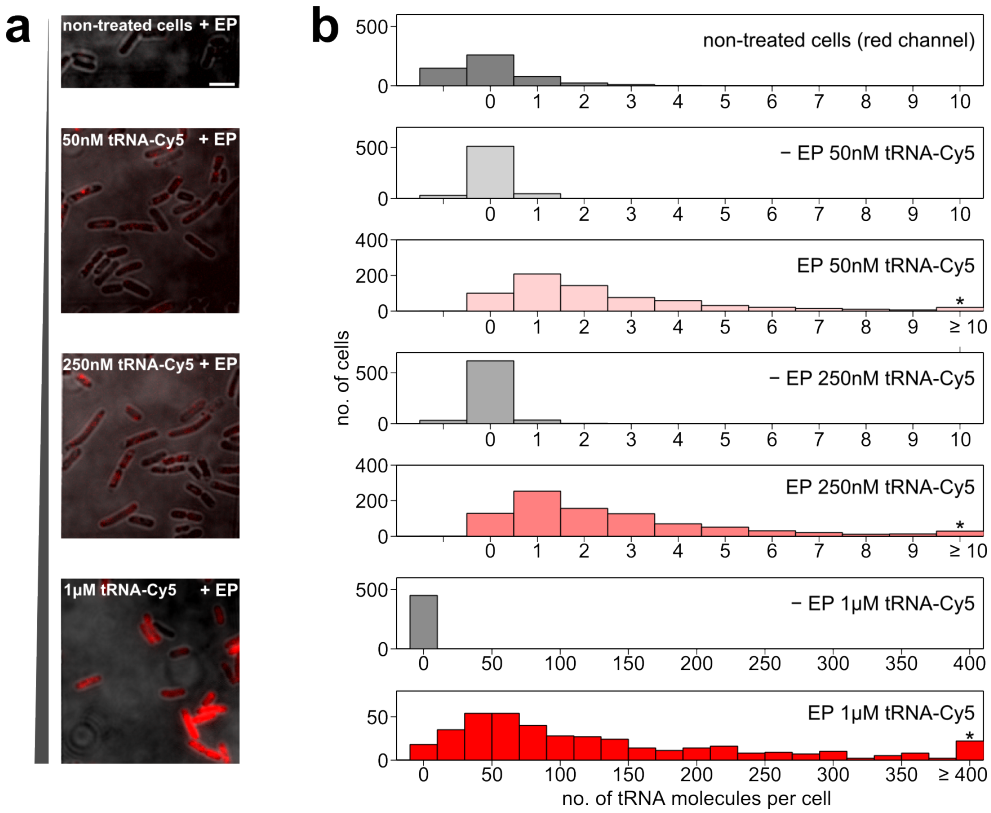

Figure 5.5: Controlling the number of internalised tRNA molecules per cell. Investigating the number of internalised tRNA-Cy5 molecules per cell at different concentration of labelled tRNA-Cy5 in cell suspension before electroporation. **a.** Example fields-of-view. **b.** Cells were loaded with 1-10 tRNA molecules when adding 50 nM tRNA-Cy5 (mean: 1.4 molecules per cell, median: 0.9), and up to 250 nM tRNA-Cy5 (mean: 1.5 molecules per cell, median: 1.0) in the cell suspension before electroporation, which is an ideal regime for single-molecule studies. Cells were loaded with about 100 tRNA molecules per cell (mean: ∼140, median: ∼100, SI Fig. 5.15 for tRNA-Cy3, and tRNA-Cy5.5) at 1 µM tRNA-Cy5 initial concentration before electroporation. Negative values result from background subtraction. Scale bar: 3 µm.

per second (230, 231), and thus a short polypeptide chain can be synthesised in our observation time, which cannot be explored with fluorescent proteins showing an observation time of 50 ms at similar conditions (115).

To summarise my initial characterisation experiments: I used an initial concentration of 50 nM tRNA-Cy5 in the electroporation buffer for all further single-molecule fluorescence localisation studies due to the average cell loading of about 1 tRNA molecule per cell resulting in a molecule density of less than 1 molecule/µm^2, which is ideal for single-molecule localisation experiments (187). I also chose Cy5 as the fluores-

cent label due to its high brightness of about 8000 ph/s, and the decreased cellular autofluorescence in the red fluorescence channel (232, 141).

5.4 The diffusion coefficient of tRNA molecules in live *E. coli*

Subsequently, I worked in the single-molecule regime and I studied tRNA localisation and the diffusive behaviour of tRNA molecules within the cellular cytoplasm. Initially, I estimated the expected diffusion coefficient for free tRNA molecules to be in the same range as for FPs. Next, I measured the apparent diffusion coefficient of tRNA-Cy5 using single-particle tracking and simulated Brownian motion within the confined cellular volume to related the experimentally-obtained apparent diffusion coefficient to an accurate diffusion coefficient.

5.4.1 Expected mobility of free tRNA and ternary complex

I expected the diffusion of unbound tRNA-Cy5 molecules to be similar to the fast diffusion of fluorescent proteins in the range of 6-13 $\mu m^2/s$ due to their similar hydrodynamic radius. Transfer RNA molecules range between 76-92 nucleotides with an average molecular weight of about 25 kDa. While the hydrodynamic radius of yeast $tRNA^{Phe}$ was predicted from the crystal structure based model to 2.6 nm and experimentally measured between 2.67 nm (ultracentrifugation), 2.73 nm (dynamic light scattering), and 2.8 nm (gel filtration) (233, 234), the hydrodynamic radius of GFP was determined to be 2.4 nm (235). The molecular weight of fluorescent proteins (FP) and their variants ranges between 26 kDa (mEos2), and 27 kDa (GFP).

Estimates of diffusion coefficients of unconjugated GFPs from fluorescence recovery after photobleaching studies range from $6.1 \pm 2.4\,\mu m^2/s$ (236), $7.1 \pm 0.3\,\mu m^2/s$ (237),

$7.7\pm2.5\,\mu m^2/s$ (238), and $9.8\pm3.6\,\mu m^2/s$ (239); a comprehensive list with different experimental conditions can be found in Nenninger *et al.* (240). Recently, a coarse-grained model of the *E. coli* cytoplasm and protein diffusion simulations, yielded a diffusion coefficient of $6.5\pm0.5\,\mu m^2/s$ for GFP (241). However, single-molecule tracking studies obtained slightly higher diffusion coefficient estimates of FPs *in vivo*, such as $8\,\mu m^2/s$ (Venus, (40)), $10\,\mu m^2/s$ (Dendra2, (225)), and $12.5\,\mu m^2/s$ (mEos2, (43)). From the inverse relation of the diffusion coefficient and hydrodynamic radius, I expected the diffusion coefficient of freely diffusing bulk tRNA about 10% smaller than for FPs and thus in the 5.5-11.5 $\mu m^2/s$ range in live *E. coli*.

Due to the tight binding (dissociation constant: $K_d \sim 200$ nM, (242)) of aminoacyl-tRNA (charged with amino acids) to elongation factor EF-Tu-GTP, forming the ternary complex, and the observation of the direct transfer from aminoacyl-tRNA synthetase to the elongation factor to the ribosomes (tRNA channelling) during protein synthesis in eukaryotic cells (243, 244, 245), it was often assumed that such a channelling mechanism exists in bacterial systems, too. To test the tRNA channelling hypothesis in bacteria and proposed rapid association of free tRNA to the ternary complex, I estimated the diffusion coefficient of the ternary complex. Due to similar size of the ternary complex and the nucleoid-associated protein Fis (246, 247), I estimated the accurate diffusion coefficient of the ternary complex to be about $4.5\,\mu m^2/s$, which was previously measured for the accurate diffusion coefficient of Fis by Uphoff *et al.* (115).

5.4.2 Single-particle tracking of tRNA-Cy5

To capture the expected fast diffusion of single tRNA molecules *in vivo*, I used stroboscopic illumination, in which I excited the cells for 1 ms at high laser powers, but exposed the camera for 5 ms (SI 5.7.3). Using the stroboscopic illumination scheme, I obtained bright diffraction-limited images of single tRNA molecules (point spread function, PSF) within live *E. coli* cells (Fig. 5.6a, t=0 s). A single tRNA molecule was

localised and linked within consecutive frames to generate a single-molecule trajectory (Fig. 5.6a, yellow trajectory at t=0.6, 0.9, 1.2 s, SI 5.7.6). These snapshots from single-molecule fluorescence movies, illustrate how single tRNA molecules explored most of the cellular environment over time (Fig. 5.6a). More trajectories are shown in Fig. 5.7a. I captured numerous of such single-molecule trajectories (N=4122) and calculated the mean-squared displacement (MSD) of tRNA molecules that were tracked in more than 3 consecutive frames. The MSD of tRNA-Cy5 *in vivo* (Fig. 5.6b, blue) and in fixed cells (black) plateau due to cellular confinement, motion blurring, and localisation precision (117). Using the plateau level of the fixed cell control, I estimated the localisation precision to be 40 nm under these experimental conditions.

Next, I calculated an apparent diffusion coefficient (D_{app}) from the MSDs of individual trajectories that were truncated to 4 steps; (115, 227) and SI 5.7.7. The D_{app}-histograms for tRNA-Cy5 *in vivo* studies showed a bimodal distribution (Fig. 5.6c and Fig. 5.7c). As expected, the diffusion coefficient distribution could be fit by two diffusive species (Fig. 5.6c), and thus, I reasoned that tRNA molecules could be either freely diffusing or bound to elongation factor thermo unstable (EF-Tu, recruiting tRNA to the ribosomal binding site), or to larger protein complexes such as tRNA-synthetase (loading of tRNAs with amino acids) and the ribosomal complex during translation (207). The inset in Fig. 5.6c shows single-molecule trajectories categorised as mobile trajectories (blue) and bound trajectories (red).

Hence, I fitted the D_{app}-distribution to two Gamma-distributions; mobile: D_{app}=3.6 µm^2/s, bound: D_{app}=0.5 µm^2/s, which was initially constrained to the ribosomal diffusion rate previously measured using similar experimental settings (43). Similar results were obtained when constraining the bound species to immobile molecules of the fixed cell control (mobile: D_{app}=3.61 µm^2/s, bound: D_{app}(fixed cells)=0.32 µm^2/s constrained, Fig. 5.7b,f-g) or when allowing a free fit to a single Gamma-distribution (mobile: D_{app}=3.6 µm^2/s, Fig. 5.7h-i). I also fitted the apparent diffusion coefficient distribu-

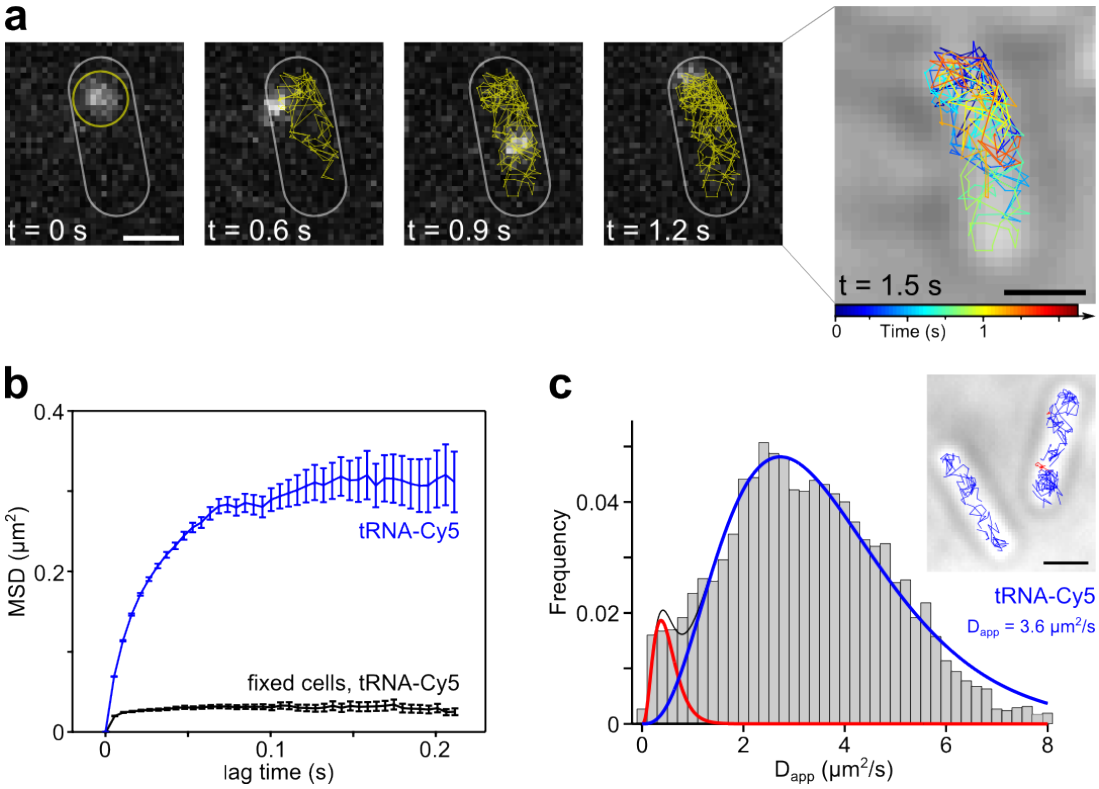

Figure 5.6: Single-molecule tracking of tRNA-Cy5 and measurement of diffusion coefficient of tRNA *in vivo*. **a.** Tracking of a single tRNA-Cy5 molecule for about 1.5 s and reconstruction of the single-molecule trajectory in the bacterial cell. **b.** Measurement of the mean-squared displacement (MSD) for tRNA-Cy5 in live cells (blue) and fixed cells (black). The MSD plateaued due to cellular confinement and motion blurring in live cells and due to the localisation precision of about 40 nm in fixed cells. **c.** Apparent diffusion coefficient distribution of tRNA-Cy5 and fit to 2 diffusive species. Inset: highlighting mobile (blue) and bound (red) trajectories in two cells (overlay with brightfield image). The slow diffusive species was constrained to ribosomal complex diffusion of D_{app}(ribosome)=0.5 μm^2/s (red, (43)) and free Gamma-distribution fit of fast diffusing species resulted in D_{app}(tRNA-Cy5)=3.6 μm^2/s (blue). Similar fitting results were obtained when constraining the bound species to immobile molecules of the fixed cell control or when allowing a free fit to a single Gamma-distribution (Fig. 5.7). Including another independent data set, the apparent diffusion coefficient of tRNA in live cells was obtained to D_{app}(tRNA-Cy5, live cells)=3.5±0.2 μm^2/s (Fig. 5.7c). Scale bar: 1 μm.

tion with two species constrained to ribosomal diffusion (red) and ternary complex diffusion (D_{app}=2.4 μm^2/s, green) and one free species (Fig. 5.7d-e) to obtain an estimate of tRNA molecules associated in the ternary complex. I still obtained results in which about 70% of molecules show fast diffusion (D_{app}>3.5 μm^2/s), showing that the majority of tRNA molecules are freely diffusing.

I finally obtained the apparent diffusion coefficient of mobile bulk *E. coli* tRNA molecules to D_{app}(tRNA-Cy5)=3.5±0.2 μm^2/s by constraining the bound species to ri-

bosomal diffusion from two independent data sets (Fig. 5.6c and Fig. 5.7c), and the fraction of bound to mobile tRNA molecules was calculated from the bimodal fit to 8±4% under the given experimental conditions.

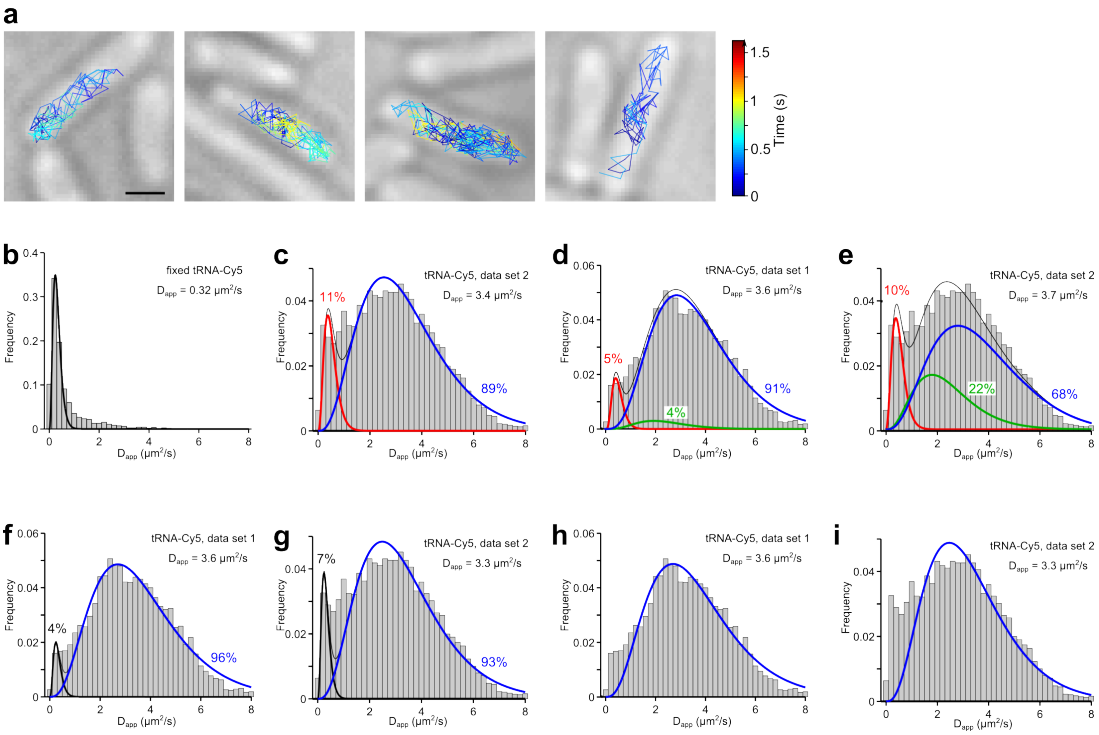

Figure 5.7: Single-molecule tracking of tRNA-Cy5 molecules and apparent diffusion coefficient measurement of tRNA-Cy5 *in vivo*. **a.** Further example single-molecule trajectories showing individual mobile tRNA molecule diffusing throughout the entire cell. Scale bar: 1 µm. **b.** Apparent diffusion coefficient distribution of fixed cell control, fitted to single Gamma-distribution, and obtaining an apparent diffusion coefficient for immobile species of D_{app}=0.32±0.16 µm^2/s (black). **c.** Data set-2 for tRNA-Cy5 apparent diffusion analysis fitted with two Gamma-distributions, of which the slow diffusing species was constrained to ribosomal diffusion (D_{app}=0.5 µm^2/s, red). **d-e.** Data set-1 and data set-2 fitted with three Gamma-distributions, of which two Gamma distributions were constrained to ribosomal diffusion (red) and diffusion of the ternary complex (D_{app}=2.4 µm^2/s, green). **f-g.** Data set-1 and data set-2 fitted with 2 Gamma-distributions, of which the slow diffusive species was constrained to fixed cell control (black). **h-i.** Data set-1 and data set-2 fitted to a single Gamma-distributions, not constrained. The apparent diffusion coefficient for tRNA-Cy5 was obtained to 3.5±0.2 µm^2/s and the overall result was not altered by the different fitting modes. The fraction of bound to mobile tRNA molecules was calculated to 8±3% (mean±std of 2 independent data sets).

5.4.3 Accurate diffusion coefficient of tRNA

Since the apparent diffusion coefficient is affected by experimental conditions such as cellular confinement, motion blurring, and localisation precision (117), I chose

to simulate single-molecule particle tracking movies to relate the measured apparent diffusion coefficients to accurate diffusion coefficients *in vivo*. I simulated free Brownian motion of uniformly distributed tRNA molecules in a confined cellular environment mimicking the same experimental conditions and performed the same single-molecule tracking analysis as for the experimental data (SI 5.7.8; $\sim$1.5 molecules/cell, 500 cells for each simulation). Figure 5.8a shows simulated tRNA localisations from 500 cells in a unit cell showing that the simulated tRNA trajectories were uniformly distributed (dotted line). From simulated tracks, I again calculated apparent diffusion coefficient histograms (Fig. 5.8b, and SI Fig. 5.17) and I related the measured apparent diffusion coefficients with the actual diffusion coefficient input for the simulations (Fig. 5.8c). From the simulations I obtained an accurate diffusion coefficient of bulk *E. coli* tRNA of D_{acc}(tRNA) = 8.1(-1.0+0.5)µm^2/s (Fig. 5.8d).

To summarise: I traced single tRNA molecules inside live *E. coli* cells and observed two diffusive species, which I attributed to tRNA molecules bound to larger protein complexes and freely diffusing tRNA. I was able to show that more than $\sim$70% of tRNA molecules diffuse freely with an accurate diffusion coefficient of about $8\,\mu m^2/s$ under these experimental conditions.

5.5 Spatial distribution of tRNA molecules *in vivo*

Next, I was interested in the spatial organisation of the tRNA molecules and specifically if I could see different spatial distributions of tRNA molecules that I previously attributed to either freely diffusing or bound to ribosomes. Since the ribosomal diffusion of about 0.1-0.5 µm^2/s (43, 224) is extremely slow compared to the measured apparent diffusion coefficient of the tRNA molecules of $3.5\pm0.2\,\mu m^2/s$, I reasoned that individual tRNA molecules could be sorted into bound and mobile populations. I obtained a diffusion coefficient threshold of $D_{thresh}<1\,\mu m^2/s$ for bound molecules,

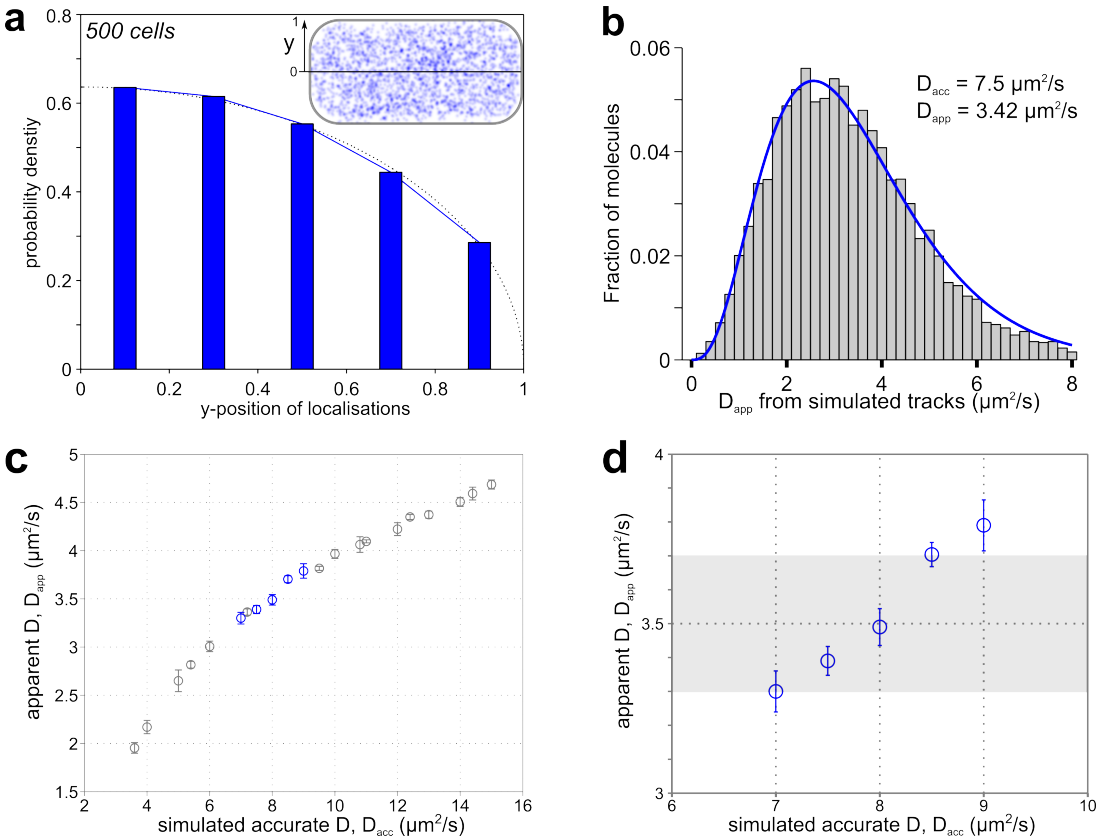

Figure 5.8: Simulation of Brownian motion in a confined cylinder-shaped container and single-molecule tracking analysis. Simulations of Brownian motion of on average 1.5 molecules/cell for 500 cells for 21 accurate diffusion coefficients. Simulated movies were analysed in the same manner as experimental single-particle tracking movies. **a.** Uniform distribution (dotted line) of simulated molecule localisations from 500 unit cells. **b.** Example apparent diffusion coefficient distributions from simulated trajectories from 500 cells with simulated accurate diffusion coefficient of 7.5 $\mu m^2/s$. **c.** Calibration plot of apparent diffusion coefficient after single-molecule tracking analysis relative to simulated accurate diffusion coefficients ranging between 3.6 $\mu m^2/s$ to 15.0 $\mu m^2/s$. **d.** Simulated accurate diffusion coefficient range that matched experimentally measured apparent diffusion coefficient interval of $3.5 \pm 0.2\,\mu m^2/s$ (highlighted in gray). Plotted in c-d. was mean$\pm$standard deviation of single species Gamma-distribution fit to 3 independent simulation runs.

such that 90% of all trajectories in the fixed cell control were categorised as bound (Fig. 5.7b). I used this apparent diffusion coefficient threshold to categorise tRNA molecule trajectories into a bound and mobile population and studied the spatial organisation of tRNA molecules classified as mobile and bound *in vivo*.

5.5.1 Non-uniform spatial distribution of tRNA molecules

To qualitatively evaluate the spatial distribution of mobile and bound tRNA molecules, I plotted the localisation of all tRNA molecules, tRNA molecules categorised as mobile (blue) and tRNA molecules categorised as bound (red) within a unit cell, normalising along cell-length and cell-width (Fig. 5.9a, SI 5.7.9). In the combined representation of mobile and bound molecules as well as for the mobile and bound species, I observed an enrichment of bound tRNA molecules at the cell periphery, whereas mobile molecules localised around the cell midline. To quantify the observation, each molecule localisation was normalised by its relative position along the short and long cell axis and the probability distribution for bound and mobile molecules was plotted along the unit cell width (Fig. 5.9b, cell periphery (gray), and mid-cell (beige)). Again, clear enrichment of bound tRNA molecule at the cell periphery and exclusion from mid-cell could be observed (Fig. 5.9b, bound population (red) relative to uniform distribution (dotted line): -23% at mid-cell, and +35% at cell periphery). Additionally, the mobile population localised predominantly along mid-cell (Fig. 5.9b, mobile population (blue) relative to uniform distribution (dotted line): +11% at mid-cell, and -19% at cell periphery); a similar trend was previously observed for the nucleoid-associated protein HU (bacterial DNA-binding protein, (225, 227)).

To validate the exclusion of bound tRNA molecules from mid-cell (cell nucleoid), I sorted cells along cell length (Fig. 5.9c, 700 cells, cell length distributions in SI Fig. 5.18). Specifically, I looked at short cells (1.7-2.9 µm), which I assumed constrained only a single chromosome, and long cells (3.1-4.3 µm) that were close to cell division with already replicated chromosomes. Looking at the distribution of tRNA localisations throughout all cell categories (Fig. 5.9c, probability heat maps), the localisation of bound tRNA at the cell periphery and mobile tRNA within the nucleoid was even more pronounced. For short cells, I again observed a clear tendency of bound molecules to localise to the cell periphery, whereas mobile molecules explore predom-

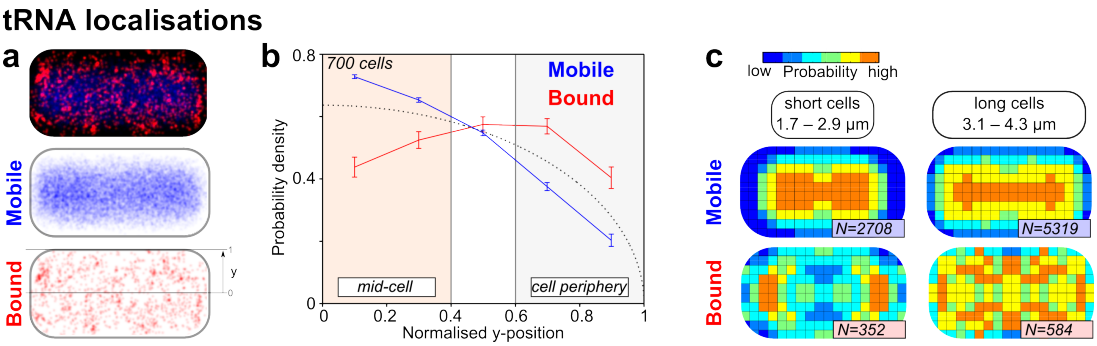

Figure 5.9: Spatial distribution of tRNA molecules in live bacterial cells. Localisations of tRNA-Cy5 molecules were normalised along cell-length and cell-width and were represented in a unit cell. **a.** Localisations of tRNA molecules classified as mobile (D_{app}>1 µm^2/s, blue) and bound (red) and combined (black background) were represented in unit cells, respectively. **b.** Probability distribution of mobile and bound molecules along cell width (y-axis, short cell axis). Bias of bound molecules to cell periphery and mobile molecules to mid-cell relative to uniform-distribution (dotted line); +11% mobile and -23% bound molecules within mid-cell (beige) and -19% mobile and +35% bound molecules in cell periphery (gray). **c.** Categorisation of tRNA localisations in unit cell for all cells, and different cell length (short cells: 1.7–2.9 µm, and long cells: 3.1–4.3 µm). Throughout all cell length tRNA molecules mainly diffuse freely (∼88% mobile versus ∼12% bound). Mobile tRNA localise predominantly at mid-cell, whereas bound tRNA molecules seem to be enriched at the cell periphery. Bound transfer RNA localisation pattern for short and long cells support their exclusion from the nucleoid, i.e. from compacted DNA in single chromosomes (short cells) and doubled chromosomes close to cell division (long cells).

inantly mid-cell, (Fig. 5.9c, middle column). The spatial distribution of mobile molecules within long cells looked similar to short cells, but two local maxima along the long cell-midline appeared, suggesting the presence of two chromosomes, of which bound tRNA molecules seemed again excluded and enriched at the cell periphery (Fig. 5.9c, right column). This result further supported the observation that mobile tRNA molecules could diffuse freely throughout the nucleoid, whereas bound tRNA molecules were localised at the cell periphery, suggesting the exclusion from the nucleoid. Notably, the fraction of bound to mobile tRNA molecules of 12±2% using a simple apparent diffusion coefficient threshold does not change throughout the cell cycle (13% and 11% for short and long cells, respectively), and is in good agreement with the result from the 2 species D_{app}-distribution fit of 8±3%.

Interestingly, the non-uniform localisation pattern of mobile and bound tRNA population, and the exclusion of bound tRNA molecules from the cell nucleoid at different

stages in the cell cycle could indicate tRNA being utilised in protein synthesis, since previous studies showed the exclusion of ribosomal complexes from the nucleoid and also an enrichment of highly transcribing RNA polymerase clusters at the cell periphery supporting the co-translational transcription mechanism (225, 227).

5.5.2 Blocking translation: change in tRNA spatial organisation

To probe the hypothesis of the translation-associated tRNA spatial distribution, I treated cells with the antibiotic Chloramphenicol (Cam) that blocks protein synthesis by binding to the 50S ribosomal subunit and inhibiting peptide bond formation and A-site binding of tRNA molecules (248). I performed the same analysis of the tRNA trajectories and first categorised tRNA molecules in mobile and bound population (Fig. 5.10a). Interestingly, bound tRNA molecules localised throughout the entire cell and the percentage of bound molecules in the cell periphery decreased significantly (from +33% down to +14%) upon Chloramphenicol treatment (Fig. 5.10b). In both short and long cells, I did not observe the localisation of bound tRNA molecules predominantly to the cell periphery any longer (Fig. 5.10c). Instead, following Cam treatment bound and mobile tRNA molecules localised throughout the entire cell following an even distribution. The loss of bound tRNA molecule species at the cell periphery suggested that the tRNA were not being used during protein synthesis any longer, which was blocked by Chloramphenicol.

Further evidence of translation-dependent localisation pattern of bound tRNA molecules at the cell periphery was obtained by studying the spatial distribution of (i) tRNA-Cy5 molecules in fixed cells (Fig. 5.11a), (ii) non-specific ssRNA-Cy5 molecules *in vivo* (Fig. 5.11b), and performing diffusion simulations (Fig. 5.8a). In all three controls, the single-molecule localisations spread through the entire cell area, where all internalised molecules were uniformly distributed, and no peripheral localisation pattern was observed for bound localisations. Interestingly, when blocking

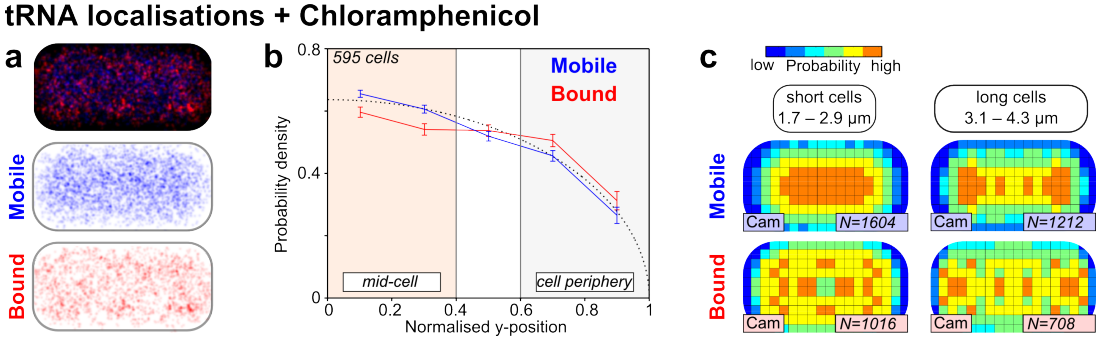

Figure 5.10: Spatial distribution of tRNA molecules upon Chloramphenicol treatment blocking translation. **a.** Representation of tRNA localisations classified as mobile and bound as in Fig. 5.9. **b.** Mobile and bound tRNA molecules were evenly distributed along cell width; +2% mobile and -8% bound molecules within mid-cell (beige) and +1% mobile and +15% bound molecules in cell periphery (gray) relative to uniform distribution (dotted line). **c.** Categorisation of tRNA localisations in unit cell for different cell length. Bias of tRNA molecules towards the cell periphery is lost upon Chloramphenicol treatment for all cell lengths categorisations.

transcription with Rifampicin, I again observed the increase of the bound tRNA fraction at the cell periphery and the more mobile species predominantly penetrating mid-cell (Fig. 5.11c) showing that the blocking of transcription does not significantly affect the spatial distribution of tRNA molecules within our observation time of about 1 h.

5.6 Discussion

To study the mobility and spatial distribution of labelled tRNA molecules in live bacteria, I modified the transfection protocol and efficiently internalised organic-dye labelled short ssRNA fragments and bulk *E. coli* tRNA into live bacteria. I counted the number of internalised tRNA molecules per cell and established single-molecule fluorescence imaging capability. Then, I localised single RNA molecules in live bacteria and measured the mobility of tRNA (accurate diffusion coefficient, D_{acc}=8.1(+0.5-1.0)µm^2/s) using single-molecule tracking and diffusion simulations. I continued by studying the spatial distribution of mobile and bound tRNA and observed an enrichment of bound tRNA molecules at the cell periphery. Antibiotic treatment disrupted

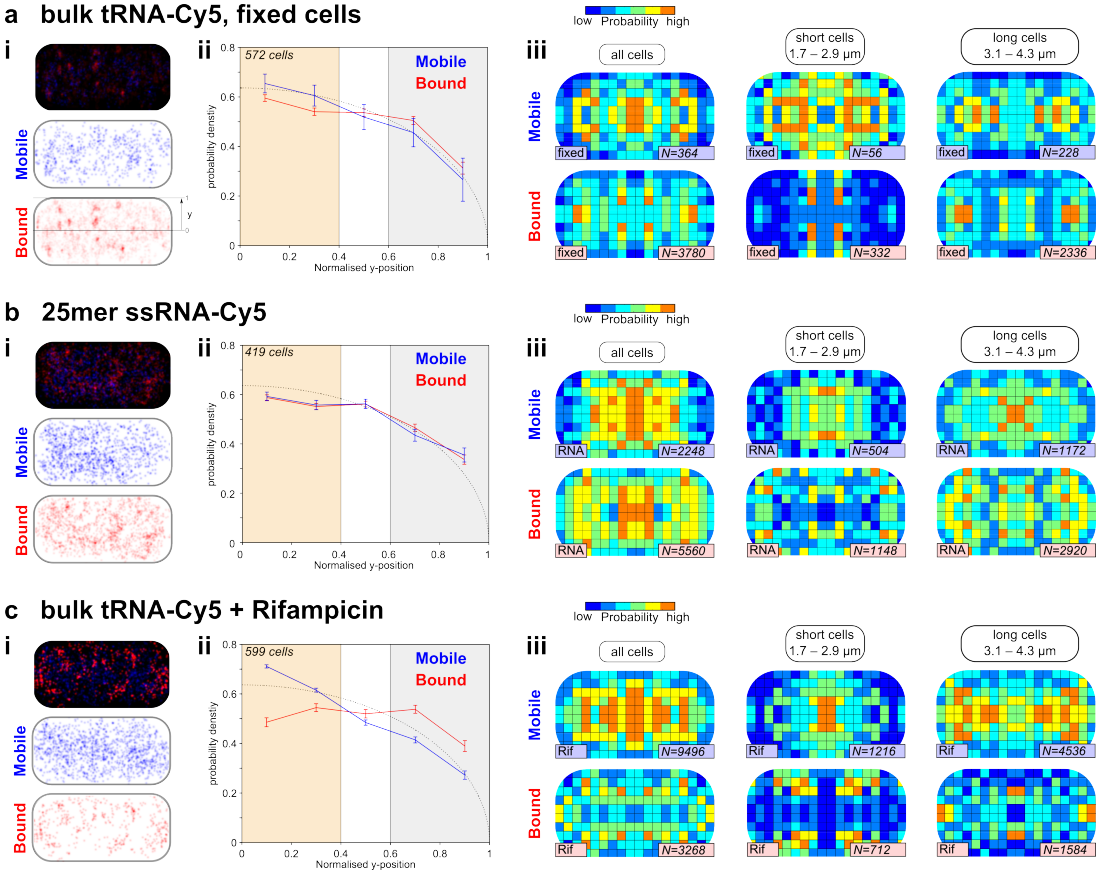

Figure 5.11: Interpreting the spatial distribution of tRNA molecules in live bacteria using **a.** fixed cell control, **b.** internalising unspecific 25mer ssRNA and **c.** Rifampicin treatment. Localisation of molecules were again normalised along cell length and cell width and were represented in a unit cell. **i.** Molecules were classified as mobile (D_{app} $>1\,\mu m^2/s$, blue), bound (red), and combined (black background). **ii.** Probability distribution of mobile and bound molecules along cell width (cell short axis). Bias of bound molecules at the cell periphery (gray) was still present after Rifampicin treatment but was lost otherwise. Mobile and bound molecules of fixed cells and unspecific RNA control were evenly distributed (dotted line). **iii.** Categorisation of localisations in unit cell for different cell length range (all cells, short cells: 1.7–2.9 µm, and long cells: 3.1–4.3 µm).

this specific localisation pattern, indicating that the spatial organisation is a feature of active translation.

Single RNA localisation in live bacteria

The efficient internalisation of RNA labelled with bright and photostable organic-dyes opens new research paths to study a large variety of RNA molecule types (short non-specific and specific ssRNA or dsRNA fragments, or stable RNA such as tRNAs) and

perform single-particle tracking in live bacteria. Labelling with small organic dyes is less perturbing to the RNA of interest than the introduction of the about 1000-fold larger “trains” of FPs fused to coat proteins to target RNA loop-sequences. Choosing an organic dye such as Cy3, Cy5, or Cy5.5 opens a wide spectral range (500 nm to 700 nm) for *in vivo* single-molecule fluorescence studies, which is of great interest due to the lower cellular autofluorescence especially in the red and infrared spectrum (249, 250).

I localised single tRNA molecules *in vivo*, which to my knowledge has not been observed so far, while working at the single-molecule level. When working at the small ensemble regime with up to hundreds of tRNA molecules/cell, other fluorescence imaging techniques such as fluorescent recovery after photobleaching (FRAP), or fluorescence correlation spectroscopy (FCS) studies could be employed to study tRNA diffusion *in vivo*. I also briefly examined the blinking behavior of Cy5-labelled tRNA molecules, in which hundreds of molecules were internalised, photobleached, and only one molecule at a time stochastically turned on again to gain single-molecule sensitivity. In Fig. 5.12 two time-traces of single-cell fluorescence intensity over time are shown exhibiting single molecule blinking events.

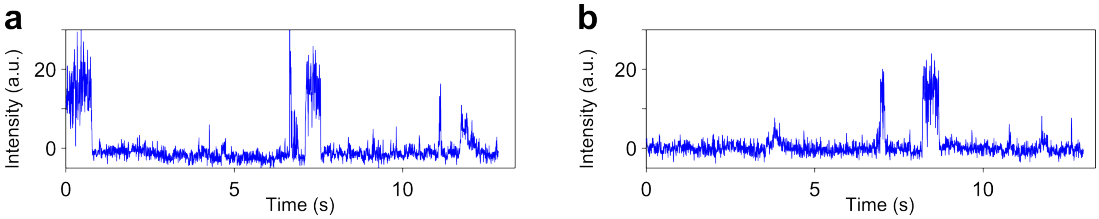

Figure 5.12: Demonstration of blinking of Cy5-labelled tRNA molecules *in vivo*. Single-cell fluorescence intensity time-traces of cells electroporated with 1 µM tRNA-Cy5 and imaged for several seconds after photobleaching the internalised fluorescence. **a-b.** Example time-traces showing stochastic increase in single-cell fluorescence signal indicating a single-molecule blinking event.

Mobility of tRNA in live bacteria

The mobility of tRNA molecules and the diffusion coefficient have not yet been reported in living bacteria. Measurements from cell lysates were performed in the 1980s, obtaining a diffusion coefficient estimate of about $60\,\mu m^2/s$ *in vitro* (251), and diffusion simulations using a bead model of tRNA resulted in a diffusion coefficient of about $10\,\mu m^2/s$ (252). Due to the similar size of tRNA molecules and fluorescent proteins (hydrodynamic radius of $2.6\,nm$ and $2.4\,nm$ for yeast $tRNA^{Phe}$ (234, 233) and GFP (235), respectively), I expected the diffusion coefficients of tRNA to be about 10% smaller than for GFP, which was obtained ranging from 6-$10\,\mu m^2/s$ in previous studies (240), SI 5.4.1. However, single-molecule tracking studies looking at the diffusion of fluorescent proteins obtained slightly higher diffusion coefficients ranging between 8-$13\,\mu m^2/s$ in the *E. coli* cytoplasm (sec. 5.4.1). Hence, the obtained diffusion coefficient of $8.1\pm1.0\,\mu m^2/s$ for tRNA molecules (Fig. 5.6c) is in very good agreement with the expected values from literature.

For my experimental conditions, I estimated the diffusion coefficient of the ternary complex to about $2.4\,\mu m^2/s$ (sec. 5.4.1). However, I still obtained about 70% of freely diffusing tRNA molecules ($D_{app}>3.5\,\mu m^2/s$) when constraining a second diffusive species to the expected apparent diffusion coefficient of the ternary complex. Thus, I reasoned that the tRNA molecules were mainly freely diffusing *in vivo*. *In vitro* studies showed that the labelled tRNA molecules could be charged with amino acids and that charged and labelled tRNA molecules efficiently bind to elongation factor EF-Tu (211). While in eukaryotic cells electroporated tRNA did not efficiently enter the tRNA channelling system (tRNA being directly transferred from tRNA synthetases to elongation factors to ribosomes without dissociating into the cytoplasms) due to tRNA binding domains (tRBDs, short polypeptide chains) present in most eukaryotic tRNA-synthetase (243, 244), these tRNA binding domains are not present in bacteria tRNA-synthetase (245). From the data, I could not find a strong evidence for

the existence of such a tRNA channelling mechanism for protein synthesis in *E. coli* and propose that tRNA molecules are mainly freely diffusing in live bacteria.

In a review by Marc Mirande (245) a more diffusion-based tRNA cycle in bacteria was proposed due to the lack of subcellular structure and high concentration of tRNA molecules in prokaryotes compared to eukaryotes. Although EF-Tu may be abundant in *E. coli*, it shows other molecular interactions for instance with the actin-like MreB proteins (shown in *Bacillus subtilis* (253) and in *E. coli* (254)) and the available fraction of free EF-Tu might be smaller in cells. Thus, I reasoned that most of the tRNA molecules in bacteria diffuse freely and binding of aa-tRNA and EF-Tu-GTP might be weaker *in vivo*.

I further examined a tRNA diffusion-based cycle and showed that the diffusion of tRNA molecules is not limiting protein synthesis; assuming high translation rates of 50 ms per amino acid (230) with 2 tRNA molecules (endogenous tRNA pool: 375000) present at all 50000 ribosomes per *E. coli* cell (255, 256), resulted in a searching and re-charging time of tRNA at the tRNA-synthetase of about 280 ms (tRNA per ribosome: 7.5, tRNA cycle time minus time of tRNA at ribosome: $7.5 \cdot 50\,\text{ms} - 2 \cdot 50\,\text{ms} = 275\,\text{ms}$). However, the tRNA molecule can already explore the entire cell within 70 ms assuming 3D free diffusion with D_{tRNA}=8 µm^2/s, and *E. coli* cell dimensions of 3 µmx1 µm: MSD(t) = $6D_{tRNA}t \geq 3\,\mu\text{m}^2 \rightarrow t \geq 70\,\text{ms}$, which is 25% of the time the tRNA is allowed to recharge and search for the ribosome assuming a diffusion-based tRNA cycle and rapid cell growth. Therefore, the diffusion of tRNA molecules is not limiting the rate of protein synthesis in bacteria.

Peripheral distribution of bound tRNA molecules

I observed an enrichment of 35% of bound tRNA at the cell periphery compared to an even distribution. This bias was even more pronounced when sorting cells into short and long cells (one and two chromosomes, respectively). I note that the less

pronounced species of bound tRNA molecules along the short cell-midline for short cells (Fig. 5.9c) could be due to the miss-categorisation of bound molecules into the mobile species by using a single diffusion coefficient threshold. Previously, simulations showed a spatial variation of the diffusion coefficient for fluorescent proteins from 8-16 $\mu m^2/s$ throughout the cell, and specifically an increase in diffusion coefficient along the short cell-midline (43). Thus, I believe that the uneven distribution of mobile and bound tRNA and the enrichment of 35% of bound tRNA at the cell periphery is a lower estimate.

Recently, the exclusion of ribosomes from the cell nucleoid was revealed by super-resolution imaging studies (229, 224). I reasoned that tRNA molecules classified as 'bound' could be associated with larger protein complexes, such as the ribosome, since the bound species matched an apparent diffusion coefficient distribution of 0.3-0.5 $\mu m^2/s$ (Fig. 5.6c) corresponding to ribosomal diffusion (43), and since the bound tRNA localisations were biased towards the cell periphery similar to reported ribosomal distributions. In bacterial systems, the strong ribosome-nucleoid segregation (less than 15% of ribosomes are located within the dense cellular nucleoid (224)) was linked to co-transcriptional translation mechanism (226), in which multiple ribosomes translate mRNA strands directly synthesised by RNA polymerase clusters. Recent studies have shown the same nucleoid segregation effect of RNA polymerase during transcription, where dense transcription sites were observed at the nucleoid periphery (227) supporting the link of transcription and translation of heavily expressed genes being relocated to the nucleoid periphery (226, 228). Further studies have shown that ribosomal subunits S30 and S50 can penetrate the entire cell and are not excluded from the nucleoid (225). Interestingly, mobile tRNA molecules could also penetrate the entire nucleoid. This strongly suggests that the translation of nascent mRNA can start throughout the nucleoid but that heavily expressed genes are moved outside the nucleoid (225) reconciling with the co-translational transcription

mechanism (227).

To further show that the bound tRNA molecules at the cell periphery could be associated with the ribosome, I calculated the ratio of bound versus mobile tRNA molecules in live *E. coli* to about 10%. This ratio is in excellent agreement with the expected value for bacteria with a division time of about 30 min, considering about 2 internalised labelled tRNA-Cy5 molecules per cell competing with the intrinsic pool of about 375 000 unlabelled tRNA molecules for maximal 2 binding sites at about 50 000 ribosomes per cell (255, 256). Using these assumptions and in rapid growth (all ribosomes occupied by tRNA molecules), I calculated an upper estimate of 25% of bound tRNA molecules at the ribosome (bound tRNA = number of ribosomal sites/total amount of tRNA), which is in good agreement with the observed 10% of bound tRNA molecules under my experimental conditions (recovery in rich media for 30 min but imaging on minimal media agarose pads for 30 min).

Spatial organisation of tRNA is maintained through translation

Following the blocking of translation with Chloramphenicol, the fraction of bound to mobile tRNA molecules nearly equalised to 0.91 at mid-cell and 1.15 at the cell periphery (0.7 and 1.7 without Cam) and mobile and bound molecules were more or less evenly distributed. Thus, I reasoned that the spatial distribution of tRNA is maintained by active protein synthesis and that tRNA molecules might be bound at ribosomal complexes outside the nucleoid (224, 225). This further proves nucleoid compaction and co-translational transcription mechanism, where large RNA polymerase clusters are moved outside the nucleoid (227) as well as ribosome assembly and protein synthesis occuring at the cell periphery (225).

To conclude, I performed the first comprehensive study of tRNA localisation at the single-molecule level in living bacteria reporting on tRNA mobility and translation-dependent spatial organisation. This study opens new avenues for single-molecule

fluorescence localisation and tracing of a large variety of RNAs labelled with organic dyes in living cells.

Contributions

I performed all experiments and data analysis.

I modified and further developed software by Dr. Stephan Uphoff for diffusion analysis, and by Mathew Stracy for spatial organisation analysis. Initial software for diffusion simulations was developed by Jaroslaw Nowak (MPhys project student) under my supervision.

The labelled bulk *E. coli* tRNA was prepared by Dr. Ian Farrell and he performed reverse HPLC measurements. The 25-mer ssRNA fragment was synthesised by Dr. Afaf El-Sagheer and labelled by Dr. Alexandra Tomescu.

5.7 Supplementary information

5.7.1 tRNA labelling and purification

Total *E. coli* tRNA (Roche Diagnostics) were labelled at dihydrouridine positions with Cy3, Cy5, or Cy5.5 as described in (211, 216). In all cases, the tRNA required HPLC purification as described in (222), in order to ensure removal of free dye. After purification, labelled tRNA contained 0.82 Cy3/tRNA, 0.80 Cy5/tRNA, and 0.67 Cy5.5/tRNA. Transfer RNAs were stored at $-80\,^{\circ}$C in 10 µM, and 1 µM stocks for use in single-cell and single-molecules studies, respectively.

5.7.2 Electroporation and sample preparation

As descibed in sec. 3.6.3, and sec. 3.6.4. Before electroporation 1 mM EDTA was added to the cell suspension and cells were electroporated at 1.4 kV, which showed highest loading while maintaining cell viability (sec. 3.3.2).

For antibiotic studies, 200 µg/mL Chloramphenicol (Cam) or 200 µg/mL Rifampicin (Rif) were added to SOC medium and cells were recovered for 30 min. Then, cells were 4x washed with PBS except for the final dilution, where cells were diluted in 100 µL PBS containing 200 µg/mL Cam or Rif and then transferred to the agarose pad. Cells were fixed by incubating electroporated cells with 3% (v:v) Paraformaldehyde for 1 h after recovery.

5.7.3 Live-cell imaging

All single-molecule fluorescence measurements were perform on a customised setup described in Appendix A.1. Cells were imaged using HILO illumination (111) by adjusting the position of the focused excitation light on the back focal plane of the objective. Typical excitation powers ranged from 15-30 W cm^{-2} for single-cell fluorescence

studies (internalisation and counting studies) at 50 ms exposure time. For single-molecule tracking studies, laser power of 400 W cm^{-2} at 637 nm was used. Stroboscopic illumination was employed, exciting the sample for 1 ms while exposing the camera chip for 5 ms to overcome motion blurring of fast diffusing tRNA molecules.

5.7.4 Evaluation of cellular loading

Cells were categories as loaded, if their overall cellular fluorescence per cell area was larger than the mean plus three standard deviation of the overall cellular fluorescence per cell area of non-electroporated cells. Using this internalisation threshold, the autofluorescence of non-electroporated and non-treated cells always led to less than 2% of loaded cells for these two control samples. More than 500 cells per sample were imaged and about 85% of cells were loaded when internalising tRNA-Cy3, about 98% of cells were loaded when electroporating tRNA-Cy5, and more than 60% of cells were loaded after electroporation of tRNA-Cy5.5. The lower loading efficiency of tRNA-Cy5.5 could be explained, since Cy5.5 is not efficiently excited at 637 nm on our microscope setup (Cy5.5 at 637 nm: 40% of maximum absorption level, whereas Cy5 at 637 nm: 80% of maximum absorption level) and hence less fluorescence will be detected above the cellular autofluorescence.

5.7.5 Counting of single tRNA molecules per cell

I performed single-cell photobleaching studies to count single tRNA molecules per cell and analysed the data as described in chapter 4, SI 4.7.5. The unitary intensity of 8.7$\pm$2.4 a.u. was obtained for Cy5, which corresponds to 7500$\pm$2100 ph/s under these experimental conditions. I obtained a unitary intensity for Cy3 of 2000$\pm$700 ph/s and for Cy5.5 of 3700$\pm$1600 ph/s. The number of internalised tRNA molecules per cell was calculated by dividing the overall cellular fluorescence by the unitary intens-

ity.

5.7.6 Single-molecule localisation and tracking

Custom-written MATLAB software was used to analyse single-molecule tracking and diffusion in live *E. coli* as described in Ref. (62) and (115). Briefly, the PSFs in each movie frame were fitted by a 2D elliptical Gaussian (free fitting parameters: x/y position, x/y width, elliptical rotation angle, amplitude, background) using initial position guesses from applying a fixed localisation-intensity threshold on the bandpass filtered fluorescence image (95). Single-molecule tracking was performed by adapting the MATLAB script based on a published algorithm (114). Localised PSFs were linked to a trajectory if they appeared in consecutive frames within a window of 7 pixels ($\sim$0.67 µm). This window size ensures 99% of steps are correctly linked for an apparent diffusion coefficient of 4 µm^2/s and 5 ms exposure time. To account for transient disappearance of the PSF within a trajectory disappearance due to blinking or missed localisation, I used a memory parameter of 1 frame.

5.7.7 Measuring the diffusion coefficient of tRNA molecules

I calculated an apparent diffusion coefficient D_{app}=MSD/(4Δt) from the mean-squared displacement (MSD) for each single-molecule trajectory with a minimum of 4 steps and longer trajectories were truncated to the initial 4 steps. Shorter trajectories were discarded for this analysis because of the higher uncertainty in D_{app}-values. It is noteworthy that D_{app} is an apparent diffusion coefficient and does not equal an accurate diffusion coefficient due to cell confinement and motion blurring (117, 115). The localisation precision was determined to be 40 nm, which manifests in a positive non-zero apparent diffusion coefficient of immobile molecule of σ^2_{loc}/Δt, which is in good agreement with the apparent diffusion coefficient of D_{app}= 0.32$\pm$0.16 µm^2/s

that was measured for the tRNA-Cy5 fixed cell control.

To obtain the apparent diffusion coefficient constant, I fitted the probability distribution of apparent diffusion coefficients calculated for individual molecules, x, with an analytical equation for the diffusion constant D using:

$$f(x, D, n) = \frac{1}{\Gamma(n)} \Big(\frac{n}{D}\Big)^n x^{n-1} \exp\Big(-\frac{n}{D}x\Big)$$

where n is the number of steps of the single-molecule trajectory used to calculate the apparent diffusion coefficient for each trajectory $x = \mathrm{MSD}_n/(4\Delta t)$; here always: $n = 4$. The apparent diffusion coefficient distribution for tRNA-Cy5 was calculated from 4-step trajectories and did not fit to a single species. I reasoned that at least two species were present: tRNA molecules freely diffusing and tRNA molecules specifically bound to larger ribosomal complexes. The apparent diffusion coefficient of the ribosomal complex was measured to 0.5 µm^2/s previously (43). I used this result to fit a two species model to the tRNA-Cy5 apparent diffusion distribution, fixing the slow-diffusing species to ribosomal apparent diffusion coefficient of D_1=0.5 µm^2/s. Then, the analytical model for the two diffusive species fit yields

$$f(x, D, A_1, A_2) = A_1 \frac{1}{6\,!}\Big(\frac{4}{D_1}\Big)^4 x^3 \exp\Big(-\frac{4}{D_1}x\Big) + A_2 \frac{1}{6\,!}\Big(\frac{4}{D}\Big)^4 x^3 \exp\Big(-\frac{4}{D}x\Big)$$

where $A_1 + A_2 = 1$ holds. I obtained an apparent diffusion coefficient of tRNA molecules *in vivo* for data set 1 of D_{app}(tRNA)=3.6$\pm$1.8 µm^2/s and for data set 2 of D_{app}(tRNA)=3.4$\pm$1.7 µm^2/s. I obtained similar values when fitting the apparent diffusion coefficient distribution with the analytical model for a single species or two diffusive species (with the slow-diffusing species being constrained to fixed cell control), showing that our results are robust against different fitting models.

To determine an apparent diffusion coefficient threshold to separate bound and mobile tRNA species, I fixed cells with 3% paraformaldehyde and measured the appar-

ent diffusion of immobilised tRNA molecules. I fitted the apparent diffusion coefficient distribution to a single diffusive species.

$$f(x, D) = \frac{1}{6\,!}\Big(\frac{4}{D}\Big)^4 x^3 \exp\Big(-\frac{4}{D}x\Big)$$

I obtained an apparent diffusion coefficient of D_{app}=0.32$\pm$0.16 µm^2/s for fixed cells from the single species fit. Taking an apparent diffusion threshold of D_{thresh}=1 µm^2/s allowed the categorisation of individual trajectories as bound and mobile. By applying this categorisation to the fixed cell control, less than 10% of the molecules were miscategorised as mobile.

The diffusion analysis method was tested previously, simulating 2D and 3D Brownian motion in a confined rod-shaped area with hemispherical end caps showing good agreement of experimental and simulated data (115). Here again, I used Brownian motion simulations to relate the apparent diffusion coefficient to an accurate diffusion coefficient of mobile tRNA of D_{app}=8.1$\pm$1.0 µm^2/s, see SI 5.7.8.

5.7.8 Diffusion simulations

Determining the apparent diffusion coefficient using single-molecule tracking does not take the cellular confinement, motion blurring and localisation imprecision into account (7, 22). To obtain the accurate diffusion coefficient D_{acc} from experimental data, I simulated Brownian motion within a cylindrical shaped cell (cell length: 2.8 µm, cell width: 1.1 µm) with hemispherical end caps (radius: 0.55 µm). Each frame was split into 100 sub-frames with Gaussian distributed displacements

$$P(x) = \frac{1}{\sqrt{4\pi D t}} \exp\left(\frac{-x^2}{4Dt}\right)$$

in each sub-frame. I implemented stroboscopic illumination (5 ms frame time and 1 ms excitation) by averaging the distribution within the first 20 sub-frames. The point-spread-function and cellular autofluorescence were obtained from experimental data. On average 1.5 molecules per cell were simulated, each molecule trajectory latest exponentially distributed with a mean value of 100 frames (0.5 s), which matched the experimentally determined photobleaching lifetime under these conditions. Each simulation was run for 500 cells and 21 different accurate diffusion coefficients, ranging from 3.6 µm^2/s to 15 µm^2/s, were simulated. Each simulation run was then analysed exactly in the same way as the experimental data.

5.7.9 tRNA spatial distribution analysis

Spatial distribution analysis was performed in MATLAB (The Mathworks). Cells were segmented from brightfield images using MicrobeTracker (257), obtaining cell meshes, outline and midlines. The probability distributions along the cell short axis were calculated by determining the distance of each localisation from the cell midline, with the distances normalised to 1 at the cell membrane.

For 2D probability plots each localisation was normalised by its relative position along the short cell axis and along the long cell axis. The analytical probability distribution for a uniform distribution within a cylindrical volume is given by:

$$pdf(\rho) = \frac{\sqrt{\max(r^2 - \rho^2, 0)}}{\frac{1}{4}\pi}$$

where ρ is the radial coordinate and r is the cylinder radius, for the unit cell holds r=1.

The spatial distribution of mobile and bound molecules was represented in a unit cell (normalisation along cell width and cell length) taking all cells into account. 2D histograms of the spatial distribution of tRNA molecules throughout the cell cycle

were obtained by binning cells according to cell length (short cells: 1.7–2.9 µm, and long cells: 3.1–4.3 µm) with short cells having a single nucleoid located in the centre of the long cell-midline and long cells having two nucleoids.

5.8 Supplementary figures

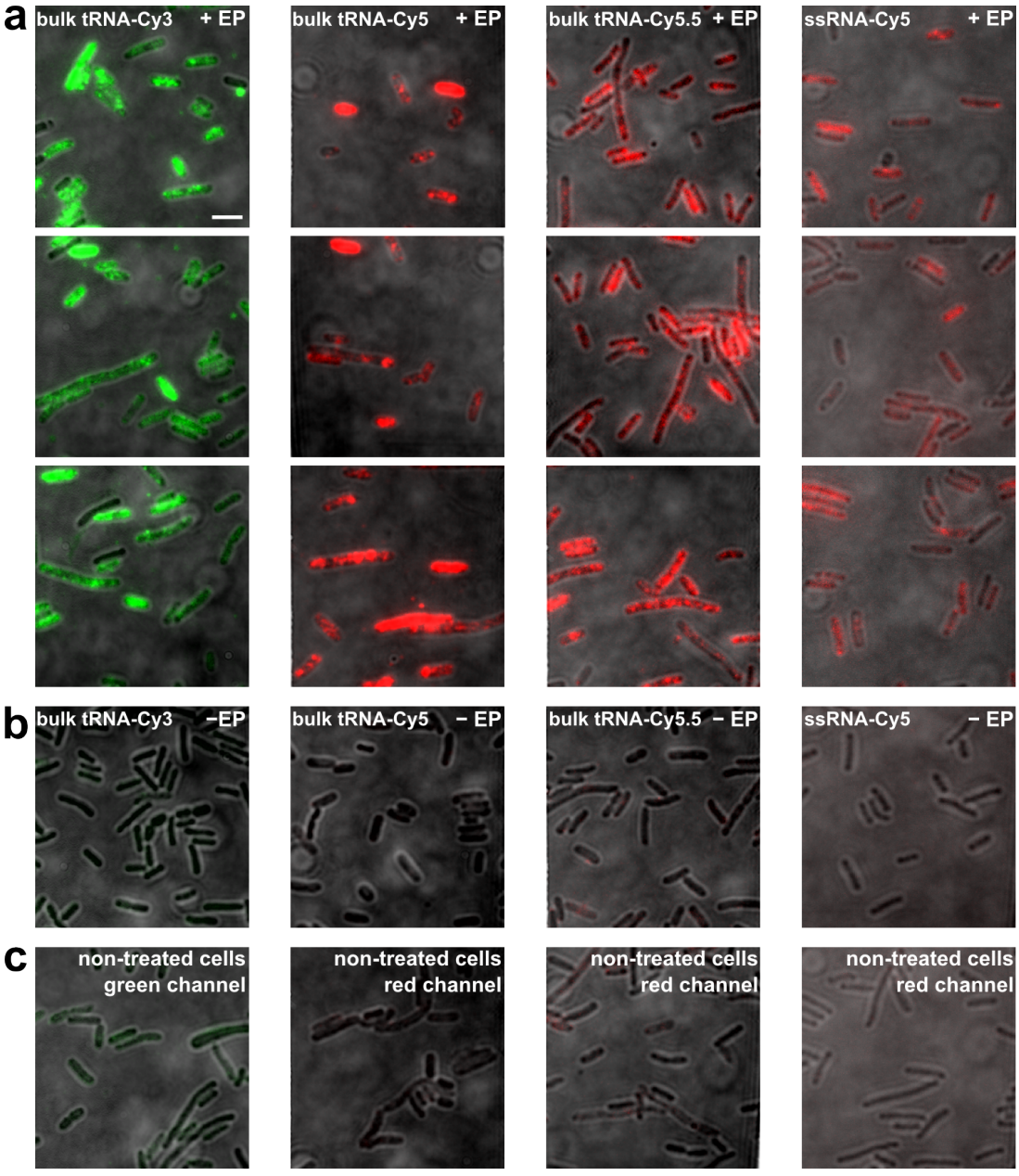

Figure 5.13: Further example fields-of-view of *E. coli* cells efficiently loaded with labelled tRNA molecules and negative controls. **a.** Efficient loading of *E. coli* cells with tRNA molecules labelled with Cy3, Cy5, and Cy5.5, and ssRNA-Cy5 (left to right) upon electroporation (+ EP). **b.** Cellular autofluorescence of cells incubated with labelled tRNA and ssRNA molecules but not electroporated (– EP). **c.** Autofluorescence of cells not treated with labelled tRNA and ssRNA molecules but electroporated. Scale bar: 3 µm.

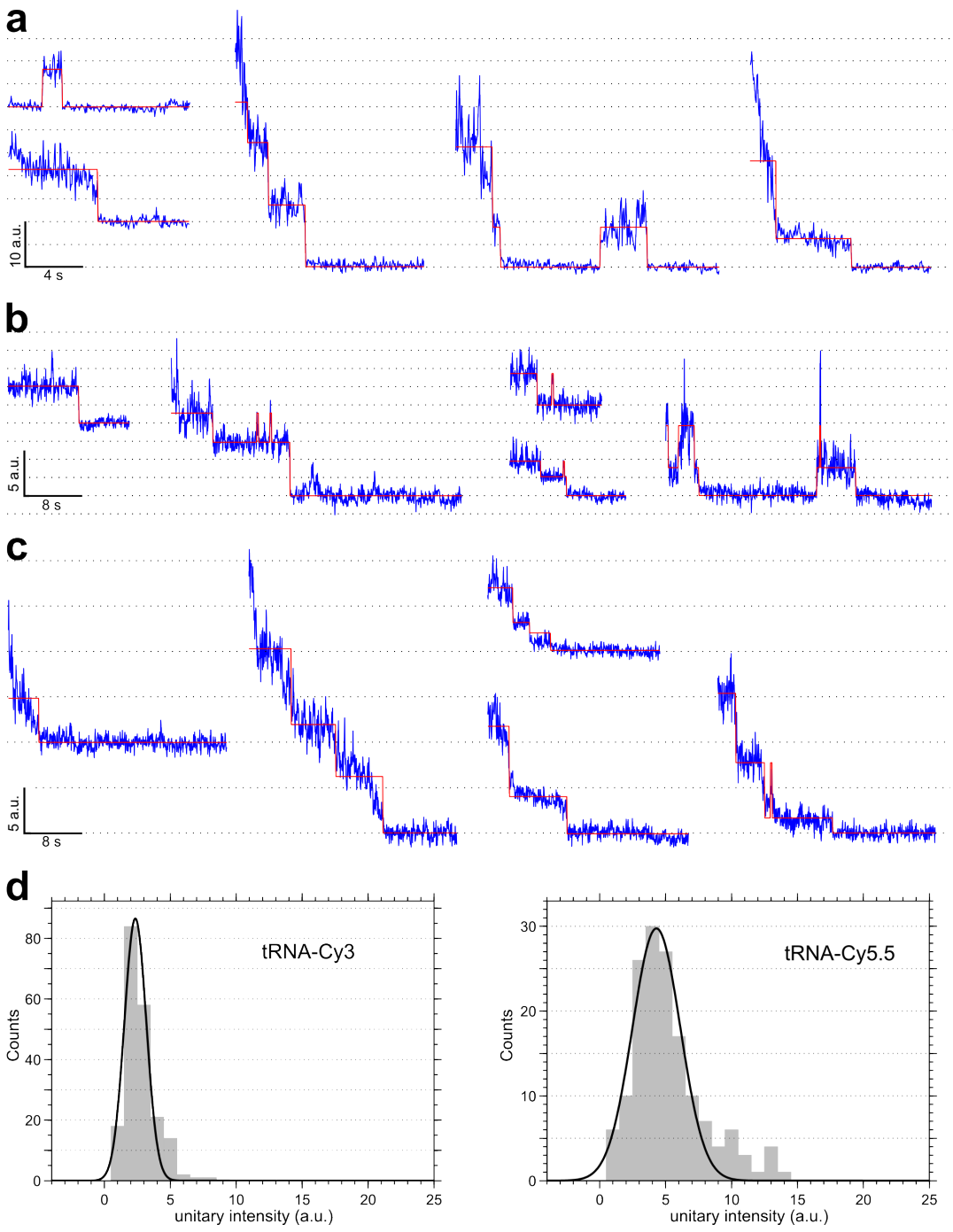

Figure 5.14: Counting the number of internalised tRNA molecules per cell. **a-c.** Single-cell photobleaching step analysis of **a.** tRNA-Cy5, **b.** tRNA-Cy3, and **c.** tRNA-Cy5.5. Example photobleaching time-traces (blue) and Hidden-Markov Model fit (red) of single photobleaching steps. **d.** Single photobleaching step height distribution of left: tRNA-Cy3, Gaussian fit centered at 2.3±0.8 a.u. corresponding to 2000±700 ph/s, and right: tRNA-Cy5.5, Gaussian fit centered at 4.3±1.8 a.u. corresponding to 3700±1600 ph/s.

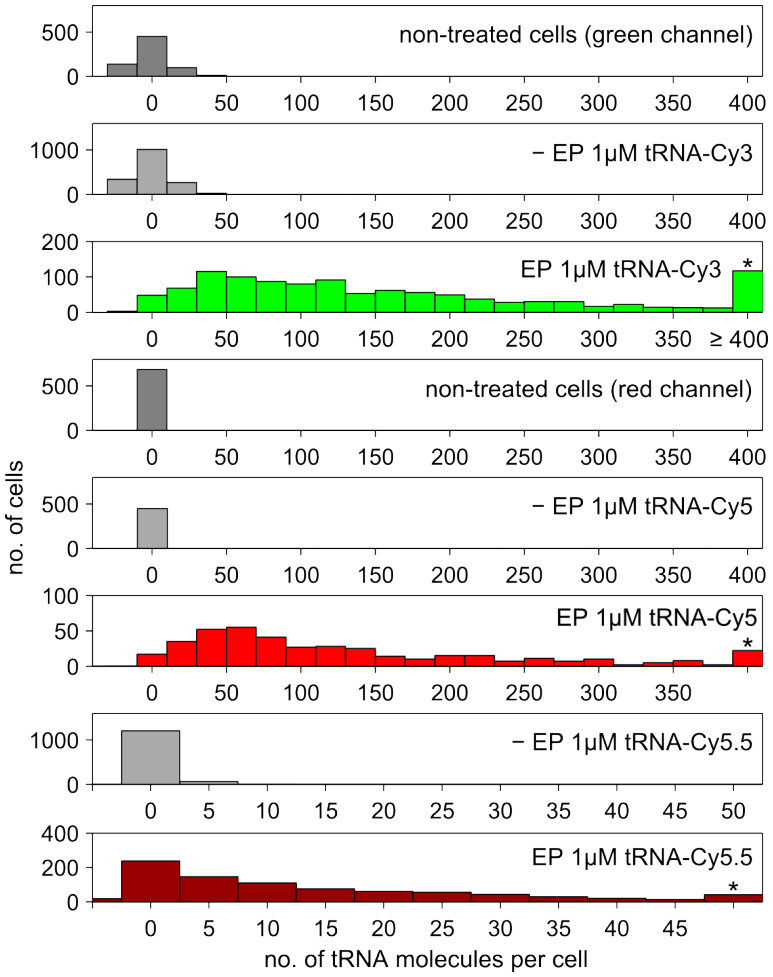

Figure 5.15: Internalisation histogram of cells electroporated at 1 µM tRNA-Cy3 (green), tRNA-Cy5 (red), and tRNA-Cy5.5 (dark-red) final concentration before electroporation and negative controls (gray). Cells were heavily loaded and about 100 labelled tRNA molecules were internalised per cell (small ensemble regime). Specifically, on average about 180 tRNA-Cy3 molecules (median: 124), and 139 tRNA-Cy5 molecules (median: 93) were internalised per cell. Negative values result from background subtraction.

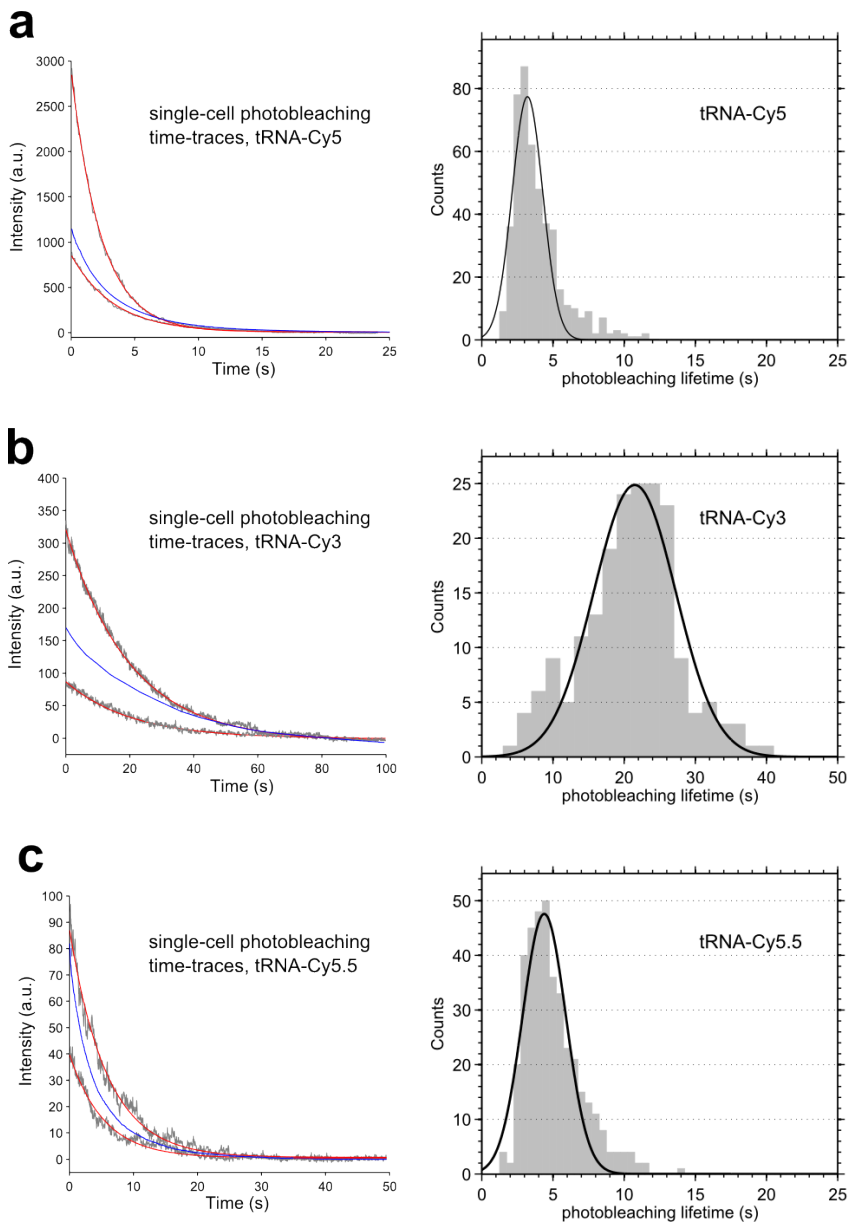

Figure 5.16: Characterisation of photobleaching lifetime of organic fluorophores *in vivo*. Cell-based photobleaching studies of heavily loaded cells with **a.** tRNA-Cy5, **b.** tRNA-Cy3, and **c.** tRNA-Cy5.5. **a-c.** Left: Example single-cell photobleaching time-traces (gray: raw data, blue: average of about 400 single-cell photobleaching time-traces) and single exponential fits (red). Right: Distribution of photobleaching lifetime from single exponential fits of single-cell photobleaching time-traces. Gaussian fit (black) of photobleaching lifetime distribution obtaining photobleaching lifetime of 3.4±1.1 s, 21.4±5.8 s, and 4.6±1.5 s for Cy5, Cy3, and Cy5.5, respectively.

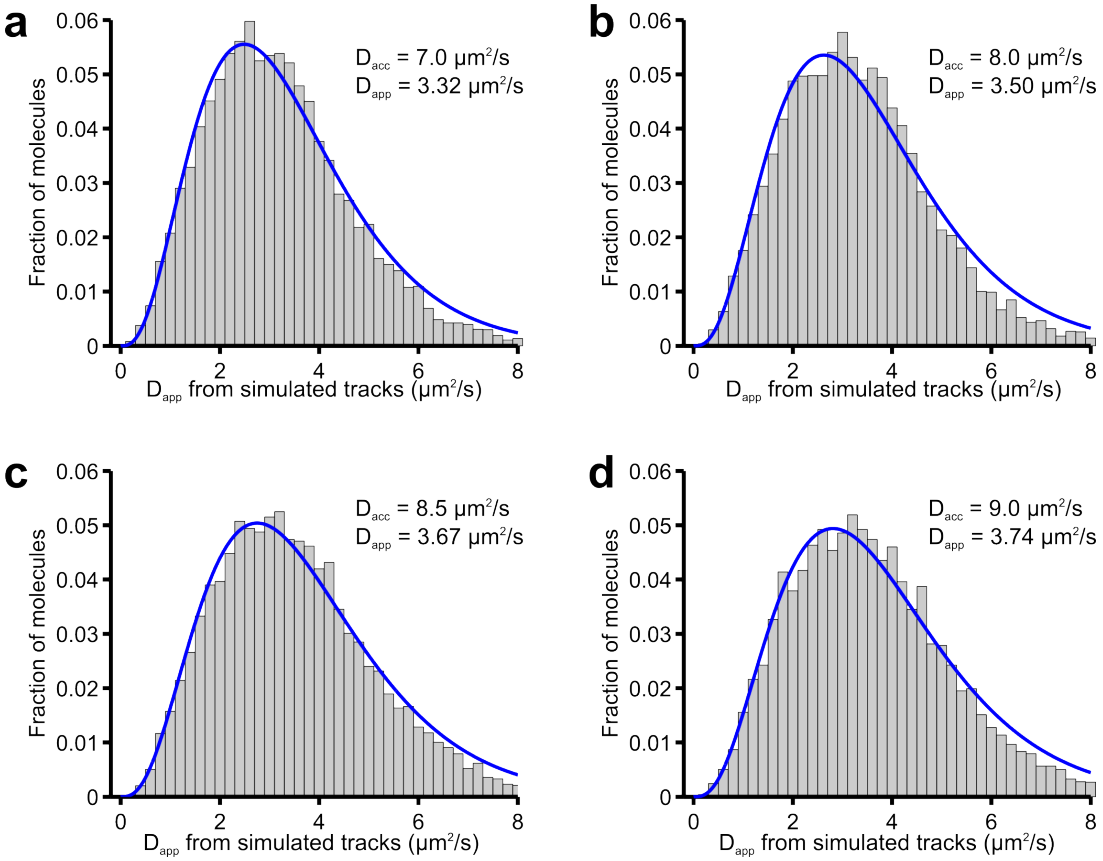

Figure 5.17: Example apparent diffusion coefficient distributions from simulated trajectories from 500 cells each. **a-d.** Apparent diffusion coefficient histograms from simulated tracks for which the input accurate diffusion coefficients ranged from 7.0 to 9.0 $\mu m^2/s$. The apparent diffusion coefficient distributions were fitted to a single diffusive species.

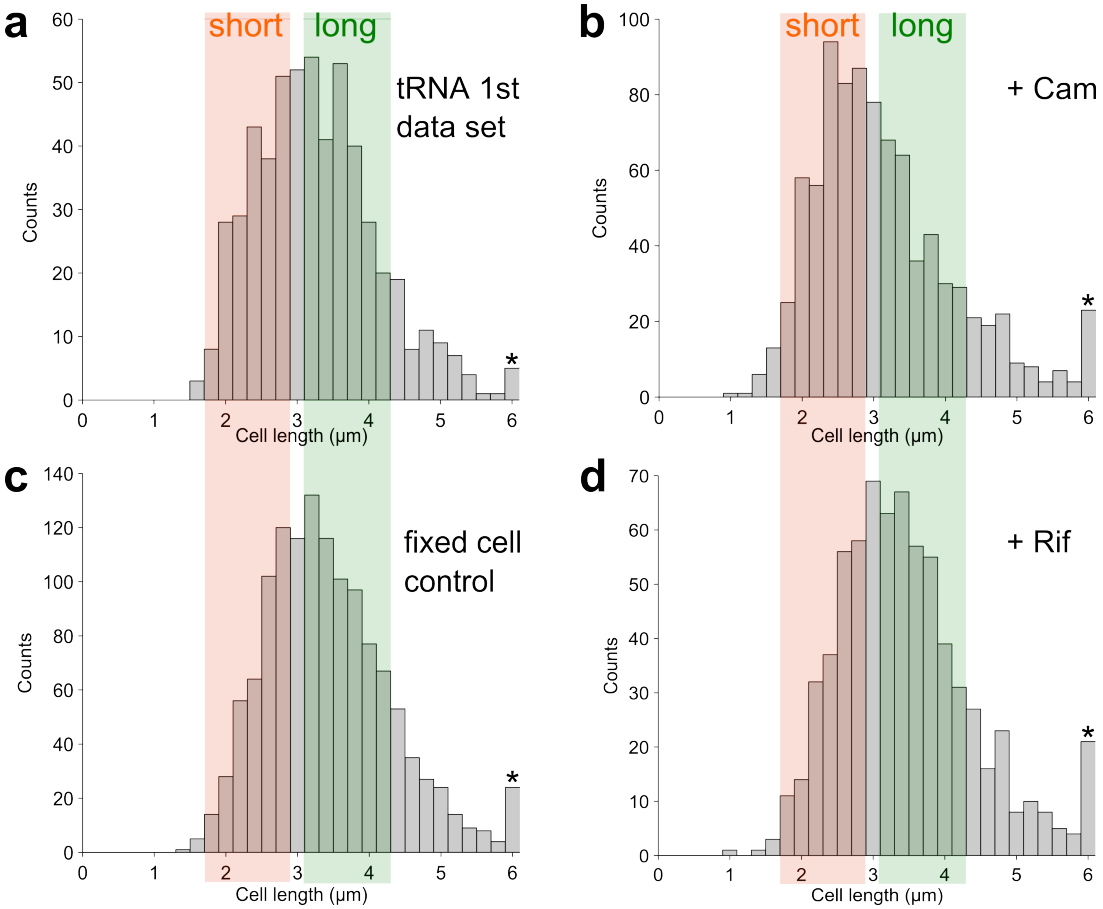

Figure 5.18: Cell length distribution and categorisation into short cells (1.7–2.9 µm, orange) and long cells (3.1–4.3 µm, green) for different experimental data sets: **a.** tRNA-Cy5 data set 1 (554 cells in total), **b.** upon Chloramphenicol treatment (890 cells in total), **c.** fixed cell control (1296 cells in total), and **d.** upon Rifampicin treatment (717 cells in total).

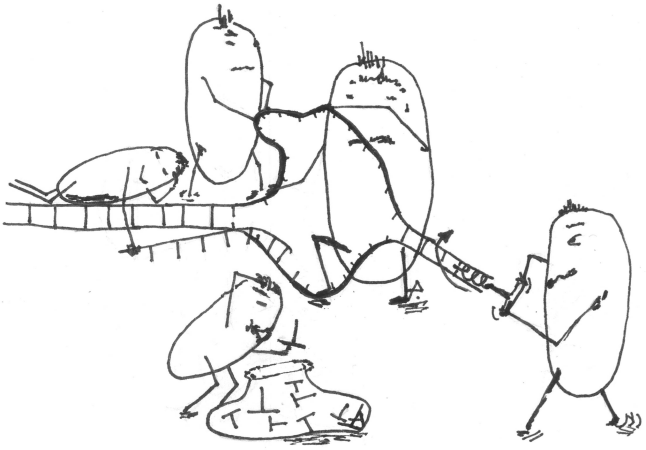

Chapter 6

Study of transcription initiation in live bacteria

6.1 Introduction

Transcription and translation are the processes by which cells express their genetic information. Interestingly, cells can regulate the expression of each of its genes with different efficiencies according to their environmental needs. The regulation mostly occurs by controlling transcription, the process by which the DNA nucleotide sequence (gene) is copied into the RNA nucleotide sequence (258). Specifically, transcription initiation is known as the most regulated step in gene expression (259). In bacteria, transcription initiates with the binding of RNA polymerase (RNAP) to promoter DNA and unwinding of about 14 bp around the transcription start site. The unwound promoter DNA forms a transcription bubble with the DNA template strand being inserted into the active site of RNAP (260). The conformational changes lead to the formation of catalytically active RNA polymerase – DNA promoter open complex (259), which is further referred to as open complex. Subsequently to open com-

plex formation, *de novo* RNA synthesis can be performed via (i) productive or (ii) abortive pathways (261, 262). In the productive pathway, RNA is synthesised within a RNAP-promoter initial transcribing complex. After synthesising 9-11 nt long nascent RNA, RNAP escapes from the promoter and enters elongation (263, 260). In abortive initiation, only short RNAs are synthesised and RNAP does not escape from the promoter. The short RNA fragments are released and RNAP reverts back to the open complex to re-initiate RNA synthesis (261, 264). The share of productive and abortive pathways is dependent on the DNA promoter sequence and also on the initial transcribed RNA sequences (262).

Crystal structures of the DNA promoter open complex (265), the RNAP holoenzyme (266, 267), as well as recent snapshots of the initial transcribing complexes (268), and the crystal structure showing a complete transcription bubble (269) shed light on the structural basis of transcription initiation. Additionally, biochemical assays such as gel assays, DNA:protein crosslinking, and RNAP footprinting have been extensively employed to study transcription initiation *in vitro* (270, 259).

However, our understanding of the regulatory mechanisms and kinetics of initial transcription is mainly limited by the presence of transient intermediates and heterogeneity (271, 262, 272). Single-molecule fluorescence studies are ideally suited to address these points, transcription reactions can be easily synchronised and single transcription events could be studied in real-time.

In 2006, Kapanidis *et. al* employed *in vitro* confocal single-molecule FRET studies and showed that transcription initiation proceeds by a DNA scrunching mechanism, by which RNAP unwinds and pulls downstream DNA into its active site cleft and stays stationary at the promoter for the duration of scrunching (105). The DNA scrunching mechanism in initial transcription was also shown to be a pre-requisite for RNAP promoter escape using magnetic tweezers by Revyakin and coworkers (273). While, the confocal microscopy single-molecule FRET approach only offered $\sim$1 ms structural

snapshots of initial transcribing protein complexes, an early single-molecule FRET study on immobilised complexes was lacking temporal resolution below 400 ms and showed photophysical fluctuations (274). Conversely, work using DNA nanomanipulation could not identify any stable intermediate protein complexes. As a result, questions concerning the kinetics and mechanisms of regulation of initial transcription such as whether abortive initiation is a pre-requisite for RNAP promoter escape similar to DNA scrunching (273) are still unclear.

Recently, our lab developed an optimised single-molecule FRET assay of immobilised transcription complexes and monitored the synthesis of *de novo* RNA *in vitro* in real-time (Duchi *et al.* in preparation). Using TIRF microscopy, Duchi and coworkers observed two distinct pauses during initial transcription that precede the escape of RNAP from the promoter. A more detailed description of their *in vitro* single-molecule FRET assay is given in sec. 6.2.1.

Despite the recent progress *in vitro*, very few studies about the mechanisms of transcription initiation *in vivo* were reported. In 2009, Goldman *et al.* observed abortive initiation also *in vivo* by pulling-down short RNA products from cell lysates (275). They proposed that the 2-4 mer abortive RNA transcripts act as primers for initial transcription and thus could control gene expression (275).

However, mechanistic and kinetic studies of transcription initiation *in vivo* are still missing. In light of the recent real-time observation of initial transcription events by Duchi *et al.* including extensive pausing of RNAP more questions about the biological relevance of these processes in live cells emerge. The impact of surface immobilisation and non-physiological buffer systems including oxygen scavenging systems in the *in vitro* assay, as well as the influence of regulatory proteins such as transcription elongation factors GreA and GreB (276, 277) on these pauses needs to be tested *in vivo*.

Here, I directly observe transcription initiation in live bacteria cells. I used electro-

poration (chapter 3, sec. 3.3) to internalise doubly-labelled promoter DNA fragments into live *E. coli* and tracked promoter DNA using HILO microscopy (111). I monitored the single-molecule FRET signature of promoter DNA with different FRET labelling schemes (chapter 4, sec. 4.4) and discovered different stages of transcription initiation on the single-molecule level in live bacteria. I observed intermediate FRET species similar as predicted for pausing events by *in vitro* studies, which were absent in non-promoter DNA and antibiotic controls.

To my knowledge, this is the first direct observation of single transcription initiation events in living cells, which should open exciting new avenues to study gene expression and gene regulation *in vivo*.

6.2 Initial transcription single-molecule FRET assays

To study transcription initiation in real-time, single-molecule FRET assays were developed in our group to monitor conformational changes of promoter DNA *in vitro* within diffusing active transcription complexes using confocal microscopy (278, 279), and on surface-immobilised transcription complexes using TIRF microscopy (Duchi *et. al* in preparation). Here, I briefly describe the single-molecule FRET assay and most striking *in vitro* results, and present ideas to move the *in vitro* transcription initiation assay into live bacteria.

6.2.1 *In vitro* single-molecule FRET studies

We used a derivative of the *lac* promoter (LacCONS+2, (280, 103, 274)), which is rate-limited in initial transcription (261, 264) with different FRET-labelling schemes (279) to observe different steps in transcription initiation. In all *in vitro* studies of our lab the FRET-dye pair Cy3B/Atto647N was used that did not seem to affect RNA polymerase binding to promoter DNA, formation of the open complex, and synthesis of short RNA

transcripts (278, 279). We used two major labelling schemes of the promoter DNA: (i) LacCONS+2(-5/-3)[1], and (ii) LacCONS+2(-15/+20) reporting on different steps in transcription initiation. Both labelling schemes are shown in Fig. 6.1 and all promoter DNA sequences used in this study are shown in the supplement, SI 6.6.1.

The first labelling scheme, LacCONS+2(-5/-3, Cy3B/Atto647N), was developed by Cordes *et al.* to observe open complex formation – the binding of RNA polymerase to promoter DNA and unwinding of promoter DNA for about 14 bp to form the transcription bubble (Fig. 6.1a). Thereby, a quenchable FRET assay was employed where the donor fluorophore Cy3B was quenched due to the physical contact with the acceptor fluorophore Atto647N (278). While this labelling scheme was ideally suited to observe the initial binding, no active initial transcription of long RNA transcripts ($>$4 mer RNA) occurred due to the close proximity of the two fluorophores to the active site within the transcription complex (278).

Duchi *et al.* used the second promoter DNA FRET labelling scheme, LacCONS+2 (-15/+20), on surface-immobilised transcription complexes to observe single transcription initiation events using TIRF microscopy in real-time. Using the LacCONS+2 (-15/+20) labelling scheme, promoter DNA-only and open complexes could not be distinguished in the *in vitro* single-molecule FRET time-traces, since the donor and the acceptor fluorophore were too far apart relative to their Förster radius of 6.2 nm (95). However, upon the addition of nucleosides and due to the DNA scrunching mechanism, the downstream DNA was pulled into the initial transcribing complex upon the synthesis of short RNA transcripts (2-7 mer) (105). Thereby, the downstream DNA rotates, and the acceptor fluorophore moves closer to the donor fluorophore, which leads to an increase in FRET (inset Fig. 6.1b).

It is noteworthy, that for *in vitro* transcription initiation studies a pre-melted version of the *lac* promoter DNA was used (SI 6.6.1) to maximise the yield of active immobilised

[1] Fluorophore position from transcription start site: non-template strand/template strand.

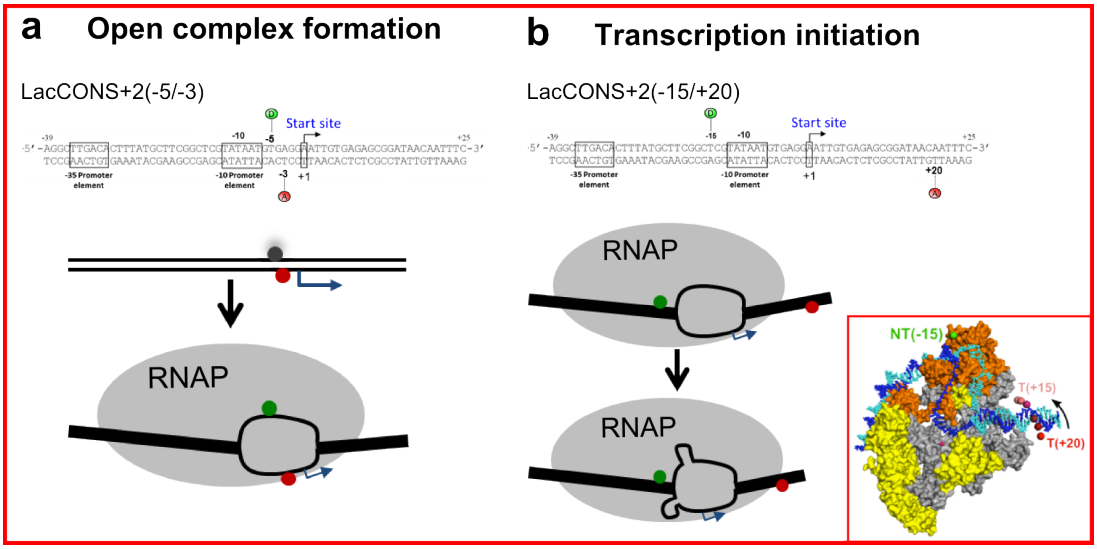

Figure 6.1: Schematic of transcription initiation single-molecule FRET assays. **a.** Single-molecule FRET labelling scheme of promoter DNA LacCONS+2(-5/-3) reporting on open complex formation (appearing of FRET signal). **b.** Single-molecule FRET assay LacCONS+2(-15/+20) accounting for different steps in transcription initiation (increase in FRET signal due to DNA scrunching mechanisms upon RNA transcript synthesis). Inset: The downstream acceptor dye (Atto647N) rotates towards the donor dye (Cy3B) during the DNA scrunching mechanism leading to an increase in FRET. The schematic was generated by Dr. Diego Duchi using software presented in (102).

complexes. When adding all nucleosides to immobilised RNA polymerase-DNA open complexes (preformed in solution) Duchi *et al.* observed a rapid increase in FRET ($\sim$1 s) from E*$\sim$0.2 to a very stable FRET level of E*$\sim$0.37 (dwell-time: $\sim$15 s) for the majority of single-molecule FRET time-traces. This first pause is sometimes followed by an increase in FRET to about E*$\sim$0.7-0.8 that they related to the escape of RNAP from the promoter.

Building on the new insights on transcription initiation by the real-time single-molecule FRET assays *in vitro*, I was interested in monitoring the different steps of transcription initiation inside live bacteria using the previously developed *in vivo* single-molecule FRET capability (chapter 4).

6.2.2 Moving *in vitro* transcription initiation studies into live cells

To observe transcription initiation in live bacteria, the idea was to use the previously established electroporation technique (chapter 3, sec. 3.3) to internalise doubly-labelled promoter DNA into live *E. coli* and observe their single-molecule FRET signatures (Fig. 6.2). The short promoter DNA fragments should be recognised by the endogenous pool of RNA polymerase (about 5000 RNAP copies per cells, (224, 227)) that bind to the promoter DNA, form the DNA transcription bubble (open complex formation) and perform RNA synthesis of short RNAs (observation of initial transcription) and potentially longer RNA transcripts ($>$9-11 nt, observation of promoter escape). Comparing the *in vivo* results with the expected FRET values from *in vitro* studies, I should be able to link different FRET signatures of promoter DNAs to (i) open complex formation, (ii) steps in transcription initiation, and even (iii) promoter escape.

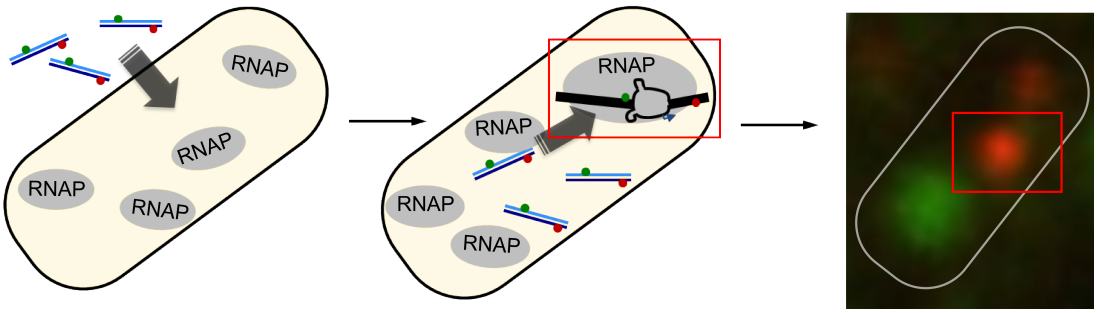

Figure 6.2: Schematic of the transcription initiation single-molecule FRET assay in live bacteria. Left to right: Electroporation of doubly-labelled promoter DNAs into live *E. coli* cells. Endogenous RNAPs ($\sim$5000 copies) recognise promoter DNA sequence and perform initial transcription steps. Live-cell imaging and single-molecule FRET analysis should show an increase in FRET signature of promoter DNA upon transcription initiation.

To begin with, we employed initial *in vitro* assays and examined the impact of electroporation on the promoter DNA FRET signature and the ability of RNA transcripts synthesis using electroporated promoter DNA.

First, I performed confocal single-molecule FRET measurements (SI 6.6.4) of electroporated and non-electroporated promoter DNA-only, and promoter DNA bound to

RNAP (open complex formation, SI 6.6.3) and compared their *in vitro* single-molecule FRET signatures (Fig. 6.3a-b). I could not observe a significant difference in shape and peak position of the single-molecule FRET distribution for LacCONS+2(-5/-3) upon formation of the open complex (Fig. 6.3a); E*=0.77$\pm$0.10 (non-electroporated DNA) versus E*=0.78$\pm$0.10 (electroporated DNA). Also, the single-molecule FRET distribution of non-electroporated and electroporated LacCONS+2(-15/+20) DNA-only and upon formation of the open complex with RNAP appeared very similar in shape. Using confocal microscopy, I was able to observe a slight shift ($\triangle$E*$\sim$0.05) to higher FRET values in the single-molecule FRET distribution of the DNA-RNAP complex compared to the DNA-only population due to RNAP binding and unwinding of the promoter DNA in the open complex. The shift was present for the electroporated and the non-eletroporated promoter DNA samples (Fig. 6.3b).

Second, *in vitro* transcription reactions were performed using electroporated and non-electroporated promoter DNA. Thereby, the promoter DNA-RNA polymerase open complex was initially formed and incubated with all nucleosides including radioactive ATP for 1 h. Radioactive ATP (radioactive isotope ^{32}P) was used to visualise RNA transcripts on 20% polyacrylamide sequencing gels using autoradiography (Fig. 6.3c). We could not observe a significant difference between short RNA transcripts from non-electroporated promoter DNA and electroporated promoter DNA. As expected, we observed a 5-fold higher amount of RNA transcripts for LacCONS+2 (-15/+20) than for the null-promoter DNA control (Fig. 6.3c). Further *in vitro* characterisation of the null-promoter DNA control using confocal single-molecule FRET measurements are shown in the supplement (SI Fig. 6.11). The *in vitro* transcription assay showed that electroporation had no effect on the promoter DNA, since electroporated promoter DNA got as efficiently transcribed as non-electroporated promoter DNA.

After characterisation of electroporated doubly-labelled promoter DNAs for the study

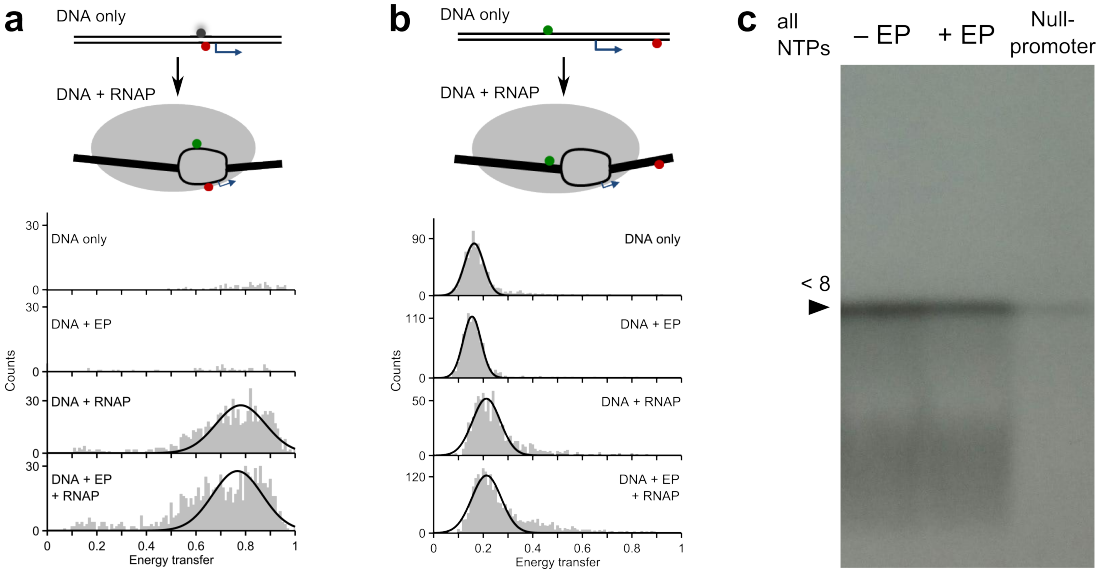

Figure 6.3: Impact of electroporation on promoter DNA, open complex formation and transcription initiation assay. **a.** Confocal single-molecule FRET assay for open complex formation showing no significant change in single-molecule FRET distribution of top to bottom: LacCONS+2(-5/-3) promoter DNA non-electroporated and electroporated, and upon formation of open complex with non-electroporated and electroporated DNA ('–EP': E*=0.77±0.10, and '+EP': E*=0.78±0.10). **b.** Confocal single-molecule FRET assay for transcription initiation showing no significant change in the single-molecule FRET distribution of top to bottom: LacCONS+2(-15/+20) promoter DNA non-electroporated and electroporated (both: E*=0.16±0.04), and upon formation of the open complex with non-electroporated and electroporated DNA (both: E*=0.21±0.06). **c.** *In vitro* transcription assay showing synthesised RNA products (synthesis of short RNA transcripts, <8 mer) after 1 h reaction time for different promoter DNA, left to right: LacCONS+2(-15/+20) non-electroporated, LacCONS+2(-15/+20) electroporated, and the null-promoter(-15/+20), SI 6.6.1. The electroporation of the promoter DNA did not seem to affect the efficiency of RNA synthesis during transcription initiation. *In vitro* transcription reactions were performed by Dr. David Bauer.

of transcription initiation *in vitro*, I next internalised these promoter DNAs into live *E. coli* to visualise and study open complex formation, and transcription initiation in live bacteria.

6.3 Observation of open complex formation *in vivo*

I studied the formation of the transcription bubble using the quenchable single-molecule FRET assay (Fig. 6.1a, (278)). I characterised the single-molecule FRET assay *in vitro* observing a high FRET species upon open complex formation. Next, I electroporated promoter DNA LacCONS+2(-5/-3) into live bacteria and also observed a

high FRET species of E*=0.83$\pm$0.09, which together with antibiotic controls supported the observation of the open complex *in vivo*. I further examined single-molecule FRET trajectories, which suggested that the open complex once formed *in vivo* is very stable ($>$10 s).

6.3.1 *In vitro* characterisation

Initially, I performed confocal single-molecule FRET measurements *in vitro* using an ALEX-scheme (SI 6.6.4) and studied the single-molecule FRET signatures of promoter DNA LacCONS+2(-5/-3) only and in complex with RNA polymerase. Whereas the promoter DNA only gave rise to very few single-molecule FRET bursts (Fig. 6.4a) due to the physical contact of donor and acceptor fluorophore and the quenching of the donor fluorophore (278), I observed a clear high FRET population of E*=0.75$\pm$0.10 for LacCONS+2(-5/-3) in complex with RNA polymerase (Fig. 6.4b).
Next, I added the antibiotic Rifampicin (Rif) during open complex formation (SI 6.6.3), which inhibits transcription initiation and blocks the synthesis of $>$3 mer RNA transcripts (281, 282). As expected, the treatment with Rifampicin did not alter the high FRET population and thus did not prevent the formation of the open complex (E*=0.72$\pm$0.10, Fig. 6.4c). I also added the antibiotic Lipiarmycin (Lpm, (283)) during the incubation of promoter DNA with RNA polymerase (SI 6.6.4). It was shown that Lipiarmycin blocks the DNA fitting into the RNA polymerase active site (284) and thus Lpm completely blocks the formation of the transcription bubble. Convincingly, I could not observe the high FRET population upon treatment with Lipiarmycin any longer (Fig. 6.4d). These *in vitro* results showed that the quenchable FRET labelling scheme was ideally suited to monitor the formation of the open complex.
While all nucleosides are present *in vivo* ($>$3 mM in mid-log growth phase (285)), it is very hard to observe the arising FRET signature upon RNA synthesis using *in vitro* confocal measurements due to the lack of synchronisation of transcription reactions

in solution and previous experiments by Cordes *et al.* with all nucleosides present were inconclusive (278). Hence, I decided to only add a subset of nucleosides: ApA, UTP, and GTP (ITC7 NTP mix) to form complexes limited to the synthesis of up to 7 mer RNA *in vitro*. I again measured single-molecule FRET efficiencies and observed a shift of the single-molecule FRET population in presence of the ITC7 NTP mix to intermediate FRET values, E*=0.54$\pm$0.10 (Fig. 6.4e). This result indicates the formation of initial transcription complexes that contain up to 7 mer RNA.

Next, I added Rifampicin and only observed a smaller shift to intermediate FRET values in presence of the ITC7 NTP mix, with E*=0.71$\pm$0.10 (Fig. 6.4). These results were in good agreement with Rifampicin blocking RNA transcripts beyond 3 mer RNA and indicated that when adding the ITC7 NTP mix RNA transcripts longer than 3 mer RNA could be synthesised. I also added Lipiarmycin and again could not observe any single-molecule FRET bursts showing that the formation of the open complex was blocked (Fig. 6.4g).

From the *in vitro* single-molecule FRET characterisations, LacCONS+2(-5/-3) should be ideally suited to study the formation of the transcription bubble of promoter DNA. The appearance of a high FRET signal upon open complex formation should be detectable *in vivo*. Antibiotic controls such as the treatment with Rifampicin and especially Lipiarmycin, which blocks open complex formation, are valuable controls to be performed in live-cell imaging to challenge *in vivo* results.

6.3.2 *In vivo* open complex formation

To test this hypothesis, I electroporated promoter DNA LacCONS+2(-5/-3) at 50 nM final concentration in the cell suspension into live *E. coli* cells (SI 6.6.2) and studied the single-molecule FRET signal of promoter DNA under green continuous illumination (SI 6.6.5). I localised single promoter DNAs in the FRET channel and performed single-particle tracking to obtain long-lasting single-molecule FRET trajectories. In-

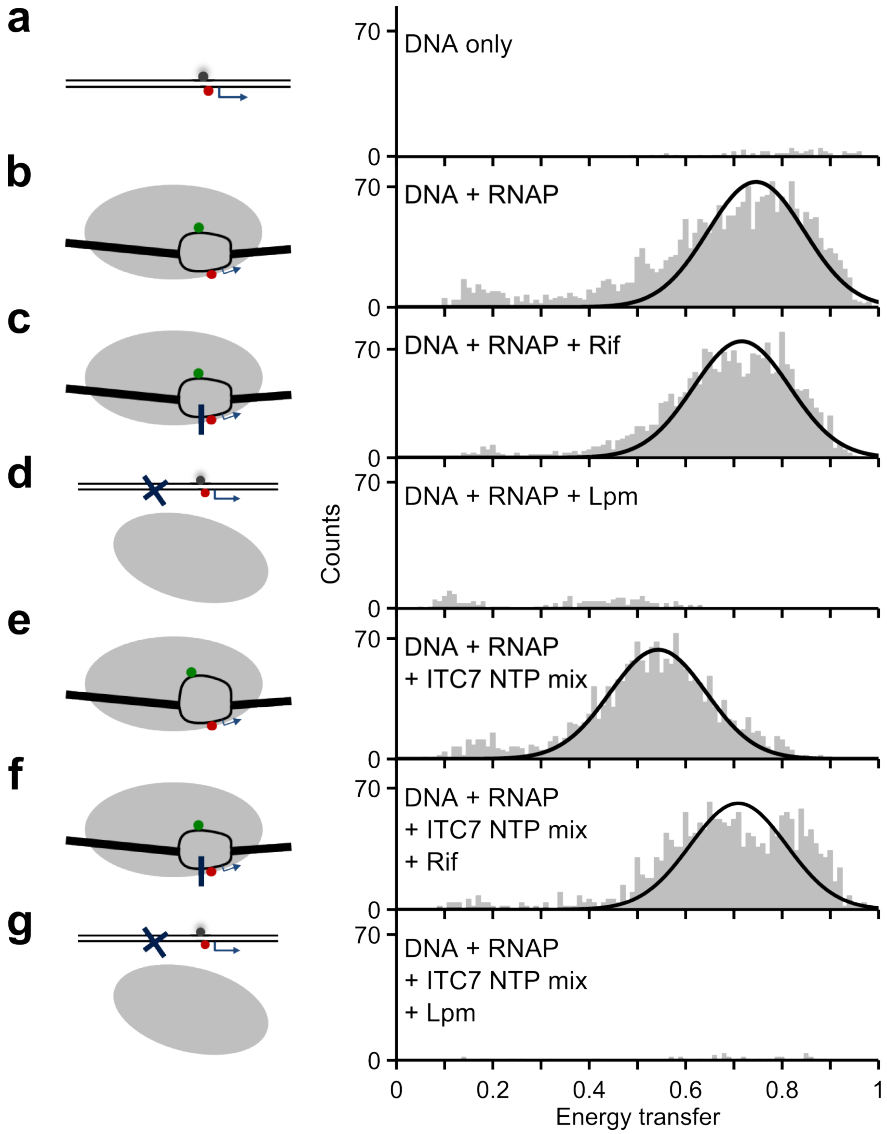

Figure 6.4: *In vitro* characterisation of single-molecule FRET assay reporting on open complex formation, promoter DNA: LacCONS(-5/-3). **a.** Promoter DNA only; no FRET signature due to quenching of donor fluorophore. **b.** Open complex formation; E*=0.75±0.10. **c.** Open complex formation in presence of Rifampicin (blocking synthesis of >3 mer RNA transcripts); E*=0.72±0.10. **d.** Open complex formation assay in presence of Lipiarmycin; no FRET signal, since open complex could not be formed. **e.** Formation of open complex and addition of nucleosides: ApA, UTP, and GTP (ITC7 NTP mix) to limit synthesis of up to 7 mer RNA *in vitro*; E*=0.54±0.10. **f.** As e. but in presence of Rifampicin; E*=0.71±0.10. **g.** As e. but in presence of Lipiarmycin; again formation of open complex was hindered.

terestingly, I observed single promoter DNA molecules exhibiting very high FRET efficiencies, a good indication of the observation of open complex formation *in vivo* (Fig. 6.5 a). From analysing more than 500 cells, I obtained a major high FRET pop-

ulation centered at E*=0.83$\pm$0.09, which was in good agreement with *in vitro* results. I also obtained smaller FRET values around E*$\sim$0.4, which suggested the active transcription of short RNA transcripts similar to the *in vitro* data with a limited set of nucleosides. The high FRET population was consistently observed in two additional independent repeats, which are shown in SI Fig. 6.12a.

Next, I treated cells with Rifampicin and again observed a high FRET population centered at E*=0.79$\pm$0.08, but only a few molecules exhibited low or intermediate FRET values (Fig. 6.5b). RNA polymerase stalls upon the addition of Rifampicin after the synthesis of short RNA transcripts ($<$4 mer RNAs) and hence no longer RNA transcripts (i.e. low or intermediate FRET signatures) were observed. Interestingly, I only could observe a few FRET events after treating with Lipiarmycin, which gave strong indication that the observed single-molecule FRET signatures of the promoter DNA report on the formation of open complex *in vivo*, which is blocked by Lipiarmycin (Fig. 6.5).

6.3.3 Single-molecule FRET time-traces of open complexes

Next, I was interested in the stability and intramolecular dynamics of the open complex *in vivo*. In *in vitro* open complex formation studies, it was shown that the transcription bubble exhibits conformational heterogeneity and dynamics on the millisecond timescale (279). Robb *et al.* hypothesised that the dynamics of the promoter DNA in the transcription bubble could affect the search for the transcription start site (279).

Here, I performed single-molecule FRET measurements in combination with single-particle tracking with 20 ms temporal resolution in green continuous wave-mode to trace single promoter DNAs *in vivo*. I obtained single-molecule FRET time-traces exhibiting high-FRET signals for more than 10 s (Fig. 6.6). Interestingly, the long-lasting single-molecule FRET time-traces seemed to show more fluctuations in the

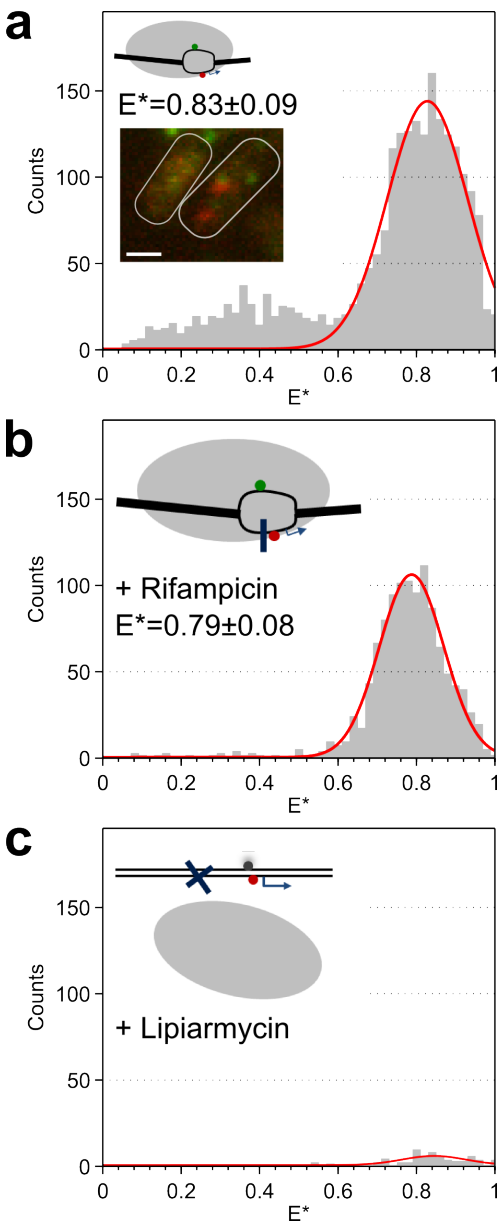

Figure 6.5: Observation of open complex formation *in vivo* by internalising LacCONS+2(-5/-3) into live *E. coli*. Single-molecule FRET histograms of **a.** electroporated cells showed main FRET distribution centered at E*=0.83±0.09 and intermediate FRET signal, **b.** electroporated cells treated with Rifampicin showed single FRET population centered at E*=0.79±0.08, and **c.** electroporated cells treated with Lipiarmycin showed no significant FRET signature. More than 500 cells were analysed for each data set. Scale bar: 1 µm.

single-molecule FRET signature than what I expected from single-molecule FRET measurements using protected high FRET DNA standards (chapter 4, Fig. 4.11). This result indicates that promoter DNA in the transcription bubble indeed exhibits

molecular dynamics.

Concurring with *in vitro* studies, the open complex appeared very stable in live bacteria and the observation span of more than 10 s might be mainly limited due to the photobleaching lifetime of the donor and acceptor fluorophores under these illumination conditions which has to be further investigated. The stability of the open complex is caused by the contacts of the RNA polymerase with the promoter region. A stable RNA polymerase open complex is needed to start RNA synthesis via a DNA scrunching mechanism (105).

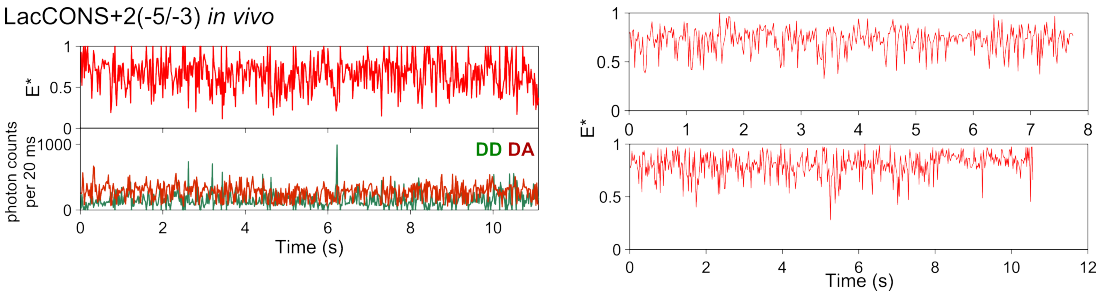

Figure 6.6: Single-molecule FRET time-traces of LacCONS+2(-5/-3) promoter DNA showed stable high FRET signatures lasting for more than 10 s, which can be attributed to open complex formation *in vivo*. The spikes in the DD-intensity trace (green) are due to adjacent biomolecules in the DD-channel (e.g. donor-only molecules) that pass nearby the molecule of interest and result in an increase in the fitted donor intensity (as presented in chapter 4, Fig. 4.11d). These spikes only occur for single frames since the tracking algorithm is excluding the loss of the single-molecule signal for more than 1 frame (memory parameter: 1 frame, see chapter 4, SI 4.7.8).

6.4 Observation of transcription initiation *in vivo*

Next, I internalised the LacCONS+2(-15/+20) FRET labelling scheme, which is sensitive to DNA scrunching and synthesis of short RNA transcripts (Fig. 6.1b) and which was used by Duchi *et al.* to observe pausing in transcription initiation (sec. 6.2.1). Initially, I characterised the single-molecule FRET signal upon open complex formation, and in presence of the ITC7 NTP mix *in vitro*, for which I observed a major FRET population at about E*$\sim$0.2 (attributed to DNA-only or open complex) and a

minor FRET population at E*$\sim$0.35 (attributed to the synthesis of short RNA transcripts). In *in vivo* single-molecule FRET studies, I again observed the intermediate FRET distribution, which was not present for the null-promoter DNA control and upon antibiotic treatment with Lipiarmycin and Rifampicin. I tracked single-molecule FRET signals from promoter DNA but I was not able to observe long-lasting intermediate FRET states (pausing events) *in vivo*.

6.4.1 *In vitro* characterisation

I again performed initial *in vitro* confocal single-molecule FRET characterisations of the LacCONS+2 promoter, this time using the -15/+20-FRET labelling scheme. While the promoter DNA-only showed a single FRET distribution centered at E*=0.16$\pm$0.04 (Fig. 6.7a), the formation of open complex led to a slight shift to higher FRET values (E*=0.21$\pm$0.06, Fig. 6.7b). The slight increase in FRET was caused by the formation of the transcription bubble and the decrease in donor and acceptor distance, which could be observed using confocal microscopy but seemed not resolvable using TIRF microscopy (Duchi *et al.*). Despite I still observed the slightly higher FRET value (ΔE*=+0.05) of the transcription bubble when treating with Rifampicin (E*=0.21$\pm$0.04), the treatment with Lipiarmycin resulted in a very similar FRET efficiency to the promoter DNA-only sample of E*=0.15$\pm$0.03 (Fig. 6.7c-d), which again showed that Lipiarmycin hindered the formation of the transcription bubble.

Next, I added the nucleoside mix containing ApA, UTP, and GTP (ITC7 NTP mix) to characterise single-molecule FRET signals arising from the synthesis of short RNA transcripts for the promoter DNA LacCONS+2(-15/+20). I observed two FRET population when adding the ITC7 NTP mix: the major FRET population centered at E*=0.18$\pm$0.04, which I attributed to the open complex and to free promoter DNA, and the intermediate FRET population centered at E*=0.33$\pm$0.10, which I attributed the scrunching of the promoter DNA due to RNA synthesis (Fig. 6.7e). When treating

with Rifampicin, I still observed the two FRET populations with the major population centered at E*=0.18±0.04. The minor population was centered at E*=0.29±0.10, which showed that up to 3 mer RNA transcripts could be synthesised (Fig. 6.7f). Again, treating with Lipiarmycin resulted in a single FRET population centered at E*=0.17±0.04, which was in good agreement with the FRET efficiency for promoter DNA alone (Fig. 6.7g).

The *in vitro* single-molecule FRET characterisations showed that LacCONS+2(-15/+20) could be used to study initial transcription events, which give rise to a second FRET population at about E*=0.33±0.10 in *in vitro* confocal measurements. The LacCONS+2 (-15/+20) promoter did not seem heavily transcribed since only about 35% of promoter-DNA-RNAP complexes occupied metastable scrunched states, which is further discussed in sec. 6.5.

6.4.2 *In vivo* transcription initiation

To observe transcription initiation *in vivo*, I electroporated promoter DNA LacCONS+2 (-15/+20) into live *E. coli* cells and performed single-molecule FRET measurements and single-particle tracking at 50 Hz under green continuous illumination (SI 6.6.5). In live cells, I observed a wider low-FRET population centered at E*=0.24±0.06 (Fig. 6.8a) and I was not able to distinguish promoter DNA-only from DNA-RNAP open complex any longer by studying the single-molecule FRET signature of the DNA promoter. Nevertheless, I observed an intermediate FRET population centered at E*=0.37±0.1, which could be due to the DNA scrunching mechanisms and the synthesis of short RNA transcripts *in vivo*. Intriguingly, the single-molecule FRET efficiency was in excellent agreement with the previously observed very stable FRET state (pause at E*∼0.37) in *in vitro* transcription initiation assays using immobilised transcription complexes and TIRF microscopy, and of E*∼0.33 using diffusing transcription complexes and confocal imaging (Fig. 6.7e). I also internalised a null-

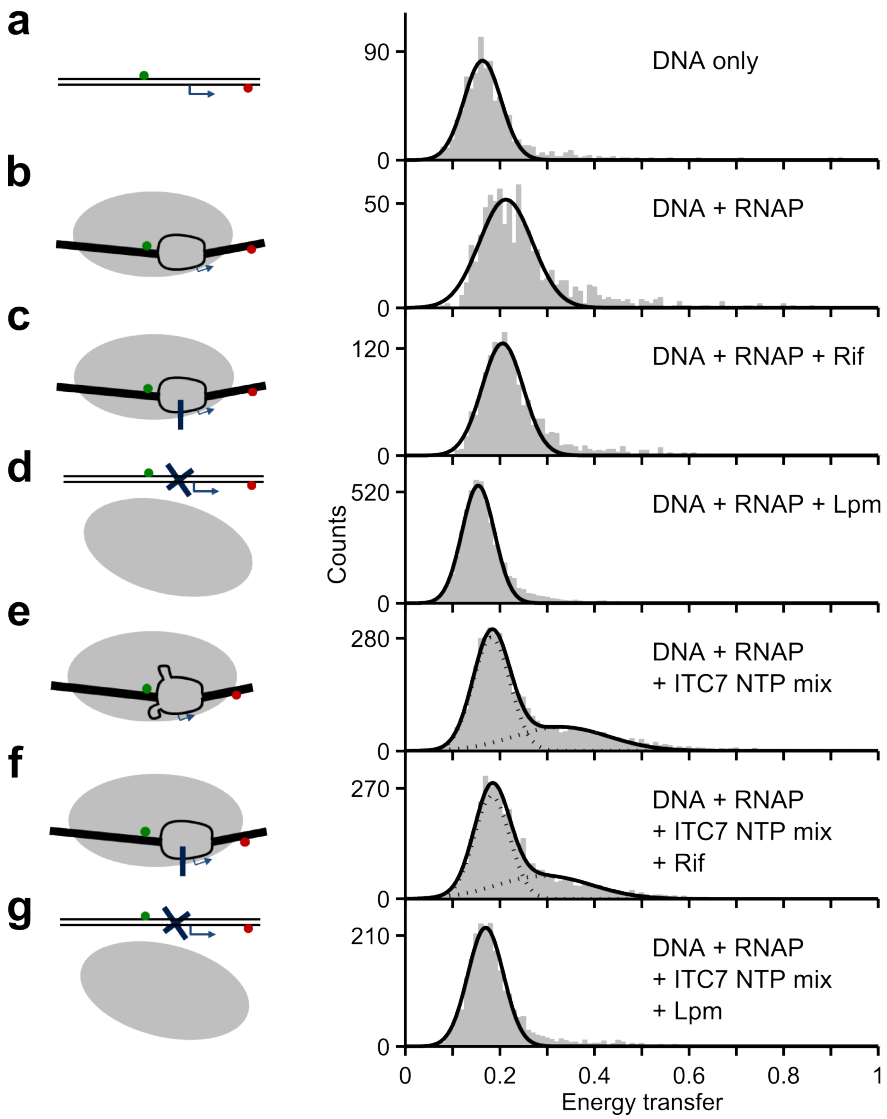

Figure 6.7: *In vitro* single-molecule FRET characterisation of LacCONS+2(-15/+20) reporting on transcription initiation. **a.** Promoter DNA only; E*=0.16±0.04. **b.** Open complex formation; E*=0.21±0.06. **c.** Open complex formation in presence of Rifampicin (blocking synthesis of >3 mer RNA transcripts); E*=0.21±0.04. **d.** Open complex formation assay in presence of Lipiarmycin; E*=0.15±0.03. **e.** Formation of open complex and addition of nucleosides: ApA, UTP, and GTP (ITC7 NTP mix) to limit synthesis of up to 7 mer RNA *in vitro*; fit to 2 Gaussian distributions: E*=0.18±0.04, and E*=0.33±0.1. **f.** As e. but in presence of Rifampicin; fit to 2 Gaussian distributions: E*=0.18±0.04, and E*=0.29±0.1. **g.** As e. but in presence of Lipiarmycin; E*=0.17±0.04.

promoter DNA fragment (SI 6.6.1) and observed a single FRET population centered at E*=0.24±0.09, which was in good agreement with *in vitro* controls (SI Fig. 6.11). The absence of the intermediate FRET population for the null-promoter DNA suggested that the synthesis of short RNA transcripts could be observed using the

LacCONS+2(-15/+20) promoter. The intermediate FRET population was present in both experimental repeats (SI Fig. 6.12b), and I also fitted the data to single Gaussian distributions, which showed worst R-square values, and I included the fits in the supplement (SI Fig. 6.12c).

To further support the observation of transcription initiation *in vivo*, I again performed antibiotic controls (SI 6.6.5). First, I treated cells with Rifampicin and obtained a major FRET distribution centered at E*=0.21$\pm$0.08 (Fig. 6.8b). Fitting of the single-molecule FRET distribution with two Gaussian distributions did not improve the R-square value of the fit, but I show the fits in the supplement for completeness (SI Fig. 6.12d). Second, upon addition of Lipiarmycin, I also only observed a single major FRET population centered at E*=0.21$\pm$0.08 (Fig. 6.8c). The lack of the intermediate FRET population upon treatment with transcription inhibitors (Rif and Lpm) gave further evidence of the observation of active transcription upon the internalisation of LacCONS+2(-15/+20) promoter DNA into live bacteria.

6.4.3 Single-molecule FRET time-traces of transcription initiation

After having observed intermediate FRET signatures that could be attributed to a pausing state during transcription initiation *in vivo*, I was interested if I could observe similar long pauses in live cells (*in vitro* dwell-times: $\sim$15 s, Duchi *et. al* (286)).

Employing single-molecule FRET studies with single-particle tracking, I observed single promoter DNAs and transcription complexes *in vivo* under green continuous illumination at 20 ms exposure time. Similar to the open complex formation assay, I was able to track single-molecule FRET signatures of promoter DNA for several seconds (Fig. 6.9). The single-molecule FRET time-traces mainly showed low-FRET signals and only fluctuated to intermediate FRET levels for very short time periods ($<$0.5 s). By examining the sampled single-molecule FRET time-traces (about 100 time-traces lasting longer than 1 s), I was not able to observe a stable single-molecule

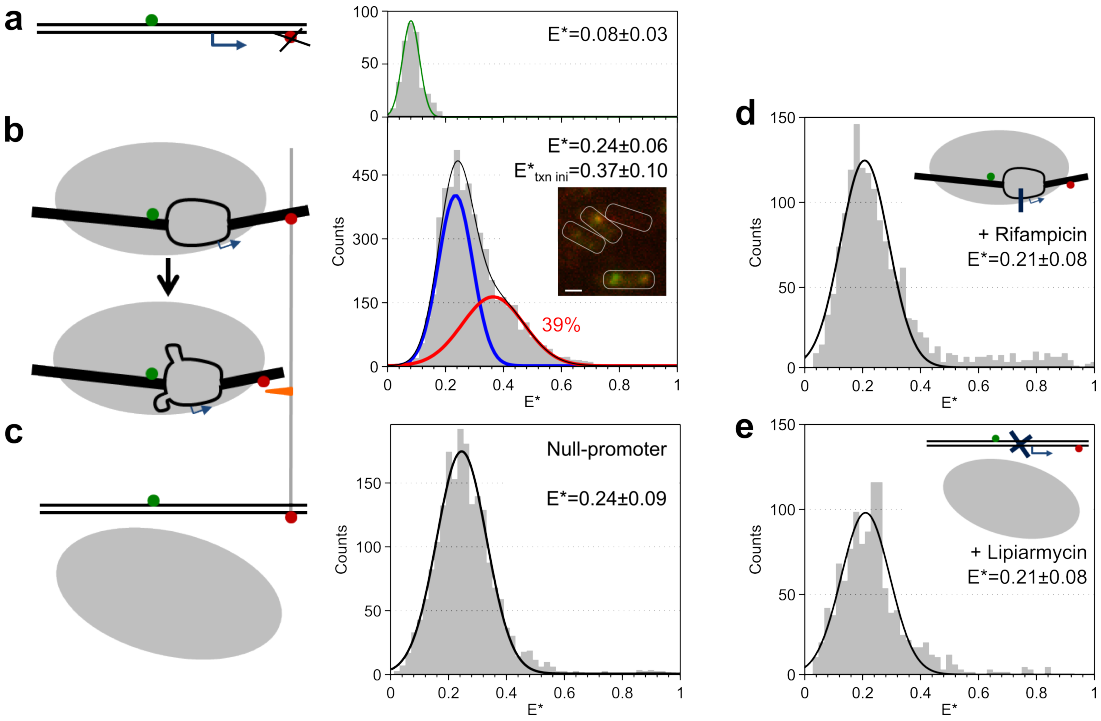

Figure 6.8: Observation of transcription initiation *in vivo*, null-promoter and antibiotic controls. Single-molecule FRET histograms of **a.** Donor-only molecules centered at E*=0.08±0.03 (blue arrow denotes the transcription start-site), **b.** cells electroporated with LacCONS+2(-15/+20) showed low-FRET population centered at E*=0.24±0.06 and intermediate-FRET population centered at E*=0.37±0.10 (vertical grey line and orange arrow depict the movement of the acceptor fluorophore closer to the RNAP complex due to the DNA scrunching mechanism in transcription initiation, which leads to an increase in the FRET signal/ the appearance of an intermediate FRET species), **c.** cells electroporated with null-promoter DNA(-15/+20) showed single FRET population centered at E*=0.24±0.09, **d.** cells electroporated with LacCONS+2(-15/+20) and treated with Rifampicin showed single FRET population centered at E*=0.21±0.08, and **e.** cells electroporated with LacCONS+2(-15/+20) treated with Lipiarmycin showed single FRET species centered at E*=0.21±0.08. More than 500 cells were analysed for each data set. Scale bar: 1 µm.

FRET signature at E*∼0.4 as expected from the *in vitro* studies (Fig. 6.9a). To increase the observation span, I increased the exposure time to 100 ms, which still allowed the tracking of large RNAP transcription complexes while monitoring their single-molecule FRET signature in cells only loaded with one labelled promoter DNA. Thus, I was able to extend the single-molecule FRET observation to more than 30 s, but again was not able to observe long pauses and again only observed transient occupation of intermediate FRET states (Fig. 6.9a, bottom right).

Next, I also analysed single-molecule FRET time-traces from null-promoter DNA

sample, and Rifampicin, and Lipiarmycin controls – example time-traces are shown in Fig. 6.9b-c. While I did not observe fluctuations to intermediate FRET levels in these controls, I found it very challenging to obtain long-lasting single-molecule FRET time-traces due to the difficulty of detecting and localising such low single-molecule FRET signatures continuously over many frames. Thus, the single-particle tracking analysis usually truncated tracks due to the noisy and low single-molecule FRET signals.

To further quantify the dwell-times of the intermediate FRET signals, and test the omission of the long-lasting pause in transcription initiation of the *lac* promoter *in vivo*, a general analysis routine for all single-molecule FRET time-traces would be needed. In addition, the observation spans could be extended to minute time-scales using time-lapse imaging of cells, which were only loaded with a single promoter DNA. These experimental improvements would require high-throughput screening of cells and will be further discussed in sec. 6.5.

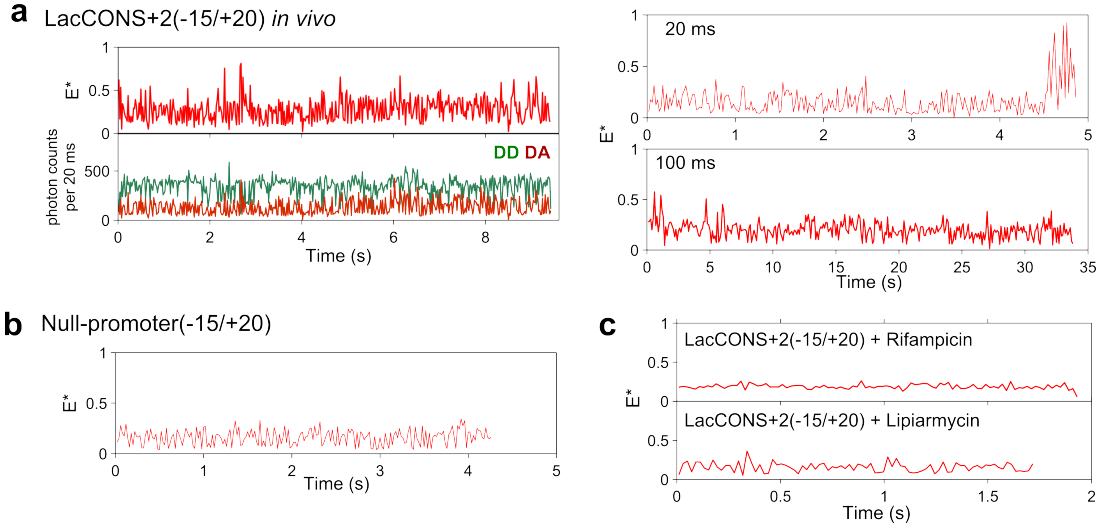

Figure 6.9: Single-molecule FRET time-traces of **a.** LacCONS+2(-15/+20) promoter DNA, **b.** null-promoter DNA, and **c.** antibiotic controls of LacCONS+2(-15/+20) promoter taken under green continuous illumination at 20 ms exposure time; if not stated otherwise.

6.5 Discussion and outlook

I efficiently internalised doubly-labelled promoter DNA fragments into live *E. coli* cells and monitored the single-molecule FRET signature of the *lac* promoter for two different labelling schemes. I studied the formation of the transcription bubble in live bacteria and showed that the open complexes were stable for more than 10 s *in vivo*. I also observed an intermediate FRET distribution that I attributed to transcription initiation and to the synthesis of short RNA transcripts, neither of which was present for null-promoter DNA and antibiotic controls. Despite the observation of intermediate FRET signals due to transcription initiation, I was not able to observe stable and seconds-long pauses during transcription initiation as was previously observed by Duchi *et al. in vitro*.

In vivo transcription initiation single-molecule FRET assay

The single-molecule FRET assays, which can be used to monitor steps in transcription initiation, have been developed in the last years and have proven helpful in studying transcription bubble formation (278) and dynamics (279), as well as single transcription initiation events *in vitro*. For *in vitro* studies, pre-melted promoter DNA fragments were used to obtain higher activity of transcription complexes (SI 6.6.1). However, the pre-melted DNA fragments (3-4 bp mismatch) as well as the blunt DNA-ends represent ideal targets for endonucleases and DNA repair machinery *in vivo* (146) and thus, they might be degraded, which results in the loss of the FRET signal *in vivo*. From initial internalisation tests of the pm LacCONS+2(-15/+20), I indeed observed less single-molecule FRET signals than in tests of the double-stranded LacCONS+2(-15/+20) promoter that was studied in this work. To overcome this concern, protected DNAs could again be synthesised, which would have to be significantly longer than the promoter region to allow unimpeded DNA unwinding around the

promoter region and beyond promoter escape. In general, the introduction of longer DNAs with labelled promoter region would be beneficial, since supercoiled DNA facilitate transcription and vice versa (287, 288, 289). Until now, I internalised up to 1 kbp singly-labelled DNAs.

In potential future work, the promoter DNA could be introduced in small plasmids of a few kbp in size, together with some antibiotic resistance. Since the transfected plasmid exhibits DNA supercoils and since it should diffuse relatively slowly, the observation of single-molecule FRET bursts due to transcription initiation and promoter escape events (choice of FRET labelling scheme) should become possible. Even several cycles of transcription could be monitored using time-lapse imaging.

Finally, two points for the improvement of the FRET labelling scheme to monitor transcription initiation for LacCONS+2(-15/+20) should be made: (i) the donor fluorophore should be attached 1-2 bp further upstream, since the rotational freedom of the Cy3B fluorophore at the +15-position seems to be constrained due to the close proximity to RNAP (Dr. David Bauer, unpublished data), and (ii) the non-template strand should be labelled downstream and the template strand should be labelled upstream to minimise the influence of the downstream fluorophore in the active site cleft during RNA synthesis.

In vivo open complex formation

The characterisation of the stability of the open complex in live cells can be complemented by internalising the LacCONS+2(-15/+15) labelling scheme which previously showed distinct single-molecule FRET species for promoter DNA only and in complex with RNA polymerase (279). To obtain information of static and dynamic heterogeneity of the open complex, an '*in vivo* variance analysis' as performed by Robb *et al.* (279) could be implemented to observe millisecond dynamics that are inaccessible to wide-field microscopy measurements. Using diffusion simulations and

assuming that FRET fluctuations from DNA FRET standards are only caused by their diffusion within the cell, the diffusion dynamics and the dynamics of the transcription bubble potentially could be deconvolved in the single-molecule FRET data.

To further test for the formation of the transcription bubble and to block dynamics, cells could be treated with the antibiotic Myxopyronin (290, 291), since it prevents the formation of the fully open transcription bubble (292). Myxopyronin mediates the opening of the RNAP clamp and inhibits the loading of template DNA into the active site cleft of RNAP and thus locks the open complex (265).

Additionally, the stability of the open complex *in vivo* (>10 s under these experimental conditions) has to be further examined. First, the photobleaching lifetime of donor and acceptor fluorophore have to be measured using the same experimental conditions, since the single-molecule FRET time-traces could be simply truncated due to photobleaching. Second, time-lapse FRET measurements of cells loaded with single promoter DNAs could be performed, which would require high-throughput live-cell imaging, and automated analysis to extend the observation span beyond several seconds to potentially several minutes.

In vivo transcription initiation and promoter escape

The lack of the long-lasting pause in *in vivo* transcription initiation experiments, which was previously observed by Duchi *et al. in vitro*, is most striking and needs further discussion.

The *in vivo* single-molecule FRET signals report on the recognition of the doubly-labelled promoter DNAs by endogenous RNAP and the assay allows the observation of open complex formation *in vivo*. In Duchi's work, the single-molecule FRET values were in good agreement with expected *in vitro* values and antibiotic controls blocking the formation of the transcription bubble supported these findings. For the LacCONS+2(-15/+20) labelling scheme reporting on transcription initiation, the in-

termediate FRET population centered at E*$\sim$0.37 was not present in null-promoter control and Rifampicin and Lipiarmycin antibiotic controls that block transcription initiation. These results suggest that the intermediate FRET population is caused by the DNA scrunching mechanisms during RNA synthesis and as shown in *in vitro* measurements corresponds to the synthesis of short RNA transcripts (<8 mer RNA) using the LacCONS+2 promoter. But for kinetic interpretation of the short intermediate FRET states, a thorough analysis of *in vivo* single-molecule FRET time-traces is needed and experiments employing an ALEX-scheme would be beneficial when interpreting single-molecule FRET time-traces.

To study the efficiency of transcription *in vivo*, a different FRET labelling scheme such as LacCONS+2(-15/+15) could be studied. This labelling scheme allows to differentiate promoter DNA-only species and open complex from their single-molecule FRET signals and thus should allow to estimate the amount of actively transcribing complexes. However, it has to be kept in mind that this FRET labelling scheme is not sensitive to monitor promoter escape *in vitro*.

To enhance the probability of promoter escape, longer DNA fragments with about 100 bp upstream should be employed to stabilise the transcription bubble (262). Promoter DNA fragments with the transcription factor (Catabolite activator protein, CAP) binding site, CAPLacCONS+2(-15/+20), have already proven beneficial to increase the rate of promoter escape *in vitro* (Dr. David Dulin, unpublished data) and should be ideally suited for *in vivo* studies. In an initial experiment, I internalised pre-melted CAPLacCONS+2(-15/+20) and observed higher FRET signals (E*$>$0.6, Fig. 6.10a), which were not present in the Rifampicin control (Fig. 6.10b). However, more data sets and control measurements are needed to attribute the high FRET signals to promoter escape events and RNAP moving to transcription elongation.

In addition, other promoter DNA sequences such as LacUV5 (more efficient promoter escape) and T7A1(very efficient promoter escape) should be investigated to

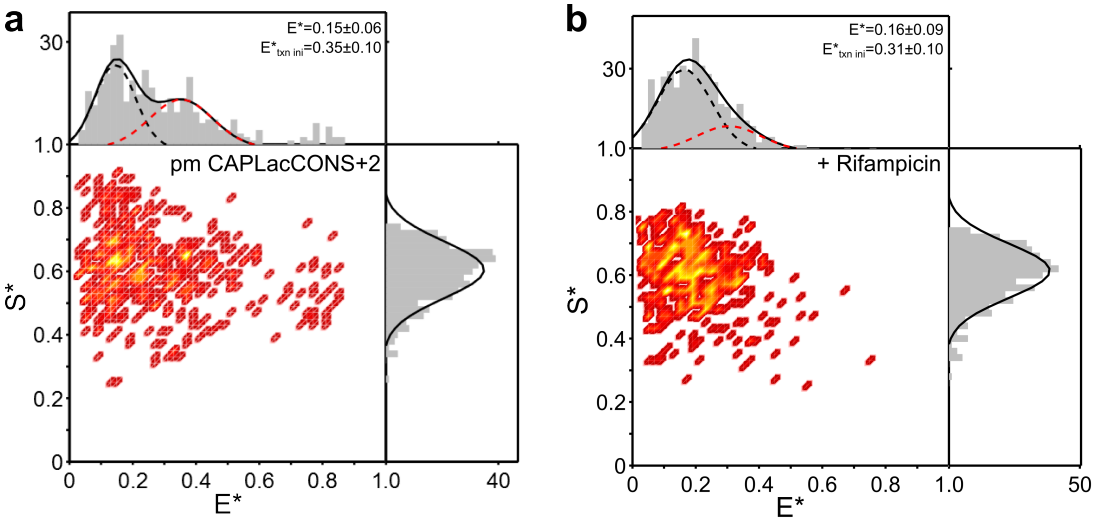

Figure 6.10: Single-molecule FRET observation of internalised pre-melted CAPLacCONS+2(-15/+20) into live *E. coli* cells. **a.** Observation of high FRET events (E*>0.6), which were absent **b.** after antibiotic treating with Rifampicin.

conclude on the regulatory effect of the pause during transcription initiation (262). Interestingly, a consensus pausing sequences, which has been found in translation start-sites (293) is caused by RNAP-nucleic acid interactions and a similar pause sequence was found in transcription elongation (294); pause sequence non-template DNA: G_{-11} G_{-10} C/T_{-1} G_{+1}, where -1 denotes the 3'-end of the RNA transcript.

The study of pausing for different promoter sequences and specifically highlighted pause-sequences *in vivo* should elucidate their roles in gene regulation and allow the study of kinetics and mechanistic steps in transcription initiation and elongation in live cells.

Contributions

I performed all experiments and data analysis, except for the *in vitro* transcription gel assay, which was performed by Dr. David Bauer. The CAPLacCONS+2(-15/+20) promoter DNAs were synthesised by Martin Kaller.

6.6 Supplementary information

6.6.1 Preparation of labelled DNA standards

Oligonucleotides were purchased from IBA GmbH. The sequences used are shown below; the highlighted **T** base was labelled either with Cy3B on the non-template strand (NT) or Atto647N on the template strand (T). The transcription start site is highlighted in blue and changes from the LacCONS+2 promoter sequence of the pre-melted promoter DNA and null-promoter DNA are highlighted in green. Long DNAs including the binding site for the transcription factor (catabolite activator protein – CAP) upstream were synthesised by Martin Kaller using ligation of short oligonucleotides ordered from IBA GmbH; CAPLacCONS+2(-15/+20), and pm CAPLacCONS+2 (-15/+20).

DNA sequences 5' to 3'

LacCONS+2(-5/-3) – NT: AGG CTT GAC ACT TTA TGC TTC GGC TCG TAT AAT G**T**G AGG AAT TGT GAG AGC GGA TAA CAA TTT C

LacCONS+2(-5/-3) – T: GAA ATT GTT ATC CGC TCT CAC AAT TCC **T**CA CAT TAT ACG AGC CGA AGC ATA AAG TGT CAA GCC T

LacCONS+2(-15/+20) – NT: GCA CCC CGG GCT TGA CAC TTT ATG CTT CGG C**T**C GTA TAA TGT GTG GAA TTG TGA GAG CGG ATA ACA ATT TCG GAT CCA TCG C

LacCONS+2(-15/+20) – T: GCG ATG GAT CCG AAA T**T**G TTA TCC GCT CTC ACA ATT CCA CAC ATT ATA CGA GCC GAA GCA TAA AGT GTC AAG CCC GGG GTG C

pm LacCONS+2(-15/+20) – NT: AGG CTT GAC ACT TTA TGC TTC GGC **T**CG TAG CCG TGT TGG AAT TGT GAG AGC GGA TAA CAA TTT C

pm LacCONS+2(-15/+20) – T: GAA A**T**T GTT ATC CGC TCT CAC AAT TCC ACA CAT TAT ACG AGC CGA AGC ATA AAG TGT CAA GCC T

Null-promoter(-15/+20) – NT: GCA CCC CGG GCT TGA CAC TTT ATG CTT CGG C**T**C GTG TGT TGT GTG GAA TTG TGA GAG CGG ATA ACA ATT TCG GAT CCA TCG C

Null-promoter(-15/+20) – T: GCG ATG GAT CCG AAA T**T**G TTA TCC GCT CTC ACA ATT CCA CAC AAC ACA CGA GCC GAA GCA TAA AGT GTC AAG CCC GGG GTG C

CAPLacCONS+2(-15/+20) – NT: CAG TGA GCG CAA CGC AAT AAA TGT GAT CTA GAT CAC ATT TTA GGC ACC CCA GGC TTG ACA CTT TAT GCT TCG GC**T** CGT ATA ATG TGT GGA ATT GTG AGA GCG GAT AAC AAT TTC

CAPLacCONS+2(-15/+20) – T: GAA ATT GTT ATC CGC TCT CAC AAT TCC ACA CAT TAT ACG AGC CGA AGC ATA AAG TGT CAA GCC TGG GGT GCC TAA AAT GTG ATC TAG ATC ACA TTT ATT GCG TTG CGC TCA CTG

pm CAPLacCONS+2(-15/+20) – NT: CAG TGA GCG CAA CGC AAT AAA TGT GAT CTA GAT CAC ATT TTA GGC ACC CCA GGC TTG ACA CTT TAT GCT TCG GC**T** CGT AGC CGT GTT GGA ATT GTG AGA GCG GAT AAC AAT TTC

pm CAPLacCONS+2(-15/+20) – T: GAA A**T**T GTT ATC CGC TCT CAC AAT TCC ACA CAT TAT ACG AGC CGA AGC ATA AAG TGT CAA GCC TGG GGT GCC TAA AAT GTG ATC TAG ATC ACA TTT ATT GCG TTG CGC TCA CTG

6.6.2 Electroporation

As described in sec. 3.6.3, and sec. 3.6.4. I added 1 mM EDTA before electroporation and electroporation was performed at 1.4 kV, which previously showed highest cell loading while maintaining cell viability (chapter 3, sec. 3.3.2).

6.6.3 Open complex formation

DNA-RNAP open complex were formed as described in (279). Briefly, promoter DNA (10 nM) and *E. coli* RNAP holoenzyme (50 nM; Epicentre, USA) were mixed in a total volume of 20 µL KG7 buffer (40 mM Hepes-NaOH pH7, 100 mM potassium glutamate, 10 mM $MgCl_2$, 1 mM DTT, 100 µg/mL bovine serum albumin, 5% glycerol, and 1 mM mercaptoethylamine) and subsequent incubation at 37 °C for 15 min.

6.6.4 Single-molecule FRET confocal microscopy

In vitro single-molecule FRET microscopy using an ALEX-scheme was performed on a custom-built confocal setup as sketched in Appendix A.2 and as previously described in chapter 3, sec. 3.6.7.

Open complex formation was performed as described above (sec. 6.6.3) and Rifampicin and Lipiarmycin were added to final concentration of 200 µg/mL wherever indicated. In initial transcription experiments, ribonucleotides ApA, UTP, and GTP at a concentration of 1 mM were added after open complex formation when indicated.

20 µL of sample at 10-50 pM final concentration of labelled promoter DNA were added onto a burned cover slide and the laser beam was focused about 20 µm into solution. Two 10 min data sets were acquired for each sample and single-molecule FRET histograms from confocal burst analysis were fitted with Gaussian distributions using least mean square fitting routines implemented in MATLAB (MathWorks).

6.6.5 Cell imaging

Single-molecule FRET measurements were performed on the setup described in appendix A.1 under HILO illumination (111) using 2 mW green excitation power and 20 ms exposure time in green continuous wave-mode, and using 2 mW green excitation power, 1 mW red excitation power, and 20 ms exposure time in ALEX-mode.

For antibiotic studies, 200 µg/mL chloramphenicol (Cam) or 200 µg/mL rifampicin (Rif) were added to SOC medium and cells were recovered for 30 min. Then, cells were 4x washed with PBS except for the final dilution, where cells were diluted in 100 µL PBS containing 200 µg/mL Cam or Rif and then transferred to the agarose pad.

6.6.6 Single-molecule FRET analysis

As described in chapter 4, sec. 4.7.8.

6.7 Supplementary figures

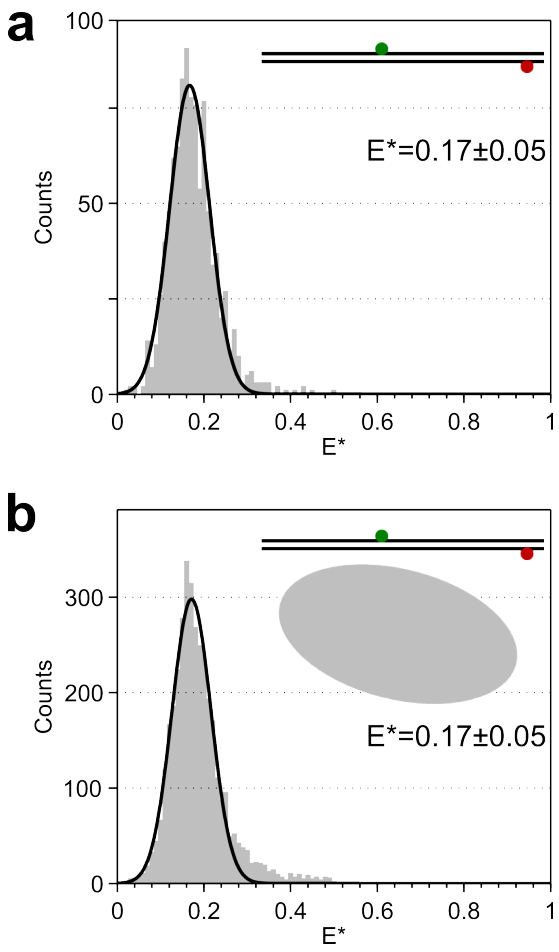

Figure 6.11: *In vitro* confocal single-molecule FRET study of **a.** null-promoter DNA-only, and **b.** after open complex formation reaction (null-promoter and RNAP present). No significant difference between the single-molecule FRET distributions could be observed.

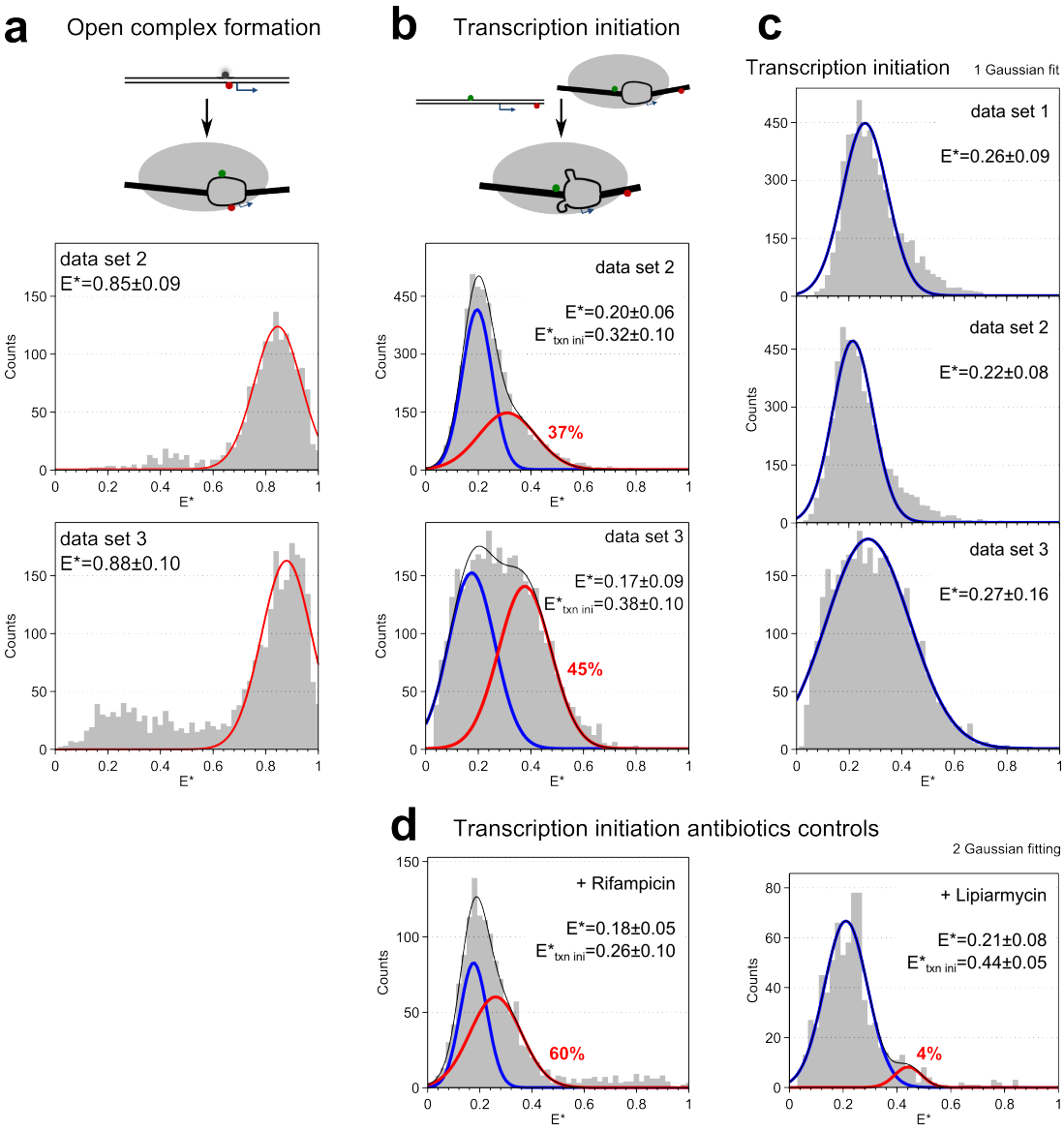

Figure 6.12: Second and third data set of *in vivo* single-molecule FRET measurements reporting on **a.** open complex formation and **b.** transcription initiation. **c.** Single Gaussian fits to FRET distributions of transcription initiation studies exhibiting higher fitting error κ^2 than double Gaussian fitting in b. **d.** Double Gaussian fits to single-molecule FRET distributions of antibiotic controls of transcription initiation.

Chapter 7

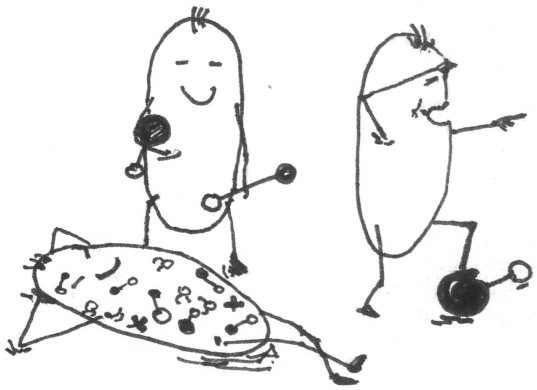

Conclusion

In vivo single-molecule FRET studies are still very challenging since doubly-labelled biomolecules with photostable and bright organic dyes have to be internalised into the living cells. Until now only a handful of studies have established *in vivo* single-molecule FRET capabilities and managed to internalise *in vitro* labelled biomolecules of interest into living prokaryotic (135, 62), and eukaryotic cells (60, 61).

In this work, I established single-molecule FRET studies in live bacterial cells and successfully overcame the three major challenges (59): (i) I optimised *in vivo* labelling, (ii) evaluated FRET-dye pairs, and (iii) performed live-cell FRET studies. To begin with, I established and optimised electroporation as means to internalise *in vitro* labelled nucleic acids and proteins into live *E. coli* cells (chapter 3). Next, I examined the performance of organic fluorophores as FRET-dye pairs, and characterised single-molecule FRET efficiencies using blunt-ended and protected DNA FRET standards (chapter 4).

Having demonstrated the single-molecule FRET capability *in vivo*, I performed initial proof-of-principle studies and studied the FRET signatures of a protein complex, the conformational changes of a DNA binding protein, and the FRET states of a gapped DNA substrate (chapter 4, sec. 4.5). Next, I determined the diffusion coefficient

of tRNA molecules and studied their spatial distribution in live bacteria (chapter 5). Finally, I studied important steps in transcription initiation such as the formation of the open complex and pausing during transcription initiation using different promoter DNA FRET labelling schemes (chapter 6).

Here, I discuss my findings in the broader context of the *in vivo* single-molecule FRET capability, highlighting remaining challenges, and outlining new exciting research paths employing single-molecule FRET to study conformational states, dynamics and potentially employ FRET as a structural tool in living cells.

Single-molecule FRET studies in live cells

In vivo **labelling** A common way to implant the superior photophysical properties of organic dyes into live-cell imaging and specifically promote *in vivo* single-molecule FRET studies is the internalisation of FRET-pair labelled proteins into live cells. To internalise *in vitro* labelled biomolecules into live bacteria, I employed electroporation (62). The major roadblock for DNA internalisation into cells via electroporation was the aggregation of nucleic acids; however, this can be successfully avoided by performing electroporation in the presence of EDTA (139). In the case of internalising proteins, the procedure's success was strongly dependent on the size and surface charge of the proteins used. We developed protocols through which the internalisation of proteins of interest can be tested and optimised (140). Potentially, the addition of chelating ions such as EDTA or the use of novel conductive polymer cuvettes could also help and prevent the aggregation of protein samples during electroporation, which has to be further investigated. Also, different internalisation methods like chemical cell permeabilisation, and heat shock could be tried, since specifically heat shock has proven to successfully internalise short DNA fragments into *E. coli* cells in other studies (135).

Due to the nature of bacterial cells, exhibiting a cell wall and cell membrane(s),

harsher electroporation settings have to be used than for electroporating mammalian cells (62, 243). Methods to internalise biomolecules into mammalian cells include sonication, electroporation, and detergent-mediated internalisation. However, microinjection seemed to become the method of choice for mammalian cells (60, 61), since different cell compartments can be targeted and the amount of internalised labelled biomolecules can be controlled. Microinjected mammalian cells show good viability post-procedure, owing partially to microinjection needles which are smaller in outer diameter ($<0.5\,\mu m$) and hence are likely to cause less damage. Yet, live-cell imaging of mammalian cells requires microscope stages with integrated temperature control, cell culture facility, and microinjection unit. Benjamin Schuler's lab recently developed such an integrated microscope stage and impressively showed its application in protein folding studies in live HeLa cells using confocal single-molecule FRET microscopy (61, 55).

Characterisation of FRET-dyes Very similar to *in vitro* single-molecule FRET measurements, organic dyes and FRET dye-pairs have to be characterised for their use in *in vivo* single-molecule FRET studies. Following such a characterisation, the FRET dye-pair Cy3B/Atto647N has proven ideally suited for studying single-molecule FRET signals *in vivo* (141). The extraordinary photostability of the acceptor fluorophore Atto647N has proven paramount for the observation of single-molecule FRET events for more than $10\,s$ in live bacteria. Additionally, the less hydrophobic dye Atto647 could also be used to monitor long-lasting single-molecule FRET signatures, while the cyanine dye Cy5 was shown not to disturb diffusion coefficient measurements in single-particle tracking studies *in vivo*.

The major limitation for *in vivo* single-molecule fluorescence or single-molecule FRET studies is still the photobleaching lifetime of organic fluorophores (295). A very attractive way of increasing the photostability of organic fluorophores was introduced

by the Blanchard lab in 2012. Altman and coworkers intermolecularly quenched cyanine fluorophores by conjugating triplet state quenchers to the dyes (69, 296). The 'Blanchard dyes' offer an up to 10-fold increase in photostability across a wide spectral range (450 nm-750 nm: Cy2, Cy3, Cy5, and Cy7). Also, the recently developed 'Janelia Fluor' dyes by the Lavis lab offer a 2-fold increase in photostability (297). These recently developed dyes should be tested in *in vivo* single-molecule fluorescence studies and should be characterised for single-molecule FRET studies. Further additives for live-cell imaging such as ProLong Diamond, and SlowFade Diamond (Thermo Fisher Scientific) could also be tested to increase the observation span of single-molecule fluorescence studies in live cells (295).

Optical instrumentation For imaging bacterial cells (1 µm in depth), I found the compromise offered by HILO illumination (111) sufficient to maintain good signal-to-noise for *in vivo* single-molecule localisation microscopy. However, as all experiments using HILO illumination were performed on a microscope setup, which was usually operated in TIRF-mode, I always had to moved the Tube-lens with a micrometer screw vertically to the optical axis to change from TIRF-mode to HILO-mode. A motorised stage moving the tube-lens and the dichroic mirror would be advisable to allow robust interchanging between TIRF and HILO illumination mode.

For imaging mammalian cells (>1 µm thickness), tissue, or even small organisms, light-sheet microscopy (LSM, (298)) appears to be a very attractive technique. The illumination of only a thin sheet of the specimen (0.5-5 µm thickness) leads to the decrease of cellular background fluorescence and increase in the observation time of the fluorescent markers in the specimen, since the illumination is mainly directed into the focal plane (299). Various forms of selective plane illumination microscopy (SPIM) in combination with fluorescence correlation spectroscopy (300), two-photon microscopy (301), and super-resolution imaging (302) employing different beam shapes

(Gaussian (298, 303), Bessel (304), Airy (305)) have been developed to date.

There have also been recent developments for single-molecule fluorescence detection. Scientific CMOS camera technology and localisation analysis routines have been improved and might soon overcome EMCCD camera technology providing larger FOVs and already image reconstruction rates of 30 Hz for super-resolution live-cell imaging (306).

Biological applications

Measuring conformational states and dynamics For detecting specific structural states of a protein of interest, the simplest single-molecule FRET assay reports on on/off-FRET signatures in presence or absence of the protein conformation similar to the study of the efficient internalisation of the E9-Im9 protein complex into live bacteria (chapter 4, sec. 4.5.1) or the quenchable single-molecule FRET assay reporting on the formation of the open complex (chapter 6, sec. 6.3). These studies do not often require difficult analysis routines and already cell-based intensity measurements could be employed to report on the dissociation of protein complexes or the stability of the open complex, making these simple single-molecule FRET assays very powerful.

Nonetheless, for the direct study of conformational changes, kinetic rates, and intermediate states in reaction paths, single-molecule FRET efficiencies have to be monitored over time. Dependent on the timescale of the conformational rearrangements and reaction times, confocal microscopy (sub-millisecond to milliseconds) or widefield microscopy (milliseconds to minutes) approaches could be employed. In the recent *in vivo* study of protein folding dynamics by König *et al.* confocal microscopy and novel analysis tools have proven powerful in monitoring intramolecular distance fluctuations of about 60 ns and protein folding dynamics on the 10 ms time-scale (61). In general, for elucidating protein conformational dynamics, experimental noise (e.g.

cellular autofluorescence, molecular motion, data acquisition etc.) has to be deconvolved from actual structural changes and more complex statistical analysis routines such as recurrence analysis (185), Hidden Markow Modelling or Bayesian analysis have to be employed to obtain single-molecule FRET states.

Linking spatial distribution with conformational changes Another level of complexity comes into play, if the conformational states should not only be linked in time but also distributed in space to relate conformational changes with the molecule's mobility or colocalisation with different cellular features. Here, widefield microscopy techniques are often advantageous, since they offer higher temporal resolution than confocal scanning techniques without sacrificing spatial information (307).
The spatial information can often be obtained quite easily, such as the localisation pattern of tRNA molecules within the bacterial cell (chapter 5). Linking the localisation pattern to cellular features might also require the introduction of a third spectrally distinct label. However, monitoring the conformational changes of diffusing molecules still remains the main challenge and requires advanced localisation analysis and single-particle tracking routines that suit the experimental data. Here, further testing and careful selection of single-particle tracking routines (116) could help to improve the tracking of the DNA binding protein KF (chapter 4, sec. 4.5.2) and could be a potential extension to the study of transcription initiation in live bacteria (chapter 6).

FRET as a structural tool The supreme challenge for *in vivo* single-molecule FRET studies remains the measurements of accurate molecular distances. Compared to other structural methods such as X-ray crystallography, and cryoelectron microscopy, which mainly report on structural snapshots, FRET offers the unique feature of directly capturing protein dynamics in living cells. Nevertheless, initial calibration studies and corrections of *in vivo* FRET efficiencies into accurate distance measurements have to be developed.

Here, protected DNA FRET standards offer a great means as *in vivo* single-molecule FRET markers and single-molecule FRET corrections could be applied as outlined in chapter 4, sec. 4.6. Then, single-molecule FRET levels of the gapped DNA substrate could be 'translated' into actual molecular distances and compared to the proposed structural models of DNA Polymerase I bound to the gapped DNA substrate (chapter 4, sec. 4.5.3).

By carefully designing the single-molecule FRET assay regarding the needs of the biological process to be studied, *in vivo* single-molecule FRET studies have the great potential to become a major tool in understanding protein conformational states and dynamics, as well as to help to elucidate kinetic rates, intermediate structural states and mechanistic details of important biological processes (such as gene expression and regulation) in the native environment of the living cells.

Appendix A

Microscope setups

A.1 Wide-field microscope setup

Widefield microscopy experiments were performed on the setup shown in Fig. A.1. The setup consisted of a customised inverted Olympus IX-71 microscope and two lasers, a 637 nm diode laser (Vortran Stradus, Vortran Laser Technology) and a 532 nm DPSS laser (MGL-III-532nm-100mW, CNI). Laser light was combined (dichroic mirror, 500 DRLP, Chroma) into a single-mode optical fiber (cut-off$<$460 nm, NA 0.13, FC-APC/FC-PC, Schäfter+Kirchhoff) and collimated before focusing on the back focal plane of the objective (UPLSAPO, oil immersion, 100x, NA 1.4, Olympus). Cellular and single-molecule fluorescence was collected through the same objective, separated from the excitation light (dichroic mirror dual-pass 545/650, Semrock), filtered through a long-pass filter (HQ545LP, Chroma) and a notch filter (NF02-633S, Semrock), and spectrally separated by a dichroic mirror (630DRLP, Omega). Each channel was imaged onto separate halves of an electron multiplying charge coupled device camera chip (iXon+, BI-887, Andor). The illumination for brightfield images comprised a white-light lamp (IX2-ILL100, Olympus), which was attached to the microscope body. Movies and images were recorded using Andor camera software.

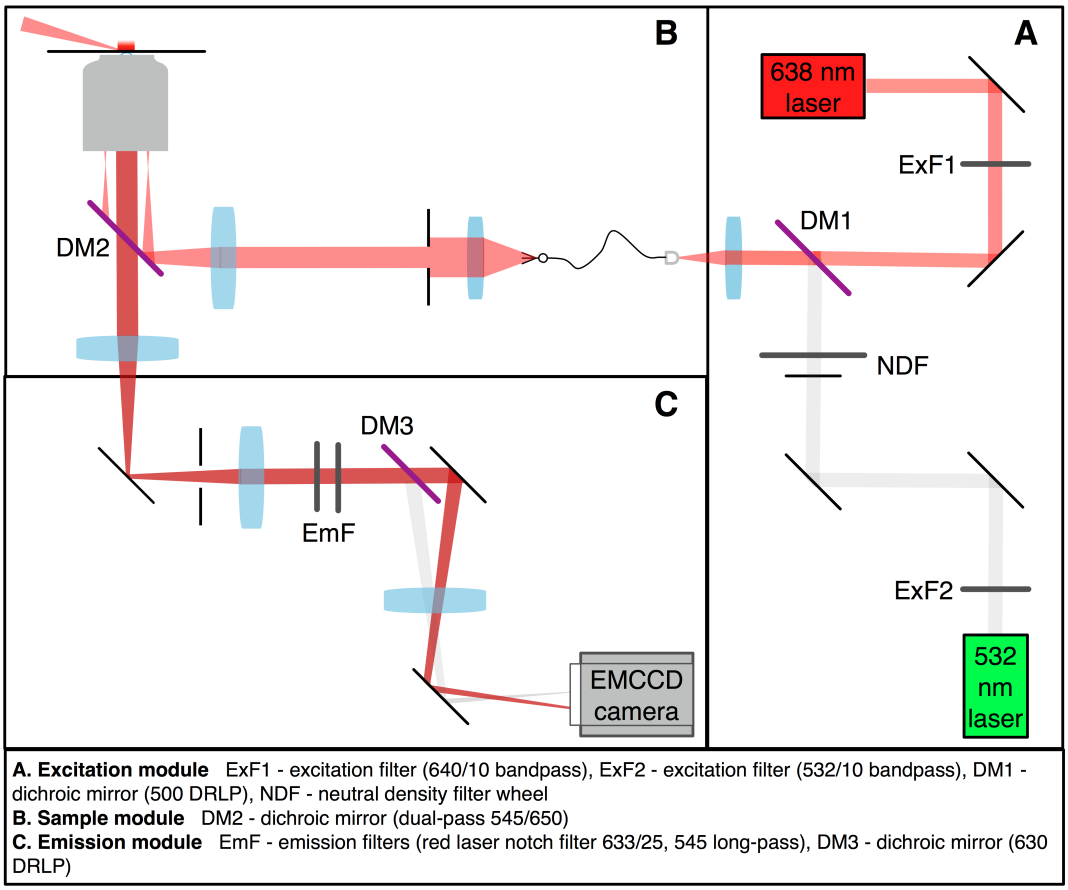

Figure A.1: Widefield microscope setup used for all live-cell imaging studies in this work. The setup was initially designed and built by Dr. Ludovic Le Reste and I maintained the setup throughout my studies.

Excitation laser powers were measured before entering the objective lens, the pixel size of the setup was measured to 96 nm, and the gain factor of the camera of 4.55 counts/photon was measured (150, 308).

A.2 Confocal microscope setup

Confocal single-molecule FRET and fluorescence correlation spectroscopy (FCS) measurements were performed on a custom-built confocal microscope (Fig. A.2). The confocal setup consisted of two laser lines, a 638 nm diode laser (Cube, Coherent, operated at 30 µW), and a 532 nm Nd:YAG laser (Samba, Cobolt, operated at

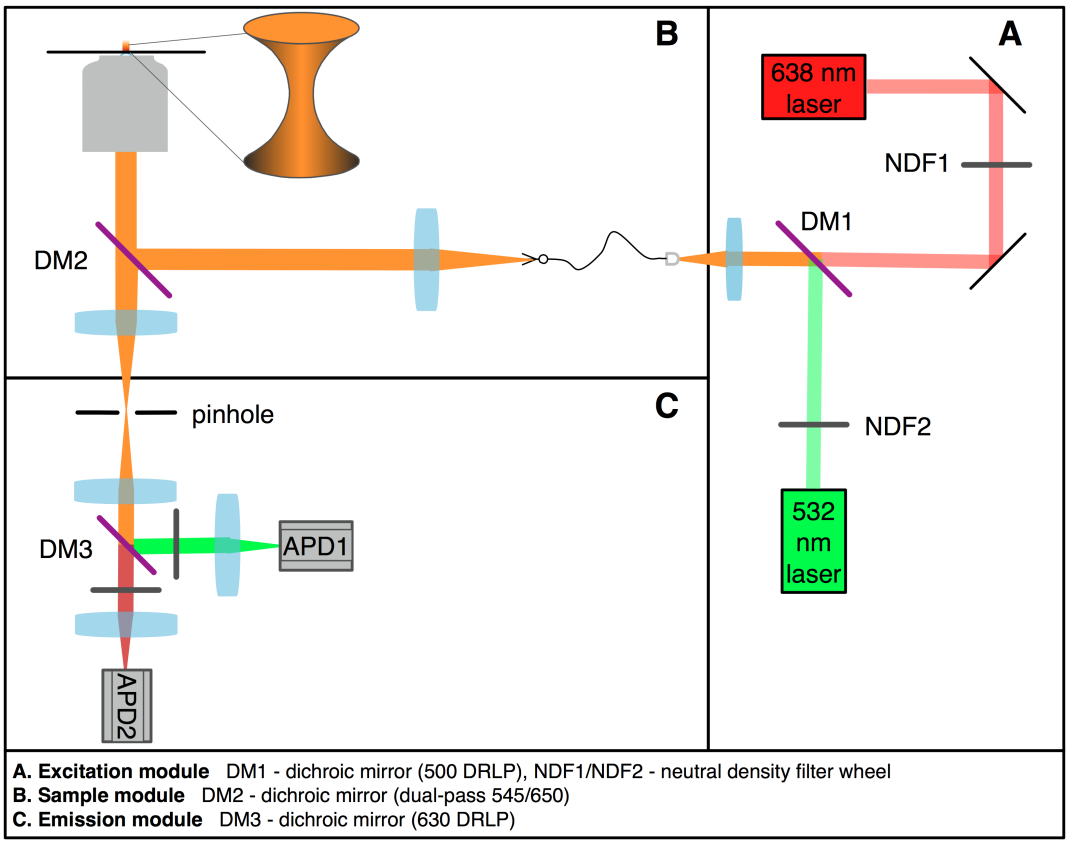

Figure A.2: Confocal microscopy setup used for all *in vitro* single-molecule FRET and FCS measurements. The setup was designed and built by Dr. Johannes Hohlbein and Dr. Geraint Evans, and maintained by both and Dr. Timothy Craggs during my studies.

120 µW), which were alternated at 20 kHz for single-molecule FRET measurements and which were operated in green continuous wave-mode for FCS measurements. The laser light was coupled into a 60x, 1.35 NA, UPlanSApo oil immersion objective (Olympus) by a dichroic beam splitter (z488/532/633rpc, Chroma). The fluorescence signal from diffusing molecule was collected by the same objective and spectrally separated by a dichroic mirror (630DRLP, Omega) and directed on two avalanche photodiodes (SPCM-AQR14, Perkin Elmer) with additional clean-up filters in front (HQ585/F70 and HQ650LP, Chroma). Photon arrival times were recorded with a PC counting board (National Instruments) and data processing was done using custom-written LabVIEW software (National Instruments).

Bibliography

[1] X. S. Xie, P. J. Choi, G. W. Li, N. K. Lee, and G. Lia. Single-molecule approach to molecular biology in living bacterial cells. *Annu Rev Biophys*, 37:417–44, 2008.

[2] S. J. Lord, H. L. Lee, and W. E. Moerner. Single-molecule spectroscopy and imaging of biomolecules in living cells. *Anal Chem*, 82(6):2192–203, 2010.

[3] S. W. Hell. Microscopy and its focal switch. *Nat Methods*, 6(1):24–32, 2009.

[4] J. Lippincott-Schwartz and S. Manley. Putting super-resolution fluorescence microscopy to work. *Nat Methods*, 6(1):21–3, 2009.

[5] M. C. Leake, J. H. Chandler, G. H. Wadhams, F. Bai, R. M. Berry, and J. P. Armitage. Stoichiometry and turnover in single, functioning membrane protein complexes. *Nature*, 443(7109):355–8, 2006.

[6] C. Eggeling, C. Ringemann, R. Medda, G. Schwarzmann, K. Sandhoff, S. Polyakova, V. N. Belov, B. Hein, C. von Middendorff, A. Schonle, and S. W. Hell. Direct observation of the nanoscale dynamics of membrane lipids in a living cell. *Nature*, 457(7233):1159–62, 2009.

[7] S. Liu, E. A. Abbondanzieri, J. W. Rausch, S. F. Le Grice, and X. Zhuang. Slide into action: dynamic shuttling of HIV reverse transcriptase on nucleic acid substrates. *Science*, 322(5904):1092–7, 2008.

[8] J. Yu, J. Xiao, X. Ren, K. Lao, and X. S. Xie. Probing gene expression in live cells, one protein molecule at a time. *Science*, 311(5767):1600–3, 2006.

[9] G. W. Li and X. S. Xie. Central dogma at the single-molecule level in living cells. *Nature*, 475(7356):308–15, 2011.

[10] S. Weiss. Fluorescence spectroscopy of single biomolecules. *Science*, 283 (5408):1676–83, 1999.

[11] E. B. Shera, N. K. Seitzinger, L. M. Davis, R. A. Keller, and S. A. Soper. Detection of single fluorescent molecules. *Chemical Physics Letters*, 174(6):553–557, 1990.

[12] W. P. Ambrose and W. E. Moerner. Phase-sensitive optical detection of ballistic phonon heat pulses using frequency-modulation spectroscopy and persistent spectral holes. *Phys Rev B Condens Matter*, 43(2):1743–1755, 1991.

[13] T. Basche and W. E. Moerner. Optical Modification of a Single Impurity Molecule in a Solid. *Nature*, 355(6358):335–337, 1992.

[14] E. Betzig and R. J. Chichester. Single molecules observed by near-field scanning optical microscopy. *Science*, 262(5138):1422–5, 1993.

[15] X. S. Xie and R. C. Dunn. Probing single molecule dynamics. *Science*, 265 (5170):361–4, 1994.

[16] M. Vrljic, S. Y. Nishimura, S. Brasselet, W. E. Moerner, and H. M. McConnell. Translational diffusion of individual class II MHC membrane proteins in cells. *Biophys J*, 83(5):2681–92, 2002.

[17] J. Deich, E. M. Judd, H. H. McAdams, and W. E. Moerner. Visualization of the movement of single histidine kinase molecules in live Caulobacter cells. *Proc Natl Acad Sci U S A*, 101(45):15921–6, 2004.

[18] O. Shimomura, F. H. Johnson, and Y. Saiga. Extraction, purification and properties of aequorin, a bioluminescent protein from the luminous hydromedusan, aequorea. *J Cell Comp Physiol*, 59:223–39, 1962.

[19] M. Chalfie, Y. Tu, G. Euskirchen, W. W. Ward, and D. C. Prasher. Green fluorescent protein as a marker for gene expression. *Science*, 263(5148):802–5, 1994.

[20] R. Y. Tsien. The green fluorescent protein. *Annu Rev Biochem*, 67:509–44, 1998.

[21] R. M. Dickson, A. B. Cubitt, R. Y. Tsien, and W. E. Moerner. On/off blinking and switching behaviour of single molecules of green fluorescent protein. *Nature*, 388(6640):355–8, 1997.

[22] G. H. Patterson and J. Lippincott-Schwartz. A photoactivatable GFP for selective photolabeling of proteins and cells. *Science*, 297(5588):1873–7, 2002.

[23] M. Heilemann, E. Margeat, R. Kasper, M. Sauer, and P. Tinnefeld. Carbocyanine dyes as efficient reversible single-molecule optical switch. *J Am Chem Soc*, 127(11):3801–6, 2005.

[24] E. Betzig. Proposed method for molecular optical imaging. *Opt Lett*, 20(3): 237–9, 1995.

[25] E. Abbé. Beiträge zur Theorie des Mikroskops und der mikroskopischen Wahrnehmung. *M. Schultzes Archiv für mikroskopische Anatomie*, 9:413–468, 1873.

[26] E. Betzig, G. H. Patterson, R. Sougrat, O. W. Lindwasser, S. Olenych, J. S. Bonifacino, M. W. Davidson, J. Lippincott-Schwartz, and H. F. Hess. Imaging intracellular fluorescent proteins at nanometer resolution. *Science*, 313(5793): 1642–5, 2006.

[27] M. J. Rust, M. Bates, and X. Zhuang. Sub-diffraction-limit imaging by stochastic optical reconstruction microscopy (storm). *Nat Methods*, 3(10):793–5, 2006.

[28] S. Manley, J. M. Gillette, G. H. Patterson, H. Shroff, H. F. Hess, E. Betzig, and J. Lippincott-Schwartz. High-density mapping of single-molecule trajectories with photoactivated localization microscopy. *Nat Methods*, 5(2):155–7, 2008.

[29] H. Shroff, C. G. Galbraith, J. A. Galbraith, and E. Betzig. Live-cell photoactivated localization microscopy of nanoscale adhesion dynamics. *Nat Methods*, 5(5):417–23, 2008.

[30] S. T. Hess, T. P. Girirajan, and M. D. Mason. Ultra-high resolution imaging by fluorescence photoactivation localization microscopy. *Biophys J*, 91(11): 4258–72, 2006.

[31] M. Bates, B. Huang, G. T. Dempsey, and X. Zhuang. Multicolor super-resolution imaging with photo-switchable fluorescent probes. *Science*, 317 (5845):1749–53, 2007.

[32] S. A. Jones, S. H. Shim, J. He, and X. Zhuang. Fast, three-dimensional super-resolution imaging of live cells. *Nat Methods*, 8(6):499–508, 2011.

[33] R. Wombacher, M. Heidbreder, S. van de Linde, M. P. Sheetz, M. Heilemann, V. W. Cornish, and M. Sauer. Live-cell super-resolution imaging with trimethoprim conjugates. *Nat Methods*, 7(9):717–9, 2010.

[34] A. Sharonov and R. M. Hochstrasser. Wide-field subdiffraction imaging by accumulated binding of diffusing probes. *Proc Natl Acad Sci U S A*, 103(50): 18911–6, 2006.

[35] S. W. Hell and J. Wichmann. Breaking the diffraction resolution limit by stimulated emission: stimulated-emission-depletion fluorescence microscopy. *Opt Lett*, 19(11):780–2, 1994.

[36] T. A. Klar and S. W. Hell. Subdiffraction resolution in far-field fluorescence microscopy. *Opt Lett*, 24(14):954–6, 1999.

[37] Y. Ito and P. Selenko. Cellular structural biology. *Curr Opin Struct Biol*, 20(5): 640–8, 2010.

[38] R. J. Ellis. Macromolecular crowding: an important but neglected aspect of the intracellular environment. *Curr Opin Struct Biol*, 11(1):114–9, 2001.

[39] R. Reyes-Lamothe, D. J. Sherratt, and M. C. Leake. Stoichiometry and architecture of active DNA replication machinery in Escherichia coli. *Science*, 328 (5977):498–501, 2010.

[40] J. Elf, G. W. Li, and X. S. Xie. Probing transcription factor dynamics at the single-molecule level in a living cell. *Science*, 316(5828):1191–4, 2007.

[41] Y. Taniguchi, P. J. Choi, G. W. Li, H. Chen, M. Babu, J. Hearn, A. Emili, and X. S. Xie. Quantifying E. coli proteome and transcriptome with single-molecule sensitivity in single cells. *Science*, 329(5991):533–8, 2010.

[42] P. J. Choi, L. Cai, K. Frieda, and X. S. Xie. A stochastic single-molecule event triggers phenotype switching of a bacterial cell. *Science*, 322(5900):442–6, 2008.

[43] B. P. English, V. Hauryliuk, A. Sanamrad, S. Tankov, N. H. Dekker, and J. Elf. Single-molecule investigations of the stringent response machinery in living bacterial cells. *Proc Natl Acad Sci U S A*, 108(31):E365–73, 2011.

[44] N. C. Shaner, P. A. Steinbach, and R. Y. Tsien. A guide to choosing fluorescent proteins. *Nat Methods*, 2(12):905–9, 2005.

[45] G. T. Dempsey, J. C. Vaughan, K. H. Chen, M. Bates, and X. Zhuang. Evaluation of fluorophores for optimal performance in localization-based super-resolution imaging. *Nat Methods*, 8(12):1027–36, 2011.

[46] T. Ha. Single-molecule fluorescence resonance energy transfer. *Methods*, 25 (1):78–86, 2001.

[47] T. Förster. Zwischenmolekulare Energiewanderung und Fluoreszenz. *Annalen der Physik*, 437:55–75, 1948.

[48] L. Stryer and R. P. Haugland. Energy transfer: a spectroscopic ruler. *Proc Natl Acad Sci U S A*, 58(2):719–26, 1967.

[49] B. Schuler, E. A. Lipman, and W. A. Eaton. Probing the free-energy surface for protein folding with single-molecule fluorescence spectroscopy. *Nature*, 419 (6908):743–7, 2002.

[50] E. A. Lipman, B. Schuler, O. Bakajin, and W. A. Eaton. Single-molecule measurement of protein folding kinetics. *Science*, 301(5637):1233–5, 2003.

[51] R. Zhao and D. Rueda. RNA folding dynamics by single-molecule fluorescence resonance energy transfer. *Methods*, 49(2):112–7, 2009.

[52] T. D. Christian, L. J. Romano, and D. Rueda. Single-molecule measurements of synthesis by DNA polymerase with base-pair resolution. *Proc Natl Acad Sci U S A*, 106(50):21109–14, 2009.

[53] Y. Santoso, C. M. Joyce, O. Potapova, L. Le Reste, J. Hohlbein, J. P. Torella, N. D. Grindley, and A. N. Kapanidis. Conformational transitions in DNA polymerase I revealed by single-molecule FRET. *Proc Natl Acad Sci U S A*, 107 (2):715–20, 2010.

[54] J. Hohlbein, L. Aigrain, T. D. Craggs, O. Bermek, O. Potapova, P. Shoolizadeh, N. D. Grindley, C. M. Joyce, and A. N. Kapanidis. Conformational landscapes of DNA polymerase I and mutator derivatives establish fidelity checkpoints for nucleotide insertion. *Nat Commun*, 4:2131, 2013.

[55] A. Plochowietz and A. N. Kapanidis. Single in the (Cell) City: a protein-folding story. *Nat Methods*, 12(8):715–6, 2015.

[56] B. Ponsioen, J. Zhao, J. Riedl, F. Zwartkruis, G. van der Krogt, M. Zaccolo, W. H. Moolenaar, J. L. Bos, and K. Jalink. Detecting cAMP-induced Epac activation by fluorescence resonance energy transfer: Epac as a novel cAMP indicator. *EMBO Rep*, 5(12):1176–80, 2004.

[57] S. Ebbinghaus, A. Dhar, J. D. McDonald, and M. Gruebele. Protein folding stability and dynamics imaged in a living cell. *Nat Methods*, 7(4):319–23, 2010.

[58] M. Guo, Y. Xu, and M. Gruebele. Temperature dependence of protein folding kinetics in living cells. *Proc Natl Acad Sci U S A*, 109(44):17863–7, 2012.

[59] M. Sustarsic and A. N. Kapanidis. Taking the ruler to the jungle: single-molecule FRET for understanding biomolecular structure and dynamics in live cells. *Curr Opin Struct Biol*, 34:52–59, 2015.

[60] J. J. Sakon and K. R. Weninger. Detecting the conformation of individual proteins in live cells. *Nat Methods*, 7(3):203–5, 2010.

[61] I. Konig, A. Zarrine-Afsar, M. Aznauryan, A. Soranno, B. Wunderlich, F. Dingfelder, J. C. Stuber, A. Pluckthun, D. Nettels, and B. Schuler. Single-molecule spectroscopy of protein conformational dynamics in live eukaryotic cells. *Nat Methods*, 2015.

[62] R. Crawford, J. P. Torella, L. Aigrain, A. Plochowietz, K. Gryte, S. Uphoff, and A. N. Kapanidis. Long-lived intracellular single-molecule fluorescence using electroporated molecules. *Biophys J*, 105(11):2439–50, 2013.

[63] W. E. Moerner. New directions in single-molecule imaging and analysis. *Proc Natl Acad Sci U S A*, 104(31):12596–602, 2007.

[64] J.R. Lakowicz. *Principles of Fluorescence Spectroscopy*, volume Third Edition. Springer, 2006.

[65] C. P. Toseland. Fluorescent labeling and modification of proteins. *J Chem Biol*, 6(3):85–95, 2013.

[66] K. Kolmakov, V. N. Belov, J. Bierwagen, C. Ringemann, V. Muller, C. Eggeling, and S. W. Hell. Red-emitting rhodamine dyes for fluorescence microscopy and nanoscopy. *Chemistry*, 16(1):158–66, 2010.

[67] M. Sauer, J. Hofkens, and J. Enderlein. *Handbook of Fluorescence Spectroscopy and Imaging*. John Wiley and Sons, 2011.

[68] T. Ha and P. Tinnefeld. Photophysics of fluorescent probes for single-molecule biophysics and super-resolution imaging. *Annu Rev Phys Chem*, 63:595–617, 2012.

[69] R. B. Altman, Q. Zheng, Z. Zhou, D. S. Terry, J. D. Warren, and S. C. Blanchard. Enhanced photostability of cyanine fluorophores across the visible spectrum. *Nature Methods*, 9(5):428–429, 2012.

[70] G. Striker, V. Subramaniam, C. A. M. Seidel, and A. Volkmer. Photochromicity and fluorescence lifetimes of green fluorescent protein. *Journal of Physical Chemistry B*, 103(40):8612–8617, 1999.

[71] B. Seefeldt, R. Kasper, T. Seidel, P. Tinnefeld, K. J. Dietz, M. Heilemann, and M. Sauer. Fluorescent proteins for single-molecule fluorescence applications. *J Biophotonics*, 1(1):74–82, 2008.

[72] M. Cooper, A. Ebner, M. Briggs, M. Burrows, N. Gardner, R. Richardson, and R. West. Cy3B: improving the performance of cyanine dyes. *J Fluoresc*, 14(2): 145–50, 2004.

[73] ATTO-TEC GmbH. `https://www.atto-tec.com/attotecshop/index.php?cat=c19_600-nm---700-nm-600-nm---700-nm.html&XTCsid=e5852996b8a067b8b14a3c0f22937e20`. last access:10 Aug, 2015.

[74] GE Healthcare. `http://www.gelifesciences.com/webapp/wcs/stores/servlet/catalog/en/GELifeSciences-de/products/AlternativeProductStructure_16502/`. last access:10 Aug, 2015.

[75] Invitrogen. `https://www.lifetechnologies.com/uk/en/home/life-science/cell-analysis/fluorophores/alexa-fluor-647.html`. last access:10 Aug, 2015.

[76] Lumiprobe. `http://www.lumiprobe.com/p/cy7-nhs-ester`. last access: 10 Aug, 2015.

[77] W. E. Moerner. Single-molecule optical spectroscopy of autofluorescent proteins. *Journal of Chemical Physics*, 117(24):10925–10937, 2002.

[78] E. M. Stennett, M. A. Ciuba, and M. Levitus. Photophysical processes in single molecule organic fluorescent probes. *Chem Soc Rev*, 43(4):1057–75, 2014.

[79] F. Yang, L. G. Moss, and Jr. Phillips, G. N. The molecular structure of green fluorescent protein. *Nat Biotechnol*, 14(10):1246–51, 1996.

[80] C. Eggeling, J. Widengren, R. Rigler, and C. A. Seidel. Photobleaching of Fluorescent Dyes under Conditions Used for Single-Molecule Detection: Evidence of Two-Step Photolysis. *Anal Chem*, 70(13):2651–9, 1998.

[81] J. Widengren, A. Chmyrov, C. Eggeling, P. A. Lofdahl, and C. A. Seidel. Strategies to improve photostabilities in ultrasensitive fluorescence spectroscopy. *J Phys Chem A*, 111(3):429–40, 2007.

[82] I. Rasnik, S. A. McKinney, and T. Ha. Nonblinking and long-lasting single-molecule fluorescence imaging. *Nat Methods*, 3(11):891–3, 2006.

[83] R. E. Benesch and R. Benesch. Enzymatic removal of oxygen for polarography and related methods. *Science*, 118(3068):447–8, 1953.

[84] Y. Harada, K. Sakurada, T. Aoki, D. D. Thomas, and T. Yanagida. Mechanochemical coupling in actomyosin energy transduction studied by in vitro movement assay. *J Mol Biol*, 216(1):49–68, 1990.

[85] M. Swoboda, J. Henig, H. M. Cheng, D. Brugger, D. Haltrich, N. Plumere, and M. Schlierf. Enzymatic oxygen scavenging for photostability without pH drop in single-molecule experiments. *ACS Nano*, 6(7):6364–9, 2012.

[86] A. Kishino and T. Yanagida. Force measurements by micromanipulation of a single actin filament by glass needles. *Nature*, 334(6177):74–6, 1988.

[87] M. Bates, T. R. Blosser, and X. Zhuang. Short-range spectroscopic ruler based on a single-molecule optical switch. *Phys Rev Lett*, 94(10):108101, 2005.

[88] J. Vogelsang, R. Kasper, C. Steinhauer, B. Person, M. Heilemann, M. Sauer, and P. Tinnefeld. A reducing and oxidizing system minimizes photobleaching and blinking of fluorescent dyes. *Angew Chem Int Ed Engl*, 47(29):5465–9, 2008.

[89] T. Cordes, J. Vogelsang, and P. Tinnefeld. On the Mechanism of Trolox as Antiblinking and Antibleaching Reagent. *Journal of the American Chemical Society*, 131(14):5018–+, 2009.

[90] G. Donnert, C. Eggeling, and S. W. Hell. Major signal increase in fluorescence microscopy through dark-state relaxation. *Nat Methods*, 4(1):81–6, 2007.

[91] Y. M. Go and D. P. Jones. Redox compartmentalization in eukaryotic cells. *Biochimica Et Biophysica Acta-General Subjects*, 1780(11):1271–1290, 2008.

[92] T. Förster. Energiewanderung und Fluoreszenz. *Naturwissenschaften*, 6:166–175, 1946.

[93] T. Ha, T. Enderle, D. F. Ogletree, D. S. Chemla, P. R. Selvin, and S. Weiss. Probing the interaction between two single molecules: fluorescence resonance energy transfer between a single donor and a single acceptor. *Proc Natl Acad Sci U S A*, 93(13):6264–8, 1996.

[94] R. M. Clegg, A. I. Murchie, A. Zechel, and D. M. Lilley. Observing the helical geometry of double-stranded DNA in solution by fluorescence resonance energy transfer. *Proc Natl Acad Sci U S A*, 90(7):2994–8, 1993.

[95] S. J. Holden, S. Uphoff, J. Hohlbein, D. Yadin, L. Le Reste, O. J. Britton, and A. N. Kapanidis. Defining the limits of single-molecule FRET resolution in TIRF microscopy. *Biophys J*, 99(9):3102–11, 2010.

[96] G. H. Patterson, D. W. Piston, and B. G. Barisas. Forster distances between green fluorescent protein pairs. *Analytical Biochemistry*, 284(2):438–440, 2000.

[97] T. Ha, A. Y. Ting, J. Liang, W. B. Caldwell, A. A. Deniz, D. S. Chemla, P. G. Schultz, and S. Weiss. Single-molecule fluorescence spectroscopy of enzyme conformational dynamics and cleavage mechanism. *Proc Natl Acad Sci U S A*, 96(3):893–8, 1999.

[98] N. K. Lee, A. N. Kapanidis, Y. Wang, X. Michalet, J. Mukhopadhyay, R. H. Ebright, and S. Weiss. Accurate FRET measurements within single diffusing biomolecules using alternating-laser excitation. *Biophys J*, 88(4):2939–53, 2005.

[99] J. Hohlbein, T. D. Craggs, and T. Cordes. Alternating-laser excitation: single-molecule FRET and beyond. *Chem Soc Rev*, 43(4):1156–71, 2014.

[100] R. E. Dale, J. Eisinger, and W. E. Blumberg. The orientational freedom of molecular probes. The orientation factor in intramolecular energy transfer. *Biophys J*, 26(2):161–93, 1979.

[101] A. Muschielok, J. Andrecka, A. Jawhari, F. Bruckner, P. Cramer, and J. Michaelis. A nano-positioning system for macromolecular structural analysis. *Nat Methods*, 5(11):965–71, 2008.

[102] S. Kalinin, T. Peulen, S. Sindbert, P. J. Rothwell, S. Berger, T. Restle, R. S. Goody, H. Gohlke, and C. A. Seidel. A toolkit and benchmark study for FRET-restrained high-precision structural modeling. *Nat Methods*, 9(12):1218–25, 2012.

[103] A. N. Kapanidis, N. K. Lee, T. A. Laurence, S. Doose, E. Margeat, and S. Weiss. Fluorescence-aided molecule sorting: analysis of structure and interactions by alternating-laser excitation of single molecules. *Proc Natl Acad Sci U S A*, 101(24):8936–41, 2004.

[104] A. A. Deniz, M. Dahan, J. R. Grunwell, T. Ha, A. E. Faulhaber, D. S. Chemla, S. Weiss, and P. G. Schultz. Single-pair fluorescence resonance energy transfer on freely diffusing molecules: observation of forster distance dependence and subpopulations. *Proc Natl Acad Sci U S A*, 96(7):3670–5, 1999.

[105] A. N. Kapanidis, E. Margeat, S. O. Ho, E. Kortkhonjia, S. Weiss, and R. H. Ebright. Initial transcription by RNA polymerase proceeds through a DNA-scrunching mechanism. *Science*, 314(5802):1144–7, 2006.

[106] R. Rigler and E. S. Elson. *Fluorescence Correlation Spectroscopy- Theory and Applications*. Springer Verlag, 1993.

[107] R. Rigler, P. Grasselli, and M. Ehrenberg. Fluorescence Correlation Spectroscopy and Application to the Study of Brownian-Motion of Biopolymers. *Physica Scripta*, 19(4):486–490, 1979.

[108] T. Funatsu, Y. Harada, M. Tokunaga, K. Saito, and T. Yanagida. Imaging of single fluorescent molecules and individual ATP turnovers by single myosin molecules in aqueous solution. *Nature*, 374(6522):555–9, 1995.

[109] D. Axelrod, N. L. Thompson, and T. P. Burghardt. Total internal inflection fluorescent microscopy. *J Microsc*, 129(Pt 1):19–28, 1983.

[110] D. Axelrod. Total internal reflection fluorescence microscopy in cell biology. *Traffic*, 2(11):764–74, 2001.

[111] M. Tokunaga, N. Imamoto, and K. Sakata-Sogawa. Highly inclined thin illumination enables clear single-molecule imaging in cells. *Nat Methods*, 5(2): 159–61, 2008.

[112] B. Zhang, J. Zerubia, and J. C. Olivo-Marin. Gaussian approximations of fluorescence microscope point-spread function models. *Appl Opt*, 46(10):1819–29, 2007.

[113] H. Deschout, F. Cella Zanacchi, M. Mlodzianoski, A. Diaspro, J. Bewersdorf, S. T. Hess, and K. Braeckmans. Precisely and accurately localizing single emitters in fluorescence microscopy. *Nat Methods*, 11(3):253–66, 2014.

[114] J. C. Crocker and D. G. Grier. Methods of digital video microscopy for colloidal studies. *Journal of Colloid and Interface Science*, 179(1):298–310, 1996.

[115] S. Uphoff, R. Reyes-Lamothe, F. Garza de Leon, D. J. Sherratt, and A. N. Kapanidis. Single-molecule DNA repair in live bacteria. *Proc Natl Acad Sci U S A*, 110(20):8063–8, 2013.

[116] N. Chenouard, I. Smal, F. de Chaumont, M. Maska, I. F. Sbalzarini, Y. Gong, J. Cardinale, C. Carthel, S. Coraluppi, M. Winter, A. R. Cohen, W. J. Godinez, K. Rohr, Y. Kalaidzidis, L. Liang, J. Duncan, H. Shen, Y. Xu, K. E. Magnusson, J. Jalden, H. M. Blau, P. Paul-Gilloteaux, P. Roudot, C. Kervrann, F. Waharte,

J. Y. Tinevez, S. L. Shorte, J. Willemse, K. Celler, G. P. van Wezel, H. W. Dan, Y. S. Tsai, C. Ortiz de Solorzano, J. C. Olivo-Marin, and E. Meijering. Objective comparison of particle tracking methods. *Nat Methods*, 11(3):281–9, 2014.

[117] X. Michalet and A. J. Berglund. Optimal diffusion coefficient estimation in single-particle tracking. *Phys Rev E Stat Nonlin Soft Matter Phys*, 85(6 Pt 1):061916, 2012.

[118] A. Keppler, S. Gendreizig, T. Gronemeyer, H. Pick, H. Vogel, and K. Johnsson. A general method for the covalent labeling of fusion proteins with small molecules in vivo. *Nat Biotechnol*, 21(1):86–9, 2003.

[119] J. Ries, C. Kaplan, E. Platonova, H. Eghlidi, and H. Ewers. A simple, versatile method for GFP-based super-resolution microscopy via nanobodies. *Nat Methods*, 9(6):582–4, 2012.

[120] C. C. Liu and P. G. Schultz. Adding new chemistries to the genetic code. *Annu Rev Biochem*, 79:413–44, 2010.

[121] M. J. Hinner and K. Johnsson. How to obtain labeled proteins and what to do with them. *Curr Opin Biotechnol*, 21(6):766–76, 2010.

[122] V. Ratner, E. Kahana, M. Eichler, and E. Haas. A general strategy for site-specific double labeling of globular proteins for kinetic FRET studies. *Bioconjug Chem*, 13(5):1163–70, 2002.

[123] M. C. Puljung and W. N. Zagotta. Labeling of specific cysteines in proteins using reversible metal protection. *Biophys J*, 100(10):2513–21, 2011.

[124] E. M. Brustad, E. A. Lemke, P. G. Schultz, and A. A. Deniz. A general and efficient method for the site-specific dual-labeling of proteins for single molecule fluorescence resonance energy transfer. *J Am Chem Soc*, 130(52):17664–5, 2008.

[125] J. Kim, M. H. Seo, S. Lee, K. Cho, A. Yang, K. Woo, H. S. Kim, and H. S. Park. Simple and efficient strategy for site-specific dual labeling of proteins for single-molecule fluorescence resonance energy transfer analysis. *Anal Chem*, 85(3):1468–74, 2013.

[126] Y. Sako, S. Minoghchi, and T. Yanagida. Single-molecule imaging of EGFR signalling on the surface of living cells. *Nat Cell Biol*, 2(3):168–72, 2000.

[127] S. K. Silverman. In vitro selection, characterization, and application of deoxyribozymes that cleave RNA. *Nucleic Acids Res*, 33(19):6151–63, 2005.

[128] J. A. Wyber, J. Andrews, and A. D'Emanuele. The use of sonication for the efficient delivery of plasmid DNA into cells. *Pharm Res*, 14(6):750–6, 1997.

[129] P. L. McNeil, R. F. Murphy, F. Lanni, and D. L. Taylor. A method for incorporating macromolecules into adherent cells. *J Cell Biol*, 98(4):1556–64, 1984.

[130] M. S. Clarke and P. L. McNeil. Syringe loading introduces macromolecules into living mammalian cell cytosol. *J Cell Sci*, 102 (Pt 3):533–41, 1992.

[131] T. Kues, A. Dickmanns, R. Luhrmann, R. Peters, and U. Kubitscheck. High intranuclear mobility and dynamic clustering of the splicing factor U1 snRNP observed by single particle tracking. *Proc Natl Acad Sci U S A*, 98(21):12021–6, 2001.

[132] J. P. Knemeyer, D. P. Herten, and M. Sauer. Detection and identification of single molecules in living cells using spectrally resolved fluorescence lifetime imaging microscopy. *Anal Chem*, 75(9):2147–53, 2003.

[133] H. Murakoshi, R. Iino, T. Kobayashi, T. Fujiwara, C. Ohshima, A. Yoshimura, and A. Kusumi. Single-molecule imaging analysis of Ras activation in living cells. *Proc Natl Acad Sci U S A*, 101(19):7317–22, 2004.

[134] W. J. Dower, J. F. Miller, and C. W. Ragsdale. High efficiency transformation of E. coli by high voltage electroporation. *Nucleic Acids Res*, 16(13):6127–45, 1988.

[135] T. Fessl, F. Adamec, T. Polivka, S. Foldynova-Trantirkova, F. Vacha, and L. Trantirek. Towards characterization of DNA structure under physiological conditions in vivo at the single-molecule level using single-pair FRET. *Nucleic Acids Res*, 40(16):e121, 2012.

[136] E. Neumann, M. Schaefer-Ridder, Y. Wang, and P. H. Hofschneider. Gene transfer into mouse lyoma cells by electroporation in high electric fields. *EMBO J*, 1(7):841–5, 1982.

[137] T. K. Wong and E. Neumann. Electric field mediated gene transfer. *Biochem Biophys Res Commun*, 107(2):584–7, 1982.

[138] M. Hibino, M. Shigemori, H. Itoh, K. Nagayama, and Jr. Kinosita, K. Membrane conductance of an electroporated cell analyzed by submicrosecond imaging of transmembrane potential. *Biophys J*, 59(1):209–20, 1991.

[139] A. Plochowietz, A. El-Sagheer, T. Brown, and A. N. Kapanidis. Protected DNA FRET standards for characterization of single-molecule FRET in live bacteria. *in preparation*, 2015.

[140] M. Sustarsic, A. Plochowietz, L. Aigrain, Y. Yuzenkova, N. Zenkin, and A. Kapanidis. Optimized delivery of fluorescently labeled proteins in live bacteria using electroporation. *Histochem Cell Biol*, 142(1):113–24, 2014.

[141] A. Plochowietz, R. Crawford, and A. N. Kapanidis. Characterization of organic fluorophores for in vivo FRET studies based on electroporated molecules. *Phys Chem Chem Phys*, 16(25):12688–94, 2014.

[142] L. Aigrain, M. Sustarsic, R. Crawford, A. Plochowietz, and A. N. Kapanidis. Internalization and observation of fluorescent biomolecules in living microorganisms via electroporation. *J Vis Exp*, (96), 2015.

[143] A. Plochowietz, I. Farrell, Z. Smilansky, B. S. Cooperman, and A. N. Kapanidis. Transfer RNA mobility and spatial organization during active translation in live bacteria studied at the single-molecule level. *in preparation*, 2015.

[144] S. C. Schultz, G. C. Shields, and T. A. Steitz. Crystal structure of a CAP-DNA complex: the DNA is bent by 90 degrees. *Science*, 253(5023):1001–7, 1991.

[145] Y. Kim, S. H. Eom, J. Wang, D. S. Lee, S. W. Suh, and T. A. Steitz. Crystal structure of Thermus aquaticus DNA polymerase. *Nature*, 376(6541):612–6, 1995.

[146] EC Friedberg. DNA repair and mutagenesis. *American Society for Microbiology*, (2nd ed.), 2006.

[147] E. Haustein and P. Schwille. Fluorescence correlation spectroscopy: novel variations of an established technique. *Annu Rev Biophys Biomol Struct*, 36: 151–69, 2007.

[148] S. A. Kooijmans, S. Stremersch, K. Braeckmans, S. C. de Smedt, A. Hendrix, M. J. Wood, R. M. Schiffelers, K. Raemdonck, and P. Vader. Electroporation-induced siRNA precipitation obscures the efficiency of siRNA loading into extracellular vesicles. *J Control Release*, 172(1):229–38, 2013.

[149] J. E. Moses and A. D. Moorhouse. The growing applications of click chemistry. *Chem Soc Rev*, 36(8):1249–62, 2007.

[150] A. Plochowietz. Single-molecule fluorescence of internalised biomolecules in live bacteria. *Thesis*, MSc by research. University of Oxford.(ORA (Oxford University Research Archive)), 2012.

[151] J. T. Keer and L. Birch. Molecular methods for the assessment of bacterial viability. *J Microbiol Methods*, 53(2):175–83, 2003.

[152] R. Crawford. Single-molecule DNA sensors and cages for transcription factors in vitro and in vivo. *Thesis*, DPhil. University of Oxford.(ORA (Oxford University Research Archive)), 2011.

[153] P.R. Selvin and T. Ha. *Single-Molecule Techniques: A Laboratory Manual*. Cold Spring Harbor Laboratory Press., 2007.

[154] K. Lymperopoulos, R. Crawford, J. P. Torella, M. Heilemann, L. C. Hwang, S. J. Holden, and A. N. Kapanidis. Single-molecule DNA biosensors for protein and ligand detection. *Angew Chem Int Ed Engl*, 49(7):1316–20, 2010.

[155] P. Muller, P. Schwille, and T. Weidemann. PyCorrFit-generic data evaluation for fluorescence correlation spectroscopy. *Bioinformatics*, 30(17):2532–3, 2014.

[156] J. Widengren, R. Rigler, and U. Mets. Triplet-state monitoring by fluorescence correlation spectroscopy. *J Fluoresc*, 4(3):255–8, 1994.

[157] J. W. Young, J. C. Locke, A. Altinok, N. Rosenfeld, T. Bacarian, P. S. Swain, E. Mjolsness, and M. B. Elowitz. Measuring single-cell gene expression dynamics in bacteria using fluorescence time-lapse microscopy. *Nat Protoc*, 7 (1):80–8, 2012.

[158] G. Q. Tang, R. Roy, R. P. Bandwar, T. Ha, and S. S. Patel. Real-time observation of the transition from transcription initiation to elongation of the RNA polymerase. *Proc Natl Acad Sci U S A*, 106(52):22175–80, 2009.

[159] B. Schuler and W. A. Eaton. Protein folding studied by single-molecule FRET. *Curr Opin Struct Biol*, 18(1):16–26, 2008.

[160] N. Di Fiori and A. Meller. The Effect of dye-dye interactions on the spatial resolution of single-molecule FRET measurements in nucleic acids. *Biophys J*, 98(10):2265–72, 2010.

[161] M. A. Morgan, K. Okamoto, J. D. Kahn, and D. S. English. Single-molecule spectroscopic determination of lac repressor-DNA loop conformation. *Biophys J*, 89(4):2588–96, 2005.

[162] S. Myong, S. Cui, P. V. Cornish, A. Kirchhofer, M. U. Gack, J. U. Jung, K. P. Hopfner, and T. Ha. Cytosolic viral sensor RIG-I is a 5'-triphosphate-dependent translocase on double-stranded RNA. *Science*, 323(5917):1070–4, 2009.

[163] H. Hwang, H. Kim, and S. Myong. Protein induced fluorescence enhancement as a single molecule assay with short distance sensitivity. *Proc Natl Acad Sci U S A*, 108(18):7414–8, 2011.

[164] H. Hwang and S. Myong. Protein induced fluorescence enhancement (pife) for probing protein-nucleic acid interactions. *Chem Soc Rev*, 43(4):1221–9, 2014.

[165] M. B. Sherman, R. H. Guenther, F. Tama, T. L. Sit, C. L. Brooks, A. M. Mikhailov, E. V. Orlova, T. S. Baker, and S. A. Lommel. Removal of divalent cations induces structural transitions in red clover necrotic mosaic virus, revealing a potential mechanism for RNA release. *J Virol*, 80(21):10395–406, 2006.

[166] K. A. Merchant, R. B. Best, J. M. Louis, I. V. Gopich, and W. A. Eaton. Characterizing the unfolded states of proteins using single-molecule FRET spectroscopy and molecular simulations. *Proc Natl Acad Sci U S A*, 104(5):1528–33, 2007.

[167] J. Vogelsang, S. Doose, M. Sauer, and P. Tinnefeld. Single-molecule fluorescence resonance energy transfer in nanopipets: improving distance resolution and concentration range. *Anal Chem*, 79(19):7367–75, 2007.

[168] G. W. Evans, J. Hohlbein, T. Craggs, L. Aigrain, and A. N. Kapanidis. Real-time single-molecule studies of the motions of DNA polymerase fingers illuminate DNA synthesis mechanisms. *Nucleic Acids Res*, 2015.

[169] S. Brasselet, E. J. G. Peterman, A. Miyawaki, and W. E. Moerner. Single-molecule fluorescence resonant energy transfer in calcium concentration dependent cameleon. *Journal of Physical Chemistry B*, 104(15):3676–3682, 2000.

[170] Y. Phillip, V. Kiss, and G. Schreiber. Protein-binding dynamics imaged in a living cell. *Proc Natl Acad Sci U S A*, 109(5):1461–6, 2012.

[171] S. van de Linde, M. Heilemann, and M. Sauer. Live-cell super-resolution imaging with synthetic fluorophores. *Annu Rev Phys Chem*, 63:519–40, 2012.

[172] S. van de Linde, S. Aufmkolk, C. Franke, T. Holm, T. Klein, A. Loschberger, S. Proppert, S. Wolter, and M. Sauer. Investigating cellular structures at the nanoscale with organic fluorophores. *Chem Biol*, 20(1):8–18, 2013.

[173] G. T. Dempsey, M. Bates, W. E. Kowtoniuk, D. R. Liu, R. Y. Tsien, and X. Zhuang. Photoswitching mechanism of cyanine dyes. *J Am Chem Soc*, 131(51):18192–3, 2009.

[174] J. Vogelsang, C. Steinhauer, C. Forthmann, I. H. Stein, B. Person-Skegro, T. Cordes, and P. Tinnefeld. Make them blink: probes for super-resolution microscopy. *Chemphyschem*, 11(12):2475–90, 2010.

[175] R. E. Thompson, D. R. Larson, and W. W. Webb. Precise nanometer localization analysis for individual fluorescent probes. *Biophys J*, 82(5):2775–83, 2002.

[176] U. Kubitscheck. *Fluorescence Microscopy: From Principles to Biological Applications*. Wiley-Blackwell, 2013.

[177] W. Lee, P. H. von Hippel, and A. H. Marcus. Internally labeled Cy3/Cy5 DNA constructs show greatly enhanced photo-stability in single-molecule FRET experiments. *Nucleic Acids Res*, 42(9):5967–77, 2014.

[178] C. Kleanthous. Swimming against the tide: progress and challenges in our understanding of colicin translocation. *Nat Rev Microbiol*, 8(12):843–8, 2010.

[179] G. Papadakos, N. G. Housden, K. J. Lilly, R. Kaminska, and C. Kleanthous. Kinetic basis for the competitive recruitment of TolB by the intrinsically disordered translocation domain of colicin E9. *J Mol Biol*, 418(5):269–80, 2012.

[180] E. Cascales, S. K. Buchanan, D. Duche, C. Kleanthous, R. Lloubes, K. Postle, M. Riley, S. Slatin, and D. Cavard. Colicin biology. *Microbiol Mol Biol Rev*, 71 (1):158–229, 2007.

[181] R. Wallis, G. R. Moore, R. James, and C. Kleanthous. Protein-protein interactions in colicin E9 DNase-immunity protein complexes. 1. Diffusion-controlled association and femtomolar binding for the cognate complex. *Biochemistry*, 34 (42):13743–50, 1995.

[182] C. Kleanthous, U. C. Kuhlmann, A. J. Pommer, N. Ferguson, S. E. Radford, G. R. Moore, R. James, and A. M. Hemmings. Structural and mechanistic basis of immunity toward endonuclease colicins. *Nat Struct Biol*, 6(3):243–52, 1999.

[183] U. C. Kuhlmann, A. J. Pommer, G. R. Moore, R. James, and C. Kleanthous. Specificity in protein-protein interactions: the structural basis for dual recognition in endonuclease colicin-immunity protein complexes. *J Mol Biol*, 301(5): 1163–78, 2000.

[184] P. H. Patel, M. Suzuki, E. Adman, A. Shinkai, and L. A. Loeb. Prokaryotic DNA polymerase I: evolution, structure, and ”base flipping” mechanism for nucleotide selection. *J Mol Biol*, 308(5):823–37, 2001.

[185] A. Hoffmann, D. Nettels, J. Clark, A. Borgia, S. E. Radford, J. Clarke, and B. Schuler. Quantifying heterogeneity and conformational dynamics from single molecule FRET of diffusing molecules: recurrence analysis of single particles (RASP). *Phys Chem Chem Phys*, 13(5):1857–71, 2011.

[186] S. J. Johnson, J. S. Taylor, and L. S. Beese. Processive DNA synthesis observed in a polymerase crystal suggests a mechanism for the prevention of frameshift mutations. *Proc Natl Acad Sci U S A*, 100(7):3895–900, 2003.

[187] S. J. Holden, S. Uphoff, and A. N. Kapanidis. DAOSTORM: an algorithm for high- density super-resolution microscopy. *Nat Methods*, 8(4):279–80, 2011.

[188] K. Jaqaman, D. Loerke, M. Mettlen, H. Kuwata, S. Grinstein, S. L. Schmid, and G. Danuser. Robust single-particle tracking in live-cell time-lapse sequences. *Nat Methods*, 5(8):695–702, 2008.

[189] S. Uphoff, S. J. Holden, L. Le Reste, J. Periz, S. van de Linde, M. Heilemann, and A. N. Kapanidis. Monitoring multiple distances within a single molecule using switchable fret. *Nat Methods*, 7(10):831–6, 2010.

[190] L. S. Churchman, Z. Okten, R. S. Rock, J. F. Dawson, and J. A. Spudich. Single molecule high-resolution colocalization of Cy3 and Cy5 attached to macromolecules measures intramolecular distances through time. *Proc Natl Acad Sci U S A*, 102(5):1419–23, 2005.

[191] A. R. Buxbaum, G. Haimovich, and R. H. Singer. In the right place at the right time: visualizing and understanding mRNA localization. *Nat Rev Mol Cell Biol*, 16(2):95–109, 2015.

[192] R. M. Long, R. H. Singer, X. Meng, I. Gonzalez, K. Nasmyth, and R. P. Jansen. Mating type switching in yeast controlled by asymmetric localization of ASH1 mRNA. *Science*, 277(5324):383–7, 1997.

[193] C. Eliscovich, A. R. Buxbaum, Z. B. Katz, and R. H. Singer. mRNA on the move: the road to its biological destiny. *J Biol Chem*, 288(28):20361–8, 2013.

[194] K. Nevo-Dinur, A. Nussbaum-Shochat, S. Ben-Yehuda, and O. Amster-Choder. Translation-independent localization of mRNA in E. coli. *Science*, 331(6020): 1081–4, 2011.

[195] A. M. Femino, F. S. Fay, K. Fogarty, and R. H. Singer. Visualization of single RNA transcripts in situ. *Science*, 280(5363):585–90, 1998.

[196] E. Bertrand, P. Chartrand, M. Schaefer, S. M. Shenoy, R. H. Singer, and R. M. Long. Localization of ASH1 mRNA particles in living yeast. *Mol Cell*, 2(4): 437–45, 1998.

[197] T. T. Weil, R. M. Parton, and I. Davis. Making the message clear: visualizing mRNA localization. *Trends Cell Biol*, 20(7):380–90, 2010.

[198] A. S. Brodsky and P. A. Silver. Identifying proteins that affect mRNA localization in living cells. *Methods*, 26(2):151–5, 2002.

[199] D. Fusco, N. Accornero, B. Lavoie, S. M. Shenoy, J. M. Blanchard, R. H. Singer, and E. Bertrand. Single mRNA molecules demonstrate probabilistic movement in living mammalian cells. *Curr Biol*, 13(2):161–7, 2003.

[200] T. J. Carrocci and A. A. Hoskins. Imaging of RNAs in live cells with spectrally diverse small molecule fluorophores. *Analyst*, 139(1):44–7, 2014.

[201] M. C. Capece, G. L. Kornberg, A. Petrov, and J. D. Puglisi. A simple real-time assay for in vitro translation. *RNA*, 21(2):296–305, 2015.

[202] J. S. Paige, K. Y. Wu, and S. R. Jaffrey. RNA mimics of green fluorescent protein. *Science*, 333(6042):642–6, 2011.

[203] E. V. Dolgosheina, S. C. Jeng, S. S. Panchapakesan, R. Cojocaru, P. S. Chen, P. D. Wilson, N. Hawkins, P. A. Wiggins, and P. J. Unrau. RNA mango aptamer-fluorophore: a bright, high-affinity complex for RNA labeling and tracking. *ACS Chem Biol*, 9(10):2412–20, 2014.

[204] V. L. Zimyanin, K. Belaya, J. Pecreaux, M. J. Gilchrist, A. Clark, I. Davis, and D. St Johnston. In vivo imaging of oskar mRNA transport reveals the mechanism of posterior localization. *Cell*, 134(5):843–53, 2008.

[205] B. McIntosh, V. Ramachandiran, G. Kramer, and B. Hardesty. Initiation of protein synthesis with fluorophore-Met-tRNA(f) and the involvement of IF-2. *Biochimie*, 82(2):167–74, 2000.

[206] H. G. Schleich, W. Wintermeyer, and H. G. Zachau. Replacement of wybutine by hydrazines and its effect on the active conformation of yeast tRNAPhe. *Nucleic Acids Res*, 5(5):1701–13, 1978.

[207] S. C. Blanchard, R. L. Gonzalez, H. D. Kim, S. Chu, and J. D. Puglisi. tRNA selection and kinetic proofreading in translation. *Nat Struct Mol Biol*, 11(10): 1008–14, 2004.

[208] S. C. Blanchard, H. D. Kim, Jr. Gonzalez, R. L., J. D. Puglisi, and S. Chu. tRNA dynamics on the ribosome during translation. *Proc Natl Acad Sci U S A*, 101 (35):12893–8, 2004.

[209] J. B. Munro, R. B. Altman, N. O'Connor, and S. C. Blanchard. Identification of two distinct hybrid state intermediates on the ribosome. *Mol Cell*, 25(4): 505–17, 2007.

[210] J. Fei, P. Kosuri, D. D. MacDougall, and Jr. Gonzalez, R. L. Coupling of ribosomal L1 stalk and tRNA dynamics during translation elongation. *Mol Cell*, 30(3):348–59, 2008.

[211] D. Pan, H. Qin, and B. S. Cooperman. Synthesis and functional activity of tRNAs labeled with fluorescent hydrazides in the D-loop. *RNA*, 15(2):346–54, 2009.

[212] W. Wintermeyer and H. G. Zachau. Fluorescent derivatives of yeast tRNAPhe. *Eur J Biochem*, 98(2):465–75, 1979.

[213] M. V. Rodnina, R. Fricke, and W. Wintermeyer. Transient conformational states of aminoacyl-tRNA during ribosome binding catalyzed by elongation factor Tu. *Biochemistry*, 33(40):12267–75, 1994.

[214] U. Kothe and M. V. Rodnina. Codon reading by tRNAAla with modified uridine in the wobble position. *Mol Cell*, 25(1):167–74, 2007.

[215] T. Betteridge, H. Liu, H. Gamper, S. Kirillov, B. S. Cooperman, and Y. M. Hou. Fluorescent labeling of tRNAs for dynamics experiments. *RNA*, 13(9):1594–601, 2007.

[216] J. Kaur, M. Raj, and B. S. Cooperman. Fluorescent labeling of tRNA dihydrouridine residues: Mechanism and distribution. *RNA*, 17(7):1393–400, 2011.

[217] T. H. Lee, S. C. Blanchard, H. D. Kim, J. D. Puglisi, and S. Chu. The role of fluctuations in tRNA selection by the ribosome. *Proc Natl Acad Sci U S A*, 104 (34):13661–5, 2007.

[218] J. Fei, J. E. Bronson, J. M. Hofman, R. L. Srinivas, C. H. Wiggins, and Jr. Gonzalez, R. L. Allosteric collaboration between elongation factor G and the ribosomal L1 stalk directs tRNA movements during translation. *Proc Natl Acad Sci U S A*, 106(37):15702–7, 2009.

[219] S. Uemura, C. E. Aitken, J. Korlach, B. A. Flusberg, S. W. Turner, and J. D. Puglisi. Real-time tRNA transit on single translating ribosomes at codon resolution. *Nature*, 464(7291):1012–7, 2010.

[220] J. Chen, A. Petrov, M. Johansson, A. Tsai, S. E. O'Leary, and J. D. Puglisi. Dynamic pathways of -1 translational frameshifting. *Nature*, 512(7514):328–32, 2014.

[221] N. Fischer, A. L. Konevega, W. Wintermeyer, M. V. Rodnina, and H. Stark. Ribosome dynamics and tRNA movement by time-resolved electron cryomicroscopy. *Nature*, 466(7304):329–33, 2010.

[222] S. Barhoom, J. Kaur, B. S. Cooperman, N. I. Smorodinsky, Z. Smilansky, M. Ehrlich, and O. Elroy-Stein. Quantitative single cell monitoring of protein synthesis at subcellular resolution using fluorescently labeled tRNA. *Nucleic Acids Res*, 39(19):e129, 2011.

[223] S. Barhoom, I. Farrell, B. Shai, D. Dahary, B. S. Cooperman, Z. Smilansky, O. Elroy-Stein, and M. Ehrlich. Dicodon monitoring of protein synthesis (DiCoMPS) reveals levels of synthesis of a viral protein in single cells. *Nucleic Acids Res*, 41(18):e177, 2013.

[224] S. Bakshi, A. Siryaporn, M. Goulian, and J. C. Weisshaar. Superresolution imaging of ribosomes and RNA polymerase in live Escherichia coli cells. *Mol Microbiol*, 85(1):21–38, 2012.

[225] A. Sanamrad, F. Persson, E. G. Lundius, D. Fange, A. H. Gynna, and J. Elf. Single-particle tracking reveals that free ribosomal subunits are not excluded from the Escherichia coli nucleoid. *Proc Natl Acad Sci U S A*, 111(31):11413–8, 2014.

[226] S. Proshkin, A. R. Rahmouni, A. Mironov, and E. Nudler. Cooperation between translating ribosomes and RNA polymerase in transcription elongation. *Science*, 328(5977):504–8, 2010.

[227] M. Stracy, C. Lesterlin, F. Garza de Leon, S. Uphoff, P. Zawadzki, and A. N. Kapanidis. Live-cell superresolution microscopy reveals the organization of RNA polymerase in the bacterial nucleoid. *Proc Natl Acad Sci U S A*, 2015.

[228] S. Bakshi, H. Choi, J. Mondal, and J. C. Weisshaar. Time-dependent effects of transcription- and translation-halting drugs on the spatial distributions of the Escherichia coli chromosome and ribosomes. *Mol Microbiol*, 94(4):871–87, 2014.

[229] W. Wang, G. W. Li, C. Chen, X. S. Xie, and X. Zhuang. Chromosome organization by a nucleoid-associated protein in live bacteria. *Science*, 333(6048): 1445–9, 2011.

[230] P. P. Dennis and H. Bremer. Differential rate of ribosomal protein synthesis in Escherichia coli B/r. *J Mol Biol*, 84(3):407–22, 1974.

[231] J. Parker. Errors and alternatives in reading the universal genetic code. *Microbiol Rev*, 53(3):273–98, 1989.

[232] N. Billinton and A. W. Knight. Seeing the wood through the trees: a review of techniques for distinguishing green fluorescent protein from endogenous autofluorescence. *Anal Biochem*, 291(2):175–97, 2001.

[233] A. Werner. Predicting translational diffusion of evolutionary conserved RNA structures by the nucleotide number. *Nucleic Acids Res*, 39(3):e17, 2011.

[234] H. Shi and P. B. Moore. The crystal structure of yeast phenylalanine tRNA at 1.93 A resolution: a classic structure revisited. *RNA*, 6(8):1091–105, 2000.

[235] T. Ando and J. Skolnick. Crowding and hydrodynamic interactions likely dominate in vivo macromolecular motion. *Proc Natl Acad Sci U S A*, 107(43): 18457–62, 2010.

[236] M. C. Konopka, I. A. Shkel, S. Cayley, M. T. Record, and J. C. Weisshaar. Crowding and confinement effects on protein diffusion in vivo. *J Bacteriol*, 188 (17):6115–23, 2006.

[237] M. Kumar, M. S. Mommer, and V. Sourjik. Mobility of cytoplasmic, membrane, and DNA-binding proteins in Escherichia coli. *Biophys J*, 98(4):552–9, 2010.

[238] M. B. Elowitz, M. G. Surette, P. E. Wolf, J. B. Stock, and S. Leibler. Protein mobility in the cytoplasm of escherichia coli. *J Bacteriol*, 181(1):197–203, 1999.

[239] G. van den Bogaart, N. Hermans, V. Krasnikov, and B. Poolman. Protein mobility and diffusive barriers in Escherichia coli: consequences of osmotic stress. *Mol Microbiol*, 64(3):858–71, 2007.

[240] A. Nenninger, G. Mastroianni, and C. W. Mullineaux. Size dependence of protein diffusion in the cytoplasm of Escherichia coli. *J Bacteriol*, 192(18):4535–40, 2010.

[241] S. Hasnain, C. L. McClendon, M. T. Hsu, M. P. Jacobson, and P. Bandyopadhyay. A new coarse-grained model for E. coli cytoplasm: accurate calculation of the diffusion coefficient of proteins and observation of anomalous diffusion. *PLoS One*, 9(9):e106466, 2014.

[242] M. Gouy and R. Grantham. Polypeptide elongation and tRNA cycling in Escherichia coli: a dynamic approach. *FEBS Lett*, 115(2):151–5, 1980.

[243] B. S. Negrutskii and M. P. Deutscher. Channeling of aminoacyl-tRNA for protein synthesis in vivo. *Proc Natl Acad Sci U S A*, 88(11):4991–5, 1991.

[244] R. Stapulionis and M. P. Deutscher. A channeled tRNA cycle during mammalian protein synthesis. *Proc Natl Acad Sci U S A*, 92(16):7158–61, 1995.

[245] M. Mirande. Processivity of translation in the eukaryote cell: role of aminoacyl-tRNA synthetases. *FEBS Lett*, 584(2):443–7, 2010.

[246] N. Bilgin, M. Ehrenberg, C. Ebel, G. Zaccai, Z. Sayers, M. H. Koch, D. I. Svergun, C. Barberato, V. Volkov, P. Nissen, and J. Nyborg. Solution structure of the ternary complex between aminoacyl-tRNA, elongation factor Tu, and guanosine triphosphate. *Biochemistry*, 37(22):8163–72, 1998.

[247] M. D. Bradley, M. B. Beach, A. P. de Koning, T. S. Pratt, and R. Osuna. Effects of Fis on Escherichia coli gene expression during different growth stages. *Microbiology*, 153(Pt 9):2922–40, 2007.

[248] J. A. Dunkle, L. Xiong, A. S. Mankin, and J. H. Cate. Structures of the Escherichia coli ribosome with antibiotics bound near the peptidyl transferase center explain spectra of drug action. *Proc Natl Acad Sci U S A*, 107(40):17152–7, 2010.

[249] J. E. Aubin. Autofluorescence of viable cultured mammalian cells. *J Histochem Cytochem*, 27(1):36–43, 1979.

[250] C. J. Tynan, D. T. Clarke, B. C. Coles, D. J. Rolfe, M. L. Martin-Fernandez, and S. E. Webb. Multicolour single molecule imaging in cells with near infra-red dyes. *PLoS One*, 7(4):e36265, 2012.

[251] R. O. Potts, Jr. Ford, N. C., and M. J. Fournier. Changes in the solution structure of yeast phenylalanine transfer ribonucleic acid associated with aminoacylation and magnesium binding. *Biochemistry*, 20(6):1653–9, 1981.

[252] J. Antosiewicz and D. Porschke. Effect of aminoacylation on tRNA conformation. *Eur Biophys J*, 17(4):233–5, 1989.

[253] H. J. Defeu Soufo, C. Reimold, U. Linne, T. Knust, J. Gescher, and P. L. Graumann. Bacterial translation elongation factor EF-Tu interacts and colocalizes with actin-like MreB protein. *Proc Natl Acad Sci U S A*, 107(7):3163–8, 2010.

[254] S. Klumpp, M. Scott, S. Pedersen, and T. Hwa. Molecular crowding limits translation and cell growth. *Proc Natl Acad Sci U S A*, 110(42):16754–9, 2013.

[255] H. Dong, L. Nilsson, and C. G. Kurland. Co-variation of tRNA abundance and codon usage in Escherichia coli at different growth rates. *J Mol Biol*, 260(5): 649–63, 1996.

[256] G. A. Mackie. RNase E: at the interface of bacterial RNA processing and decay. *Nat Rev Microbiol*, 11(1):45–57, 2013.

[257] O. Sliusarenko, J. Heinritz, T. Emonet, and C. Jacobs-Wagner. High-throughput, subpixel precision analysis of bacterial morphogenesis and intracellular spatio-temporal dynamics. *Mol Microbiol*, 80(3):612–27, 2011.

[258] B. Alberts, A. Johnson, J. Lewis, M. Raff, K. Roberts, and P. Walter. *Molecular Biology of the Cell*. Garland Science, 5 edition, 2007.

[259] R. M. Saecker, Jr. Record, M. T., and P. L. Dehaseth. Mechanism of bacterial transcription initiation: RNA polymerase - promoter binding, isomerization to initiation-competent open complexes, and initiation of RNA synthesis. *J Mol Biol*, 412(5):754–71, 2011.

[260] K. S. Murakami and S. A. Darst. Bacterial RNA polymerases: the wholo story. *Curr Opin Struct Biol*, 13(1):31–9, 2003.

[261] A. J. Carpousis and J. D. Gralla. Cycling of ribonucleic acid polymerase to produce oligonucleotides during initiation in vitro at the lac UV5 promoter. *Biochemistry*, 19(14):3245–53, 1980.

[262] L. M. Hsu. Monitoring abortive initiation. *Methods*, 47(1):25–36, 2009.

[263] J. Mukhopadhyay, A. N. Kapanidis, V. Mekler, E. Kortkhonjia, Y. W. Ebright, and R. H. Ebright. Translocation of sigma(70) with RNA polymerase during transcription: fluorescence resonance energy transfer assay for movement relative to DNA. *Cell*, 106(4):453–63, 2001.

[264] J. D. Gralla, A. J. Carpousis, and J. E. Stefano. Productive and abortive initiation of transcription in vitro at the lac UV5 promoter. *Biochemistry*, 19(25): 5864–9, 1980.

[265] A. Chakraborty, D. Wang, Y. W. Ebright, Y. Korlann, E. Kortkhonjia, T. Kim, S. Chowdhury, S. Wigneshweraraj, H. Irschik, R. Jansen, B. T. Nixon, J. Knight, S. Weiss, and R. H. Ebright. Opening and closing of the bacterial RNA polymerase clamp. *Science*, 337(6094):591–5, 2012.

[266] K. S. Murakami, S. Masuda, E. A. Campbell, O. Muzzin, and S. A. Darst. Structural basis of transcription initiation: an RNA polymerase holoenzyme-DNA complex. *Science*, 296(5571):1285–90, 2002.

[267] D. G. Vassylyev, S. Sekine, O. Laptenko, J. Lee, M. N. Vassylyeva, S. Borukhov, and S. Yokoyama. Crystal structure of a bacterial RNA polymerase holoenzyme at 2.6 A resolution. *Nature*, 417(6890):712–9, 2002.

[268] R. S. Basu, B. A. Warner, V. Molodtsov, D. Pupov, D. Esyunina, C. Fernandez-Tornero, A. Kulbachinskiy, and K. S. Murakami. Structural basis of transcription initiation by bacterial RNA polymerase holoenzyme. *J Biol Chem*, 289(35): 24549–59, 2014.

[269] Y. Zuo and T. A. Steitz. Crystal structures of the E. coli transcription initiation complexes with a complete bubble. *Mol Cell*, 58(3):534–40, 2015.

[270] D. F. Browning and S. J. Busby. The regulation of bacterial transcription initiation. *Nat Rev Microbiol*, 2(1):57–65, 2004.

[271] L. M. Hsu. Promoter clearance and escape in prokaryotes. *Biochim Biophys Acta*, 1577(2):191–207, 2002.

[272] T. Kubori and N. Shimamoto. A branched pathway in the early stage of transcription by Escherichia coli RNA polymerase. *J Mol Biol*, 256(3):449–57, 1996.

[273] A. Revyakin, C. Liu, R. H. Ebright, and T. R. Strick. Abortive initiation and productive initiation by RNA polymerase involve DNA scrunching. *Science*, 314(5802):1139–43, 2006.

[274] E. Margeat, A. N. Kapanidis, P. Tinnefeld, Y. Wang, J. Mukhopadhyay, R. H. Ebright, and S. Weiss. Direct observation of abortive initiation and promoter escape within single immobilized transcription complexes. *Biophys J*, 90(4): 1419–31, 2006.

[275] S. R. Goldman, R. H. Ebright, and B. E. Nickels. Direct detection of abortive RNA transcripts in vivo. *Science*, 324(5929):927–8, 2009.

[276] M. T. Marr and J. W. Roberts. Function of transcription cleavage factors GreA and GreB at a regulatory pause site. *Mol Cell*, 6(6):1275–85, 2000.

[277] N. Opalka, M. Chlenov, P. Chacon, W. J. Rice, W. Wriggers, and S. A. Darst. Structure and function of the transcription elongation factor GreB bound to bacterial RNA polymerase. *Cell*, 114(3):335–45, 2003.

[278] T. Cordes, Y. Santoso, A. I. Tomescu, K. Gryte, L. C. Hwang, B. Camara, S. Wigneshweraraj, and A. N. Kapanidis. Sensing DNA opening in transcription using quenchable Forster resonance energy transfer. *Biochemistry*, 49 (43):9171–80, 2010.

[279] N. C. Robb, T. Cordes, L. C. Hwang, K. Gryte, D. Duchi, T. D. Craggs, Y. Santoso, S. Weiss, R. H. Ebright, and A. N. Kapanidis. The transcription bubble of the RNA polymerase-promoter open complex exhibits conformational heterogeneity and millisecond-scale dynamics: implications for transcription start-site selection. *J Mol Biol*, 425(5):875–85, 2013.

[280] V. Mekler, E. Kortkhonjia, J. Mukhopadhyay, J. Knight, A. Revyakin, A. N. Kapanidis, W. Niu, Y. W. Ebright, R. Levy, and R. H. Ebright. Structural organization of bacterial RNA polymerase holoenzyme and the RNA polymerase-promoter open complex. *Cell*, 108(5):599–614, 2002.

[281] W. R. McClure and C. L. Cech. On the mechanism of rifampicin inhibition of RNA synthesis. *J Biol Chem*, 253(24):8949–56, 1978.

[282] E. A. Campbell, N. Korzheva, A. Mustaev, K. Murakami, S. Nair, A. Goldfarb, and S. A. Darst. Structural mechanism for rifampicin inhibition of bacterial RNA polymerase. *Cell*, 104(6):901–12, 2001.

[283] C. Coronelli, R. J. White, G. C. Lancini, and F. Parenti. Lipiarmycin, a new antibiotic from Actinoplanes. II. Isolation, chemical, biological and biochemical characterization. *J Antibiot (Tokyo)*, 28(4):253–9, 1975.

[284] A. Tupin, M. Gualtieri, J. P. Leonetti, and K. Brodolin. The transcription inhibitor lipiarmycin blocks DNA fitting into the RNA polymerase catalytic site. *EMBO J*, 29(15):2527–37, 2010.

[285] M. H. Buckstein, J. He, and H. Rubin. Characterization of nucleotide pools as a function of physiological state in Escherichia coli. *J Bacteriol*, 190(2):718–26, 2008.

[286] D. Duchi, D. L. V. Bauer, L. Fernandez, G. W. Evans, N. C. Robb, L. C. Hwang, K. Gryte, A. I. Tomescu, P. Zawadzki, Z. Morichaud, K. Brodolin, and A. N. Kapanidis. RNA polymerase pausing during initial transcription. *in preparation*, 2015.

[287] A. Travers and G. Muskhelishvili. DNA supercoiling - a global transcriptional regulator for enterobacterial growth? *Nat Rev Microbiol*, 3(2):157–69, 2005.

[288] H. Y. Wu, S. H. Shyy, J. C. Wang, and L. F. Liu. Transcription generates positively and negatively supercoiled domains in the template. *Cell*, 53(3):433–40, 1988.

[289] Y. P. Tsao, H. Y. Wu, and L. F. Liu. Transcription-driven supercoiling of DNA: direct biochemical evidence from in vitro studies. *Cell*, 56(1):111–8, 1989.

[290] J. Mukhopadhyay, K. Das, S. Ismail, D. Koppstein, M. Jang, B. Hudson, S. Sarafianos, S. Tuske, J. Patel, R. Jansen, H. Irschik, E. Arnold, and R. H. Ebright. The RNA polymerase "switch region" is a target for inhibitors. *Cell*, 135(2):295–307, 2008.

[291] G. A. Belogurov, M. N. Vassylyeva, A. Sevostyanova, J. R. Appleman, A. X. Xiang, R. Lira, S. E. Webber, S. Klyuyev, E. Nudler, I. Artsimovitch, and D. G. Vassylyev. Transcription inactivation through local refolding of the RNA polymerase structure. *Nature*, 457(7227):332–5, 2009.

[292] A. Srivastava, M. Talaue, S. Liu, D. Degen, R. Y. Ebright, E. Sineva, A. Chakraborty, S. Y. Druzhinin, S. Chatterjee, J. Mukhopadhyay, Y. W. Ebright, A. Zozula, J. Shen, S. Sengupta, R. R. Niedfeldt, C. Xin, T. Kaneko, H. Irschik,

R. Jansen, S. Donadio, N. Connell, and R. H. Ebright. New target for inhibition of bacterial RNA polymerase: 'switch region'. *Curr Opin Microbiol*, 14(5): 532–43, 2011.

[293] M. H. Larson, R. A. Mooney, J. M. Peters, T. Windgassen, D. Nayak, C. A. Gross, S. M. Block, W. J. Greenleaf, R. Landick, and J. S. Weissman. A pause sequence enriched at translation start sites drives transcription dynamics in vivo. *Science*, 344(6187):1042–7, 2014.

[294] I. O. Vvedenskaya, H. Vahedian-Movahed, J. G. Bird, J. G. Knoblauch, S. R. Goldman, Y. Zhang, R. H. Ebright, and B. E. Nickels. Interactions between RNA polymerase and the "core recognition element" counteract pausing. *Science*, 344(6189):1285–9, 2014.

[295] V. Marx. Probes: paths to photostability. *Nature Methods*, 12(3):187–190, 2015.

[296] N. Akyuz, E. R. Georgieva, Z. Zhou, S. Stolzenberg, M. A. Cuendet, G. Khelashvili, R. B. Altman, D. S. Terry, J. H. Freed, H. Weinstein, O. Boudker, and S. C. Blanchard. Transport domain unlocking sets the uptake rate of an aspartate transporter. *Nature*, 518(7537):68–+, 2015.

[297] J. B. Grimm, B. P. English, J. J. Chen, J. P. Slaughter, Z. J. Zhang, A. Revyakin, R. Patel, J. J. Macklin, D. Normanno, R. H. Singer, T. Lionnet, and L. D. Lavis. A general method to improve fluorophores for live-cell and single-molecule microscopy. *Nature Methods*, 12(3):244–+, 2015.

[298] J. Huisken, J. Swoger, F. Del Bene, J. Wittbrodt, and E. H. Stelzer. Optical sectioning deep inside live embryos by selective plane illumination microscopy. *Science*, 305(5686):1007–9, 2004.

[299] C. J. Engelbrecht and E. H. Stelzer. Resolution enhancement in a light-sheet-based microscope (SPIM). *Opt Lett*, 31(10):1477–9, 2006.

[300] A. P. Singh, J. W. Krieger, J. Buchholz, E. Charbon, J. Langowski, and T. Wohland. The performance of 2D array detectors for light sheet based fluorescence correlation spectroscopy. *Opt Express*, 21(7):8652–68, 2013.

[301] T. V. Truong, W. Supatto, D. S. Koos, J. M. Choi, and S. E. Fraser. Deep and fast live imaging with two-photon scanned light-sheet microscopy. *Nat Methods*, 8 (9):757–60, 2011.

[302] F. Cella Zanacchi, Z. Lavagnino, M. Perrone Donnorso, A. Del Bue, L. Furia, M. Faretta, and A. Diaspro. Live-cell 3D super-resolution imaging in thick biological samples. *Nat Methods*, 8(12):1047–9, 2011.

[303] P. J. Keller and E. H. Stelzer. Quantitative in vivo imaging of entire embryos with Digital Scanned Laser Light Sheet Fluorescence Microscopy. *Curr Opin Neurobiol*, 18(6):624–32, 2008.

[304] T. A. Planchon, L. Gao, D. E. Milkie, M. W. Davidson, J. A. Galbraith, C. G. Galbraith, and E. Betzig. Rapid three-dimensional isotropic imaging of living cells using Bessel beam plane illumination. *Nat Methods*, 8(5):417–23, 2011.

[305] T. Vettenburg, H. I. Dalgarno, J. Nylk, C. Coll-Llado, D. E. Ferrier, T. Cizmar, F. J. Gunn-Moore, and K. Dholakia. Light-sheet microscopy using an Airy beam. *Nat Methods*, 11(5):541–4, 2014.

[306] F. Huang, T. M. Hartwich, F. E. Rivera-Molina, Y. Lin, W. C. Duim, J. J. Long, P. D. Uchil, J. R. Myers, M. A. Baird, W. Mothes, M. W. Davidson, D. Toomre, and J. Bewersdorf. Video-rate nanoscopy using sCMOS camera-specific single-molecule localization algorithms. *Nat Methods*, 10(7):653–8, 2013.

[307] J. A. Conchello and J. W. Lichtman. Optical sectioning microscopy. *Nat Methods*, 2(12):920–31, 2005.

[308] P. F. May, J. N. Pinkney, P. Zawadzki, G. W. Evans, D. J. Sherratt, and A. N. Kapanidis. Tethered fluorophore motion: studying large DNA conformational changes by single-fluorophore imaging. *Biophys J*, 107(5):1205–16, 2014.